Electronic Thesis and Dissertation Repository

9-19-2012 12:00 AM

An Image-Based Tool to Examine Joint Congruency at the Elbow

Emily A. Lalone, *The University of Western Ontario*

© Emily A. Lalone 2012

Follow this and additional works at: https://ir.lib.uwo.ca/etd

Part of the Biological Engineering Commons

AN IMAGE-BASED TOOL TO EXAMINE JOINT CONGRUENCY AT THE ELBOW

(Spine Title: An Image-Based Tool to Examine Joint Congruency at the Elbow)

(Thesis format: Integrated Article)

by

Emily Allen Lalone

Graduate Program
in
Biomedical Engineering

A thesis submitted in partial fulfillment
of the requirements for the degree of
Doctor of Philosophy

School of Graduate and Postdoctoral Studies
The University of Western Ontario
London, Ontario, Canada

© Emily A. Lalone 2012

THE UNIVERSITY OF WESTERN ONTARIO
School of Graduate and Postdoctoral Studies

CERTIFICATE OF EXAMINATION

Supervisor

_____
Dr. James Johnson

Co-Supervisors

_____
Dr. Graham King

_____
Dr. Terry Peters

Examiners

_____
Dr. Hanif Ladak

_____
Dr. Jim Dickey

_____
Dr. Ken Faber

_____
Dr. David Wilson

The thesis by

Emily Allen <u>Lalone</u>

entitled:
**An Image-Based Tool to
Examine Joint
Congruency at the
Elbow**
is accepted in partial fulfillment of the
requirements for the degree of Doctor
of Philosophy

Date_____   _____
                                Chair of the Thesis Examination Board

ABSTRACT

Post-traumatic osteoarthritis commonly occurs as a result of a traumatic event to the articulation. Although the majority of this type of arthritis is preventable, the sequence and mechanism of the interaction between joint injury and the development of osteoarthritis (OA) is not well understood. It is hypothesized that alterations to the joint alignment can cause excessive and damaging wear to the cartilage surfaces resulting in OA. The lack of understanding of both the cause and progression of OA has contributed to the slow development of interventions which can modify the course of the disease. Currently, no techniques have been developed to examine the relationship between joint injury and joint alignment. Therefore, the objective of this thesis was to develop a non-invasive image-based technique that can be used to assess joint congruency and alignment of joints undergoing physiologic motion. An inter-bone distance algorithm was developed and validated to measure joint congruency at the ulnohumeral joint of the elbow. Subsequently, a registration algorithm was created and its accuracy was assessed. This registration algorithm registered 3D reconstructed bone models obtained using x-ray CT to motion capture data of cadaveric upper extremities undergoing simulated elbow flexion. In this way, the relative position and orientation of the 3D bone models could be visualized throughout the motion. Radial head arthroplasty was used to illustrate the utility of this technique. Once this registration was refined, the inter-bone distance algorithm was integrated to visualize the joint congruency of the ulnohumeral joint undergoing simulated elbow flexion. The effect of collateral ligament repair was examined. This technique proved to be sensitive enough to detect large changes in joint congruency in spite of only small changes in the motion pathways of the ulnohumeral joint following simulated ligament repair. Efforts were also made in this thesis to translate this research into a clinical environment by examining CT scanning protocols that could reduce the amount of radiation exposure required to image patient's joints. For this study, the glenohumeral joint of the shoulder was examined as this joint is particularly sensitive to potential harmful effects of radiation due to its proximity to highly radiosensitive organs. Using the CT scanning techniques examined in this thesis, the effective dose

applied to the shoulder was reduced by almost 90% compared to standard clinical CT imaging.

In summary, these studies introduced a technique that can be used to non-invasively and three-dimensionally examine joint congruency. The accuracy of this technique was assessed and its ability to predict regions of joint surface interactions was validated against a gold standard casting approach. Using the techniques developed in this thesis the complex relationship between injury, loading and mal-alignment as contributors to the development and progression of osteoarthritis in the upper extremity can be examined.

KEYWORDS:

Elbow, registration, joint congruency, 3D reconstruction, x-ray CT, orthopaedic, motion capture, ulnohumeral joint.

CO-AUTHORSHIP STATEMENTS:

Chapter 1:   Emily Lalone - sole author

Chapter 2:   Emily Lalone- concept and design of study, acquisition of data, data analysis, interpretation of data, drafting document; Colin McDonald- concept and design of study, interpretation of data, data analysis, reviewed manuscript; Louis Ferreira- interpretation of data, reviewed manuscript; Terry Peters- concept and design of study, interpretation of data, reviewed manuscript; Graham King- concept and design of study, interpretation of data, reviewed manuscript; James Johnson- concept and design of study, interpretation of data, reviewed manuscript.

Chapter 3:   Emily Lalone -concept and design of study, acquisition of data, data analysis, interpretation of data, drafting document; Colin McDonald- concept and design of study, interpretation of data, data analysis, reviewed manuscript; Louis Ferreira- interpretation of data, reviewed manuscript; Terry Peters- concept and design of study, interpretation of data, reviewed manuscript; Graham King- concept and design of study, interpretation of data, reviewed manuscript; James Johnson- concept and design of study, interpretation of data, reviewed manuscript.

Chapter 4:   Emily Lalone -concept and design of study, acquisition of data, data analysis, interpretation of data, drafting document;   Terry Peters- concept and design of study,   interpretation of data, reviewed manuscript; Graham King- concept and design of study, interpretation of data, reviewed manuscript; James Johnson- concept and design of study, interpretation of data, reviewed manuscript.

Chapter 5:   Emily Lalone -concept and design of study, acquisition of data, data analysis, interpretation of data, drafting document;   Josh Giles- Data Analysis, Revised Manuscript, Bashar Alolabi- concept and design of study, acquisition of data, reviewed manuscript; Terry Peters- concept and design of study, interpretation of data, reviewed manuscript; Graham King- concept and design of study, interpretation of data, reviewed manuscript; James Johnson- concept and design of study, interpretation of data, reviewed manuscript.

Chapter 6:   Emily Lalone -concept and design of study, acquisition of data, data

analysis, interpretation of data, drafting document; Anne-Marie Fox- concept and design of study, acquisition of data, reviewed manuscript;   Angela Kedgley- concept and design of study, acquisition of data, reviewed manuscript; Thomas Jenkyn, concept and design of study, reviewed manuscript, George Athwal, concept and design of study, reviewed manuscript; Terry Peters- concept and design of study, interpretation of data, reviewed manuscript; Graham King- concept and design of study, interpretation of data, reviewed manuscript; James Johnson- concept and design of study, interpretation of data, reviewed manuscript.

Chapter 7:   Emily Lalone - sole author

ACKNOWLEDGEMENTS:

CONTENTS

LIST OF CHARTS

LIST OF FIGURES

Chapter 1 – Introduction

OVERVIEW

The objective of this thesis was to develop an imaged-based technique to quantify and examine congruency of the ulnohumeral joint of the elbow, to validate its use and examine its accuracy, and to examine the utility of this technique in the setting of a simulated orthopaedic injury. This chapter reviews the relevant anatomy, kinematics and joint biomechanics of the elbow. A review of current contact area measurement techniques is also included as well as a synopsis of three-dimensional rendering techniques used in biomechanics. The chapter concludes with the rationale, objectives and hypothesis of this work.

1.1 The Elbow

The elbow represents one of the most complex and functionally important joints in the upper extremity. It can be described as a trochoginglymoid joint because of the combination of trochoid motion (rotation) and ginglymus motion (hinge) (Morrey, 2000b). The elbow consists of three bones, the humerus, radius and ulna which form three articulations (Figure 1.1). The radius and ulna contact at the proximal end of the forearm as the proximal radioulnar joint. The radius articulates with the distal humerus as the radiocapitellar joint and the proximal ulna articulates with the humerus as the ulnohumeral joint (Figure 1.1). In addition to the interacting shapes of the articulations, the elbow is stabilized by two groups of ligaments and twenty-four muscles which allow the elbow to move from an average of 0.6 ± 3.1 degrees of extension to 142.9 ± 5.6 flexion as well as rotate from approximately 75° of pronation to 85° of supination (Boone and Azen, 1979).

1.1.1   OSSEOUS ANATOMY

The three bones of the elbow provide the primary structural and load bearing support.

Distal Humerus - The distal humerus consists of two condyles, forming the articulating surfaces of the trochlea and capitellum (Figure 1.2). The most prominent aspects of the humerus are the medial and lateral epicondyles. These bony landmarks serve as attachment sites for the medial and lateral collateral ligaments respectively. Additionally, there are three fossae on the distal humerus, which function as stabilizers during extremes of flexion and extension. Proximal to the posterior surface of the trochlea is the olecranon fossa (Figure 1.3). This fossa receives the olecranon process of the proximal ulna during extension. Similarly, the coronoid fossa, located on the anterior side of the trochlea, receives the coronoid process of the proximal ulna during flexion. The radial fossa which appears proximal to capitellum on the anterior aspect of the humerus, serves as an endpoint for the radius at maximum flexion (Morrey, 2000a).

Proximal Radius - The proximal end of the radius articulates with the spherical shaped capitellum of the humerus (Figure 1.4). The head of the radius approximates an ellipse with a concave dome which when contacting the capitellum, forms a ball and socket joint. Additionally, the head of the radius articulates with the lesser sigmoid notch of the ulna to allow for forearm rotation. Distal to the head, the bone tapers to form the radial neck (Morrey, 2000a).
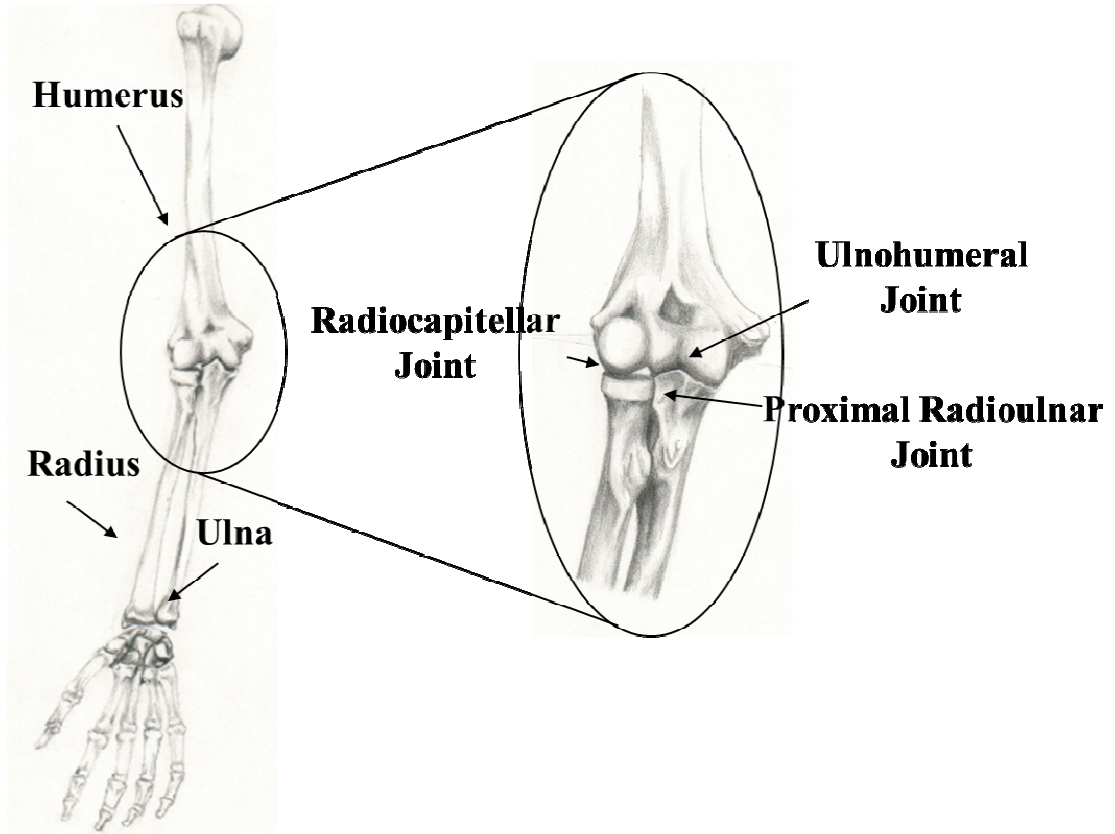
Figure 1.1: The Joints of the Upper Extremity
The three bones of the elbow: the humerus, the radius and the ulna. These bones come together to form three joints of the elbow: the ulnohumeral, radiocapitellar, proximal radioulnar joint
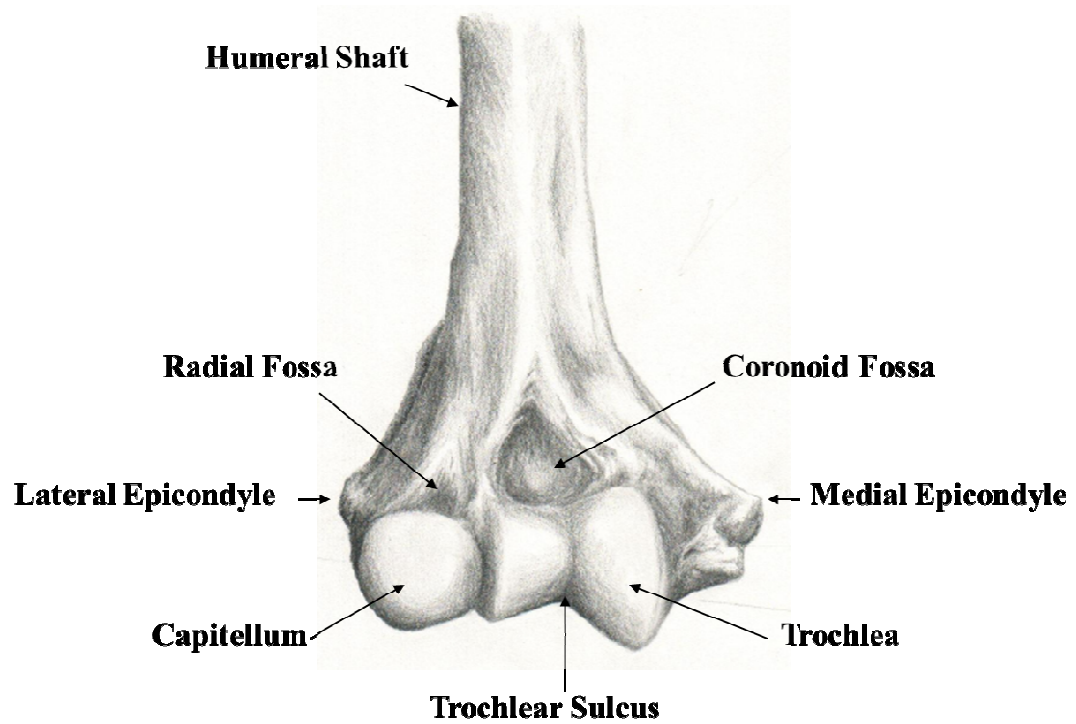
Figure 1.2: Anterior View of Distal Humerus

The osseous landmarks of the distal humerus: the trochlea and capitellum form the articular surfaces of the distal humerus. The humeral shaft, trochlear sulcus, medial and lateral epicondyles are anatomical landmarks.
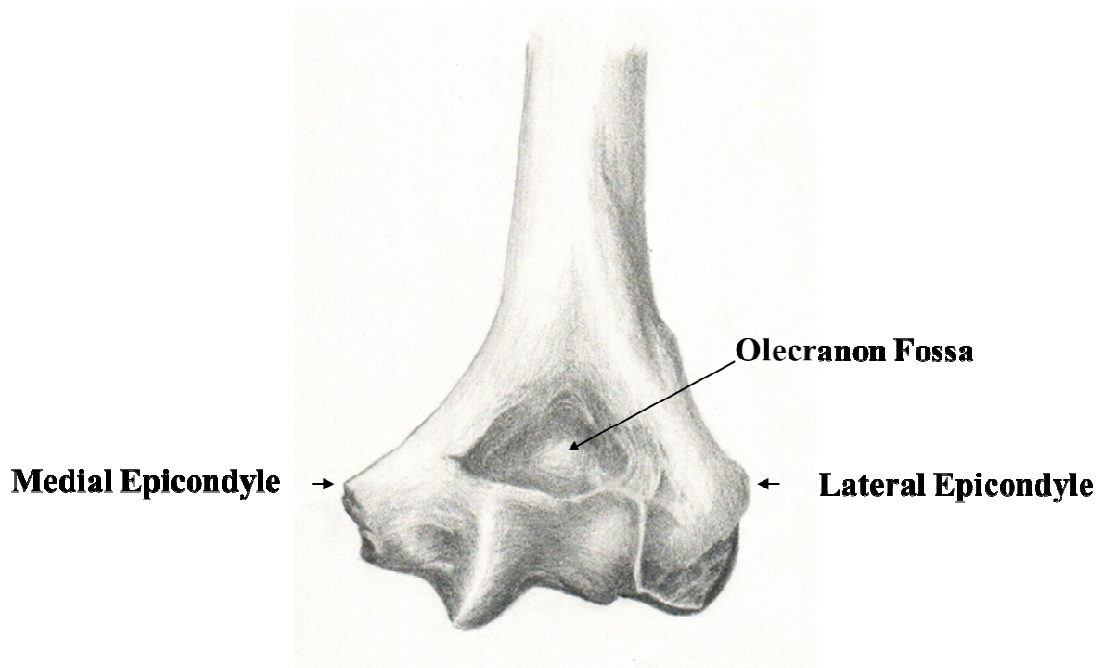
Figure 1.3: Posterior View of Distal Humerus
The osseous landmarks of the posterior humerus include the medial and lateral epicondyles as well as the olecranon fossa.
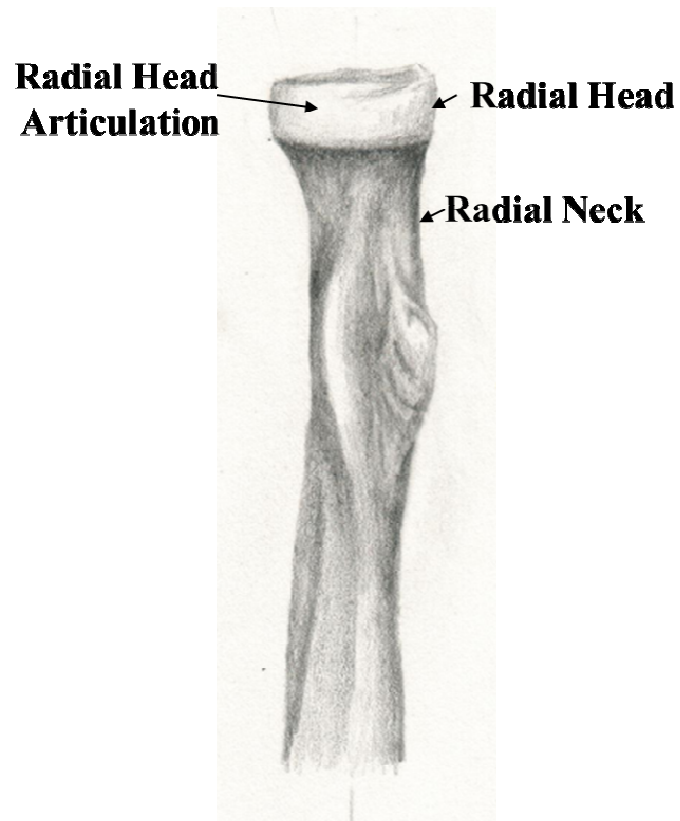
Figure 1.4: Anterior View of Proximal Radius
The radial head forms the proximal articulation of the radius which articulates with the capitellum of the humerus and with the lesser sigmoid notch of the proximal ulna. The radial head tapers to the radial neck.

Ulna - The proximal aspect consists of the greater sigmoid notch which articulates with the trochlea of the distal humerus (Figure 1.5). The greater sigmoid notch is an important contributor to elbow stability (Morrey, 2000a). The proximal tip of the ulna is the olecranon which contacts the olecranon fossa in full extension. Similarly, the most distal tip of the greater sigmoid notch is the coronoid process which, at full flexion, contacts the coronoid fossa on the anterior surface of the humerus. On the lateral aspect of the coronoid process, the lesser radial notch articulates with the radial head forming the proximal radioulnar joint.
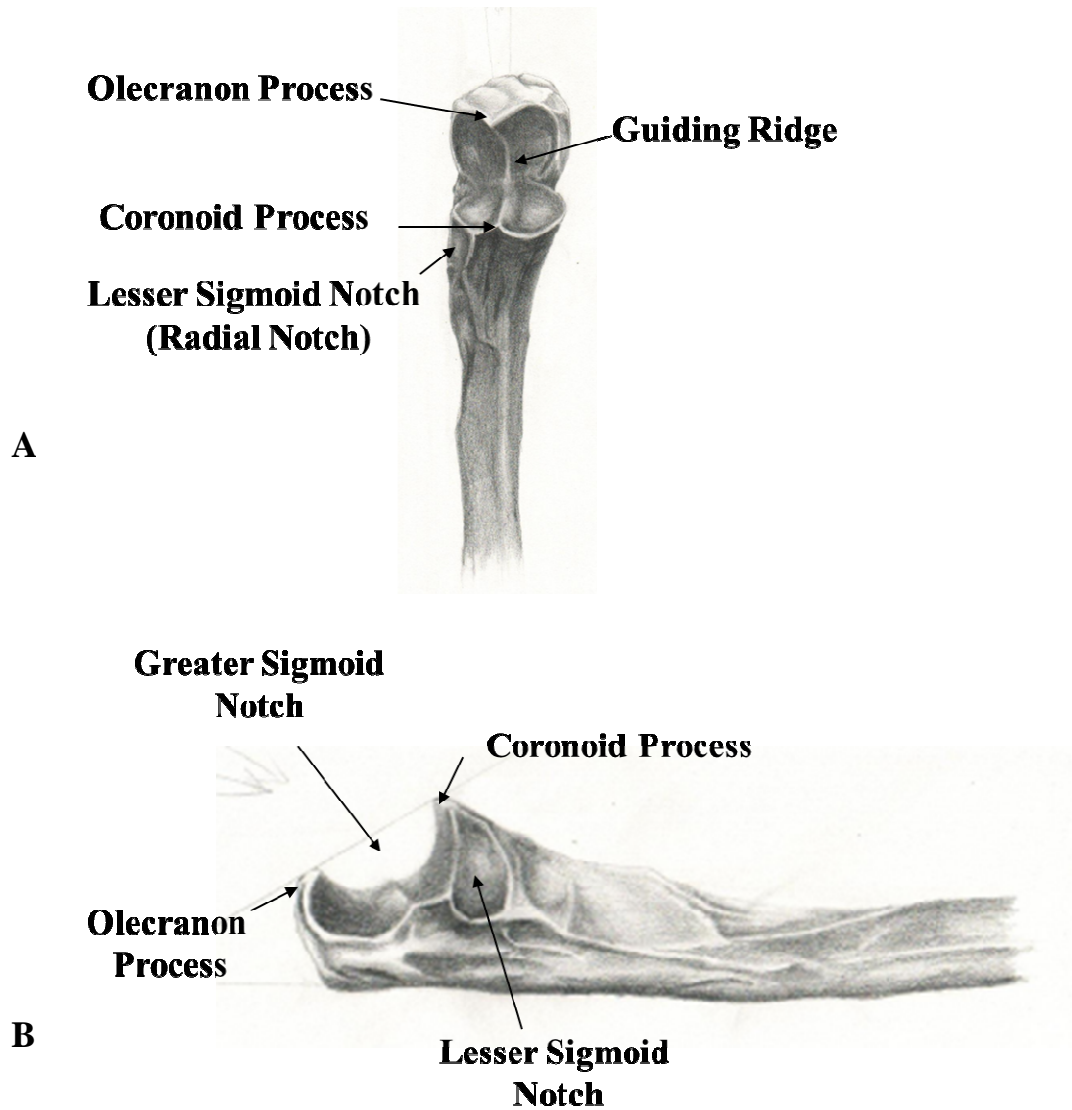
Figure 1.5: Proximal Ulna
A) Anterior Ulna Landmarks: the radial notch articulates with the radial head of the proximal radius.
B) Lateral Ulna Landmarks: the greater sigmoid notch articulates with the trochlea of the distal humerus.

1.1.2   LIGAMENTS AND JOINT CAPSULE

The ligamentous contributors to elbow stability are the medial and lateral collateral ligaments (Figure 1.6). The medial collateral ligament consists of three major components: the anterior and posterior bundle and the transverse ligament. The anterior bundle of the medial collateral ligament is the major valgus joint stabilizer (Schwab *et al.*, 1980). The lateral collateral ligament consists of the radial collateral ligament, the lateral ulnar collateral ligament, which is analogous to the anterior bundle of the MCL, and the annular ligament (O'Driscoll *et al.*, 1991). In addition to the collateral ligaments, the anterior and posterior joint capsule provides stability to the elbow. This fibrous capsule completely surrounds the elbow and contains the synovial fluid which lubricates the joint.
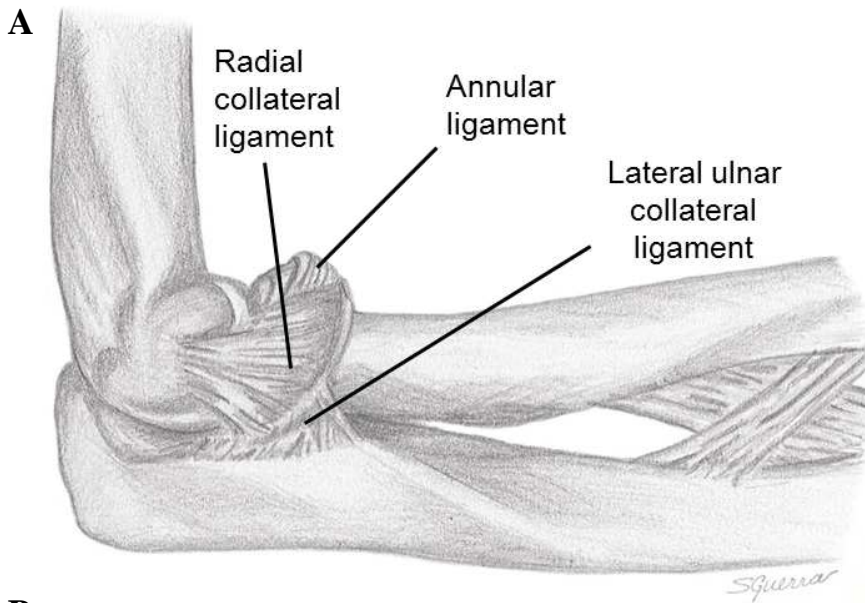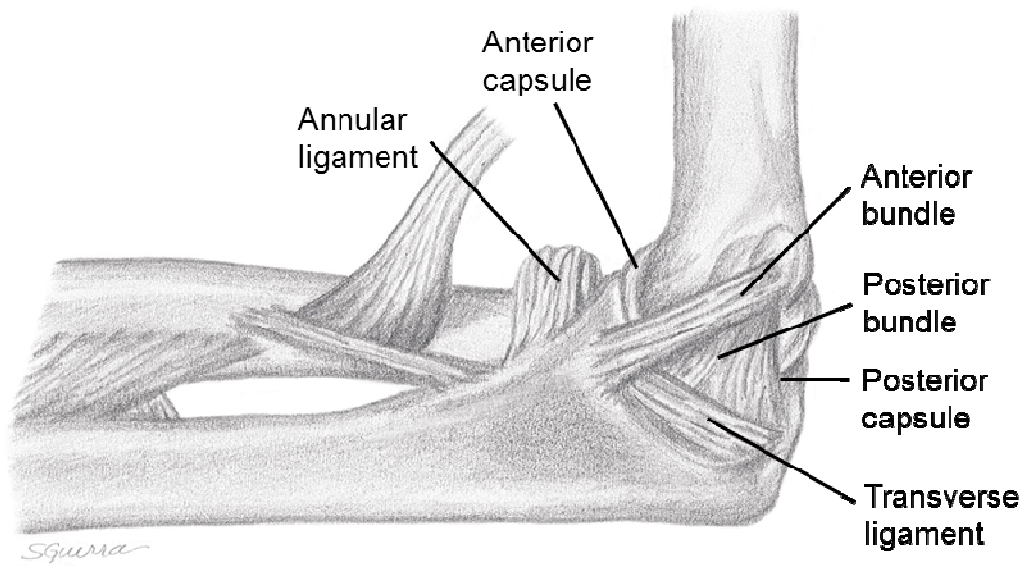
Figure 1.6: Ligaments and Joint Capsule
Medial (A) and lateral (B) views of the elbow showing ligaments (Figure HULC©).

1.1.3   MUSCLES

The major muscles involved in elbow flexion and extension are the biceps, brachialis, brachioradialis, triceps and the anconeus (Figure 1.7). The biceps is a major flexor of the elbow and has a large cross-sectional area. In the pronated position, this muscle is also a strong supinator (Morrey, 2000a). The biceps is superficial to the brachialis, which is also an important elbow flexor. The brachialis has the largest cross sectional area of all the flexors. The brachioradialis muscle is also an important elbow flexor. The triceps is the main extensor of the elbow and receives some additional help from the anconeus muscle which is a weak extensor and stabilizer of the elbow. In addition to the aforementioned muscles, numerous smaller muscles arise from the medial and lateral epicondyles to provide motions of the wrist and fingers, rotation of the forearm, and to assist flexion/extension of the elbow.

Forearm supination and pronation are achieved using the pronator teres/pronator quadratus to pronate and the biceps/supinator to supinate the forearm.
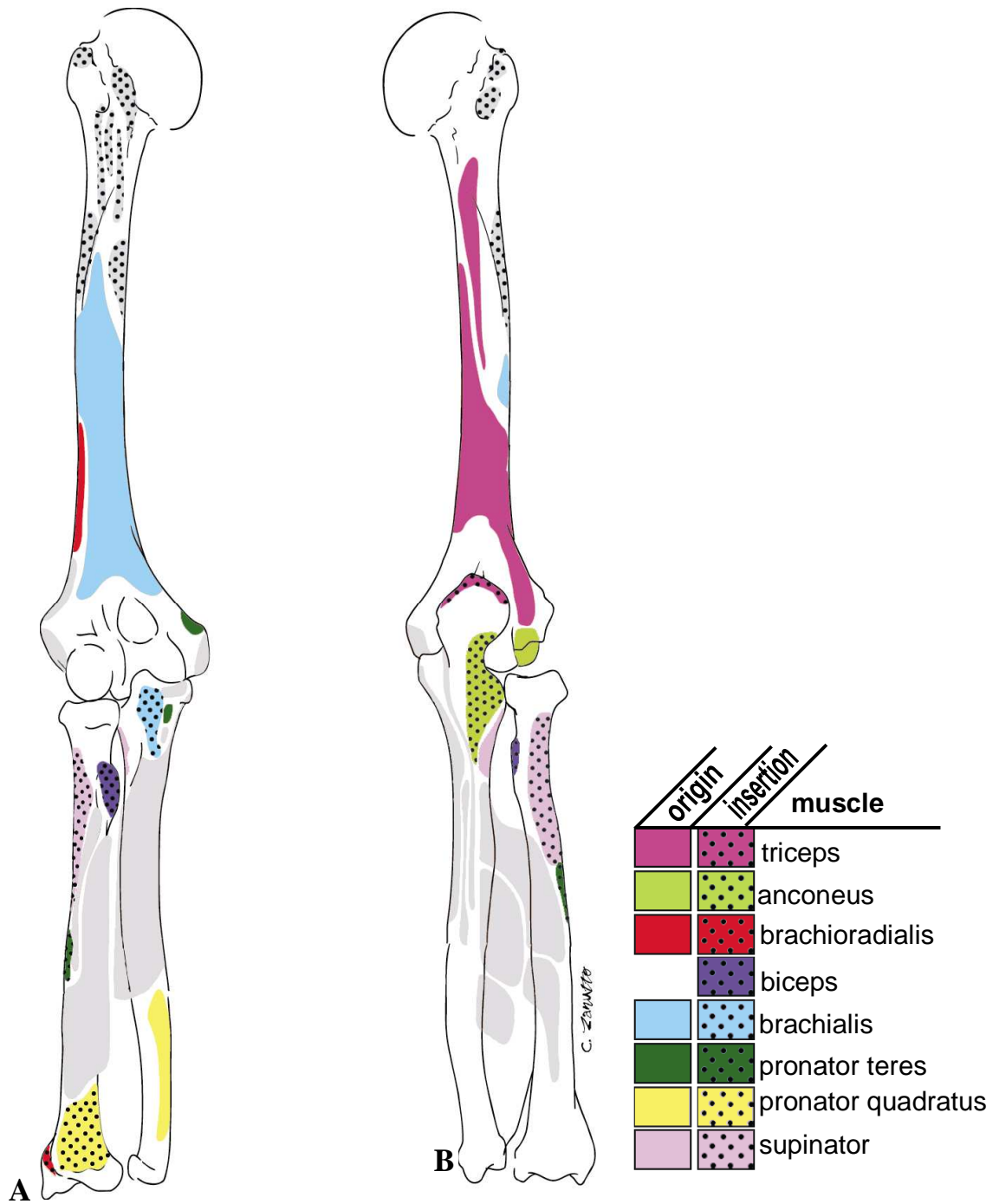
Figure 1.7: Muscles

Anterior (A) and posterior (B) views of the upper limb indicating the origin and insertion locations of the muscles responsible for elbow flexion/extension and rotation (Figure HULC©).

1.2   The Ulnohumeral Joint

1.2.1   ANATOMY

The ulnohumeral joint is one of the most congruent joints in the body (Figure 1.8). The humerus and ulna are anatomically oriented to produce a congruent articulation that can withstand strenuous lifting up to three times body weight (An *et al.*, 1981). The articulating surface of the humerus, in the ulnohumeral joint is termed the trochlea. This trochlea is separated into a medial and lateral surface by a trochlear groove (sulcus). In the lateral plane, the orientation of the articular surface is rotated anteriorly 30 degrees with respect to the long axis of the humerus (Morrey, 2000a). In the transverse plane, the anterior surface is rotated inward approximately 5 degrees and in the frontal plane, it is titled 6 degrees in valgus (Morrey, 2000a). This bony surface articulates with the ulna at the proximal end of the forearm. The greater sigmoid notch forms an arc of 190 degrees and is separated into the medial and lateral facets by the guiding ridge (Morrey, 2000a). This ridge is received by the trochlear groove on the distal humerus. The opening of the greater sigmoid notch is oriented approximately 30 degrees posterior to the long axis of the ulna which matches the 30 degrees angulation of the trochlea.
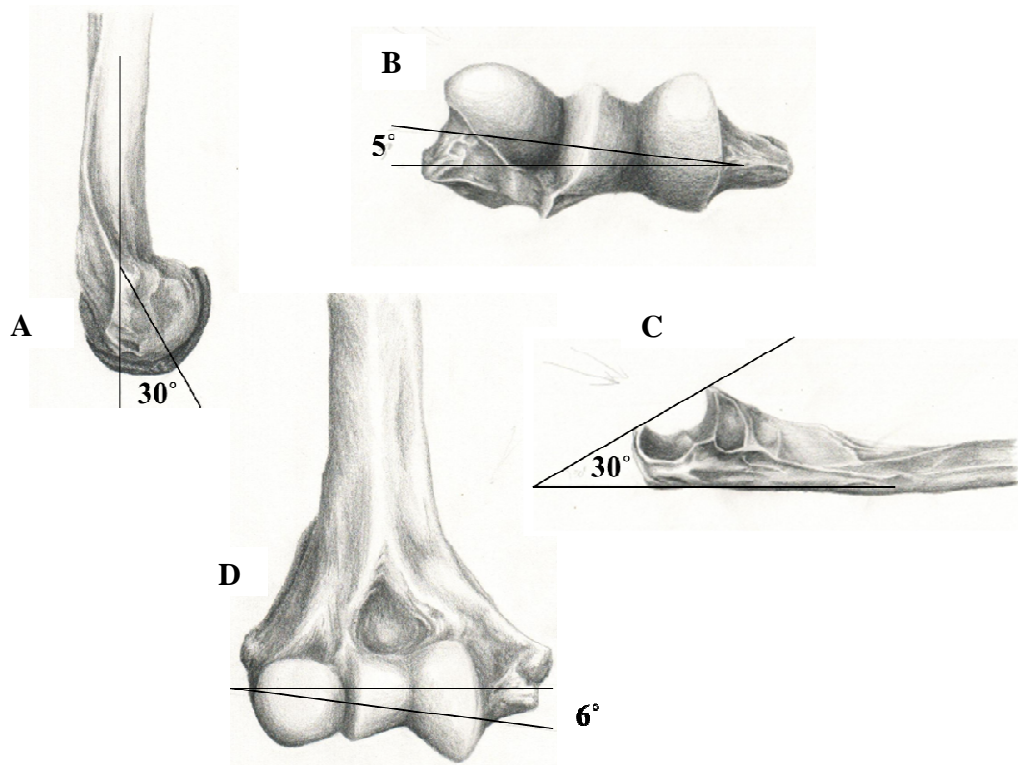
Figure 1.8: Ulnohumeral Structures
A) Lateral Distal Humerus
B) Transverse Distal Humerus
C) Lateral Proximal Ulna
D) Anterior Distal Humerus

1.2.2 ULNOHUMERAL KINEMATICS

The ulnohumeral joint is often referred to as a 'sloppy hinge' because of its inherent laxity. Varus-valgus laxity refers to the difference in varus or valgus angulation when the joint is positioned in the varus gravity loaded condition compared to the valgus gravity loaded position. The ulnohumeral joint has an estimated 6-8 degrees of laxity during flexion and extension of the elbow (Bottlang *et al.*, 2000; King *et al.*, 1994)(Figure 1.9). Additionally, due to the orientation of the articular components of the elbow, the arm is slightly positioned valgus in extension and becomes more varus as the elbow flexes (King *et al.*, 1994). Biomechanical studies use screw-displacement axes (SDA) derived from tracked passive and active kinematic studies to help define the flexion axis of the elbow (Bottlang *et al.*, 2000; Duck TR *et al.*, 2003; London, 1981; Morrey and Chao, 1976). Duck TR *et al.*, (2003) found that the SDAs deviated from the average in both orientation and position throughout all *in vitro* simulated motions. This implies that the axis of flexion varies with joint position indicating that the ulnohumeral joint behaves like a sloppy hinge. Additionally, the ulna was found to rotate, with respect to the humerus externally during extension (Morrey and Chao, 1976).

The axis of rotation of the radius around a fixed ulna passes from the radial head to the distal end of the ulna (Morrey and Chao, 1976). Morrey & Chao *et al.* found that the ulna rotates internally 5 degrees throughout early flexion and 5 degrees externally in late flexion with the arm in neutral, pronation or supination. This was believed to be caused by the configuration of the ulnohumeral articulation and ligament constraints.
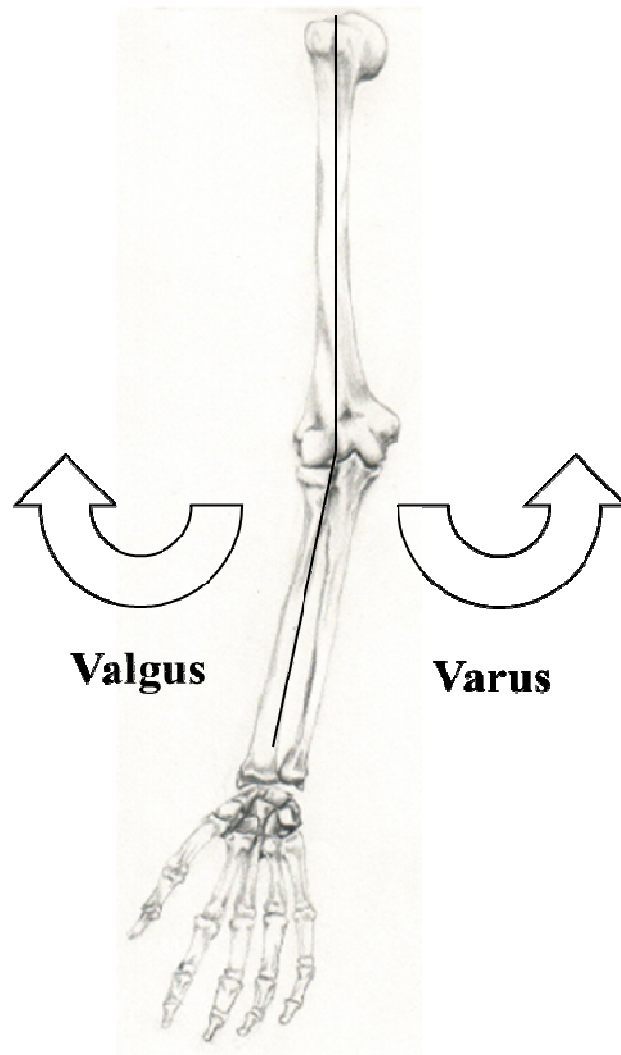
Figure 1.9: Valgus Angulation of the Elbow
In full extension, there is an inherent valgus position of the ulna with respect to the humerus. However, as the elbow is flexed, the ulna is positioned slightly varus to the humerus.

1.2.3   ARTICULATION AND CONGRUENCY

Although the ulnohumeral joint is one of the most congruent joints in the body, this joint does not exist as a perfectly congruent hinge. Rather, the sigmoid notch has a slightly greater diameter than that of the trochlea forming a "deep" ball and socket joint. Considerable research elucidating the effects of this incongruity on load transfer and contact has been conducted (Eckstein *et al.*, 1993; Eckstein *et al.*, 1994; Eckstein *et al.*, 1995a; Eckstein *et al.*, 1995b; Merz *et al.*, 1997).

Eckstein *et al.* (1994) examined, using silicone casting, the contact patterns that occur at the ulnohumeral joint as a function of load. The results of this study found that on the proximal ulna, there appears to be a bicentric distribution of contact, with two maxims of contact occurring on the olecranon and coronoid process. These regions were separated by a non-articulating portion. This study reported that at 10N of axial compression, 9% of the total articular surface of the proximal ulna was contacting and at 1280 N, 73% of the total articular surface was contacting (Eckstein *et al.*, 1994). In general, with increasing load, this bicentric pattern decreased as the two maxims merged at the centre of the joint forming a uniform load distribution across the articulating surface. Goodfellow and Bullough (1967) found that this unique pattern of contact, as a result of inherent incongruity, decreased with age. In these older specimens, the contact pattern was more diffuse and more centrally positioned.

To determine the physiologic adaptive significance of this 'concave incongruity', Eckstein *et al.* (1995a) used finite element analysis to predict contact patterns based on

various geometries of the articulating surfaces. Two models were proposed; the first was a perfectly congruent ball and socket, and the second depicted the ulnar concave as elliptical shape with a diameter that was 10% larger than the convex surface of the trochlea. When the joints were simulated with an axial load, the first model predicted a load distribution that had a maximum load at the centre of the joint that decreased towards the joint margins. In the second model, the load distribution started at the margins and with increasing joint reaction forces, the contact expanded toward the centre of the joint. Eckstein *et al.* (1995a, 1995b) found that when the tissues deformed at higher applied loads, the peak stresses, in the incongruent joint, did not appear in the depth of the socket but are relatively evenly distributed, and that the peak compressive stress were considerably lower in the incongruous case over the congruous case. In general, in the most congruent joint, the central location of load would result in an overuse of the central region, causing deterioration of the cartilaginous surfaces as well as an under use of the periphery. Studies have shown that concave incongruity serves to optimize the distribution of stress by providing a more uniform distribution of stress when compared to the most congruent case (Bullough *et al.*, 1968; Bullough, 1981; Greenwald and O'Connor, 1971). Bullough *et al.* (1981) examined the effects of 'concave incongruity' of the proximal ulna on the metabolic activity of the chondrocytes. This study concluded that with regular change in contact, which is inherent in the loading of the concavely incongruent joint, the synovial fluid is promoted to move from cartilaginous layers to the joint space thereby nourishing the articular cartilage. In general, concave incongruity has

an important effect on ulnohumeral load transmission and the distribution of lubricating synovial fluid within the joint capsule. Concave incongruity may be regarded as a vital factor for the long term stability and joint function for a lifetime.

Another phenomenon examined in the ulnohumeral joint is the inhomogeneous distribution of cartilage across the proximal ulna. Tillmann (1978) found that there are three main 'models' of cartilage distribution. The first of these, found in 65% of subjects, has olecranon and coronoid facets in the trochlear notch separated by a non-articular zone of bone. The second model, which occurs in 30% of individuals, has the cartilage divided into two areas on the medial and lateral side. In this model, the medial side had two facets separated by a transverse non-articulating region. Finally, in the third model, the full ulnar surface was covered with cartilage. This distribution occurs in 5% of older subjects.

1.2.3.1 Biomechanics and Load Transfer

Osseous as well as soft tissue stabilizers are the limiting factors of elbow flexion (Morrey, 2000b). The abutment of the olecranon process in the olecranon fossa and the tension in the anterior capsule and flexor muscles limits extension. Similarly, in flexion, the abutment of the coronoid process in the coronoid fossa, tension in the posterior capsule and the extensor muscles in conjunction with the bulk mass of the forearm and upper arm allow approximately 145-150 degrees of flexion (Morrey, 2000b).

Shiba *et al.* (1988) examined the geometry of the ulnohumeral joint and found that there appeared to be two distinct bearing surfaces of the ulnohumeral joint articulation; one mainly in early flexion and the other, in terminal flexion. In full flexion, part of the

surface of the olecranon loses contact with the central groove of the trochlea. Similarly, in full extension, part of the coronoid process loses contact with the trochlear groove. In general, the cartilaginous surfaces would appear to contact each other fully only between 55 and 125 degrees of elbow flexion. These findings suggest that perhaps this is an adaptive phenomenon that prevents overuse of the entire cartilage surface throughout the full range of motion.

Contact area is used to determine the area across which an applied load acts. However, in order to determine the pressure distribution, the joint forces, and more specifically, the resultant force vector, must be established. When examining the load transfer mechanics of the elbow, both the osseous and elbow position must be considered. With the arm fully extended and axially loaded, the distribution of stress across the ulnohumeral joint is approximately 40% and 60% at the radiocapitellar joint (Halls A.A. and Travill A., 1964; Walker PS, 2008). Amis *et al.* (1980) predicted elbow joint forces for strenuous exercises and found that the elbow will be not be subjected to tensile loads during strenuous pulling exercises such as when holding a handle. Rather, compressive forces of several kiloNewtons occur during strenuous exercises occur at both the radiocapitellar and ulnohumeral joints.

1.3   Osteoarthritis and Degenerative Diseases

Osteoarthritis is the most prevalent form of arthritis and it is traditionally characterized as a disease of the articular cartilage, but also is present with degenerative changes to the subchondral bone, ligamentous stabilizers and the joint capsule (Felson *et*

al., 2000). The exact mechanism of onset of osteoarthritis is unknown, but the current theory is that osteoarthritis develops as a result of joint mal-alignment, muscle weakness and altered joint congruency, within a context of susceptibility (Felson *et al.*, 2000). Various genetic factors and systematic factors (age, sex, weight, and nutrition) predispose the joint to the development of osteoarthritis following a mechanical perturbation such as an acute injury. Hunter *et al.* (2009) examined the relationship between alignment and osteoarthritis and found that mal-alignment influenced the rate of progression of the disease as alterations in the load distribution and congruency degrade the articular surfaces and underlying subchondral bone. Currently the diagnosis of osteoarthritis is determined through clinical examination, and is then confirmed using planar radiographs. The radiographs are assessing overall joint space, changes to the subchondral bone and are also used to identify regions of abnormal bone growth and calcification. While there are no known cures for osteoarthritis, treatments of this disease range from physiotherapy rehabilitation, pharmacological approaches (intra-articular steroid, analgesics)and surgical interventions (arthroscopic debridement/lavage/arthroplasty) (Gallo *et al.*, 2008; Ugurlu *et al.*, 2009).

1.4 Methods to Quantify Articular Contact

The elucidation of contact characteristics in joints is essential in the investigation of various degenerative diseases as it provides a diagnostic tool for the detection of diseases such as osteoarthritis. In biomechanical studies, contact area is used to determine joint contact stress, as force per area. This is estimated by incorporating the precise force transmission that results in a joint, and uses the knowledge of where that contact occurs (contact area). Quantifying contact area is beneficial to clinicians in the development of diagnostic tools, and has many biomedical research applications.

1.4.1 DIRECT APPROACHES

Over the past 30 years, there has been considerable research developing various methods for quantifying contact area in articulating joints (Ateshian *et al.*, 1994; Black *et al.*, 1981; Bullough *et al.*, 1968; Bullough, 1981; Harris *et al.*, 1999; Haut, 1989; Huberti and Hayes, 1984; Matsuda *et al.*, 1997; Ronsky *et al.*, 1995; Stormont *et al.*, 1985). Initial techniques consisted of direct yet invasive approaches. These techniques, by nature, employed the use of cadaveric specimens and included pressure sensitive films (Harris *et al.*, 1999; Haut, 1989; Huberti and Hayes, 1984; Matsuda *et al.*, 1997; Ronsky *et al.*, 1995), dye staining (Black *et al.*, 1981) and casting techniques (Ateshian *et al.*, 1994; Momose *et al.*, 1999; Stormont *et al.*, 1985). These approaches required direct access into the joint, often requiring sectioning of the joint capsule and soft tissues that support the joint. Not only are these techniques invasive, they may compromise the stability of the

joint, thereby affecting the native contact mechanics. They do however, directly and accurately quantify contact area.

Stormont *et al.* (1985) compared pressure sensitive film, dye staining and the silicone casting technique to investigate the contact area of the elbow joint. The results of this investigation indicated that overall, the casting technique provided the most reproducible and reliable technique to directing quantify contact area. As such, this method is deemed the gold standard of contact area elucidation and is used as a means of validating all other approaches.

1.4.1.1   *Pressure Sensitive Films*

Pressure sensitive film records pressures applied to the joint in a loaded condition. Perhaps the most popular film employed has been the Fuji Film Pressure Sensitive Film® (Fuji Film Corporation, New York, NY) which consists of two polyurethane composite films that produce a red stain when loaded in compression. Film A, which consists of the microcapsule layer contains chemicals. Film C, also contains microcapsules, however, they contain colour-developing chemicals. Under compression, the microcapsules burst and the two components interact resulting in a red stain. The intensity of the redness is calibrated, using an indenter, to the magnitude of pressure. The film is inserted directly between the articulating surfaces of the joint, and after compression, the film must be removed. This method is not only tedious to use, and also only depicts the contact area and loads that occur across the joint, not the contact of each articulation (meaning it is not possible to see the locations on the humerus that are in contact with the ulna and vice

versa, instead only a single contact measurement is made representing joint contact). Additionally, various artifacts occur as a result of orienting and positioning the film in the joint while trying to preserve the native anatomy of the joint. Such artifacts include crimping or crinkling, sliding and shear stress staining. These artifacts result in an overestimation of the estimated contact area. It has also been shown that pressure sensitive films are thermo-sensitive. Therefore, careful regulation of testing temperature is required to ensure a proper reading (Ronsky et al., 1995).

Another type of pressure-sensitive film is TekScan®, a plastic laminated, thin film (0.1mm) pressure transducer. The sensor has two 9.2 cm^2 sensing arrays, each with 2288 sensing elements called sensels (Harris *et al.*, 1999). The film is first conditioned and calibrated and is then inserted into the joint articulating surfaces. It records (at a rate of 2 frames per second) and displays the results in either two or three dimensions. Harris *et al.* (1999) compared the Fuji Film® with the K-scan (TekScan®, South Boston, USA) and found that the K-scan proved to be an easy, reproducible and reliable measurement technique that could capture contact under various loads and flexion angles. In general, the TekScan® displayed a smaller standard deviation when compared to the pressure sensitive film, and displayed less variation in the sensor shapes and pressure ranges. Experimentally, the TekScan® was less tedious to use as one sheet could be employed to measure successive loads instead of replacing the film between various loading scenarios (Harris *et al.*, 1999). There were however, limitations to this approach, as is true with all direct approaches; they are by nature, invasive. The TekScan® technique may alter the

topography of the bearing surfaces as the sensor has a finite thickness of 0.1mm; however, this is still thinner than the pressure sensitive film. Also, crimping of the sensors can occur which introduces artifacts. In general, TekScan® offers an improved method relative to the pressure sensitive film approach.

1.4.1.2 *Dye Staining*

Dye staining employs the use of stain or dye to locate and quantify the contact area. This technique involves a three stage staining sequence. Initially, a thin layer of blue dye is placed on a non-contacting surface within the joint. The joint is then subsequently reduced and an impression of contact is created on the opposing surface. The stain can be removed from the surface using neutralization, and the entire process can be repeated (Black *et al.*, 1981). As with the pressure sensitive films, this technique is extremely tedious. Additionally, the dye staining is less and less obvious with successive measurements making it less suitable for repeated testing. Artifacts that are associated with this technique usually involve the introduction of air bubbles in the dye material which could significantly overestimate the contact area. In other instances, the dye is not able to penetrate the joint cavity to reach all the articulating surfaces resulting in a severe underestimate of the measured contact as well as a gross error in the actual location of contact.

1.4.1.3 *Silicone Casting: Filling Non-Contact Space*

Casting of the joint surfaces provides one of the most visible and comprehensive means of elucidating contact area. Originally, methacrylate cement and wax were used,

but more recently silicone based rubbers have been employed (Fujikawa *et al.*, 1983; Stormont *et al.*, 1985). In this method, the joint is distracted and a casting material (Reprosil® Dentsply International Inc., Milford, DE) is injected into the joint. The joint is reduced to the intact orientation and held until the cast has solidified. After removing the impression material from the joint, the contact can be observed and quantified. Composed primarily of silicone, Reprosil® has low viscosity and is relatively shrink resistant. Additionally, the silicone is durable and permits the cast to be removed after each trial and reapplied to either end of the joint therefore capturing the contact on both articulating surfaces and orienting the examiner with the location of contact (Stormont *et al.*, 1985).

Direct approaches, by nature, are invasive. As such, the use of cadaveric specimens is required in direct approach techniques. Cadaveric specimens, although useful in many biomechanical research applications, have certain limitations that are associated with their use. Studies using cadavers have been criticized for not being representative of the physiologically active arm as they cannot reproduce completely the physical muscular force across the joint (Anderst and Tashman, 2003). Furthermore cadavers are typically elderly and may have some articular degeneration which may influence the resulting contact area. Additionally, these direct approaches may alter the joint kinematics by virtue of the capsular incisions needed to place and remove the sensing material. However, given the more restrictive limitations of computational models, cadaver-based experimentation provides the only means to investigate a variety of clinical questions prior to implementation in patients.

1.4.2   IN-DIRECT, NON-INVASIVE APPROACHES

Recently, computed tomography (CT) (Marai *et al.*, 2004) and magnetic resonance (MR) imaging (Besier *et al.*, 2005; Boyer *et al.*, 2008; Cohen *et al.*, 1999; Eisenhart-Rothe *et al.*, 2004; Gold *et al.*, 2004a; Goto *et al.*, 2004; Hinterwimmer *et al.*, 2005; Salsich *et al.*, 2003; Wan *et al.*, 2006; Wretenberg *et al.*, 2002) based approaches have been developed to non-invasively quantify the osseous interactions and contact that occur in the joint (Marai *et al.*, 2004). These various imaging modalities can accurately generate a 3-dimensional (3D) surface model of the articulating joint. CT provides excellent contrast between bone and soft tissue. The contrast in CT imaging is due to differences in attenuation of X-rays due to differences in electron density. The non-attenuated x-rays are detected by a solid state detector (Hsieh J 2003). CT imaging differs from conventional radiographs in that it is able to acquire 3D volume data by acquiring successive x-ray images as it rotates around a patient. Recent advances have allowed CT scanners to continuously scan around a stationary patient in a helical loop. Hounsfield units (HU) (Equation 1.1) are used to express differences in attenuation and are therefore a measure of radiodensity relative to that of water.

$$HU_{Tissue} = \frac{\mu_{tissue} - \mu_{water}}{\mu_{water}} \cdot 1000 \qquad \text{Equation 1.1}$$

where μ_{tissue} and μ_{water} are the linear attenuation coefficients of tissue and water respectively

MRI has recently become commonly used in clinical practice, whereby magnetic fields and radiofrequency signals replace x-rays and the energy source used to generate images (McRobbie D.W. *et al.*, 2007). MRI sequences can be used to detect hydrogen molecules in tissue. Both MRI and CT images provide successive volumetric datasets that are represented as slices (tomographs) that can be reconstructed into 3D models. In the investigation of joint biomechanics, these medical imaging technologies provide 3D surfaces which can be used to examine joint surfaces and obtain measurements using various approaches. The first of these approaches consists of computational methods which measures the amount of cartilage-cartilage contact. The other approaches use the 3D imaging to measure the joint space and minimum distance between the articulating bones.

1.4.2.1   Computational Approaches

Two-Dimensional Approaches: Gold *et al.* (2004) developed and evaluated an MR imaging protocol to quantify patellofemoral *in vivo* cartilage contact area during weight bearing activities. This method, involved a healthy volunteer bearing his or her own weight while leaning against a custom MR compatible back support. After imaging, contact area measurements were made by three independent observers. In each MR slice, regions of grey-on-grey pixels, or contacting pixels were manually identified and the length of the contact pixels, on the surface of the articulation, was two-dimensionally measured. Grey-on-grey pixel lengths were then measured for each slice of the MR image. Contact area was determined by multiplying the length of grey-on-grey pixels in

each image by the slice thickness and summing the values across the joint (Gold *et al.*, 2004). Brechter and Powers (2002) used a MR-based similar method to quantify contact area, within the joint where there was no distinct separation between the borders of the two structures. This was seen as "white-on-white" pixels. This line of contact was then multiplied by the slice thickness and summed across the entire joint. If the line of contact was curved, several straight lines were used. The major advantage of these methods is their applicability to *in vivo* studies thereby circumventing the problems associated with cadavers. This additionally offers insight into the joint mechanics that occur in younger subjects compared to that of the relatively older age group of the cadaveric specimens. These methods also are able to be applied clinically as a means of predicting or monitoring degenerative diseases of the joint. However, these methods are not automated and require a significant amount of user input. Additionally, these approaches can only examine contact in 2-dimensional (2D) slices and in statically loaded conditions. Additionally, as these images only examine 2D slices, errors can be introduced when the measured lengths are attenuated in the third dimension (Losch *et al.*, 1997).

Three-Dimensional Approaches: Proximity Mapping: Proximity maps have been employed by a number of investigators in various joints in the body and provide a 3D measure of joint congruency or joint contact area (Anderst and Tashman, 2003; Ateshian *et al.*, 1994; Bey *et al.*, 2008b; Eisenhart-Rothe *et al.*, 2004; Goto *et al.*, 2004; Losch *et al.*, 1997; Marai *et al.*, 2004; Marai *et al.*, 2006; Scherrer PK *et al.*, 1979). This approach assumes that regions of higher contact pressures within a joint correspond to regions of

closest proximity (Marai *et al.*, 2004). These methods calculate contact area of joints non-invasively from 3D bone surface models obtained using CT (Anderst and Tashman, 2003; Cohen *et al.*, 1999; Marai *et al.*, 2004) or MR imaging (DeFrate *et al.*, 2004; Goto *et al.*, 2004). These 3D reconstructions of the joint are used to create proximity maps using various software algorithms.

CT-Based Technique: The proximity maps generated using CT represent the inter-bone distances between subchondral bone surfaces (Anderst and Tashman, 2003; Marai *et al.*, 2004). X-ray computed tomography is not a reliable soft tissue image acquisition device and is therefore primarily used to image osseous structures. Therefore, biomedical studies using CT often set their threshold values for the pre-processing of the volumetric data, to visualize only the osseous structures. Using CT to obtain a volumetric model of the joint allows for easy segmentation of the contact surfaces within a joint with the absence of the soft tissue. Joint contact in these studies is defined by examining joint congruency or overall joint space based on the assumption that regions that are closer together also are the same regions that are most likely in contact. Contact area in these studies is defined as the subchondral surface area on the bone that is a prescribed threshold distance.

MR Imaging Techniques: Magnetic resonance imaging allows for direct visualization of the soft tissues, namely the cartilage. Thickness measurements can then be obtained using this 3D technique. However, in using MR imaging, accurate segmentation of the cartilage surfaces in regions where the bones are contacting is difficult. This is however, crucial when using the proximity method where depiction of the actual outer surfaces of each

bone and measurement of joint space is used. Contact area in these studies uses knowledge of the minimum distance rather than a prescribed distance (Cohen *et al.*, 1999; DeFrate *et al.*, 2004).

When employing a direct approach to measure joint contact, little knowledge is obtained of the relative intensity of the contact within the determined region of contact. Casting, staining and dying techniques segment regions across the articulating surfaces that are either contacting or not contacting. Proximity mapping assumes that regions that are closer in proximity or distance are more likely to contact than regions that are further apart. Therefore, contour maps can be generated to show the predicted joint contact area for different threshold values. This allows for visualization of the relative intensity of contact within a region, and can be used to find a centroid of joint contact. This centroid can then be measured at various positions throughout the arc of motion, allowing the contact pattern to be tracked as well. Additionally, these methods can be fully automated and used to examine contact in a dynamic manner throughout a range of motion.

1.4.2.2 Three-Dimensional Model Rendering

The aforementioned computational approaches require the joint to be statically positioned during imaging. Using these images, surface area measurements of joint contact can be determined. Using these previous techniques in isolation would limit the investigation of the joint biomechanics to statically loaded joints which does not represent the physiologic motion a joint undergoes. Therefore, registration techniques and 3D rendering approaches have been developed to allow investigators to examine the joint

biomechanics of joints undergoing physiologic motion. Bone models are reconstructed from various medical imaging datasets and then rendered according to some form of 'tracked' motion. In this way, the position and orientation of the bones in a joint can be reconstructed or 'rendered' at any frame throughout an arc of motion. By combining these techniques as well as a computational approach, joint biomechanics can be reconstructed and measured in real-time, and or during a physiologic motion.

The two predominant approaches used to 'render' 3D models are Radiostereometric Analysis (RSA) using markers, or using contour (model)-based RSA and registration. Both RSA and registration are possible in orthopaedics as the bones are considered to be rigid bodies themselves. As such, the position and orientation of any two points on the rigid body is assumed to be fixed throughout motion. Motion measurement systems employing optical tracking or video-based motion capture systems are non-invasive, but produce skin motion artifacts that introduce error into the measurement system. RSA techniques therefore provide an alternative to these approaches and are extremely accurate (Kedgley *et al.*, 2009; Tashman and Anderst, 2003). In this approach, a minimum of three radiopaque markers (tantalum beads) are inserted into the cortical bone surface. Single-plane or bi-plane fluoroscopic cameras are used to track the position and orientation of each bead during motion. These images are calibrated and analyzed using established stereometric techniques to measure dynamic joint motion. Model based tracking has also been shown to be accurate and uses bi-plane x-ray images but tracks the

contour of the cortical bone and matches each frame to a 3D reconstruction of the joint obtained from CT and is less invasive (Bey *et al.*, 2008a; Wan *et al.*, 2006).

Rigid body registration is an alternative approach to 'render' reconstructed models. The transformation is six degrees of freedom (3 rotations, 3 translations) with no deformation or scaling. Sadowsky *et al.* (2002) describes registration as the finding the transformations from one coordinate system to another such that the objects in the first coordinate system are aligned with that of the second. In orthopaedics 3D-3D rigid body registration is employed as reconstructed 3D models are registered to physical 3D objects, or 3D reconstructed models obtained from two different volumetric images are registered (different time points or different imaging modalities).

Surface-Based Registration: There are many types of surface based registration, the most commonly employed is the Iterative Closest Point (ICP) Registration introduced by Besl PJ and McKay ND (1992), that represents a surface as a collection of points. The first step of the ICP is to establish correspondence between two sets of points (on the two surfaces being registered). Subsequently, it iteratively generates a transformation that would minimize the distance between corresponding points using a least-squares solution. This process is repeated until the mean distance between the corresponding points after registration has reached a specified distance or number of iterations (Yaniv, 2008). Often an initialization or alignment step is added to this registration where manually selected course alignment points are selected on both models being registered to increase the probability of finding a solution. The accuracy of surface-based registration is typically

examined by comparing the 'fit' of the registered surfaces either qualitatively using a colourmap, or quantitatively by examining inter-surface distances. The accuracy of a surface-based registration is improved when that surface contains unique features with regions of high curvature (Maurer *et al.*, 1996; Maurer, Jr. *et al.*, 1998).

Paired-Point Based Registration: Surface-based registration in computer assisted surgery and in many medical applications matches surface contours (represented as points) typically obtained from a digitization of an actual surface (100-1000 points) and surface contours extracted from reconstructed bony models. The number of points on each surface does not have to correspond (target surface typically has more points). In paired-point registration, corresponding points are identified before the registration and are homologous. As with surface-based registration, paired-point registration also employs a least-squares minimization algorithm to find a transformation that minimizes the distance between homologous points after registration. Homologous points are often referred to as fiducial markers from the Latin word *fiducia* meaning to trust-the location of these homologous markers is fixed. Clinically, anatomical landmarks are chosen on prominent structures. McDonald *et al.* (2007) investigated the accuracy of employing anatomical landmarks in paired-point registration on the distal humerus and measured a registration accuracy value of 1.9±1.0mm. An alternative approach uses external markers which have shown to be more accurate than using anatomical markers (McDonald *et al.*, 2007). Previous studies have shown that surface-based registration is less accurate than paired-point registration employing externally fixated fiducial markers (Horn B.K.P,

1987; Sadowsky *et al.*, 2002; Sugano *et al.*, 2001).The closed-form solution of the paired-point registration described by Horn *et al.* is commonly employed (Horn B.K.P, 1987).

To assess the accuracy of paired-point registration, Maurer, Jr. *et al.*, (1997) introduced three terms that can be used to describe the overall accuracy of a paired-point registration. Fiducial registration error (FRE), first termed by Maurer, Jr. *et al.* (1997) is the root mean squared vector in fiducial alignment between the image of the fiducial markers and the physical location of the fiducial markers attached to the bone. Fiducial registration error should be used to assess the effectiveness of the experimental registration procedure. For example, FRE should be assessed during experimental testing to ensure proper localization of the fiducials in physical space (to ensure that the tracking system is working properly) and also to ensure that the fiducial markers themselves correspond. However, FRE is not necessarily related to the overall accuracy of the registration (Fitzpatrick, 2009). Target registration error (TRE), is the difference in position of a target marker, located on the region of interest (other than the fiducials) after registration (Maurer, Jr. *et al.*, 1997). Fiducial localization error (FLE) is the error associated with determining the exact location of each fiducial marker.

The overall accuracy of this technique is largely independent of the object being registered (Fitzpatrick *et al.*, 1998). This independence is achieved because (in direct contrast to a surface-based registration algorithm that uses points derived from the surface of the anatomy for the purpose of registration) only the fiducial or landmark configuration is used in the registration itself. Therefore, the fiducial configuration itself is an important

factor governing the accuracy of the overall configuration. West *et al.*, (2001) published a set of guidelines to follow when employing fiducial markers in paired-point rigid body registration. This publication states that the most accurate point-based registration methods employ markers that are rigidly attached to the bone. West *et al.* (2001) stated that when employing fiducial markers, the fiducial markers should be positioned on the rigid body being registered in a non-collinear configuration. Additionally, the area of clinical interest should be positioned in the centroid of the overall fiducial configuration. West *et al.* (2001) however notes that the position of each fiducial should be as far as possible from each other while maintaining the centroid position of the configuration. Finally, when using paired-point registration, the number of corresponding points (the centre of each fiducial) should be maximized; however this increase in accuracy of the registration rapidly decreases after 5 or 6 markers (Sadowsky *et al.*, 2002). For bone mounted marker systems, the traditional number of fiducials employed ranges from 3-5. This value typically corresponds to a fiducial localization error of less than 1mm (Sadowsky *et al.*, 2002; West *et al.*, 2001).

Both registration and RSA techniques have advantages and disadvantages that make use of their algorithm appropriate in different experimental studies. In this current thesis, the paired-point registration is used, along with proximity mapping to non-invasively examine joint mechanics of cadaveric joints in the upper extremity undergoing simulated physiologic motion.

1.5   Thesis Rationale

Arthritis is a common sequel of fractures and ligamentous injuries. Although numerous studies have attempted to understand the cause and therefore the prevention of this complication, the mechanism remains elusive. Joint kinematics has, in the past, been employed to examine deleterious effects of various clinical conditions on joint stability. While this has proven very useful to ascertain the effect of various injuries and interventions in general, it does not provide direct insight into the changes that may occur at the joint articulations. This is of extreme importance as clinically, degeneration of the articular cartilage is common sequelae of joint injuries.

Joint congruency and contact area are both difficult parametric values to obtain in a non-invasive manner. As well, investigating the joint mechanics under physiologic conditions either requires tedious rendering approaches, or is limited to small ranges of motion. The ulnohumeral joint provides a significant challenge both in its motion pathways (kinematics) as well as in its osseous and articular morphology. However, problems with elbow instability and degenerative diseases persist. As such the development of a technique to non-invasively examine joint congruency and mechanics that is accurate, validated and is capable of examining surface interactions while undergoing continuous physiologic motion is needed. As well, kinematic descriptors such as varus/valgus laxity are currently used in the clinic and laboratory to examine elbow stability. These quantitative measurements of joint function are useful to investigate the efficacy and success of various surgical interventions tested in cadaveric studies and to

evaluate patient prognosis. However, these descriptors do not allow direct visualization of articular interactions in six degrees of freedom. Therefore, registration algorithms must be developed to directly visualize joint motion pathways to further examine the effect various clinical outcomes have on joint stability and prognosis. Future applications of this technology to evaluate joint congruency during ligament reconstructions and joint replacement surgery may allow for improved outcomes following these commonly performed procedures.

The clinical implications of using an imaging technique to non-invasively quantify joint contact and tracking will eventually permit the assessment of patients in the clinic and will also potentially lead to an improved understanding of the causes, prevention and treatment of various cartilage diseases. In view of this, standards of patient safety in medical imaging must be examined to minimize the deleterious effects of commonly employed medical examinations. Minimum dose scanning protocols must be established to allow clinicians and researchers to accurately obtain volumetric data from patients to examine joint congruency, but with consideration of patient safety. The knowledge gained from this research will lead to an increased understanding to the influence of joint mal-alignment on resulting joint mechanics as it relates to the understanding of risk factors that lead to degenerative and debilitating changes which are prevalent in the joints of the upper extremity.

1.6 Objectives and Hypotheses

The specific objectives of this thesis are to:

1. Determine the efficacy of employing imaging modalities to quantify joint congruency at the ulnohumeral joint of the elbow.

2. Employ a paired-point fiducial and surface based registration approach to render 3D models of the ulnohumeral joint undergoing simulated elbow flexion.

3. Evaluate the accuracy of employing optical tracking to improve the accuracy of the registration algorithm to render 3D ulnohumeral motion pathways as well as assess the accuracy of this revised registration algorithm and validate the use of joint proximity mapping to investigate ulnohumeral joint congruency .

4. Apply this registration and joint proximity mapping technique to quantify the effect of ligament repair and rehabilitation technqiues on congruency at the ulnohumeral articulation as well as quantify the relationship between traditional kinematics descriptors of joint motion (such as valgus position) with the measured joint congruency.

5. Determine the minimum dosage requirement to accurately obtain volumetric images of the shoulder joint to investigate joint congruency at the glenohumeral joint and extend the application of the joint proximity mapping technique to the glenohumeral joint.

The following hypotheses were tested:

1. The inter-bone distance algorithm used to assess overall joint congruency will be able to accurately predict regions of joint contact as determined by the gold standard experimental casting technique.

2. Three-dimensional visualization of the ulnohumeral joint undergoing continuous elbow flexion will be achieved using a previously developed elbow motion simulator and a paired-point registration technique. Rendered motion pathways of the ulnohumeral joint during radial head excision and replacement will coincide with graphical representations of valgus angulation as a function of elbow flexion.

3. Low error values in the quantification of joint congruency will be achieved using optical trackers (registration error < 1.00mm) and small changes in the kinematics of the ulnohumeral joint will result in marked differences in the overall joint congruency (less congruent) following collateral ligament repair.

4. Radiation dose can be reduced by more than 90% of that currently employed clinically while still allowing accurate measurements of joint congruency.

1.7   Thesis Overview

Chapter 2 describes the development of an inter-bone distance algorithm to non-invasively examine joint congruency at the ulnohumeral joint. Results from a single specimen are shown investigating the effect of load and elbow flexion angle on ulnohumeral joint congruency. This technique is then validated using the gold standard, experimental casting technique.

Chapter 3 describes a paired-point registration technique to render 3D models of the ulnohumeral joint according to magnetically tracked elbow flexion. Continuous elbow flexion is achieved using a previously developed elbow motion simulator. Fiducial markers will be fixed to the denuded humerus and ulna and will be used in the registration to position the humerus and ulna according to the tracked motion that was achieved while the intact elbow was in the simulator. Traditional kinematics examining valgus angulation will be analyzed in five specimens and compared to the 3D models of the ulnohumeral joint throughout elbow flexion. The effect of radial head excision and replacement, on ulnohumeral joint stability will be examined. Coupled motion of the ulna with respect to the humerus will be visualized using the registration technique employed in this study. The accuracy of this registration will also be examined in a single specimen.

Chapter 4 explores the efficacy of employing optical tracking to increase the accuracy of the registration technique employed in Chapter 3 to extend this technique to incorporate the inter-bone distance algorithm and examine joint congruency of joints undergoing continuous elbow flexion in the elbow motion simulator. The accuracy of this revised registration approach will be examined in four specimens and the extension of this technique to include the inter-bone distance algorithm will be validated in a single specimen using the gold standard, experimental casting technique.

Chapter 5 examines the effect of collateral ligament repair on the stability and ulnohumeral joint congruency in five specimens undergoing active and passive elbow flexion using the registration and inter-bone distance algorithm described in previous

chapters. The relationship between traditional kinematics and joint congruency measures will be examined.

Chapter 6 investigates the use of x-ray CT as it relates to employing the inter-bone distance algorithm clinically. This chapter investigates the effect of tube current (5 protocols) and pitch ratio (3 protocols) on the effective dose applied to five statically positioned glenohumeral cadavers. The application of the inter-bone distance algorithm will be extended to the glenohumeral joint of the shoulder as this is a radiosensitive region of the body. A minimum amount of tube current and pitch ratio will be determined to develop a scanning protocol that applies the minimum radiation exposure to the patient, while maintaining a level of high diagnostic image quality and utility. The inter-bone distance algorithm is applied to each cadaver in all dose varying protocols and compared.

Chapter 7 provides the conclusions as well as future directions of this research.

1.8 References

Amis, A.A., Dowson, D., and Wright, V. (1980) Elbow joint force predictions for some strenuous isometric actions. *J Biomech.* 13[9], 765-775.

An, K.N., Hui, F.C., Morrey, B.F., Linscheid, R.L., and Chao, E.Y. (1981) Muscles across the elbow joint: a biomechanical analysis. *J.Biomech.* 14[10], 659-669.

Anderst, W.J. and Tashman, S. (2003) A method to estimate *in vivo* dynamic articular surface interaction. *J Biomech.* 36[9], 1291-1299.

Ateshian, G.A., Kwak, S.D., Soslowsky, L.J., and Mow, V.C. (1994) A stereophotogrammetric method for determining in situ contact areas in diarthrodial joints, and a comparison with other methods. *J Biomech.* 27[1], 111-124.

Besier, T.F., Draper, C.E., Gold, G.E., Beaupre, G.S., and Delp, S.L. (2005) Patellofemoral joint contact area increases with knee flexion and weight-bearing. *J Orthop.Res.* 23[2], 345-350.

Besl PJ and McKay ND . (1992) A Method for Registration of 3-D Shapes. *IEEE Transactions on Pattern Analysis and Machine Intelligance* 14, 239-256.

Bey, M.J., Kline, S.K., Tashman, S., and Zauel, R. (2008a) Accuracy of biplane x-ray imaging combined with model-based tracking for measuring *in vivo* patellofemoral joint motion. *J.Orthop.Surg.Res.* 3, 38.

Bey, M.J., Kline, S.K., Zauel, R., Lock, T.R., and Kolowich, P.A. (2008b) Measuring dynamic *in vivo* glenohumeral joint kinematics: technique and preliminary results. *J Biomech.* 41[3], 711-714.

Black, J.D., Matejczyk, M.B., and Greenwald, A.S. (1981) Reversible cartilage staining technique for defining articular weight-bearing surfaces. *Clin.Orthop.Relat Res.* [159], 265-267.

Boone, D.C. and Azen, S.P. (1979) Normal range of motion of joints in male subjects. *J Bone Joint Surg Am.* 61[5], 756-759.

Bottlang, M., O'Rourke, M.R., Madey, S.M., Steyers, C.M., Marsh, J.L., and Brown, T.D. (2000) Radiographic determinants of the elbow rotation axis: experimental identification and quantitative validation. *J.Orthop Res.* 18[5], 821-828.

Boyer, P.J., Massimini, D.F., Gill, T.J., Papannagari, R., Stewart, S.L., Warner, J.P., and Li, G. (2008) *In vivo* articular cartilage contact at the glenohumeral joint: preliminary report. *J.Orthop.Sci.* 13[4], 359-365.

Brechter, J.H. and Powers, C.M. (2002) Patellofemoral joint stress during stair ascent and descent in persons with and without patellofemoral pain. *Gait.Posture.* 16[2], 115-123.

Bullough, P., Goodfellow, J., Greenwald, A.S., and O'Connor, J. (1968) Incongruent surfaces in the human hip joint. *Nature* 217[5135], 1290.

Bullough, P.G. (1981) The geometry of diarthrodial joints, its physiologic maintenance, and the possible significance of age-related changes in geometry-to-load distribution and the development of osteoarthritis. *Clin.Orthop Relat Res.* [156], 61-66.

Cohen, Z.A., McCarthy, D.M., Kwak, S.D., Legrand, P., Fogarasi, F., Ciaccio, E.J., and Ateshian, G.A. (1999) Knee cartilage topography, thickness, and contact areas from MRI: *in vitro* calibration and *in vivo* measurements. *Osteoarthritis.Cartilage.* 7[1], 95-109.

DeFrate, L.E., Sun, H., Gill, T.J., Rubash, H.E., and Li, G. (2004) *In vivo* tibiofemoral contact analysis using 3D MRI-based knee models. *J.Biomech.* 37[10], 1499-1504.

Duck, T.R., Dunning, C.E., King, G.J., and Johnson, J.A. (2003) Variability and repeatability of the flexion axis at the ulnohumeral joint. *J.Orthop.Res.* 21[3], 399-404.

Eckstein, F., Lohe, F., Hillebrand, S., Bergmann, M., Schulte, E., Milz, S., and Putz, R. (1995a) Morphomechanics of the humero-ulnar joint: I. Joint space width and contact areas as a function of load and flexion angle. *Anat.Rec.* 243[3], 318-326.

Eckstein, F., Lohe, F., Muller-Gerbl, M., Steinlechner, M., and Putz, R. (1994) Stress distribution in the trochlear notch. A model of bicentric load transmission through joints. *J.Bone Joint Surg Br.* 76[4], 647-653.

Eckstein, F., Lohe, F., Schulte, E., Muller-Gerbl, M., Milz, S., and Putz, R. (1993) Physiological incongruity of the humero-ulnar joint: a functional principle of optimized stress distribution acting upon articulating surfaces? *Anat.Embryol.(Berl)* 188[5], 449-455.

Eckstein, F., Merz, B., Muller-Gerbl, M., Holzknecht, N., Pleier, M., and Putz, R. (1995b) Morphomechanics of the humero-ulnar joint: II. Concave incongruity determines the distribution of load and subchondral mineralization. *Anat.Rec.* 243[3], 327-335.

Eisenhart-Rothe, R., Siebert, M., Bringmann, C., Vogl, T., Englmeier, K.H., and Graichen, H. (2004) A new *in vivo* technique for determination of 3D kinematics and contact areas of the patello-femoral and tibio-femoral joint. *J Biomech.* 37[6], 927-934.

Felson, D.T., Lawrence, R.C., Dieppe, P.A., Hirsch, R., Helmick, C.G., Jordan, J.M., Kington, R.S., Lane, N.E., Nevitt, M.C., Zhang, Y., Sowers, M., McAlindon, T., Spector, T.D., Poole, A.R., Yanovski, S.Z., Ateshian, G., Sharma, L., Buckwalter, J.A., Brandt, K.D., and Fries, J.F. (2000) Osteoarthritis: new insights. Part 1: the disease and its risk factors. *Ann.Intern.Med.* 133[8], 635-646.

Fitzpatrick, J.M. (2009) Fiducial Registration Error and Target Registration Error are Uncorrelated. *SPIE Medical Imaging 2009: Visualization, Image-Guided Procedures and Modeling* 7261, 726102-1-726102-12.

Fitzpatrick, J.M., West, J.B., and Maurer, C.R., Jr. (1998) Predicting error in rigid-body point-based registration. *IEEE Trans.Med.Imaging* 17[5], 694-702.

Fujikawa, K., Seedhom, B.B., and Wright, V. (1983) Biomechanics of the patello-femoral joint. Part I: A study of the contact and the congruity of the patello-femoral compartment and movement of the patella. *Eng Med.* 12[1], 3-11.

Gallo, R.A., Payatakes, A., and Sotereanos, D.G. (2008) Surgical options for the arthritic elbow. *J Hand Surg Am* 33[5], 746-759.

Gold, G.E., Besier, T.F., Draper, C.E., Asakawa, D.S., Delp, S.L., and Beaupre, G.S. (2004) Weight-bearing MRI of patellofemoral joint cartilage contact area. *J Magn Reson.Imaging* 20[3], 526-530.

Goodfellow, J.W. and Bullough, P.G. (1967) The pattern of aging of the articular cartilage of the elbow joint. *J Bone Joint Surg Am.* 49B, 175.

Goto, A., Moritomo, H., Murase, T., Oka, K., Sugamoto, K., Arimura, T., Nakajima, Y., Yamazaki, T., Sato, Y., Tamura, S., Yoshikawa, H., and Ochi, T. (2004) *In vivo* elbow biomechanical analysis during flexion: three-dimensional motion analysis using magnetic resonance imaging. *J Shoulder Elbow Surg.* 13[4], 441-447.

Greenwald, A.S. and O'Connor, J.J. (1971) The transmission of load through the human hip joint. *J Biomech.* 4[6], 507-528.

Halls A.A. and Travill A. (1964) Transmission of Pressures across the Elbow Joint. *Anat.Rec.* 150, 243-247.

Harris, M.L., Morberg, P., Bruce, W.J., and Walsh, W.R. (1999) An improved method for measuring tibiofemoral contact areas in total knee arthroplasty: a comparison of K-scan sensor and Fuji film. *J Biomech.* 32[9], 951-958.

Haut, R.C. (1989) Contact pressures in the patellofemoral joint during impact loading on the human flexed knee. *J Orthop.Res.* 7[2], 272-280.

Hinterwimmer, S., Gotthardt, M., Eisenhart-Rothe, R., Sauerland, S., Siebert, M., Vogl, T., Eckstein, F., and Graichen, H. (2005) *In vivo* contact areas of the knee in patients with patellar subluxation. *J.Biomech.* 38[10], 2095-2101.

Horn B.K.P . (1987) Closed-form solution of absolute orientation using unit quaternions. *Optical Society of America* 4[4], 629-642.

Hsieh J (2003) Introduction. In *Computed Tomography Principles, Design, Artifacts and Recent Advances* SPIE- The International Society for Optical Engineering. Pp. 1-18.

Huberti, H.H. and Hayes, W.C. (1984) Patellofemoral contact pressures. The influence of q-angle and tendofemoral contact. *J Bone Joint Surg.Am.* 66[5], 715-724.

Hunter, D.J., Sharma, L., and Skaife, T. (2009) Alignment and osteoarthritis of the knee. *J.Bone Joint Surg.Am.* 91 Suppl 1, 85-89.

Kedgley, A.E., Birmingham, T., and Jenkyn, T.R. (2009) Comparative accuracy of radiostereometric and optical tracking systems. *J.Biomech.* 42[9], 1350-1354.

King, G.J., Itoi, E., Niebur, G.L., Morrey, B.F., and An, K.N. (1994) Motion and laxity of the capitellocondylar total elbow prosthesis. *J Bone Joint Surg Am.* 76[7], 1000-1008.

London, J.T. (1981) Kinematics of the elbow. *J Bone Joint Surg Am.* 63[4], 529-535.

Losch, A., Eckstein, F., Haubner, M., and Englmeier, K.H. (1997) A non-invasive technique for 3-dimensional assessment of articular cartilage thickness based on MRI. Part 1: Development of a computational method. *Magn Reson.Imaging* 15[7], 795-804.

Marai, G.E., Crisco, J.J., and Laidlaw, D.H. (2006) A kinematics-based method for generating cartilage maps and deformations in the multi-articulating wrist joint from CT images. *Conf.Proc.IEEE Eng Med.Biol.Soc.* 1, 2079-2082.

Marai, G.E., Laidlaw, D.H., Demiralp, C., Andrews, S., Grimm, C.M., and Crisco, J.J. (2004) Estimating joint contact areas and ligament lengths from bone kinematics and surfaces. *IEEE Trans.Biomed.Eng* 51[5], 790-799.

Matsuda, S., Ishinishi, T., White, S.E., and Whiteside, L.A. (1997) Patellofemoral joint after total knee arthroplasty. Effect on contact area and contact stress. *J Arthroplasty* 12[7], 790-797.

Maurer, C.R., Aboutanos, G.B., Dawant, B.M., Maciunas, R.J., and Fitzpatrick, J.M. (1996) Registration of 3-D images using weighted geometrical features. *IEEE Trans.Med.Imaging* 15[6], 836-849.

Maurer, C.R., Jr., Fitzpatrick, J.M., Wang, M.Y., Galloway, R.L., Jr., Maciunas, R.J., and Allen, G.S. (1997) Registration of head volume images using implantable fiducial markers. *IEEE Trans.Med.Imaging* 16[4], 447-462.

Maurer, C.R., Jr., Maciunas, R.J., and Fitzpatrick, J.M. (1998) Registration of head CT images to physical space using a weighted combination of points and surfaces. *IEEE Trans.Med.Imaging* 17[5], 753-761.

McDonald, C.P., Brownhill, J.R., King, G.J., Johnson, J.A., and Peters, T.M. (2007) A comparison of registration techniques for computer- and image-assisted elbow surgery. *Comput.Aided Surg.* 12[4], 208-214.

McRobbie D.W., Moore E.A., Grave M.J., and Prince M.R. (2012) Seeing is believing: introduction to image contrast. In *MRI From Picture to Proton* Cambridge University Press. Pp. 30-46.

Merz, B., Eckstein, F., Hillebrand, S., and Putz, R. (1997) Mechanical implications of humero-ulnar incongruity--finite element analysis and experiment. *J.Biomech.* 30[7], 713-721.

Momose, T., Nakatsuchi, Y., and Saitoh, S. (1999) Contact area of the trapeziometacarpal joint. *J Hand Surg.[Am.]* 24[3], 491-495.

Morrey, B.F. (2000a) *Anatomy of the Elbow Joint. In: The Elbow and Its Disorders(b).* W.B.Saunders Company, Philadelphia.

Morrey, B.F. (2000b) *Biomechanics of the Elbow. In: The Elbow and Its Disorders(a).*

Morrey, B.F. and Chao, E.Y. (1976) Passive motion of the elbow joint. *J Bone Joint Surg Am.* 58[4], 501-508.

O'Driscoll, S.W., Bell, D.F., and Morrey, B.F. (1991) Posterolateral rotatory instability of the elbow. *J Bone Joint Surg Am.* 73[3], 440-446.

Ronsky, J.L., Herzog, W., Brown, T.D., Pedersen, D.R., Grood, E.S., and Butler, D.L. (1995) *In vivo* quantification of the cat patellofemoral joint contact stresses and areas. *J Biomech.* 28[8], 977-983.

Sadowsky, O., Yaniv, Z., and Joskowicz, L. (2002) Comparative *in vitro* study of contact- and image-based rigid registration for computer-aided surgery. *Comput.Aided Surg.* 7[4], 223-236.

Salsich, G.B., Ward, S.R., Terk, M.R., and Powers, C.M. (2003) *In vivo* assessment of patellofemoral joint contact area in individuals who are pain free. *Clin.Orthop.Relat Res.* [417], 277-284.

Scherrer PK, Hillberry BM, and Van Sickle DC . (1979) Determining the *in vivo* areas of contact in the canine shoulder. *J.Biomech.Eng* 101, 271-278.

Schwab, G.H., Bennett, J.B., Woods, G.W., and Tullos, H.S. (1980) Biomechanics of elbow instability: the role of the medial collateral ligament. *Clin.Orthop* [146], 42-52.

Shiba, R., Sorbie, C., Siu, D.W., Bryant, J.T., Cooke, T.D., and Wevers, H.W. (1988) Geometry of the humeroulnar joint. *J Orthop Res.* 6[6], 897-906.

Stormont, T.J., An, K.N., Morrey, B.F., and Chao, E.Y. (1985) Elbow joint contact study: comparison of techniques. *J.Biomech.* 18[5], 329-336.

Sugano, N., Sasama, T., Sato, Y., Nakajima, Y., Nishii, T., Yonenobu, K., Tamura, S., and Ochi, T. (2001) Accuracy evaluation of surface-based registration methods in a computer navigation system for hip surgery performed through a posterolateral approach. *Comput.Aided Surg.* 6[4], 195-203.

Tashman, S. and Anderst, W. (2003) *In vivo* measurement of dynamic joint motion using high speed biplane radiography and CT: application to canine ACL deficiency. *J.Biomech.Eng* 125[2], 238-245.

Tillmann, B. (1978) A contribution to the functional morphology of articular surfaces. *Norm.Pathol.Anat.(Stuttg)* 34, 1-50.

Ugurlu, M., Senkoylu, A., Ozsoy, H., Demirkale, I., Kilicarslan, K., and Dogan, M. (2009) Outcome of ulnohumeral arthroplasty in osteoarthritis of the elbow. *Acta Orthop Belg.* 75[5], 606-610.

Walker PS (2008) *Human Joints and Their Artificial Replacements.*

Wan, L., de Asla, R.J., Rubash, H.E., and Li, G. (2006) Determination of *in vivo* articular cartilage contact areas of human talocrural joint under weightbearing conditions. *Osteoarthritis.Cartilage.* 14[12], 1294-1301.

West, J.B., Fitzpatrick, J.M., Toms, S.A., Maurer, C.R., Jr., and Maciunas, R.J. (2001) Fiducial point placement and the accuracy of point-based, rigid body registration. *Neurosurgery* 48[4], 810-816.

Wretenberg, P., Ramsey, D.K., and Nemeth, G. (2002) Tibiofemoral contact points relative to flexion angle measured with MRI. *Clin.Biomech.(Bristol., Avon.)* 17[6], 477-485.

Yaniv (2008) Rigid Registration. In *Image-Guided Interventions Technology and Applications* (Edited by Peter and Cleary K.) Springer. Pp. 159-192.

Chapter 2 – Development of an Image-Based Technique to Examine Joint Congruency at the Elbow

OVERVIEW

This chapter describes the development of an image-based technique to examine joint congruency; as a surrogate of joint contact. To demonstrate the utility of this technique, joint congruency was examined in a cadaveric specimen under statically loaded and unloaded conditions throughout elbow flexion. This technique was then validated using experimental casting[1].

2.1   Introduction

In the investigation of joint biomechanics, knowledge of joint contact area is useful in identifying normal and pathologic mechanics. As described in detail in Chapter 1 (Section 1.4.1) a variety of *in vitro* methods have been employed to elucidate contact within diarthrodial joints, including various casting (Eckstein *et al.*, 1994; Eckstein *et al.*, 1995; Liew *et al.*, 2003; Stormont *et al.*, 1985), staining (Black *et al.*, 1981; Stormont *et al.*, 1985), and stereophotogrammetric (SPG) techniques (Ateshian *et al.*, 1994; Soslowsky *et al.*, 1992). Few studies have investigated *elbow* contact area and of those, direct access to the joint's articular surfaces has been required (Eckstein *et al.*, 1994; Goel *et al.*, 1982; Goodfellow and Bullough, 1967; Goto *et al.*, 2004; Stormont *et al.*, 1985).

---

[1] A version of this has been published: Lalone EA, McDonald CP, Ferreira LM, Peters TM, King GW, Johnson JA. Development of an image-based technique to examine joint congruency at the elbow. Computer Methods in Biomechanics and Biomedical Engineering. 2012 Jan 13 [Epub ahead of print].

These invasive methods employ partial or complete joint exposure thereby altering the joint's kinematics by disturbing soft tissue stabilizers, thus making them less clinically relevant.

Medical imaging based approaches employing x-ray computed tomography (CT) (Marai *et al.*, 2004) and magnetic resonance imaging (MRI) (Besier *et al.*, 2005; Boyer *et al.*, 2008; Cohen *et al.*, 1999; Eisenhart-Rothe *et al.*, 2004; Gold *et al.*, 2004; Goto *et al.*, 2004; Heino and Powers, 2002; Hinterwimmer *et al.*, 2005; Salsich *et al.*, 2003; Wan *et al.*, 2006; Ward *et al.*, 2003; Wretenberg *et al.*, 2002) have been developed in an effort to non-invasively quantify the joint mechanics and contact area. The implications of using imaging to determine joint interactions are significant as they provide a powerful clinical tool for patient evaluation. Losch *et al.* (1997) noted that few techniques have taken advantage of the volumetric data set, instead using three-dimensional (3D) imaging technologies to examine serial slices through the joint in a two-dimensional (2D) fashion (Brechter and Powers, 2002; Gold *et al.*, 2004; Salsich *et al.*, 2003; Wretenberg *et al.*, 2002). This approach can produce erroneous results, since components of 3D lengths and angles can be attenuated when being measured from a 2D perspective (Losch *et al.*, 1997). However, 3D joint surface analysis is difficult to achieve when examining topographically complex joints such as the ulnohumeral joint of the elbow.

Computational models employing 3D volumetric data have been developed and employed proximity mapping (Anderst and Tashman, 2003; Ateshian *et al.*, 1994; Bey *et al.*, 2008; Eisenhart-Rothe *et al.*, 2004; Goto *et al.*, 2004; Losch *et al.*, 1997; Marai *et al.*,

2004; Scherrer PK *et al.*, 1979; Soslowsky *et al.*, 1992). This approach was first introduced by Scherrer *et al.* (1979) and can be used with MRI images measuring cartilage-cartilage distance (Cohen *et al.*, 1999; DeFrate *et al.*, 2004) or bone-bone distances (Goto *et al.*, 2004) or alternatively, with CT images measuring bone-bone distances (Anderst and Tashman, 2003; Cohen *et al.*, 1999; Goto *et al.*, 2004; Marai *et al.*, 2004). Although these methods provide non-invasive approaches to examining joint contact area, the experimental validation of these computational methods has not been conducted (Anderst and Tashman, 2003; Cohen *et al.*, 1999; Goto *et al.*, 2004; Marai *et al.*, 2004).

The objective of this chapter was to develop an approach for measuring joint congruency using 3D volumetric images generated by CT and proximity mapping. Joint space measurements were obtained using an inter-bone distance algorithm to examine overall joint congruency, a surrogate for joint contact. The chief assumption was that regions which are in close proximity, as measured from the subchondral bony surfaces, represent regions of joint contact.

This technique was used to measure ulnohumeral joint congruency in a cadaveric elbow with simulated muscle loading at various angles of flexion (0˚, 30˚, 60˚ and 90˚). Validation of this technique was conducted in a static joint loading device, using a casting technique (Stormont *et al.*, 1985) as a gold standard comparison.

2.2 Methods

An overview of the data analysis and experimental protocol is shown in Figure 2.1.

2.2.1 SPECIMEN PREPARATION AND LOADING

One fresh-frozen upper extremity was selected (Male, 48 years) that exhibited minimal degenerative arthritis. The specimen was sectioned at mid-diaphysis of the humerus and the distal portion was thawed at room temperature for 18 hours. The tendons of the brachialis, biceps and triceps muscles were isolated for the purpose of joint loading (during imaging) through simulated muscle tension. Braided Dacron® fishing line (18 gauge) was sutured to the tendons using a locking Krakow stitch. The specimen was mounted in a CT-compatible custom designed elbow joint positioning and muscle loading device (Figure 2.2). This device allowed elbow flexion angle adjustments for muscle loading at various static flexion angles. Muscle tension was simulated using static weights. The biceps and brachialis tendon sutures were tensioned together with a 44N weight. A second 44N weight tensed the triceps tendon suture. Pulleys allowed for the approximation of *in vivo* muscle lines of action.
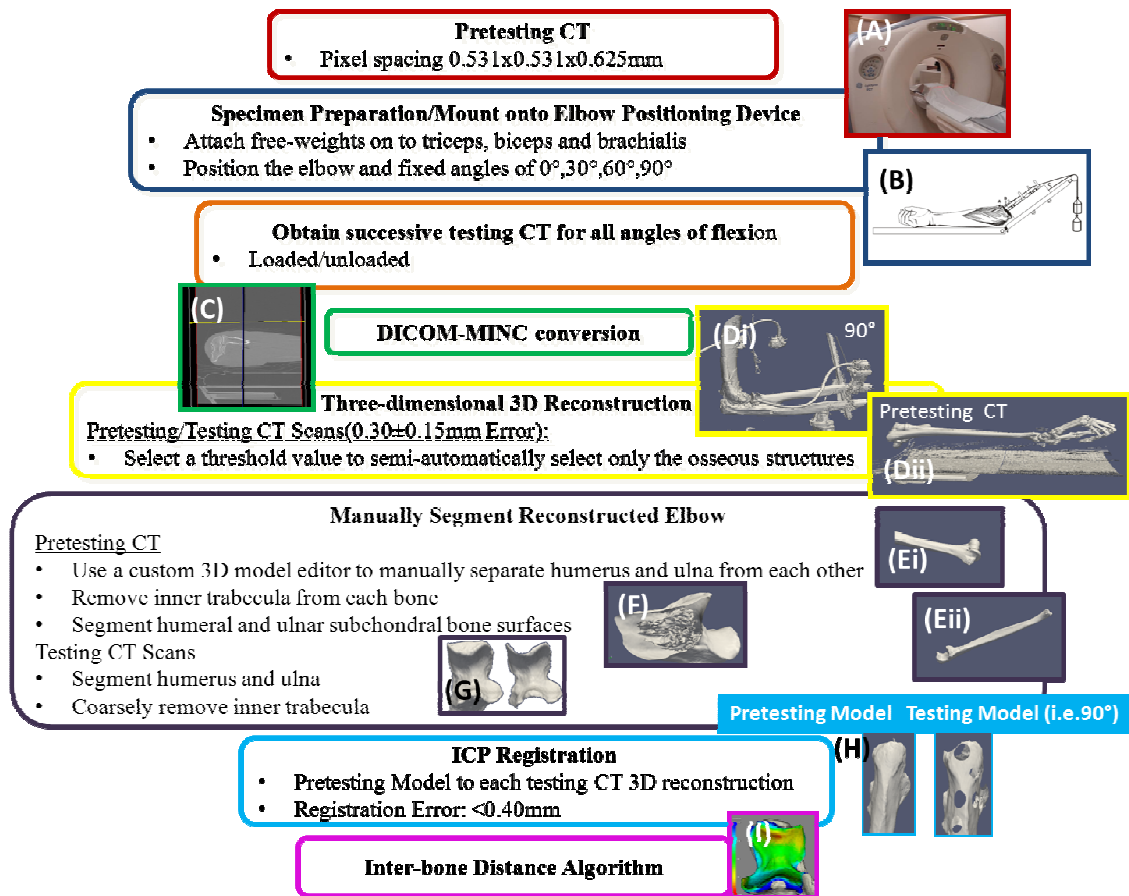
Figure 2.1: Overview of Data Analysis and Experimental Protocol
A) A pre-testing CT is acquired prior to testing.
B) Successive CT scans are acquired while the specimen is in the elbow positioning device.
C) The DICOM images are converted to a single MINC file and used to reconstruct a 3D model.
D) A 3D reconstruction from the pre-testing CT and successive testing scans (Di) is created using a semi-automatic thresholding technique. The pre-testing model (Dii) however undergoes an additional post-processing manual segmentation to E) isolate the humerus and ulna (F) remove inner trabecula and (G) isolate the subcondral region of the humerus and ulna.
H) The pre-testing model is then registered using a surface based ICP registration technique to map the pre-testing model to the location of each testing 3D reconstruction.
I) The inter-bone distance algorithm is then applied to each registered model at each angle of flexion in the loaded and unloaded condition.

Free Weights

Flexion angle adjustment cable
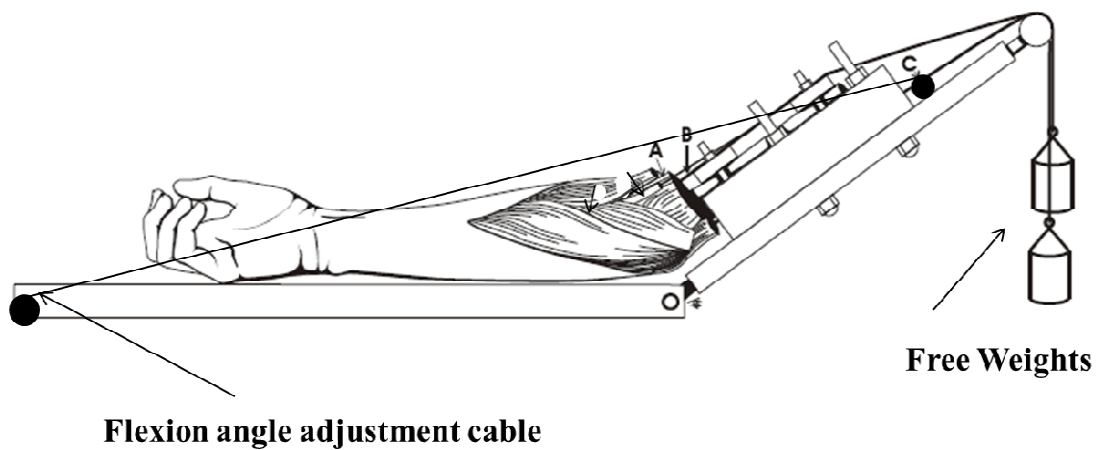
Figure 2.2: Elbow Joint Positioning and Muscle Loading Device
The specimen was placed in a CT compatible jig, which maintained a fixed elbow flexion angle by adjustment and positioned at 0^0, 30^0, 60^0 and 90^0 of flexion using a goniometer. The wrist was positioned in neutral forearm rotation. Free weights were attached to the tendons (44N on triceps, 44N on biceps and brachialis together).
A) Isolated tendon attached to tendon sutures.
B) Humeral clamp positioned over the humerus.
C) Triceps tendon sutures positioned to represent in-vivo lines of action (also for biceps and brachialis tendon).

2.2.2 VOLUMETRIC IMAGE ACQUISITION

Volumetric data of the intact specimen were acquired prior to testing (pre-testing CT) and while in the loading device on test day (GE Lightspeed VCT 64 Slice CT Scanner, New Berlin, WI). The loading device was positioned in the CT scanner so that the long axis of the gantry was roughly parallel to the long axis of the forearm. Approximately 400 slices were acquired for each specimen with a 20x20cm field of view, a 512x512 reconstruction matrix, a 0.53x0.53x0.625mm voxel size, and technique factors of 146mAs, and 120 kVp. CT images were acquired with the prepared arm fixed at 0˚, 30˚, 60˚ and 90˚ of elbow flexion. Arm position was verified using a goniometer and CT images were acquired in the unloaded and loaded states.

2.2.3 SEGMENTATION AND BONE SURFACE MODELING

Successive DICOM files generated from each CT scan were converted to a MINC file (Montreal Neurological Institute and Hospital, 2010) (Figure 2.1C). Three-dimensional surface models were created using custom software by manually selecting a segmentation threshold to visualize only the bony aspects of the volumetric image (Marching Cubes Algorithm, VTK Version 4.2.1, Visualization Toolkit, Kitware, Clifton Park, NY) (Schroeder W *et al.*, 1998)(Figure 2.1D). The reconstructed bone model represents the subchondral region below the articular surface of the humerus and ulna. To ensure that a proper threshold was selected, successive 2D slices were overlaid with the reconstructed subchondral surface to ensure that the threshold selected accurately corresponded to the outer surface of the imaged osseous anatomy. In a separate specimen,

the accuracy of this reconstruction was assessed by obtaining digitizations of a cartilage-devoid humeral bone and comparing a surface reconstruction of these point clouds to a 3D model obtained from CT (Appendix I). The mean distance between these two surfaces was 0.30±0.15mm. The humerus and ulna were separated from each other and from the radius and saved as a separate file (Figure 2.1E). Additionally, the inside of the bone model, corresponding to the cancellous bone, was manually removed to preserve only the outer surface of the bone (Figure 2.1F).This process decreases the overall computation time required for the inter-bone distance algorithm. For the pre-testing bone reconstruction, the subchondral surface was manually segmented (Figure 2.1G) and divided into medial and lateral zones (Figure 2.3). For the humerus, these zones were divided along the deepest groove of the trochlea (Figure 2.3A). For the ulna, these zones were divided along the guiding ridge of the greater sigmoid notch (Figure 2.3B). Only the subchondral bone surfaces were used in the inter-bone distance algorithm as these regions correspond to the joint articulation. Inter-bone distances were not measured for the suprachondylar regions of the bones. The entire subchondral bone region of the humerus and ulna were used to measure the surface area of the subchondral surface.
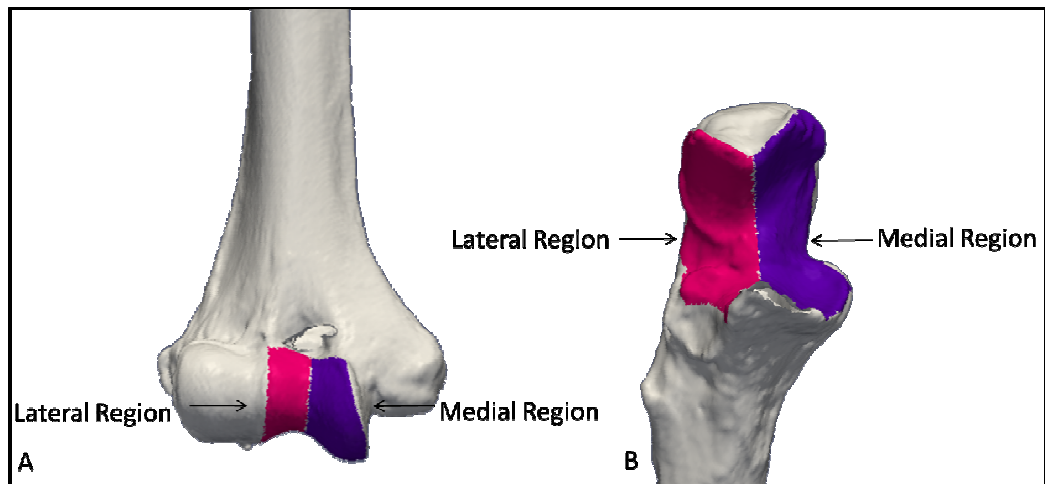
Figure 2.3: Humeral and Ulnar Articular Zones
A) Medial (purple) and lateral (pink) regions were created using the trochlea to divide the articular surface of the humerus.
B) Medial and lateral regions were created used the greater sigmoid notch on the ulna.

2.2.4   BONE SURFACE MODEL REGISTRATION

Bone surface models (humerus, ulna and segmented subchondral bone models) from the pre-testing CT were registered to corresponding models of each statically loaded CT scenario (0˚,30˚,60˚,90˚) using the Iterative Closest Point (ICP) surface-based registration algorithm (Besl PJ and McKay ND, 1992). To ensure optimal alignment, three anatomical landmarks were initially selected on each surface model and a paired-point registration was performed for coarse alignment. This was then refined by applying the ICP registration with an end condition of surface misalignment ≤ 0.001mm RMS or a maximum of 100 iterations. A pilot study determined that the mean distance between the two surface models between the last two iterations (max. =100) of the algorithm was 0.0009mm (70 iterations) and 0.0022mm (100 iterations) for the humerus and ulna, respectively. The overall accuracy of the ICP registration was also examined in a single specimen between the pre-testing and a testing CT. The mean distance between the two registered surfaces was calculated by examining the distances between all of the closest points, resulting in a mean value of 0.38±0.12mm (max: 1.056mm, min: 0.02mm, 43377 points) for the humerus and 0.31±0.13mm (max: 1.60mm, min: 0.01mm, 41898 points) for the ulna. This registration was performed to save on the amount of post-processing time required for multiple CT scans. Instead, this detailed segmentation was only performed on the pre-testing 3D reconstruction and then registered to the position and orientation of the humerus and ulna in each testing CT scan (0°, 30°, 60° and 90°). Additionally, the subchondral surface area of the humerus and ulna were only segmented

once and registered to each testing scan. As the surface area of the humerus and ulna are used in Equation 2.1 in the inter-bone distance algorithm, it was important to ensure that this value does not change between scans. Finally, an additional motivation for requiring this pre-testing CT was to facilitate the use of this proximity mapping technique clinically. In order to reduce the amount of radiation exposure, a single high resolution scan of the elbow would be obtained, followed by successive low-dose scans at each angle of flexion. The high resolution scans were then registered to the low dose scans in the same manner as described above.

2.2.5   INTER-BONE DISTANCE ALGORITHM

Joint congruency was calculated using an inter-bone distance algorithm. Proximity mapping was used to provide an image of the overall joint congruency. The surface area across the subchondral bone can be measured for a given level of proximity. The scale used on the proximity map was selected by considering cartilage thickness and joint space (Appendix B, C). In this study, a region in which inter-bone distances were less than 4mm was classified as a '(close) proximity region'. Within this proximity region (< 4.0mm), 'levels of proximity' were also employed measuring the surface area of the subchondral bone within high proximity (< 0.5mm), medium proximity (< 1.5mm), low proximity (< 2.5mm) and ultra-low proximity (< 3.5mm).

The 3D surface reconstructions (Figure 2.4A) are represented as collections of polygons (Figure 2.4B, C) and each polygonal surface is contained by a wireframe mesh (Figure 2.4D). Using custom software written with VTK, minimum inter-model bone

distances were calculated using a nearest point-to-point distance algorithm, where the

points correspond to the vertices within each triangular mesh (Figure 2.4E, F).
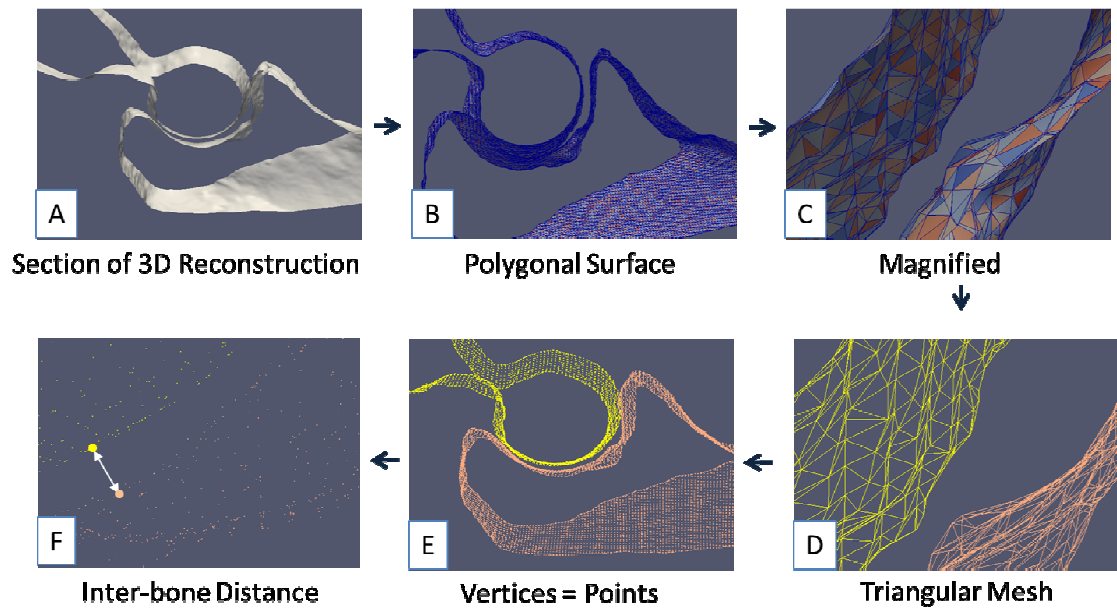
Figure 2.4: Schematic of Inter-bone Distance Algorithm
A) A cross-section of the reconstructed bony models.
B) 3D Reconstruction is composed of polygons.
C) Magnified view of polygonal surface showing individual cells.
D) A wireframe encloses this polygonal surface.
E) At each vertex on the triangular mesh, a point resides at each vertex on the mesh.
F) These points are the points used in the inter-bone distance algorithm.

The algorithm first lists the Cartesian coordinates of all points on the humeral and ulnar surface models, and assigns a location-specific identification number (ID). This function defined within VTK (FindPoint) assigns identification numbers to each point that was based on the Cartesian coordinates of that point within the CT coordinate system for each 3D reconstruction. Therefore, two points having the same Cartesian coordinate will have identical ID numbers and the distance between these points would be zero. The algorithm therefore uses these identification numbers to determine which points (on opposing surfaces) are closest in proximity based on their location specific ID number. The 3D distance between these closest points was then calculated.

The surface area of the proximity region was determined using the following relationship:

$$\frac{SA_{\text{subchondral}}}{N_{\text{subchondral}}} = \frac{SA_{\text{presecribeddistance}}}{N_{\text{prescribeddistance}}} \qquad \text{Equation 2.1}$$

The surface area of the subchondral bone model was determined by summing the area of all its polygons ($SA_{\text{subchondral bone}}$). The number of points contained on the subchondral reconstruction was also recorded ($N_{\text{subchondral bone}}$). The inter-bone distance algorithm lists all of the minimum distance values measured. The algorithm then returns the number of points found that have a prescribed inter-bone distance value ($N_{\text{prescribed distance}}$). The surface area of the entire proximity region (< 4mm), or given proximity level (high, med, low, ultra-low) was determined by using re-arranging Equation 2.1 and

corresponds to the surface area on the subchondral surface ($SA_{prescribeddistance}$) within a prescribed inter-bone distance threshold. An analogous calculation to measure the surface area of the proximity region (< 4.00mm) was also performed for each zone of the subchondral surface on the humeral and ulna articular surface (medial/lateral regions).

For visualization, inter-bone distances were displayed using an iso-contoured proximity map which was created by assigning distances a colour value that was then projected onto the bone. A scale (0mm: red, 4mm: blue) was chosen to display all of the inter-bone distances that are less than 4mm, while all distances greater than 4mm are shown as dark blue.

2.2.6   VALIDATION

2.2.6.1   *Experimental Protocol*

A separate cadaveric elbow (Female, 61 years) was employed in the validation experiment. An intact pre-testing CT of the elbow was acquired using a helical scanner 64-slice computed tomography (CT) scanner (GE Discovery CT750 HD, Waukesha, WI). Approximately 400 slices of the specimen were acquired using the same scanning protocol as in Section 2.2.2. All soft tissues were then removed and the humerus and ulna were separated, and mounted into a previously developed joint compression apparatus that produced a prescribed load of 100N across the ulnohumeral joint (Figure 2.5) (Willis SR, 2006). The bones were aligned to achieve 90° of flexion using a goniometer and then potted using DenStone® cement (Miles Inc. South Bend, IN, USA).

Approximately 150 slices of the specimen were then acquired with the specimen under load using the same scanning parameters as the pre-testing CT. A specialized casting technique was employed to quantify joint contact. A medium viscosity regular body dental casting material (Reprosil Medium Body Vinyl Polysiloxine Impression Material, DENTSPLY International Inc., York, PA) was injected with a syringe between the articular surfaces of the ulnohumeral joint. The compression force was applied to the specimen, and the cast was allowed to set for 15 minutes before retrieval. Articular contact displaces the casting material and leaves a vacant region of where the contact occurred. This casting process was repeated four times to evaluate repeatability. Digital images were obtained of the solidified casts using a camera.

To quantify contact, the bones were released from the compression jig, and each cast was replaced onto the surface of the ulna. Once repositioned, the contacting regions of the cast (vacant regions) were digitized with a pointed stylus using a six degree-of-freedom electromagnetic tracking system (Flock of Birds, Ascension Technologies Corp., Burlington, VT). A 3D surface model of the resulting contact patch was constructed using MATLAB (Math Works Inc. MA, USA). The surface area of this patch, corresponding to the total contact area, was then calculated.
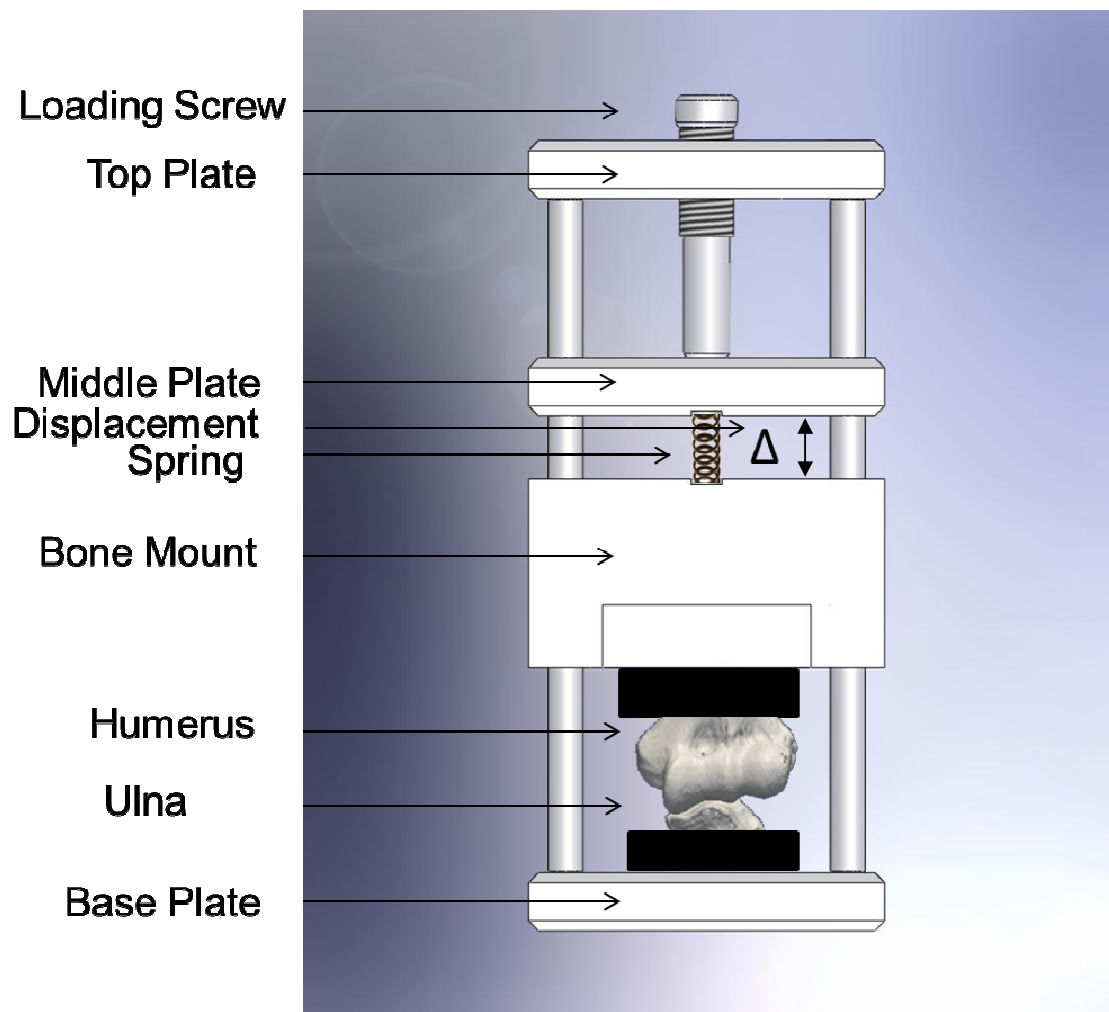
Figure 2.5: Joint Loading Device
A previously developed CT compatible joint loading device was employed to apply a repeatable axial load to the ulnohumeral joint while undergoing imaging. The potted specimen is located on the base of the loading device. The top and middle plates are lowered to engage the spring which is located on the bone mount. The loading screw depresses the spring (by an amount Δ) causing a displacement of the bone mount thus applying an axial load. Calibration of this spring was achieved using a load-cell. (Willis SR, 2006)

2.2.6.2 *Inter-bone Distance Analysis*

Using the inter-bone distance algorithm and the obtained volumetric images, proximity maps were generated as described in Section 2.2.5. The proximity map and the corresponding experimental casts were then compared numerically. To compare the inter-bone distance algorithm and the experimental casting numerically, forty-one inter-bone distances (0-4mm with 0.1mm increments) were inserted into the inter-bone distance algorithm and the resulting areas for the humerus and ulna were obtained. In this study, pre-defined values for inter-bone distances were used to define the four levels of proximity. In theory however, the surface area of a given proximity region can be measured using *any* inter-bone distance value. Therefore, experimental casting was employed to provide insight into the corresponding inter-bone distance threshold that would yield the surface area on the bone that was equal to the contact area as defined by the cast and to ensure that this inter-bone distance algorithm was less than the 4mm used on the proximity maps.

2.3 Results

2.3.1 EFFECT OF FLEXION/LOAD

The proximity maps (< 4mm) for the unloaded and loaded conditions are shown for the humerus (Figure 2.6) and the ulna (Figure 2.7) at each position of elbow flexion (0°, 30°, 60°, and 90°). Using these proximity maps, it was possible to examine how the joint congruency and proximity region track across the articulation through a range of motion. At full extension, the proximity region was located on the posterior side of the

humerus and there are no regions of close proximity on the anterior surface of the humerus. However, with increasing flexion, this region of close proximity tracks to the anterior surface of the humerus. This effect can be seen in both the unloaded and loaded scenarios.
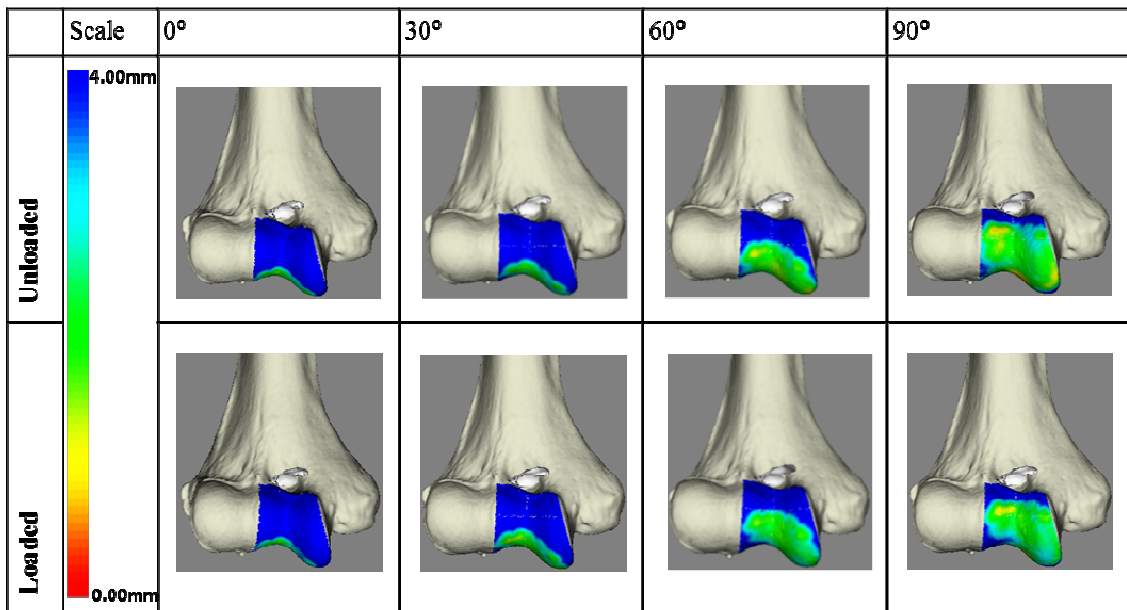
Figure 2.6: Anterior Humerus Proximity Maps
Inter-bone distance proximity maps throughout four statically loaded and unloaded positions. Note that regions that are red correspond to close proximity while blue corresponds to distant. As elbow flexion increases, the regions of close proximity translate from the posterior to anterior region of the distal humerus.
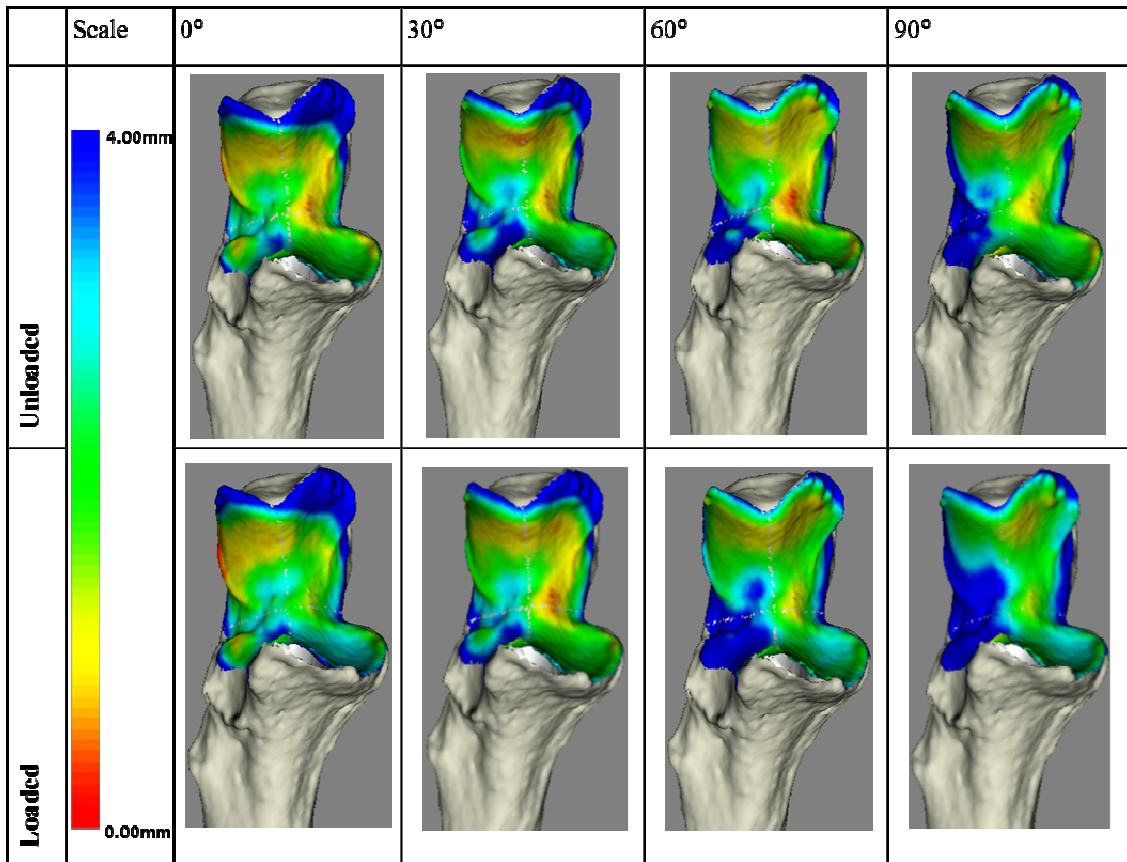
Figure 2.7: Anterior Ulna Proximity Maps

Loaded and unloaded proximity maps for the anterior ulna at each angle of flexion. During all angles of elbow flexion, the proximity region appears in a diffuse pattern. Once a load is applied the same proximity region becomes more concentrated with a decrease in the superior and inferior lateral region.

Examining the distribution of the proximity region on both the medial or lateral region of the humerus and ulna, the proximity maps indicate that for each condition, the proximity regions occur evenly across the medial and lateral zones in early flexion (extension) and then are predominately on the medial side in full flexion. This observation was supported quantitatively in Table 2.1 showing the ratio of the medial to lateral proximity region for the four flexion angles in the unloaded and loaded conditions. Proximity regions (< 4mm) for the medial and lateral side of the humerus and ulna were normalized by dividing the surface area (of the proximity region) by the total the surface area of the medial/lateral region.

Examining the effect of load in this testing protocol, it appears that at all angles of elbow flexion; the proximity region appears in a diffuse pattern that extends transversely across the superior region of the greater sigmoid notch and inferiorly to the medial side of the ulna. However once a load was applied to the joint, this same proximity region becomes more concentrated with a decrease in the superior and inferior lateral region of the ulna.

This decrease in the overall size of the proximity region with load was verified by examining the proximity levels. Levels of proximity (high, medium, low and ultra-low) for the ulna were examined for each loaded/unloaded flexed position as shown in Figure 2.8. Analogous calculations of contact area were performed for the humerus and ulna. With the exception of 30°, there was a decrease in surface area for each proximity level with loading. In general, the surface area of each proximity level for all static positions

for both the humerus and ulna were all less than 1200mm^2. The surface area of the subchondral bone for the humerus was 1590mm^2 (8796 points) and 1636mm^2 (8438 points) for the ulna.

	HUMERUS	ULNA
Unloaded 0˚	0.90	0.89
Unloaded 30˚	0.99	0.94
Unloaded 60˚	1.07	1.08
Unloaded 90˚	1.16	1.26
Loaded 0˚	0.84	0.84
Loaded 30˚	0.96	0.91
Loaded 60˚	1.21	1.20
Loaded 90˚	1.47	1.55

Table 2.1: Ratio of medial to lateral contact for the humerus and ulna in each loading scenario (Threshold = 4mm)

Proximity regions (< 4mm) for the medial and lateral side of the humerus and ulna were normalized by dividing the surface area (of the proximity region) by the total the surface area of the medial/lateral region. The proximity regions occur evenly across the medial and lateral zones in early flexion (extension) and then are predominately on the medial side in full flexion.
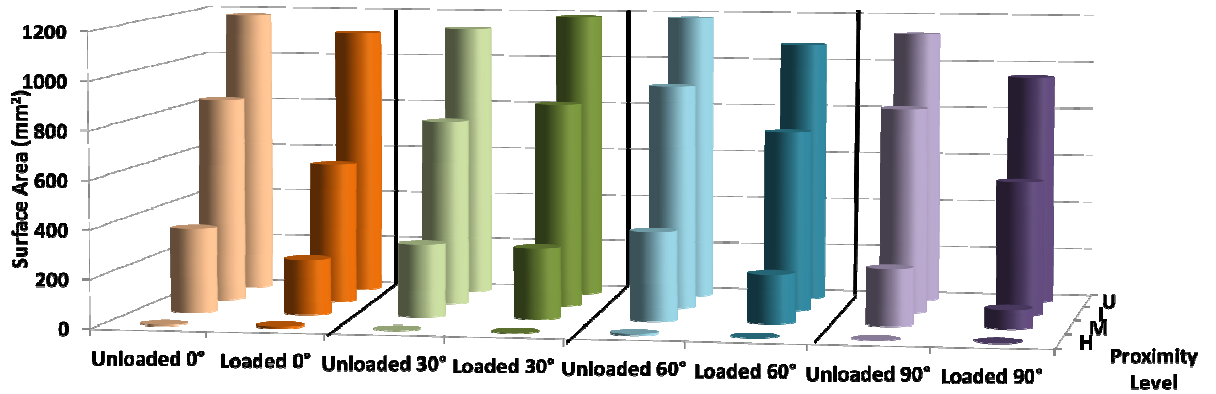
Figure 2.8: Quantification of Joint Congruency at each Proximity Level (Ulna)
Surface Area values for each level of proximity (High, Med, Low and Ultra-low) are shown between loaded and unloaded scenarios at 0°, 30°, 60° and 90 °of flexion. The surface area decreased once the load was applied at 0°, 60° and 90° of flexion.

2.3.2   VALIDATION

Experimental casting has been previously reported to be a very repeatable technique as well as the gold standard technique to examine joint contact area (Stormont *et al.*, 1985). The results of a single cast are shown in Figure 2.9A. The mean contact area measured was $124.30\pm8.22mm^2$. This image was taken with the cast against a light source to show where the cast material was very thin corresponding to closer proximity regions. The experimental cast had a large upper and lower medial region of contact which occurred on the periphery of the joint. On the lateral side, the cast showed a large superior region of joint contact that extended down the lateral side of the ulna, but did not fully contact. Also on the lateral side, there was a large lower region of contact at the coronoid process that then extended to the centre of the joint ending in another contacting region.

On the proximity map (Figure 2.9B), a similar five-zone pattern can be noted. The red-orange regions of the proximity map correspond to regions of closer proximity, and map to the same upper and lower medial regions of the experimental cast. On the lateral side, the same 'stripe' region of cast can been seen as a yellow-orange stripe of lateral 'close proximity' on the proximity map.
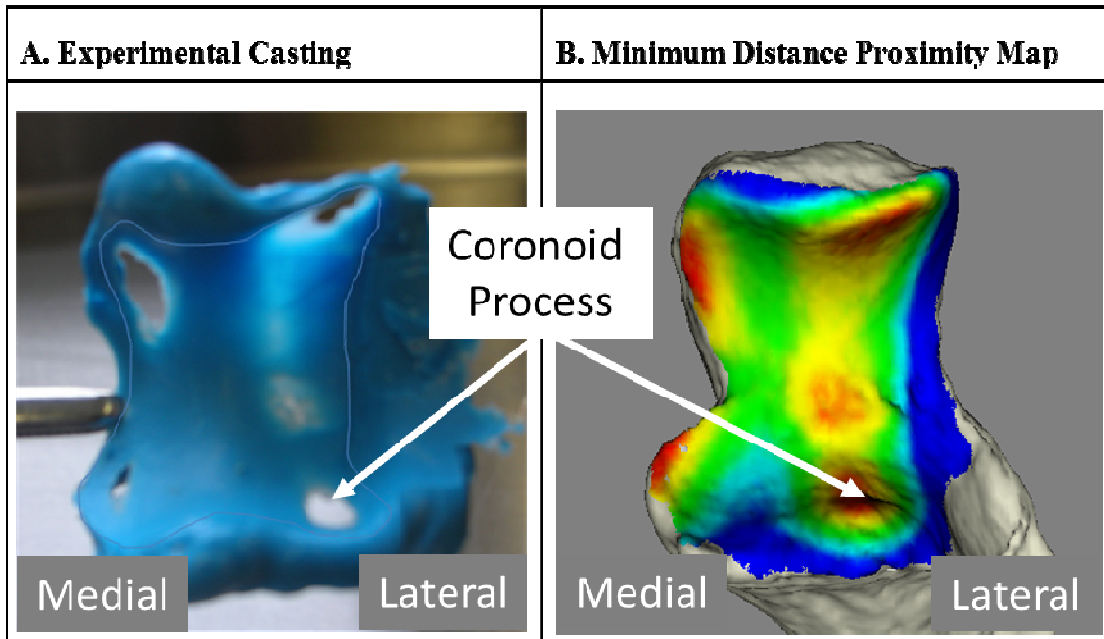
Figure 2.9: Comparison of Experimental Casting vs. Proximity Mapping
A) The contact pattern measured using the silicone casting material.
B) The corresponding ulnar proximity map is shown and compared to that of experimental casting. The coronoid process of the ulna is shown in both images as a reference.

The relationship between prescribed threshold level and resulting surface area for the humerus and ulna is shown in Figure 2.10. At 4mm of inter-bone distance, the surface area on the humerus or ulna does not exceed 800mm$^{2.}$ The total surface area of the humeral subchondral bone was 1367.61mm^2 and 1009.46mm^2 for the ulna.

The contact area for the cast was 261mm^2. Using the graph in Figure 2.10, this corresponded to a prescribed distance of 1.2-1.3mm using the inter-bone distance algorithm. These prescribed distance values were within the range of those used in the inter-bone distance algorithm (< 4mm). The intersection of the cast contact with this graph indicates the range of 'true distance'.
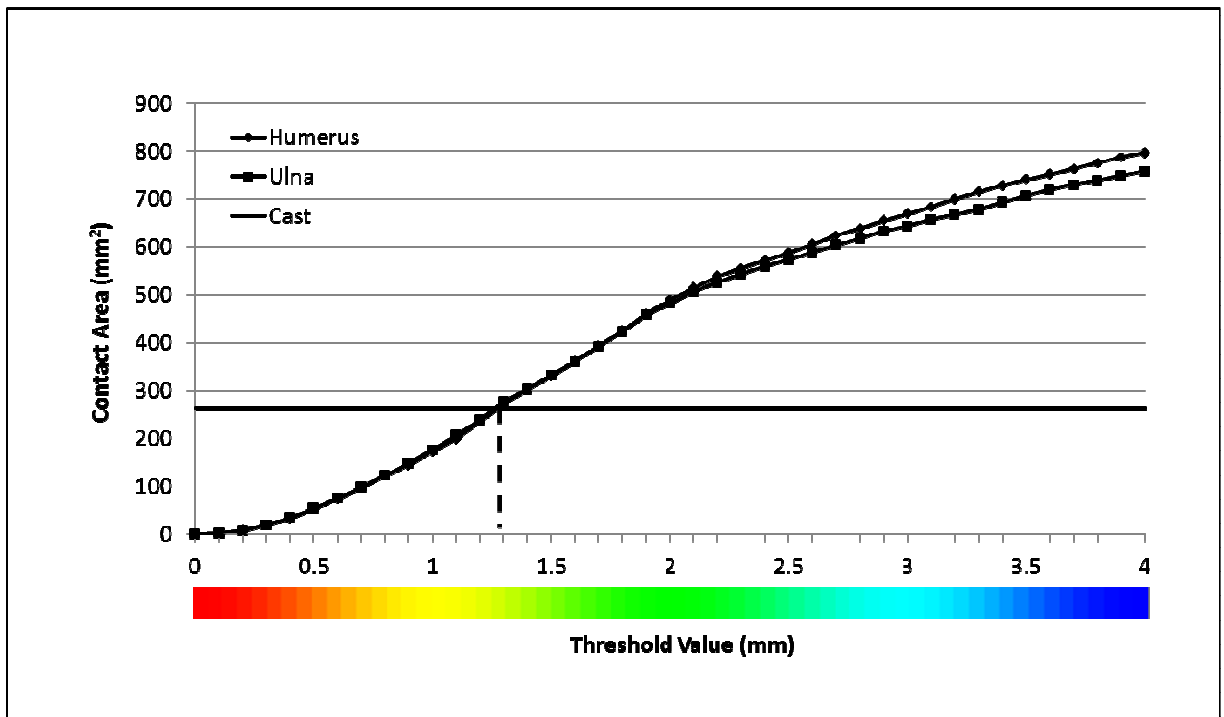
Figure 2.10: The Effect of Threshold Selection on Calculated Joint Contact Area
Forty-one (41) threshold inter-bone distance values were inserted into the inter-bone distance algorithm to obtain a measurement of the surface area of the subchondral bone that was within a prescribed distance from the opposing articular surface. Note that the humerus and the ulna have different subchondral bone surface areas; therefore the contact area measurements between the humerus and ulna differ. The contact area of the experimental cast is also shown to identify the corresponding threshold.

2.4 Discussion

The current study presents an approach for modeling joint congruency in articulations implied from actual measurements of subchondral bone distance. This technique was validated using experimental casting to verify that using the inter-bone distance algorithm; it was possible to locate regions across the articulating surface that are most likely to be in contact.

Results for this study are for a single specimen only and therefore cannot be used to describe trends in ulnohumeral joint contact. Rather, the purpose of this study was to introduce the developed inter-bone distance, validate its use, and demonstrate the utility of this technique in a single specimen to examine the general effect of load and flexion angle.

Few studies have investigated ulnohumeral contact (Eckstein *et al.*, 1994; Goel *et al.*, 1982; Goodfellow and Bullough, 1967; Goto *et al.*, 2004; Stormont *et al.*, 1985; Walker PS, 2008). The reported trends in ulnohumeral contact patterns throughout elbow flexion and under loaded conditions are similar to the results of the current investigation. (Goto *et al.*, 2004) also used proximity maps to determine typical contact patterns at the ulnohumeral joint and found that on the humerus, the contact pattern on the trochlear surface was predominantly on the medial facet of the trochlea for any possible elbow position (0°, 90°, 135°). The inter-bone distance algorithm in this current study also

indicated that there was a tendency for the proximity region to be concentrated on the medial side of the ulna and the trochlea at 60° and 90°.

The results of this current study also found that in full extension, the proximity regions occurred near the olecranon fossa of the humerus (posterior), the region on the humerus that receives the olecranon process on the ulna during full extension. However, throughout flexion, the proximity region tracks anteriorly as the elbow becomes increasingly flexed. The current study therefore demonstrated the anterior tracking of the contact area on the humerus during flexion as described by Shiba *et al.* (1988).

Stormont *et al.* (1985) indicated that experimental casting was the most reproducible direct method of measuring joint contact. Experimental casting measures the contact area between two opposing surfaces. The joint inter-bone distance provides a measure of joint space, or overall joint congruency. The two techniques examine joint interaction, but the inter-bone distance algorithm does not account for joint cartilage. Therefore, at no point in time, unless the cartilage is missing, should the two 3D *bone* reconstructions actually contact. The measured joint space is a combination of the perceived gap (where cartilage would be if CT could provide contrast between the cartilage and bone) and the surrounding joint space caused by the geometry of the condylar surfaces. Therefore, the measured outcome variables are slightly different and are hence difficult to quantitatively compare.

Initially, the joint cast and the proximity map of the validation specimen are compared qualitatively. It was interesting to note in Figure 2.9 that the experimental cast

has regions that are close to contacting, but not actually contacting. This was a consistent characteristic for the ulnohumeral joint as the thickness of the cartilage is not consistent across the greater sigmoid notch, and sometimes the distribution of the cartilage is not even homogeneous as described in Chapter 1 (Section 1.2.3) (Tillmann, 1978). As a result, there appears to be regions of the cast where the two surfaces do contact (vacant regions), but also where there appears to be 'thinning' regions of the cast. As part of the validation, it was essential to ensure that these thinning regions corresponded to the same regions on the proximity map that were in 'close' proximity.

To quantitatively compare the contact area as measured from the cast and that of the proximity map, the inter-bone distance was considered. In the absence of cartilage, a single value for 'inter-bone distance', which would correspond to the combined cartilage thickness for this specimen, would not be appropriate given the in-homogeneities present in the cartilage thickness. Rather, joint congruency was examined and used to measure the overall distribution of the joint space.

The surface area obtained from the experimental cast was used to determine an approximate value for inter-bone distance as shown in Figure 2.10. The inter-bone distance algorithm provided a range of contact area values based on varying inter-bone distances. Figure 2.10 shows that these two sets of curves intersect at approximately 1.2-1.3mm. As part of this validation, it was important to ensure that this 1.2-1.3mm distance was less than 4mm, which was the inter-bone distance threshold, used in all of the proximity maps. This value may be slightly lower than the expected thickness of

cartilage, as the articular surfaces for the validation protocol may have become slightly dehydrated as the joint capsule was dissected, despite copious hydration of the exposed surface during testing. Additionally, the viscoelastic and time-dependent response of cartilage to the applied load was not considered in this study. To ensure that the silicone cast had sufficiently hardened, the load was applied for approximately 10 minutes. During this time, the cartilage surfaces may have deformed. Therefore any deformation of that occurred would not have been accounted for as the reconstructed models were obtained directly after injecting the casting material.

Figure 2.10 shows the relationship between threshold and calculated contact area. As the threshold increases, so too does the number of recruited points. Since total surface area of the humerus and ulna are not the same, therefore the curve of the humerus and ulna diverge as the number of points on the ulna (smaller surface) saturate and further points on the humerus are recruited.

It is important to note that the contact patterns presented in this study provide an estimate of the articular interactions. The proximity method has an inherent limitation in that it does not consider cartilage thickness, location and deformation. A single inter-bone distance value was chosen to be able to obtain a measure of the surface area within a given level or proximity in various loading and elbow flexion positions. While this provides insight into the relative distribution of joint congruency undergoing loaded elbow flexion, it does not enable an absolute measure of contact area to be calculated. DeFrate *et al.* (2004) suggested that examining joint proximity in the absence of cartilage

may actually overestimate the calculated contact area in the knee. Therefore, further refinement of this algorithm is needed to incorporate the cartilage thickness and to determine if the same overestimation of contact area occurs at the elbow.

Proximity mapping is a well-established technique to examine joint surface interactions (Chapter 1 Section 1.4.2.1). Nevertheless, previous studies employing this technique to examine joint contact area have been reluctant to term the measured surface area 'contact' (Anderst and Tashman, 2003; Goto *et al.*, 2004; Marai *et al.*, 2004). Anderst *et al.* refer to these contact regions as 'size of subchondral surface areas within very close contact' whereas Goto *et al.* refers to the same areas as regions of 'inferred contact region' or Marai *et al.* 'estimated joint contact area'. This is partially due to the fact that cartilage is not accounted for in the analysis. Additionally, none of these methodologies have been validated. The current study is the first proximity mapping technique, to our knowledge that has been validated using a casting technique. Contact area was defined in this study as a proximity region with corresponding levels of proximity. We developed an inter-bone distance algorithm to examine overall joint congruency to be used as a surrogate for joint contact. Therefore, joint contact can be defined in this study under the stated assumptions and within the given limitations of the technique. With further refinement of the algorithm and consideration of the cartilage thickness, this technique can be used to reliably, and accurately measure joint contact area.

Used in an *in vitro* biomechanical laboratory, this image-based algorithm can examine the effect of various ligamentous and osseous injuries on the resulting joint congruency. The clinical importance of any contact area algorithm is the overall magnitude and distribution, and most importantly the change in these parameters in the context of an injury or mal-alignment, and as it relates to degenerative cartilage diseases. In its current form, this technique does not require direct access to the joint and therefore preserves the ligamentous and capsular stabilizers. Cadaveric specimens can be loaded into the repeatable elbow positioning device while intact and subsequently after a simulated injury and reconstructive techniques have been performed. However, in its current form, the biomechanical analysis is limited to statically loaded scenarios. The objective of this chapter was to develop the inter-bone distance algorithm and validate its use. Further refinement of this algorithm is however required to investigate the effect of inertia as well as dynamic stabilizers on resulting joint congruency.

The approach presented in this study will eventually allow clinicians and researchers to gain insight into how joint stability and gross bony position affect these articulations. Ultimately, this will lead to an increased understanding to the cause of various cartilage degenerative diseases that result following most orthopaedic trauma.

2.5 References

Anderst, W.J. and Tashman, S. (2003) A method to estimate *in vivo* dynamic articular surface interaction. *J Biomech.* 36[9], 1291-1299.

Ateshian, G.A., Kwak, S.D., Soslowsky, L.J., and Mow, V.C. (1994) A stereophotogrammetric method for determining in situ contact areas in diarthrodial joints, and a comparison with other methods. *J Biomech.* 27[1], 111-124.

Besier, T.F., Draper, C.E., Gold, G.E., Beaupre, G.S., and Delp, S.L. (2005) Patellofemoral joint contact area increases with knee flexion and weight-bearing. *J Orthop.Res.* 23[2], 345-350.

Besl PJ and McKay ND . (1992) A Method for Registration of 3-D Shapes. *IEEE Transactions on Pattern Analysis and Machine Intelligence* 14, 239-256.

Bey, M.J., Kline, S.K., Zauel, R., Lock, T.R., and Kolowich, P.A. (2008) Measuring dynamic *in vivo* glenohumeral joint kinematics: technique and preliminary results. *J Biomech.* 41[3], 711-714.

Black, J.D., Matejczyk, M.B., and Greenwald, A.S. (1981) Reversible cartilage staining technique for defining articular weight-bearing surfaces. *Clin.Orthop.Relat Res.* [159], 265-267.

Boyer, P.J., Massimini, D.F., Gill, T.J., Papannagari, R., Stewart, S.L., Warner, J.P., and Li, G. (2008) *In vivo* articular cartilage contact at the glenohumeral joint: preliminary report. *J.Orthop.Sci.* 13[4], 359-365.

Brechter, J.H. and Powers, C.M. (2002) Patellofemoral joint stress during stair ascent and descent in persons with and without patellofemoral pain. *Gait.Posture.* 16[2], 115-123.

Cohen, Z.A., McCarthy, D.M., Kwak, S.D., Legrand, P., Fogarasi, F., Ciaccio, E.J., and Ateshian, G.A. (1999) Knee cartilage topography, thickness, and contact areas from MRI: *in vitro* calibration and *in vivo* measurements. *Osteoarthritis.Cartilage.* 7[1], 95-109.

DeFrate, L.E., Sun, H., Gill, T.J., Rubash, H.E., and Li, G. (2004) *In vivo* tibiofemoral contact analysis using 3D MRI-based knee models. *J.Biomech.* 37[10], 1499-1504.

Eckstein, F., Lohe, F., Hillebrand, S., Bergmann, M., Schulte, E., Milz, S., and Putz, R. (1995) Morphomechanics of the humero-ulnar joint: I. Joint space width and contact areas as a function of load and flexion angle. *Anat.Rec.* 243[3], 318-326.

Eckstein, F., Lohe, F., Muller-Gerbl, M., Steinlechner, M., and Putz, R. (1994) Stress distribution in the trochlear notch. A model of bicentric load transmission through joints. *J.Bone Joint Surg Br.* 76[4], 647-653.

Eisenhart-Rothe, R., Siebert, M., Bringmann, C., Vogl, T., Englmeier, K.H., and Graichen, H. (2004) A new *in vivo* technique for determination of 3D kinematics and contact areas of the patello-femoral and tibio-femoral joint. *J Biomech.* 37[6], 927-934.

Goel, V.K., Singh, D., and Bijlani, V. (1982) Contact areas in human elbow joints. *J.Biomech.Eng* 104[3], 169-175.

Gold, G.E., Besier, T.F., Draper, C.E., Asakawa, D.S., Delp, S.L., and Beaupre, G.S. (2004) Weight-bearing MRI of patellofemoral joint cartilage contact area. *J.Magn Reson.Imaging* 20[3], 526-530.

Goodfellow, J.W. and Bullough, P.G. (1967) The pattern of aging of the articular cartilage of the elbow joint. *J Bone Joint Surg Am.* 49B, 175.

Goto, A., Moritomo, H., Murase, T., Oka, K., Sugamoto, K., Arimura, T., Nakajima, Y., Yamazaki, T., Sato, Y., Tamura, S., Yoshikawa, H., and Ochi, T. (2004) *In vivo* elbow biomechanical analysis during flexion: three-dimensional motion analysis using magnetic resonance imaging. *J Shoulder Elbow Surg.* 13[4], 441-447.

Heino, B.J. and Powers, C.M. (2002) Patellofemoral stress during walking in persons with and without patellofemoral pain. *Med.Sci.Sports Exerc.* 34[10], 1582-1593.

Hinterwimmer, S., Gotthardt, M., Eisenhart-Rothe, R., Sauerland, S., Siebert, M., Vogl, T., Eckstein, F., and Graichen, H. (2005) *In vivo* contact areas of the knee in patients with patellar subluxation. *J.Biomech.* 38[10], 2095-2101.

Liew, V.S., Cooper, I.C., Ferreira, L.M., Johnson, J.A., and King, G.J. (2003) The effect of metallic radial head arthroplasty on radiocapitellar joint contact area. *Clin.Biomech.(Bristol., Avon.)* 18[2], 115-118.

Losch, A., Eckstein, F., Haubner, M., and Englmeier, K.H. (1997) A non-invasive technique for 3-dimensional assessment of articular cartilage thickness based on MRI. Part 1: Development of a computational method. *Magn Reson.Imaging* 15[7], 795-804.

Marai, G.E., Laidlaw, D.H., Demiralp, C., Andrews, S., Grimm, C.M., and Crisco, J.J. (2004) Estimating joint contact areas and ligament lengths from bone kinematics and surfaces. *IEEE Trans.Biomed.Eng* 51[5], 790-799.

Montreal Neurological Institute and Hospital. (2010) MINC. *McConnell Brain Imaging Centre*.

Salsich, G.B., Ward, S.R., Terk, M.R., and Powers, C.M. (2003) *In vivo* assessment of patellofemoral joint contact area in individuals who are pain free. *Clin.Orthop.Relat Res.* [417], 277-284.

Scherrer PK, Hillberry BM, and Van Sickle DC . (1979) Determining the *in vivo* areas of contact in the canine shoulder. *J.Biomech.Eng* 101, 271-278.

Schroeder W, Martin K, and Lorensen B . (1998) The Visualization Toolkit. Upper Saddle River, NJ, Prentice Hall.

Shiba, R., Sorbie, C., Siu, D. W., Bryant, J.T., Cooke, T. D., Wevers, H.W. (1988) Geometry of the Humeroulnar Joint. *J. Orthop. Res.* 6[6], 897-906.

Soslowsky, L.J., Flatow, E.L., Bigliani, L.U., Pawluk, R.J., Ateshian, G.A., and Mow, V.C. (1992) Quantitation of in situ contact areas at the glenohumeral joint: a biomechanical study. *J.Orthop.Res.* 10[4], 524-534.

Stormont, T.J., An, K.N., Morrey, B.F., and Chao, E.Y. (1985) Elbow joint contact study: comparison of techniques. *J.Biomech.* 18[5], 329-336.

Tillmann, B. (1978) A contribution to the functional morphology of articular surfaces. *Norm.Pathol.Anat.(Stuttg)* 34, 1-50.

Walker PS (2008) *Human Joints and Their Artificial Replacements.*

Wan, L., de Asla, R.J., Rubash, H.E., and Li, G. (2006) Determination of *in vivo* articular cartilage contact areas of human talocrural joint under weightbearing conditions. *Osteoarthritis.Cartilage.* 14[12], 1294-1301.

Ward, S.I., Teefey, S.A., Paletta, G.A., Jr., Middleton, W.D., Hildebolt, C.F., Rubin, D.A., and Yamaguchi, K. (2003) Sonography of the medial collateral ligament of the elbow: a study of cadavers and healthy adult male volunteers. *AJR Am.J Roentgenol.* 180[2], 389-394.

Willis SR (2006) Contact area measurements at the native and implant reconstructed radiocapitellar joint of the elbow. MESc University of Western Ontario.

Wretenberg, P., Ramsey, D.K., and Nemeth, G. (2002) Tibiofemoral contact points relative to flexion angle measured with MRI. *Clin.Biomech.(Bristol., Avon.)* 17[6], 477-485.

Chapter 3 – Visualization of 3D Elbow Kinematics Using Reconstructed Bony Surfaces

OVERVIEW

The objective of this chapter was to develop a technique to render reconstructed bone models undergoing simulated elbow flexion. Using registration and the inter-bone distance algorithm (Chapter 2), it was possible to quantify the congruency of the elbow undergoing simulated active flexion. The clinical focus of this chapter was radial head excision and arthroplasty as well as the influence of dynamic stabilizers of the elbow. Valgus motion of the elbow was achieved in five cadaveric specimens using a previously developed elbow motion simulator. Visualization of the motion of the ulna with respect to humerus at the ulnohumeral joint was obtained using a contact-based registration technique. Employing fiducial markers, the rendered humerus and ulna were positioned according to the simulated motion.[2]

3.1 Introduction

Various methods have been employed to accurately measure human joint kinematics both *in vivo* and *in vitro* (Beingessner *et al.*, 2004; Ferreira *et al.*, 2010; Ferreira *et al.*, 2011; Fraser *et al.*, 2008; Johnson *et al.*, 2005; King *et al.*, 1999; Pichora *et al.*, 2007; Pollock *et al.*, 2009). Commonly used descriptors of joint kinematics include varus-valgus joint laxity, changes in internal and external rotation, or changes in varus-valgus angulation of one bone relative to another. Typically, a graphical representation of the motion pathway of the bones within the joint are presented describing the effect of various clinical variables on joint stability. While these descriptors have shown to be useful in developing new therapeutic techniques and devices to restore overall stability following injury, they do not provide specific information regarding the joint itself.

To increase our understanding of joint mechanics, simultaneous visualization of kinematics with the joint morphology can be useful. Several approaches have been developed to achieve this goal and involve obtaining volumetric or planar images of joints using MRI (Fellows *et al.*, 2005) (or cine phase contrast MRI) (Barrance *et al.*, 2005; Muhle *et al.*, 1999; Sheehan *et al.*, 1998; Shellock *et al.*, 1993), CT imaging (Muhle *et al.*, 1999) or stereometric methods (Anderst *et al.*, 2009; Bey *et al.*, 2006). While these studies can visualize the relative position and orientation of the bones articulating in joints, they are limited in the ranges and types of motions that can be achieved using these forms of medical imaging.

Other techniques developed to visualize 3D joint kinematics link the anatomical geometry obtained from CT or MRI to the information obtained using a motion analysis

system such as spatial linkage devices, (Sholukha *et al.*, 2006; Van Sint *et al.*, 2002; Van Sint *et al.*, 2006) electromagnetic (Jackson *et al.*, 1994) and optical systems (Sugano *et al.*, 2001). Anatomical landmarks, surface digitizations or external markers are digitized and used to register the coordinate system associated with the tracked motion to the coordinate system of the 3D reconstruction. The majority of these approaches however require multiple digitization procedures which are tedious in practice, and ultimately limit investigations to statically loaded joint positions (Fischer *et al.*, 2001; Sugano *et al.*, 2001).

The objective of this study was to develop a registration protocol that can be used to link kinematic data of joints undergoing continuous elbow flexion, with the 3D subject-specific anatomy obtained using CT. Using the techniques described herein, continuous motion of the joint can be tracked and analyzed post hoc, thereby preserving the intact normal joint kinematics. External fiducial markers are registered to the tracked simulated motion using a contact-based registration technique. The applications of this technique will be numerous and include functional anatomy, techniques in computer-assisted surgery and as a biomechanical tool used to investigate the role of joint mal-alignment and joint stability following injury. The specific aim of this current study was to evaluate the feasibility and utility of this approach, by performing an *in vitro* study using radial head resection and arthroplasty as a provocative and restorative model respectively.

3.2 Methods

An overview of the experimental protocol is shown in Figure 3.1.

3.2.1 VOLUMETRIC IMAGE ACQUISITION

Five fresh-frozen upper extremities (70 ±10 yrs, 3 Right, 2 Left, 4 Females, 1 Male) sectioned at the mid-humerus were employed. A pre-testing 3D image of each specimen was obtained prior to testing using a 64-slice CT scanner (GE Lightspeed VCT 64 Slice CT Scanner, New Berlin, WI) (Figure 3.1, 1). Approximately 600 slices were acquired for each specimen with a field of view set at 20-22x20-22cm and a 512x512 reconstruction matrix (146mAs, 120 kVp). The size of the voxels was approximately 0.4x0.4x0.625mm. A 3D model of the joint was obtained using the marching cubes algorithm available within the Visualization Toolkit (VTK, Kitware, Clifton Park, NY)(Schroeder W *et al.*, 1998). A manually set threshold was chosen to visualize only the bony aspects of the cadaveric specimen as described in Chapter 2 (Section 2.2.3). This current study investigated bony alignment and position of the ulnohumeral joint comprised of the distal humerus and proximal ulna of the forearm. Therefore, the ulna and humerus were manually segmented and saved as separate volumetric files.

3.2.2 SPECIMEN PREPARATION

Prior to testing, the specimens were thawed at room temperature for 20 hours. The distal end of the humeral shaft was completely denuded of all soft tissues to allow for fixation into the upper extremity testing system (Figure 3.1, 2). The tendons of the triceps (TRI), biceps (BIC), brachialis (BRA) and brachioradialis (BRD) were exposed and

sutures were secured to each tendon. A magnetic receiver mount was rigidly attached to the distal ulna and humerus. A receiver mount was also attached to the proximal humerus. Receivers were securely fastened to the mounts for accurate spatial tracking.
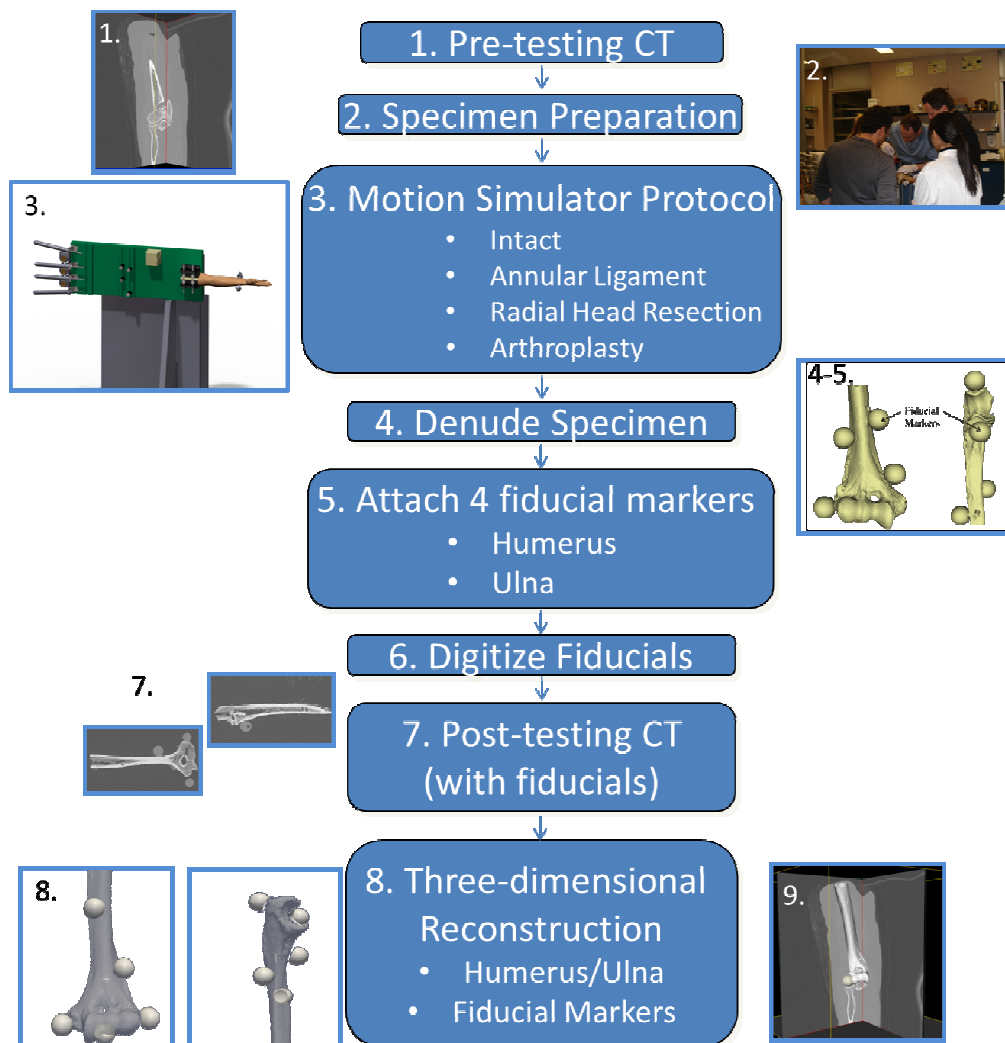
Figure 3.1: Overview of Experimental Protocol

1. A pre-testing CT is acquired

2. The tendons of relevant muscles were isolated and sutured to prepare for elbow flexion simulation.

3. Elbow flexion was simulated using a previously developed motion simulator. Elbow flexion was repeated in the valgus gravity dependent position for the each clinical scenario.

4. Subsequent to testing, the specimen was denuded and disarticulated.

5. Fiducial markers were attached to the humerus and ulna.

6. The fiducials were digitized using a tracked stylus.

7. A post-testing CT was acquired.

8. Three-dimensional reconstructions of each fiducial marker as well as the humerus and ulna were created.

A Steinmann pin was drilled through the long finger metacarpal into the radius to prevent wrist motion. A 3.5 mm drill tap was placed through the radius and ulna with the forearm maintained in neutral rotation to prevent forearm rotation. All skin incisions were closed used #2 Vicryl skin suture and the specimen was kept hydrated throughout testing using normal saline.

3.2.3   TESTING AND KINEMATIC MEASUREMENTS

Elbow extension was simulated using a previously developed testing apparatus that employs active muscle loading to achieve elbow and forearm motion as shown in the valgus gravity dependent position in Figure 3.2 (Ferreira *et al.*, 2010). Muscle loading protocols are used which attempt to maintain constant velocity (Ferreira *et al.*, 2010). Motion of the humerus and ulna and relative to the transmitter was recorded using an electromagnetic tracking device (Flock of Birds, Ascension Technology, Burlington VT). The device was sensitive enough to read positional and rotational changes of 0.2mm and 0.1° (Milne *et al.*, 1996). The mean positional error for this device is 0.5mm with a maximum of 1.0mm. The mean rotational error is 1.6% of the rotational increment (Milne *et al.*, 1996). Ferromagnetic materials were removed from the testing apparatus prior to motion simulation to prevent interference with the magnetic signal. A pointed stylus attached to a receiver was employed for digitization of the anatomical landmarks required to generate the elbow coordinate system. The humerus was secured in the upper extremity testing apparatus (Figure 3.1, 3).
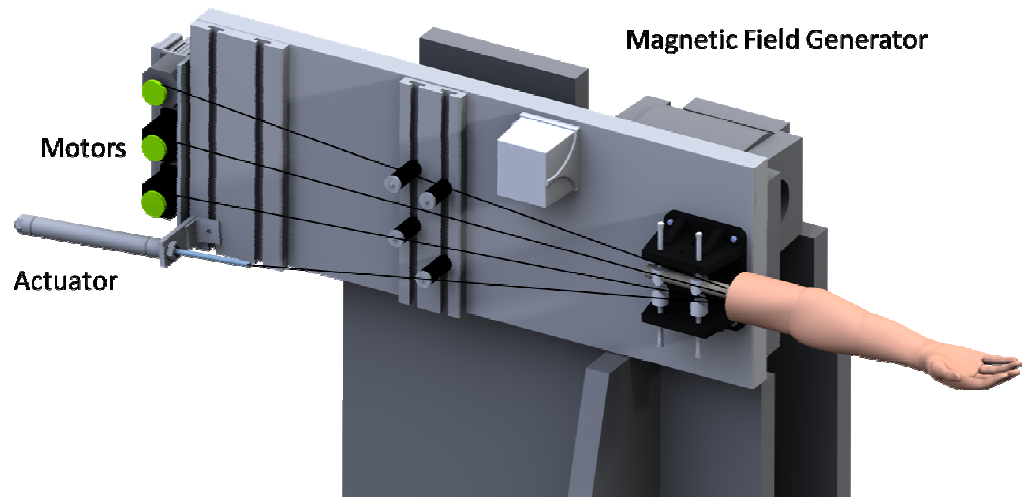
Figure 3.2: Elbow simulator
The cadaveric specimen is surgically prepared and then mounted to the simulator using a clamp in the valgus gravity dependent orientation. The tendons of the relevant muscles are attached using cables to the motors and actuators.

The sutured tendon of the BRD was attached to a computer-controlled pneumatic actuator simulating the line of action of the muscle *in vivo*. The tendons of the BRA, TRI and BIC were attached to three separate servo motors.

3.2.4   EXPERIMENTAL PROTOCOL

Active elbow extension was simulated with the specimen in the valgus gravity dependent position, initially in the *intact* condition. An anterior approach with sectioning of the anterior portion of the annular ligament and anterior capsule was used for radial head excision and arthroplasty. To evaluate the effect, if any, of the surgical approach, the annular ligament and anterior capsule were surgically repaired using sutures and the simulation protocol for flexion and extension was repeated (*annular ligament*). The sutures were removed from the annular ligament and the radial head was resected at the head-neck junction using a reciprocating bone saw. The annular ligament and capsule were then repaired and active elbow flexion and extension was repeated (*radial head resected*).

The resected radial head was templated and an appropriate sized metallic radial head implant was inserted into the elbow (Evolve®, Wright Medical Technology, USA). The annular ligament and anterior capsule was again repaired and the simulation protocol was repeated (*radial head replaced*).

At the end of the simulation protocol, the elbow and wrist were disarticulated and denuded of all soft tissue (Figure 3.1, 4). Surface digitizations of relevant anatomical landmarks on the humerus and ulna were obtained.

3.2.5   FIDUCIAL PLACEMENT/REGISTRATION

A contact-based registration technique employing the use of external fiducial markers was used to register the pre-testing computed tomography (CT) data to the kinematic data collected during experimentation. Custom software was written within the visualization toolkit to perform the paired-point registration on the reconstructed bony models (Schroeder W *et al.*, 1998). On the denuded bones, four 19 mm delrin spheres were securely attached to both the humerus and the ulna as shown in (Figure 3.1, 5). Two spheres were positioned medial/lateral distally, and two medial/lateral proximally (Figure 3.3). The location of the fiducial spheres did not exceed 10 cm from the joint articulation of interest. The location of the centre of each fiducial was obtained by manually digitizing the surface using a 3 pointed tracked pointed stylus and the electromagnetic tracking system ($^{\mathrm{Re}ceiver}_{Fiducials}P$) (Figure 3.1, 6). These digitized points were sphere-fitted using a least squares sphere-fitting algorithm. On average, 8000 points were digitized on the surface of each fiducial marker and used in the sphere-fit algorithm. A post-testing CT scan was performed (with the same scanning parameters) to obtain the coordinates of each fiducial marker with respect to the 3D reconstructed model of the humerus and ulna ($^{CT}_{Fiducials}P$) (Figure 3.1, 7). A 3D model of the humerus and ulna was created (Section 1.2.1). Additionally, a separate manually selected threshold was selected to obtain a 3D model of each fiducial. Each 3D fiducial marker was then segmented and sphere-fitted to obtain the location of the centre of each fiducial (Figure 3.1, 8).

The initial intact pre-testing CT was registered to the post-testing CT (containing the fiducial markers) using the iterative closest point (ICP) surface based registration algorithm and three coarse alignment points (Besl PJ and McKay ND, 1992).
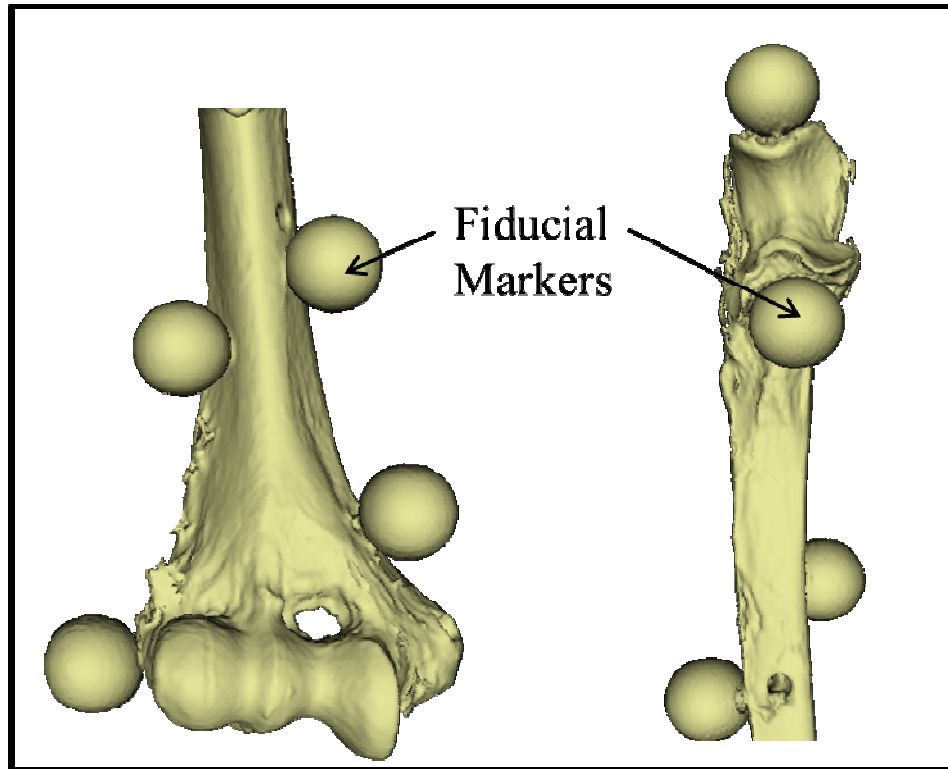
Figure 3.3: Fiducial Marker Configuration
Four 19mm delrin spheres were attached to the denuded humerus and ulna for registration.

3.2.6   KINEMATIC ANALYSES

The centres of the digitized anatomical landmarks on the humerus and ulna were used to generate an anatomically relevant coordinate system. On the humerus, a trace of the capitellum, the trochlear groove and the perimeter of the humeral shaft was obtained using the tracked pointed stylus. The capitellum digitization was sphere-fitted using the least-squares algorithm and the centre of the capitellum was found. The trochlear groove and humeral shaft trace were both circle-fitted using the least-squares circle fitting algorithm and the centre of the each trace was obtained. On the ulna, a trace of greater sigmoid notch ridge was obtained and circle fitted, a single point on the distal ulnar styloid was digitized and a medial point, not on the anatomy, near the proximal end of the ulna was digitized. Orthogonal planes to the flexion/extension axis for the humerus and ulna were oriented proximally and anteriorly. The centre of the capitellum and trochlea defined the flexion/extension axis of the humerus. Kinematic data obtained from the tracking system were then transformed to the anatomic coordinate systems to express the motion of the ulna with respect to the humerus throughout elbow flexion (Johnson *et al.*, 2000).

A transformation matrix ($^{Lab}_{Re\,cever}T$) of kinematic data recorded during simulated motion was obtained at discrete instances throughout flexion (0-120°) describing the position and orientation of the ulna and humerus with respect to the global lab coordinate system using custom software. Such matrices describe discrete positional data of the continuous elbow motion.

For the registration method used in this study, this transformation matrix was used to transform the relative position of each fiducial on both the humerus and ulna according to each frame of motion using matrix operations. This operation is given by (for each of the four fiducials on the humerus and ulna separately),

$$_{\text{Re}ciever}^{Lab}T \bullet {}_{Fiducials}^{\text{Re}ciever}P = {}_{Fiducial}^{Lab}P$$

($@15°,30°,45°,60°,75°,90°,105°,120°$)

This operation was repeated for all 4 fiducial centres on both bones, for every 15 degrees, thereby registering the fiducials (collected post-experimentation) to the global CS used during experimentation.

Using Horn's closed form solution paired-point registration, a rigid body transformation of the homologous fiducial markers located on the 3D surface models and the transformed fiducial markers digitized using the tracking system was obtained[9]. This registration was repeated at 15°, 30°, 45°, 60°, 75°, 90°, 105° and 120°.

$$_{Fiducials}^{Lab}P \leftarrow REGISTRATION \rightarrow {}_{Fiducials}^{CT}P = {}_{CT}^{Lab}T$$

This transformation was then applied to both the origin of the humerus and ulna independently to transform the bony models into their rendered position according to the tracked simulated motion. The positional ulnar-ulnar differences between the radial head

intact, radial head resected and radial head replaced scenarios were then directly visualized using this approach. Figure 3.4 shows a flowchart of this registration protocol.
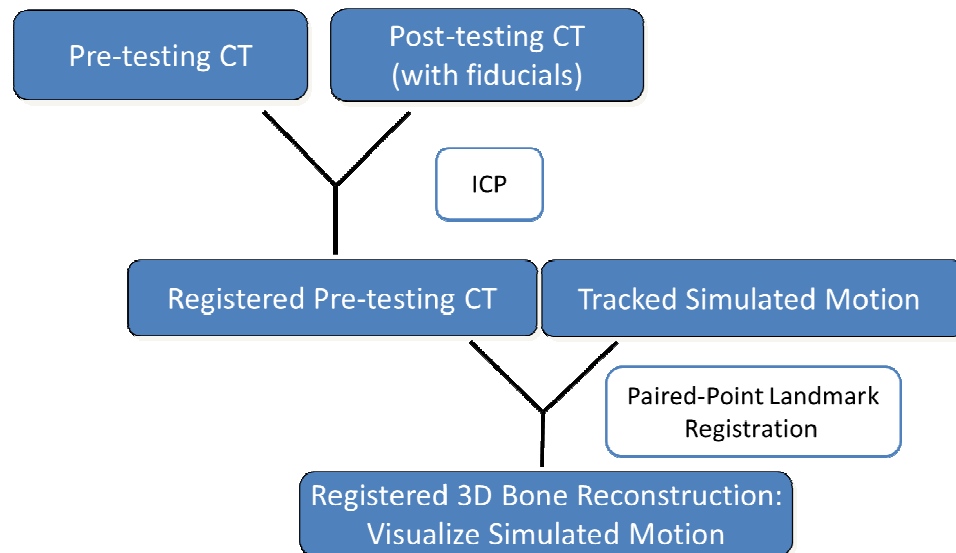
Figure 3.4: Registration Protocol for Visualization

In the first phase of the registration protocol, the iterative closest point registration algorithm was used to register the pre-testing *model to the position of the post-testing CT model (containing the fiducial markers). During the second phase, paired-point fiducial landmark registration was used to register the bony models (obtained from CT) to the location of the forearm during simulated motion. Using this approach, the position of the ulna and humerus could be rendered according to the simulated motion.*

3.2.7   KINEMATIC DESCRIPTORS

Typical kinematic descriptors report the motion of the humerus and ulna with respect to each other as an indicator of elbow stability. In this study, valgus angulation (which describes the outward or lateral angulation of the long axis of the ulna with respect to the long axis of the humerus) was investigated. Valgus angulation was obtained using Euler angle decomposition (flexion-extension, varus-valgus angulation, internal-external rotation) of the kinematic data using custom written software. Valgus angulation (expressed in degrees) was examined at $15°$ intervals throughout flexion in the intact, annular ligament, radial head resected and radial head replaced scenarios. A repeated-measures analysis of variance test with Bonferroni correction was used to detect statistical differences in the kinematic data for each radial head testing condition (intact/annular ligament control/resected/replaced) for all five specimens. Statistical significance was set at $p < 0.05$.

3.2.8   FIDUCIAL REGISTRATION ACCURACY

To assess the accuracy of this registration, the centre of the registered CT fiducials was compared to the ground truth digitized fiducial centres (after registration) and the root-mean-squared (RMS) difference (for all fiducials on each bone) was calculated. These RMS values (a separate value for each bone) corresponded to the error associated with registering the two sets of fiducial markers to one another and is termed the fiducial registration error (FRE) (Chapter 1, Section 1.4.2)(Maurer, Jr. *et al.*, 1997). During

digitization of the fiducial markers, the FRE was calculated to ensure that this value was near 0.5mm or less.

3.2.9 TARGET REGISTRATION ACCURACY

An overview of the experimental protocol is shown in Figure 3.5. The target registration accuracy of this technique was examined using a separate denuded humerus and ulna (Female, 63 years). Target registration error (TRE) is a clinically meaningful error measurement as it gives the error associated with the registration for a given point within the region of interest (Maurer, Jr. *et al.*, 1997). Fitzpatrick *et al.*, (1998) stated that the accuracy of a marker-based registration is largely independent from the object being registered. A target is typically a landmark with known location that can be measured subsequent to registration and is used to assess the overall accuracy of the registration in the region of the target. In this error experiment volumetric images of the intact specimen were acquired (Figure 3.5, 1). Subsequent to this, all soft tissues were removed (Figure 3.5, 2) and humeral and ulnar magnetic trackers were secured to each bone (Figure 3.5, 3). Four fiducials were secured to the humerus and ulna using the same configuration described previously Section 1.2.5 (Figure 3.5, 4). Additionally, a fifth fiducial marker was attached near the articulation on the ulna and humerus. The two bones were then positioned in a joint reduced configuration and seven static position recordings were collected describing the position and orientation of each tracker with respect to the global coordinate system (Figure 3.5, 5). Subsequent to this, the fiducials and targets were

digitized system ($_{Fiducials}^{Re\,ceiver}P$), ($_{Target}^{Re\,ceiver}P$) (Figure 3. 5, 6). A post-testing CT scan of the

bones with the fiducials was then acquired (Figure 3.5, 7). The bones, fiducials ($_{Fiducials}^{CT}P$)

and targets ($_{T\arg ets}^{CT}P$) were then reconstructed and segmented (Figure 3. 5, 8). Registration

was performed using the same protocol as described in Figure 3.4. Transformation

matrices describing the position and orientation of each bone were then obtained (

$_{\text{Re}ciever}^{Lab}T$) (without making a coordinate system as this was static motion and therefore

flexion angle was not necessary). The position of each fiducial (and target) within the lab

coordinate system during each frame of motion obtained using Equation 3.1. Similarly,

the position of each target with respect to the laboratory coordinate system, for each static

motion recording (representing the ground truth) was obtained using:

$$_{\text{Re}ciever}^{Lab}T \bullet {}_{T\arg et}^{\text{Re}ciever}P = {}_{T\arg et}^{Lab}P \qquad \text{Equation 3.3}$$

Paired-point registration (Equation 3.2) was then used and applied to the humerus

and ulna, as well as to the reconstructed target marker.
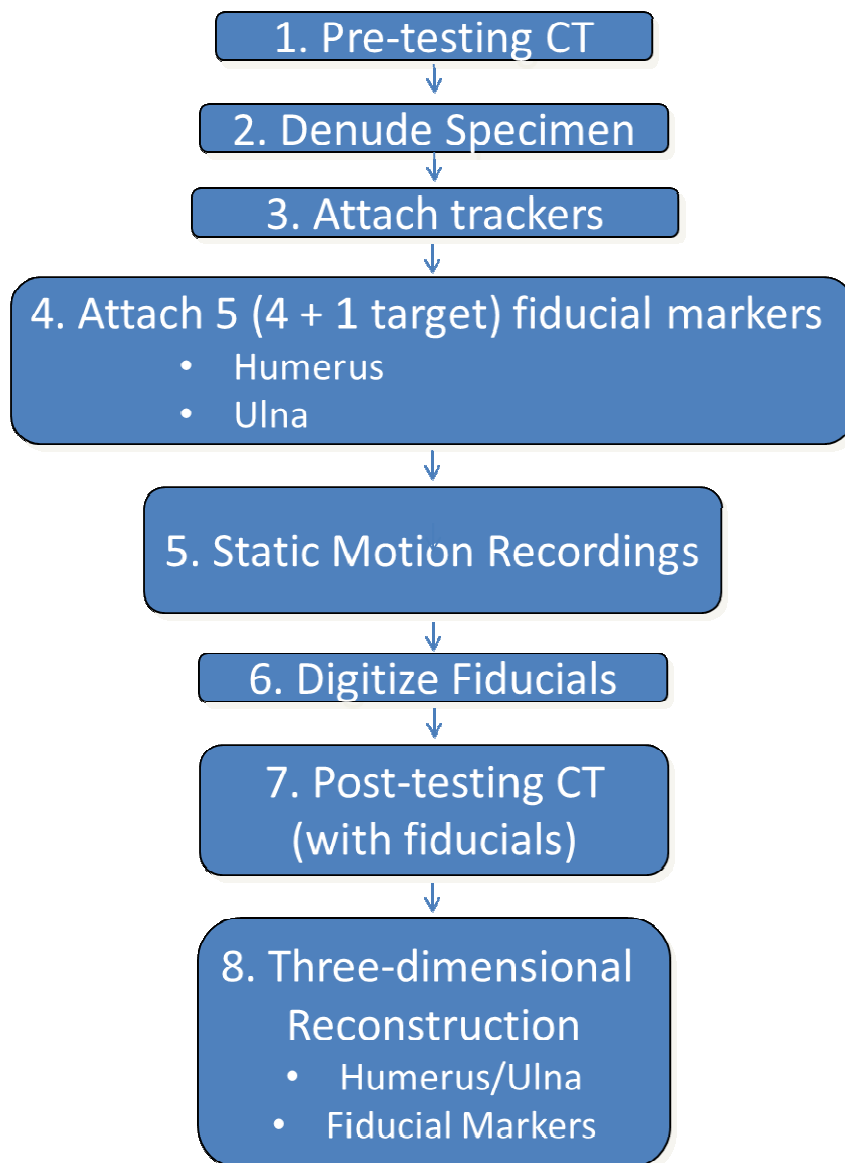
Figure 3.5: Overview of Target Registration Protocol

1. A pre-testing CT was acquired

2. Specimen was denuded and disarticulated

3. Attach magnetic trackers

4. Fiducial markers were attached to the humerus and ulna (4/bone + 1 target).

5. 7 Static motion recordings were taken

6. The fiducials were digitized using a tracked stylus.

7. A post-testing CT was acquired.

8. Three-dimensional reconstructions of each fiducial marker as well as the humerus and ulna were created.

This transformed target represents the location of the fiducial in the lab coordinate system after registration. To obtain the target registration error (TRE), the registered target location value was compared to the ground truth location of the target and the root-mean squared distance was calculated. This error was examined for 7 instances during the static motion recording. It is important to note that the fiducials in this error experiment were digitized using a calibrated indent in a piece of delrin as opposed to the-pointed stylus that is used in the experimental protocol of this study. This digitization approach was chosen to represent the best case scenario when using magnetic tracking. Digitizing with the pointed stylus was very error prone and difficult in use.

3.3   Results

The objective of this study was to develop a visualization technique that could be used in biomechanical studies to visualize bony alignment and joint stability using registration and reconstructed 3D models obtained from CT. Radial head arthroplasty was investigated in this study as a model of subtle elbow stability. Traditional kinematic motion analysis was compared to the new visualization approach. We observed close agreement between the kinematic output and the registered bony 3D models showing the joint position.

3.3.1   TRADITIONAL KINEMATIC ANALYSIS

Figure 3.6 shows the change in the average (n=5) valgus angulation of the ulna with respect to the humerus in the intact, radial head resected and radial head replaced scenarios. There was no significant difference between the intact and annular ligament

repaired scenarios elbow (p>0.05). Therefore, all results shown graphically and visually of the intact radial head scenario correspond to the native intact condition.

In the valgus gravity dependent position, valgus angulation was significantly increased following resection of the radial head, and then restored to that of the intact scenario once the radial head was *replaced* (p=0.02).This difference decreased throughout elbow flexion, but no effect of flexion was statistically significant (p>0.05). With the radial head *intact,* there was a 7.29±1.23° (max: 9.10°) valgus angulation of the ulna with respect to the humerus. Following *radial head resection*, the valgus angulation increased to 8.47±1.39° (max: 11.04°). This increase in valgus angulation was statistically significant (p=0.08). However, once the radial head was *replaced* the valgus angulation was similar to that of the native radial head (7.08±1.23°, max: 8.92°) (p>0.05).
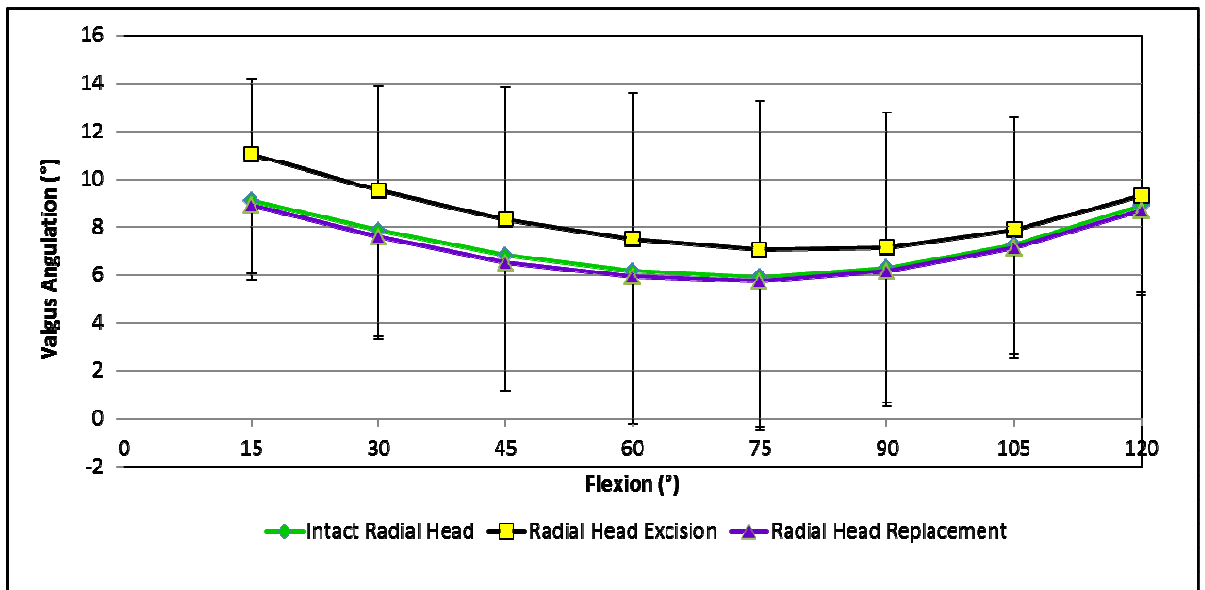
Figure 3.6: Valgus angulation for intact, radial head resected and radial head replaced elbow

Valgus angulation of the intact and radial head replaced scenario exhibit similar trends in valgus angulation throughout elbow flexion. During radial head excision, the amount of valgus angulation statistically increases compared to that of the intact radial head scenario (p=0.08) (n=5, Intact, Radial Head Replaced: Mean - SD, Radial Head Resected: Mean + SD).

.

3.3.2   THREE-DIMENSIONAL VISUALIZATION

Similar results were also obtained using the visualization approach. Figure 3.7A shows an anterior view of the elbow in the intact and radial head resected condition. Viewing the superimposed view of the *intact* and *resected* radial head scenario, it was possible to see the increase in valgus angulation of the ulna with respect to the humerus. For this particular specimen, at 15°, there was a 2.54° increase in valgus angulation following *radial head resection.* Figure 3.7B shows the *intact* and *replaced* scenarios superimposed, showing no difference a minimal amount of valgus angulation. For this particular specimen, the difference between the *intact* and *replaced* scenarios was 0.02°. This indicates that following radial head arthroplasty, the valgus angulation is restored to that of the intact radial head scenario.
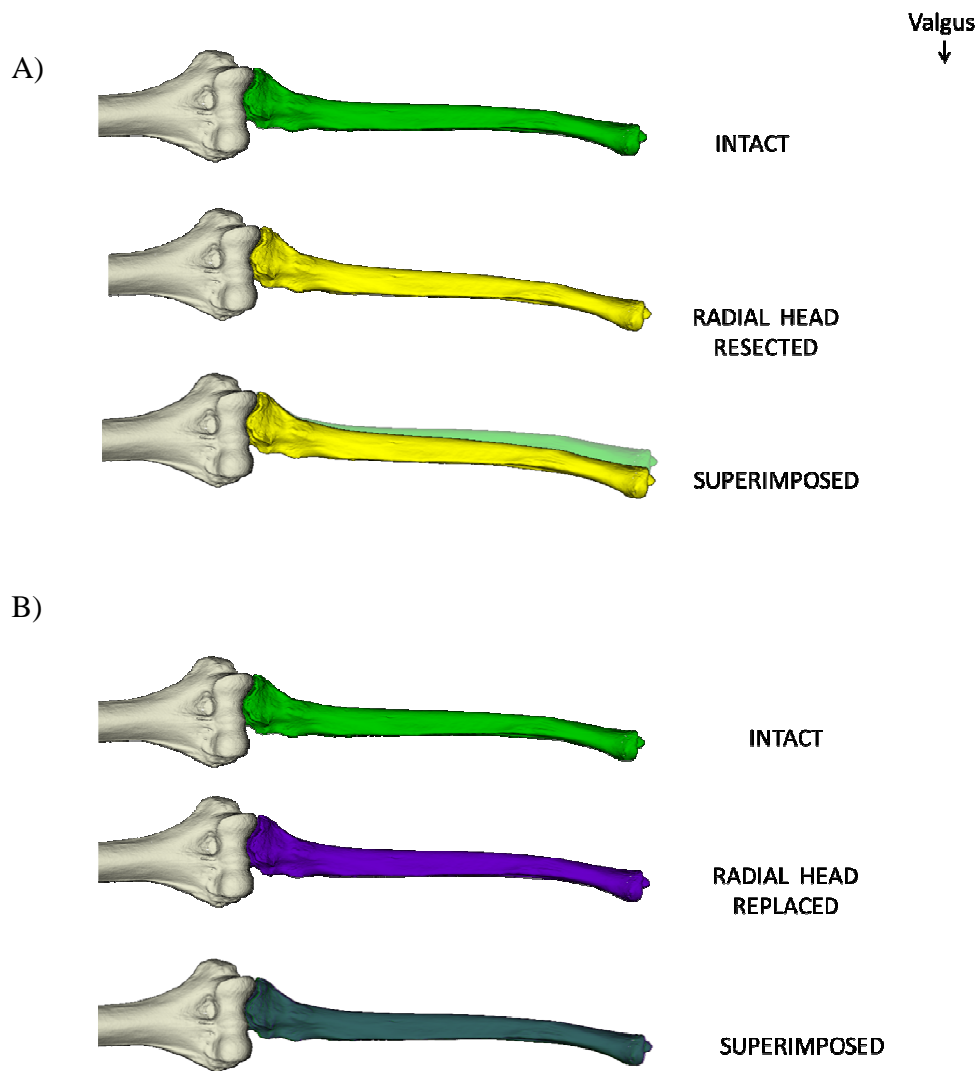
Figure 3.7: Anterior view of a Ulnohumeral Joint (15°) in the intact, radial head resected and radial head replaced elbow

A) Visualization of the bony models showed an increase in valgus angulation with radial head resection when superimposed with the intact radial head scenario.

B) Subsequent to radial head replacement, the valgus angulation of the resected bony model was restored to that of the intact scenario indicating minimal difference in valgus angulation between to the two models in the superimposed view.

A distal view of the ulna (Figure 3.8A) located near the wrist was examined throughout elbow flexion to identify the greatest change in the valgus angulation of the ulna in each radial head scenario (Figure 3.8B). The effect of valgus angulation in this view also indicated a decrease as the elbow is flexed into higher degrees of elbow flexion, which is also seen graphically. To visualize the tracking of the ulna through elbow flexion, a medial view of the ulna is shown in Figure 3.9. A uniform circle created by the greater sigmoid notch is shown as the ulna tracks around a stationary humerus throughout flexion.

A)

B)

Radial Head Intact   Radial Head Resected   Radial Head Replaced
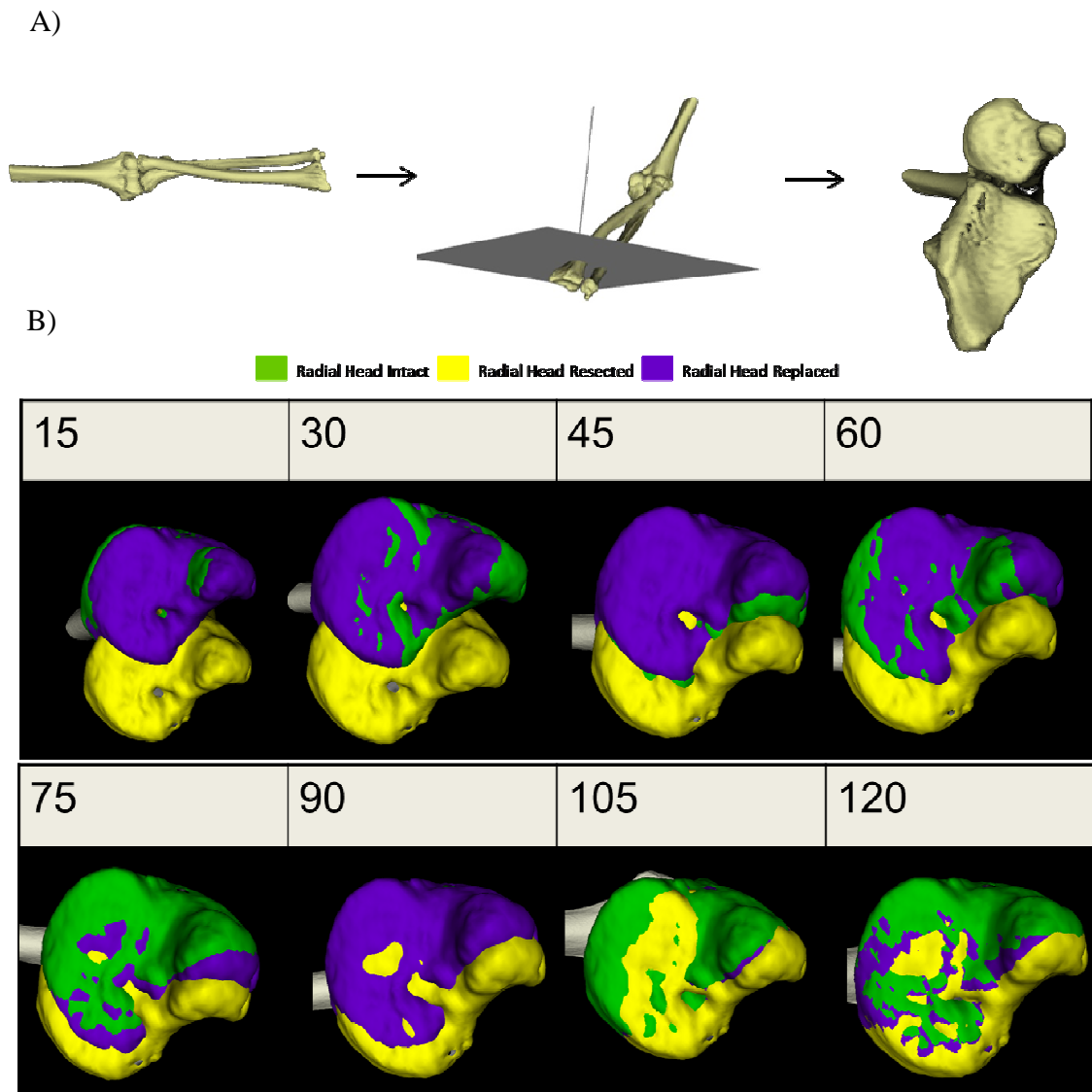
Figure 3.8: View of Distal Radioulnar Joint for the intact, radial head resected and radial head replaced elbow

A) Diagram of a representative forearm indicating location of the distal radioulnar joint
B) Distal view of the ulna near the wrist throughout elbow flexion for the radial intact, resected and replaced scenarios in the valgus gravity dependent position.
At the distal end of the ulna, increases in valgus angulation can be readily visualized. The increase in valgus angulation and subsequent decrease after radial head replacement can be visualized in the 3D model.
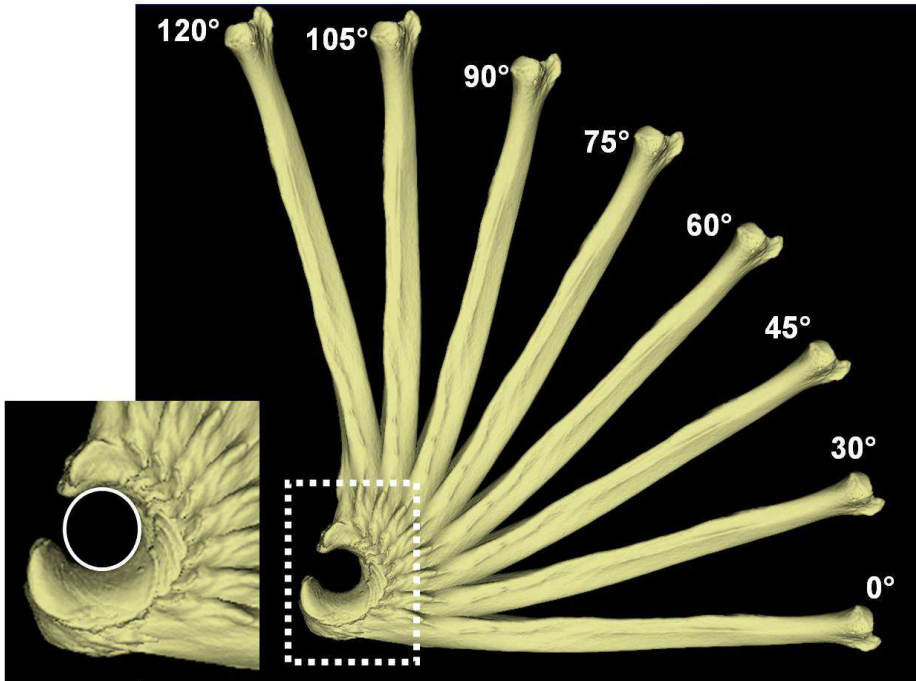
Figure 3.9: Ulnar position throughout elbow flexion.
Examining the greater sigmoid notch region isolated, a circle can be fit following the path of motion.

3.3.3   REGISTRATION ERROR

Table 3.1 contains the fiducial registration accuracies for each specimen tested. The mean fiducial registration error (FRE) value for the humerus was 0.46±0.12mm and 0.55±0.12mm for the ulna.

Similarly, sphericity values for the digitized fiducials were recorded. The mean sphericity value of the electromagnetically tracked digitized fiducials was 0.34±0.13mm. Both of these measurements (FRE and sphericity) were to ensure that the best possible digitization of each fiducial, given the inherent error associated with the tracking system, the best digitization was achieved.

The average target registration error (TRE) of the error experiment for the humerus and ulna was 0.93±0.00mm and 2.40±0.00mm respectively. The distance between the target on the humerus and ulna was calculated while the joint was in the reduced static position (ground truth) and after registration was calculated for each of the 7 samples of static motion. On average, the RMS difference between these two targets was 2.99±0.52mm indicating that the relative registration error between the two articulating surfaces was approximately 3mm.

Specimen	HUMERUS FRE (mm)	ULNA FRE (mm)
1	0.43	0.63
2	0.29	0.55
3	0.42	0.40
4	0.56	0.46
5	0.59	0.70

Table 3.1: Fiducial Registration Error
Fiducial registration error was calculated (mm) for each specimen for both the humerus and ulna.

3.4   Discussion

Joint stability and motion pathways are typically reported as graphical representations of kinematic descriptors throughout the arc of motion and between varying degrees of clinical variables. This traditional graphical approach is useful when quantitatively examining the motion pathways and kinematic descriptors of motion. The results of this study confirm the findings of other studies investigating the effect of radial head arthroplasty on elbow stability (Beingessner *et al.*, 2004). However, using this approach, the increase in valgus angulation after resection and subsequent decrease in angulation following radial arthroplasty, can be readily seen and understood visually in the 3D model of the ulna in all 6 DoF (note that the graphical representation is only considering a single degree of freedom). Unlike the traditional graphical approach used to investigate elbow stability, this visualization approach allows coupled motion of the bones to be examined. Therefore the current approach presented in this study represents a complementary technique that can be used to qualitatively examine motion pathways. Future work using this technique will be to examine the other 5 degrees of freedom graphically to compare the results of the visualization approach with that of the graphical approach and potentially gain new insight into the other differences in the position of the ulna with respect to the humerus that are a result of the radial head excision.

This is the first study that we know of which attempts to register bony anatomy with continuous tracked simulated motion. The ulnar to ulnar differences throughout elbow flexion can be examined using this registration approach. A comparison of the

visualization and the graphical approach was performed to determine the visual trends in the valgus angulation that are consistent with the graphical representation and current literature. Figure 3.9 shows the medial view of successive ulnas tracking around a stationary humerus. The circular profile of the greater sigmoid notch representative of the path created by successive ulna positions throughout elbow flexion indicates that the registration is tracking through elbow flexion successfully. If the registration was not tracking with flexion, this path would not be circular.

Fiducial based registration has been found to be an accurate alternative to anatomically based paired point registration in other studies (Sadowsky *et al.*, 2002; Sugano *et al.*, 2001). Sadowsky *et al.*(2002) noted that solely anatomically based paired point registration is prone to error due to the fact that the registration accuracy relies on the correct identification of key anatomical landmarks in both modalities undergoing registration. The current study employed fiducial markers for use in the paired-point registration algorithm. Registration was performed subsequent to testing thereby preserving the native kinematics of the simulated elbow flexion. Fiducial registration error was measured as an indicator of the type of overall registration accuracy expected to find. However, consistent with the findings of Fitzpatrick *et al.* the fiducial registration error did not prove to be an indicative parametric for the amount of overall registration accuracy measured (Fitzpatrick *et al.*, 1998; Fitzpatrick and West, 2001). The registration error (corresponding to the rigid body registration of the ulna and humerus separately) was found to be less than 2.5mm. Despite this error, <3° changes in the valgus angulation of the ulna with respect to the humerus can be visualized. Subsequent to registration, a 3D

view of the ulna with respect to the humerus was visualized. These 3D renderings indicated a small amount of overlap present between the articulating surfaces. This overlap is indicative of the registration error. Therefore, in the error experiment, the corresponding distances between the ulnar and humeral targets were measured. On average, the relative registration error was approximately 3mm. The elbow is a relatively congruous joint and therefore does not have a large amount of inter-joint space. Therefore, a relative registration error of 3mm results in an overlapping of the humeral and ulnar surfaces. Therefore, although this registration technique allowed gross changes in the amount of valgus angulation to be visualized, extending this approach to examining joint alignment of the ulna with respect to the humerus requires greater registration accuracy.

This study has some limitations including the registration error. Future work on this technique will improve the accuracy using optical tracking and refined fiducial landmark techniques. Digitizing the fiducial markers proved to be very labor intensive and error prone. Sphericity values in this study were less than 0.5mm which is excellent given the electromagnetic tracking system that was employed in this study. However, using a more accurate optical tracking system, the accuracy in identifying of the centre of each fiducial will be increased. With an increase in the overall accuracy of the registration algorithm, it will then be possible to integrate the inter-bone distance algorithm, applied to these 3D rendered models, to examine 3D joint congruency.

In conclusion, a novel approach to visualize elbow joint kinematics and stability was presented. This technique relates the anatomical geometry of the joint, obtained using

medical imaging, with the recorded motion of the joint. This method allows clinicians and investigators to visualize the relative coupled motion of the position of the bones within the joint and therefore allow clinicians and researchers to gain new insight into the causes of and treatments for various clinical orthopaedic diseases and injuries.

3.5　References

Anderst, W., Zauel, R., Bishop, J., Demps, E., and Tashman, S. (2009) Validation of three-dimensional model-based tibio-femoral tracking during running. *Med.Eng Phys.* 31[1], 10-16.

Barrance, P.J., Williams, G.N., Novotny, J.E., and Buchanan, T.S. (2005) A method for measurement of joint kinematics *in vivo* by registration of 3-D geometric models with cine phase contrast magnetic resonance imaging data. *J.Biomech.Eng* 127[5], 829-837.

Beingessner, D.M., Dunning, C.E., Gordon, K.D., Johnson, J.A., and King, G.J. (2004) The effect of radial head excision and arthroplasty on elbow kinematics and stability. *J Bone Joint Surg.Am.* 86-A[8], 1730-1739.

Besl PJ and McKay ND . (1992) A Method for Registration of 3-D Shapes. *IEEE Transactions on Pattern Analysis and Machine Intelligance* 14, 239-256.

Bey, M.J., Zauel, R., Brock, S.K., and Tashman, S. (2006) Validation of a new model-based tracking technique for measuring three-dimensional, *in vivo* glenohumeral joint kinematics. *J.Biomech.Eng* 128[4], 604-609.

Fellows, R.A., Hill, N.A., Gill, H.S., MacIntyre, N.J., Harrison, M.M., Ellis, R.E., and Wilson, D.R. (2005) Magnetic resonance imaging for *in vivo* assessment of three-dimensional patellar tracking. *J.Biomech.* 38[8], 1643-1652.

Ferreira, L.M., Bell, T.H., Johnson, J.A., and King, G.J. (2011) The effect of triceps repair techniques following olecranon excision on elbow stability and extension strength: an *in vitro* biomechanical study. *J Orthop Trauma* 25[7], 420-424.

Ferreira, L.M., Johnson, J.A., and King, G.J. (2010) Development of an active elbow flexion simulator to evaluate joint kinematics with the humerus in the horizontal position. *J.Biomech.* 43[11], 2114-2119.

Fischer, K.J., Manson, T.T., Pfaeffle, H.J., Tomaino, M.M., and Woo, S.L. (2001) A method for measuring joint kinematics designed for accurate registration of kinematic data to models constructed from CT data. *J.Biomech.* 34[3], 377-383.

Fitzpatrick, J.M. and West, J.B. (2001) The distribution of target registration error in rigid-body point-based registration. *IEEE Trans.Med.Imaging* 20[9], 917-927.

Fitzpatrick, J.M., West, J.B., and Maurer, C.R., Jr. (1998) Predicting error in rigid-body point-based registration. *IEEE Trans.Med.Imaging* 17[5], 694-702.

Fraser, G.S., Pichora, J.E., Ferreira, L.M., Brownhill, J.R., Johnson, J.A., and King, G.J. (2008) Lateral collateral ligament repair restores the initial varus stability of the elbow: an *in vitro* biomechanical study. *J.Orthop.Trauma* 22[9], 615-623.

Jackson, W.T., Hefzy, M.S., and Guo, H. (1994) Determination of wrist kinematics using a magnetic tracking device. *Med.Eng Phys.* 16[2], 123-133.

Johnson, J.A., Beingessner, D.M., Gordon, K.D., Dunning, C.E., Stacpoole, R.A., and King, G.J. (2005) Kinematics and stability of the fractured and implant-reconstructed radial head. *J Shoulder Elbow Surg.* 14[1 Suppl S], 195S-201S.

Johnson, J.A., Rath, D.A., Dunning, C.E., Roth, S.E., and King, G.J. (2000) Simulation of elbow and forearm motion *in vitro* using a load controlled testing apparatus. *J.Biomech.* 33[5], 635-639.

King, G.J., Zarzour, Z.D., Rath, D.A., Dunning, C.E., Patterson, S.D., and Johnson, J.A. (1999) Metallic radial head arthroplasty improves valgus stability of the elbow. *Clin.Orthop* [368], 114-125.

Maurer, C.R., Jr., Fitzpatrick, J.M., Wang, M.Y., Galloway, R.L., Jr., Maciunas, R.J., and Allen, G.S. (1997) Registration of head volume images using implantable fiducial markers. *IEEE Trans.Med.Imaging* 16[4], 447-462.

Milne, A.D., Chess, D.G., Johnson, J.A., and King, G.J. (1996) Accuracy of an electromagnetic tracking device: a study of the optimal range and metal interference. J.Biomech. 29[6], 791-793.

Muhle, C., Brossmann, J., and Heller, M. (1999) Kinematic CT and MR imaging of the patellofemoral joint. *Eur.Radiol.* 9[3], 508-518.

Pichora, J.E., Fraser, G.S., Ferreira, L.F., Brownhill, J.R., Johnson, J.A., and King, G.J. (2007) The effect of medial collateral ligament repair tension on elbow joint kinematics and stability. *J.Hand Surg.Am.* 32[8], 1210-1217.

Pollock, J.W., Pichora, J., Brownhill, J., Ferreira, L.M., McDonald, C.P., Johnson, J.A., and King, G.J. (2009) The influence of type II coronoid fractures, collateral ligament injuries, and surgical repair on the kinematics and stability of the elbow: an *in vitro* biomechanical study. *J.Shoulder.Elbow.Surg.* 18[3], 408-417.

Sadowsky, O., Yaniv, Z., and Joskowicz, L. (2002) Comparative *in vitro* study of contact- and image-based rigid registration for computer-aided surgery. *Comput.Aided Surg.* 7[4], 223-236.

Schroeder W, Martin K, and Lorensen B . (1998) The Visualization Toolkit. Upper Saddle River, NJ, Prentice Hall.

Sheehan, F.T., Zajac, F.E., and Drace, J.E. (1998) Using cine phase contrast magnetic resonance imaging to non-invasively study *in vivo* knee dynamics. *J.Biomech.* 31[1], 21-26.

Shellock, F.G., Mink, J.H., Deutsch, A.L., Foo, T.K., and Sullenberger, P. (1993) Patellofemoral joint: identification of abnormalities with active-movement, "unloaded" versus "loaded" kinematic MR imaging techniques. *Radiology* 188[2], 575-578.

Sholukha, V., Leardini, A., Salvia, P., Rooze, M., and Van Sint, J.S. (2006) Double-step registration of *in vivo* stereophotogrammetry with both *in vitro* 6-DOFs electrogoniometry and CT medical imaging. *J.Biomech.* 39[11], 2087-2095.

Sugano, N., Sasama, T., Sato, Y., Nakajima, Y., Nishii, T., Yonenobu, K., Tamura, S., and Ochi, T. (2001) Accuracy evaluation of surface-based registration methods in a computer navigation system for hip surgery performed through a posterolateral approach. *Comput.Aided Surg.* 6[4], 195-203.

Van Sint, J.S., Salvia, P., Feipel, V., Sobzack, S., Rooze, M., and Sholukha, V. (2006) *In vivo* registration of both electrogoniometry and medical imaging: development and application on the ankle joint complex. *IEEE Trans.Biomed.Eng* 53[4], 759-762.

Van Sint, J.S., Salvia, P., Hilal, I., Sholukha, V., Rooze, M., and Clapworthy, G. (2002) Registration of 6-DOFs electrogoniometry and CT medical imaging for 3D joint modeling. *J.Biomech.* 35[11], 1475-1484.

Chapter 4 – Accuracy Assessment of an Imaging Technique to Examine Ulnohumeral Joint Congruency During Elbow Flexion

OVERVIEW

The objective of this chapter was to integrate the proximity mapping technique developed in Chapter 2 with the registration technique used to render 3D models (Chapter 3) into a single technique which can be used to investigate joint congruency undergoing simulated elbow flexion. The accuracy of the registration technique developed in Chapter 3 was increased and was measured in this current chapter in four specimens using fiducial and target registration error to assess the positional and angular accuracy. Additionally, the overall technique was validated using the casting technique. Preliminary data of an intact cadaveric elbow was shown to demonstrate the utility of this technique.[3]

4.1 Introduction

Understanding joint contact mechanics is important when considering the etiology of various degenerative joint diseases such as Osteoarthritis (OA). Osteoarthritis commonly occurs following joint injuries and is then referred to as post-traumatic arthritis. The injury could be an articular surface fracture, joint dislocation or disruption of the ligaments. The associated degenerative changes may occur due to chondral damage as a result of the initial trauma, or as a result of articular incongruity present as a result of residual subclinical joint instability (McKee *et al.*, 1998; Ring *et al.*, 2002). The exact mechanism and cause of this debilitating disease is unknown (Hunter *et al.*, 2005; Hunter

[3]A version of this has been published: Lalone EA, Peters TM, King GW, Johnson JA. Accuracy assessment of an imaging technique to examine ulnohumeral joint congruency during elbow flexion. Computer Aided Surgery. 2012; 17(3): 142-52.

et al., 2009). Altered cartilage contact patterns and forces due to abnormal joint kinematics as a consequence of mal-alignment or instability, was thought to be a common cause of osteoarthritis in a genetically predisposed joint (Felson *et al.*, 2000; Hunter *et al.*, 2009; Van de Velde *et al.*, 2009). Currently, no techniques have been reported to quantify articular mechanics in joints undergoing physiologic motion and certainly not in pathologic and surgically treated scenarios. This consideration is of extreme clinical importance as typically, joint instability manifests itself with symptoms emanating from the joint.

Therefore, the objective of this study was to develop and validate a non-destructive imaging approach to examine joint contact mechanics of the ulnohumeral joint undergoing physiologic motion. The inter-bone distance algorithm described in Chapter 2 in its current form, can only be used to examine joint congruency in statically loaded scenarios. Chapter 3 described a technique that can be used to render 3D bone models of joints undergoing simulated elbow flexion using landmark registration. The objective was to then employ the inter-bone distance algorithm, to these rendered models, to examine joint congruency of joints undergoing continuous motion. However, the accuracy of this technique was not sufficient to examine inter-bone distances. Therefore, the objective of this chapter was to refine this registration algorithm and to employ optical tracking to increase the accuracy of the overall registration. The inter-bone distance algorithm was then applied to these rendered motions to assess joint congruency of joints undergoing *simulated elbow flexion*. Fiducial and target registration error metrics were used to evaluate the positional and angular accuracy of the registration technique. The

ability of this technique to predict regions of joint contact was also assessed using experimental casting. Additionally, a registration phantom was used to assess the repeatability of the experimental protocol. Finally, preliminary data is also shown to demonstrate the utility of this approach.

4.2   Methods

4.2.1   ELBOW SIMULATOR EXPERIMENTAL PROTOCOL

4.2.1.1   *Volumetric Image Acquisition*

Four intact cadaveric upper extremities (77±3yrs: M) were employed in this study. A computed tomography (CT) scan of each specimen was obtained prior to testing (pre-testing CT) using a 64-slice scanner (GE Discovery CT750 HD, Waukesha, WI). Approximately 350 slices were acquired for each specimen with a field of view set at 20x20cm and a 512x512 reconstruction matrix (292mAs, 120 kVp). The size of the voxels was approximately 0.6x0.6x0.625mm. The scanning protocol used was consistent with standard clinical settings with the arm positioned parallel to the long axis of the gantry.

4.2.1.2   *Specimen Preparation*

Each specimen was surgically prepared as described in Chapter 3 (Section 3.2.2), however in addition to the tendons attached to the servomotors (biceps brachii, brachialis and triceps), the tendons of the brachioradialis, pronator teres, supinator, wrist flexors (flexor carpi radialis and flexor carpi ulnaris) and extensors (extensor carpi radialis brevis and extensor carpi ulnaris) were isolated, secured to sutures and connected to pneumatic

actuators using stainless steel cables. All soft tissues including the joint capsule and collateral ligaments remained intact throughout preparation and were kept hydrated using saline throughout testing.

4.2.1.3   Elbow Motion Simulator/Experimental Set-up

Active elbow joint flexion was simulated using an elbow motion simulator that utilizes computer-controlled actuators and motors as described in Section 3.2.3 (Ferreira *et al.*, 2010). Simulated active motion was achieved with the elbow in the valgus gravity dependent position as shown in Figure 4.1. Frames of motion that corresponded to 15°, 30°, 45°, 60°, 75°, 90°, 105° and 120° of elbow flexion were analyzed. Throughout elbow flexion, the ulna articulated and tracked around a stationary humerus. To track the motion of the ulna with respect to the humerus, 3D optical position sensors were used (Optotrak Certus®, NDI, Waterloo, ON, Canada). The Optotrak motion capture system is an infrared-based tracking system. The position sensors themselves are 'active' trackers which emit infra-red lights allowing the camera to track the sensors position. For the humerus, two position sensors were attached to the simulator near the humerus. The motion of the humerus with respect to the simulator was constant. For the ulna, two position sensors were rigidly attached to the bone using a bone mount that was securely affixed to the distal-dorsal region of the ulna. These markers allowed the camera to track the motion of the ulna throughout flexion. To maintain the an in-plane accuracy of 0.1mm and 0.15mm perpendicular to the camera, a direct line of sight between the camera and the position sensors was maintained and kept within 2.5m.
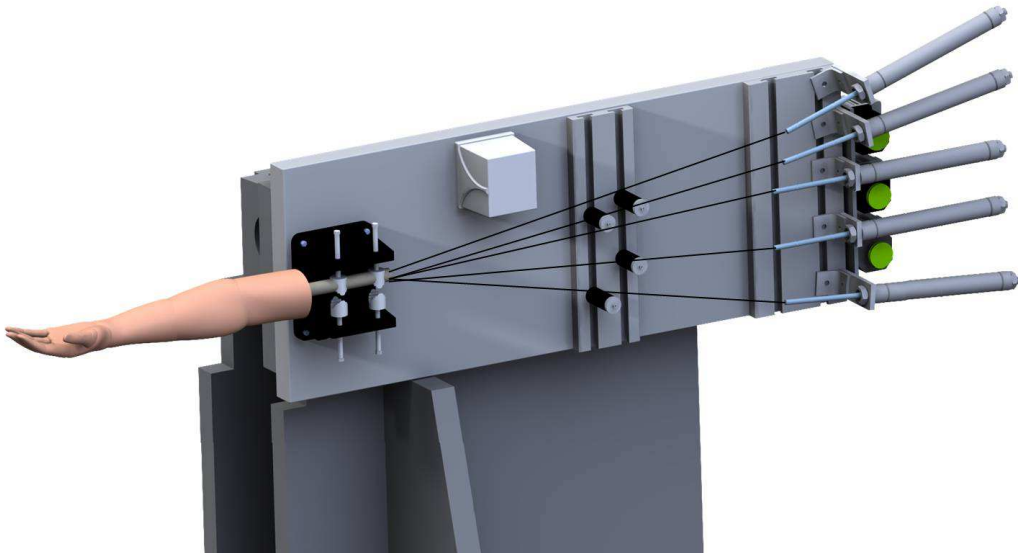
Figure 4.1: Elbow Simulator
The cadaveric specimen was surgically prepared and then mounted to the simulator using the clamp. The tendons of the relevant muscles involved in elbow flexion were attached to cables and then attached to motors and actuators.

4.2.1.4   *Fiducial Configuration*

The overall accuracy of a paired-point registration technique is largely independent of the object being registered as noted by Fitzpatrick *et al.* (1998). This independence is achieved because only the fiducial or landmark configuration is used in the registration itself. This is in direct contrast to a surface-based registration algorithm that uses points derived from the surface of the anatomy for the purpose of registration. Therefore, the fiducial configuration itself is an important factor governing the accuracy of the overall configuration. West *et al.* (2001) published a set of guidelines to follow when employing fiducial markers in paired-point rigid body registration. It was noted that the most accurate point-based registration methods employ markers that are rigidly attached to the bone. The current application of this registration is for use in an *in vitro* study where cadaveric specimens are used in conjunction with a motion simulator. Therefore, our current study, invasiveness of the bone mounted markers was not of concern. West *et al.* (2001) stated that when employing fiducial markers, the fiducial markers should be positioned on the rigid body being registered in a non-collinear configuration. Additionally, the area of clinical interest (articulation) should be positioned in the centroid of the overall fiducial configuration. West *et al* (2001) however did note that the position of each fiducial should be as far as possible from each other while maintaining the centroid position of the configuration. The configuration of the fiducial markers in this chapter was optimized to be consistent with previously reported guidelines (West *et al.*, 2001).

Subsequent to testing, all soft tissues were removed and the elbows were disarticulated for the target registration experiment. Four fiducial markers (19mm optically reflective nylon spheres attached to threaded screws) were secured to the denuded bones. This configuration is shown in Chapter 3 (Section 3.2.5). Care was taken to ensure that two fiducials were placed distally and two proximally as well as medially and laterally. In this protocol, an additional 5th fiducial was positioned anteriorly on the articulation (region of interest) of the humerus and ulna (Figure 4.2) to assess the target registration error. The centre of each fiducial marker was localized using a calibrated cupped stylus (Figure 4.3). An optical position tracker was attached to the shaft of the stylus. The inner diameter of the stylus was consistent with the radius of curvature of the fiducial markers and was calibrated using a pivot test to locate the centre of each fiducial when the cupped stylus is placed on the fiducial. The accuracy of this calibration resulted in a maximum 3D RMS Error of 0.25mm. The 3D RMS error is produced by applying the result of the pivot procedure to each frame of the pivot procedure and calculating an overall RMS error for the collection.
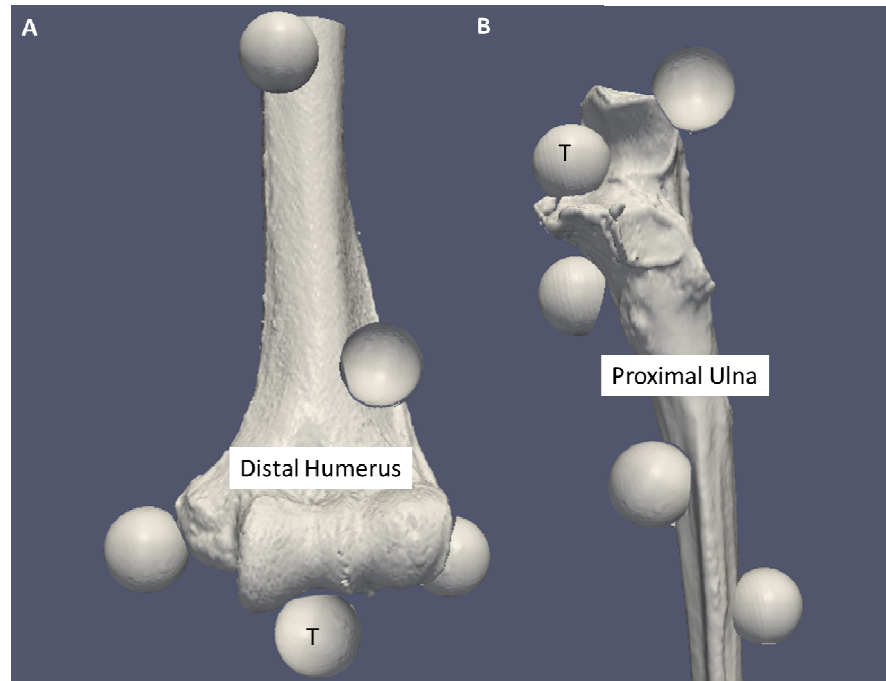
Figure 4.2: Fiducial Configuration
Fiducial configuration as shown in Chapter 3 (Section 3.2.5) with the additional target fiducial marker used to assess target registration error.
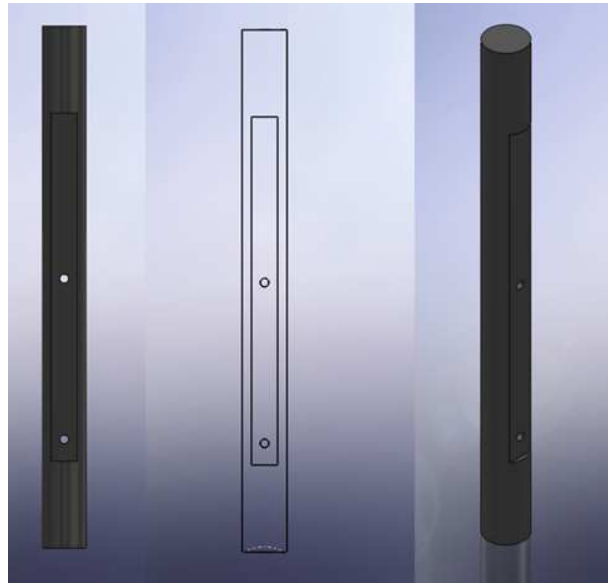
Figure 4.3: Calibrated Cup-Stylus

A calibrated stylus was used to localize the centre of each fiducial marker in the laboratory coordinate system. An optical position sensor was securely attached to the stylus using the screw holes. The inner diameter at one end of the stylus was machined to receive the 19mm diameter fiducial marker.

4.2.1.5   *Image Acquisition-Post Experimental Testing*

A second volumetric image of each specimen was acquired after testing with the mounted fiducial markers. Approximately 350 slices were acquired using the same CT scanning parameters as employed in the pre-testing scan.

4.2.2   REGISTRATION PHANTOM

A single nylon rectangle (90mmx150mmx25mm) was used to assess the effect of reconstruction threshold as well as to assess the repeatability of localizing the fiducial markers used for registration purposes. Four markers were attached to the block by drilling and tapping the rectangle. A fourth fiducial was attached to the top of the rectangle which was considered the target (Figure 4.4). An optical position sensor was secured to the surface of the block. A single fiducial configuration was used to assess the effect of threshold selection on registration accuracy.

Figure 4.4: Registration Phantom
Four fiducial markers and a single target fiducial marker were attached to the phantom. The configuration shown is not assumed to be representative of the configuration used in the actual experimental set up using the simulator. Instead, in this experiment, the effect of localization and object thresholding are examined within a single fiducial configuration. (T) corresponds to the target fiducial marker.

Note: The optical sensor is shown on the bottom of the phantom but is distorted as a result of the electrical and metal components during the CT scan.

4.2.2.1   Volumetric Image Acquisition/3D Reconstruction

A 3D image of each specimen was obtained prior to testing using a 64-slice computed tomography (CT) scanner (GE Discovery CT750 HD, Waukesha, WI). The size of the voxels was approximately 0.6x0.6x0.625mm. A 3D model of the phantom was obtained using the marching cubes algorithm available within the Visualization Toolkit (VTK, Kitware, Clifton Park, NY)(Schroeder W *et al.*, 1998). A series of manually set thresholds were chosen to visualize the outermost surface of the phantom. The thresholds examined in this study were 4000, 4500, 5000, 5500, 6000, 6500, 7000, 7500, 8000 and 8500. These values are unit-less and are based on intensity of the voxels found within the imaged volume. Reconstruction of the fiducial markers from the CT image is required to sphere-fit and identify the location of the centre of each fiducial within the CT coordinate system.

4.2.2.2   Experimental Protocol

For the block registration phantom experiment, a static motion recording was recorded. The motion of the block was recorded with respect to the laboratory coordinate system. To assess the repeatability of localizing each fiducial marker, five sets of single point digitizations were used in five separate registrations and the accuracy of each registration was obtained. The position of each fiducial was transformed from the laboratory coordinate system to be with respect to the block tracker using the technique described in Chapter 3 (Section 3.2.6). The segmenting threshold used when reconstructing the fiducial markers in the CT coordinate system was maintained at 4500 so the effect of threshold segmentation would not confound the accuracy assessment.

4.2.3 EXPERIMENTAL CAST VALIDATION

4.2.3.1 *Volumetric Image Acquisition*

A computed tomography scan of an additional single cadaveric specimen (Male, 69 years) was obtained prior to testing (pre-testing CT) using a 64-slice scanner (GE Discovery CT750 HD, Waukesha, WI). Approximately 350 slices were acquired for each specimen with a field of view set at 20x20cm and a 512x512 reconstruction matrix (146mAs, 140 kVp). The size of the voxels was approximately 0.6x0.6x0.625mm. The overall joint space was manually measured from this pre-testing CT. Using custom software, points were manually identified across the two subchondral bone surfaces in a volumetric CT image using two orthogonal planes. The distance between these two sets of points (two opposing subchondral bone surfaces) was used to approximate the overall thickness of the joint space for this particular specimen. This value was then inserted into the inter-bone distance algorithm to measure the surface area across the joint and compare that to the experimental cast.

4.2.3.2 *Specimen Preparation/Experimental Protocol*

The specimen was completely denuded of all soft tissue. Prior to testing, both the humerus and ulnar articular surfaces were submerged in saline to ensure that all surfaces were well hydrated. The humerus was clamped into the simulator and position trackers were attached to the simulator and ulna as described in Section 3.2.3. Four fiducial markers were rigidly fixed to the denuded bone in a configuration similar to that described previously for the TRE experimental protocol. Experimental casting material (Reprosil Medium Body Vinyl Polysiloxine Impression Material, DENTPLY

International Inc. – York, PA, USA) was prepared and placed in the greater sigmoid notch of the proximal ulna, similar to the process described in Section 2.2.6 in Chapter 2. The ulna was positioned on the humerus in a reduced fashion and rigidly held until the cast set. A recording of the static position was acquired once the cast had solidified. The ulna was removed from the humerus and the cast was positioned on the proximal ulna. Using an optically tracked calibrated pen-point stylus, the region of experimental cast which was vacant (corresponding to the area of joint contact) was digitized. A 3D surface model of the resulting contact patch was constructed using MATLAB (Math Works Inc. MA, USA). The surface area of this patch, corresponding to the total contact area, was then calculated. The cast was then photographed using a digital camera with the cast placed in front of a light source to visualize regions of the cast where the surfaces were in close proximity, but not necessarily contacting. Adjacent to the cast, a stepped calibration phantom was used to calibrate the relative thickness of casting material (Figure 4.5).
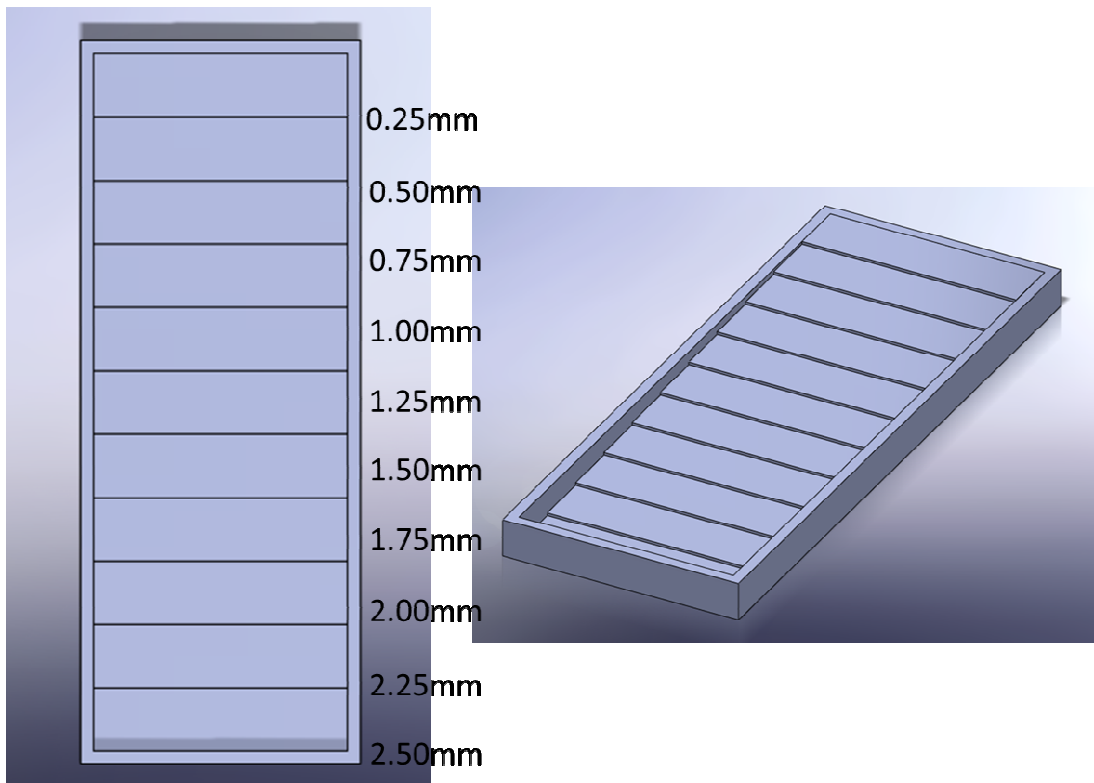
Figure 4.5: Cast Thickness Calibration
Casting material was injected into this template to create cast with known thicknesses.
The thicknesses increased in a step-wise manner from 0-2.5mm thick.

Additionally, to compare the computational and cast techniques, an edge filter was used to extract the surface of the digitized cast, which was then overlaid onto the proximity map. The measured joint space was used as a threshold in the inter-bone distance algorithm to compare the results from using the cast and the algorithm.

Twenty recordings of each fiducial marker/target were digitized with respect to the corresponding bone position sensor, using a cupped stylus. The geometric *centre* of the fiducial/target was found by averaging the position recordings.

A post-testing CT scan was acquired with the fiducial markers secured to the humerus and ulna using the same CT scanning techniques as for the pre-testing CT.

4.2.4   DATA ANALYSIS

4.2.4.1   Three-Dimensional Reconstruction

The CT images were processed using custom software and surface models were created as described in Chapter 2 (Section 2.2.3). The subchondral regions below the articular surface of the humerus and ulna were again manually segmented into separate 3D models. In this chapter however, four subchondral zones on the ulna, were created (Figure 4.6). Planes were created to divide the ulnar subchondral bone surface into medial-superior (MS), medial-inferior (MI), lateral-superior (LS) and lateral-inferior (LI) zones. To create these zones, the sagittal plane was created which intersected the olecranon and coronoid process, and a transverse plane was created along the transverse ridge of the ulna (typically devoid of cartilage) on the greater sigmoid notch. The humeral subchondral bone was not divided into zones.
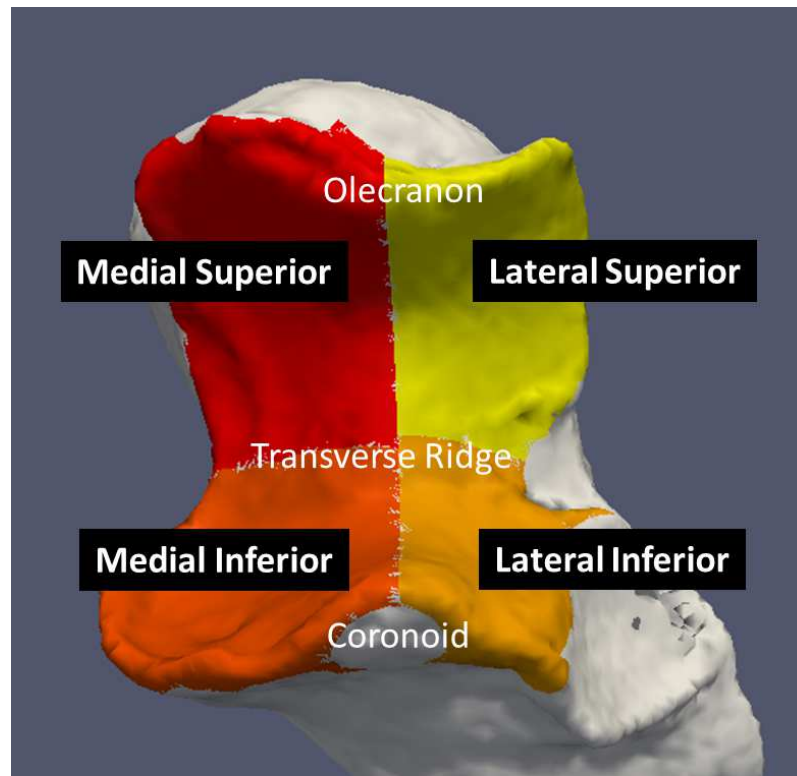
Figure 4.6: Ulnar Subchondral Zones
Four zones were created by dividing the ulnar subchondral bone medially and laterally down the ridge of the greater sigmoid notch (extending from the olecranon to the coronoid process). A second plane was created along the tranverse ridge dividing the ulna into superior and inferior regions.

4.2.4.2 *Registration*

Subsequent to testing, anatomical landmarks were digitized using a calibrated pointed stylus, and anatomically relevant coordinate systems were created as described in detail in Chapter 3 (Section 3.2.6). The registration and post-hoc kinematic analysis described in detail in Chapter 3 (Section 3.2.6) was employed and is described briefly here (Figure 4.7). Bone surface models from the pre-testing CT were registered to the post-testing CT (containing the fiducial markers) using the Iterative Closest Point (ICP) surface-based registration algorithm (Besl PJ and McKay ND, 1992). To ensure optimal alignment, three anatomical landmarks were initially selected on each surface model and a paired-point registration was performed for coarse alignment. Using the 3D reconstructions of the fiducials, the centres of each fiducial were localized with respect to the CT coordinate system using a least-squares sphere fit algorithm.

Homologous fiducial markers in both the CT coordinate system and in the laboratory coordinate system (Figure 4.7B) were used in the landmark transform to produce a registration transformation matrix relating the CT to the laboratory coordinate system. This transform was applied to the humerus and ulna 3D bony models separately allowing their relative position to be rendered according to the tracked motion (Figure 4.7C).

Similarly for the validation, paired-point landmark registration was also used to register the position and orientation of the 3D reconstructed bones to their relative position. However, no coordinate system was used in this registration.
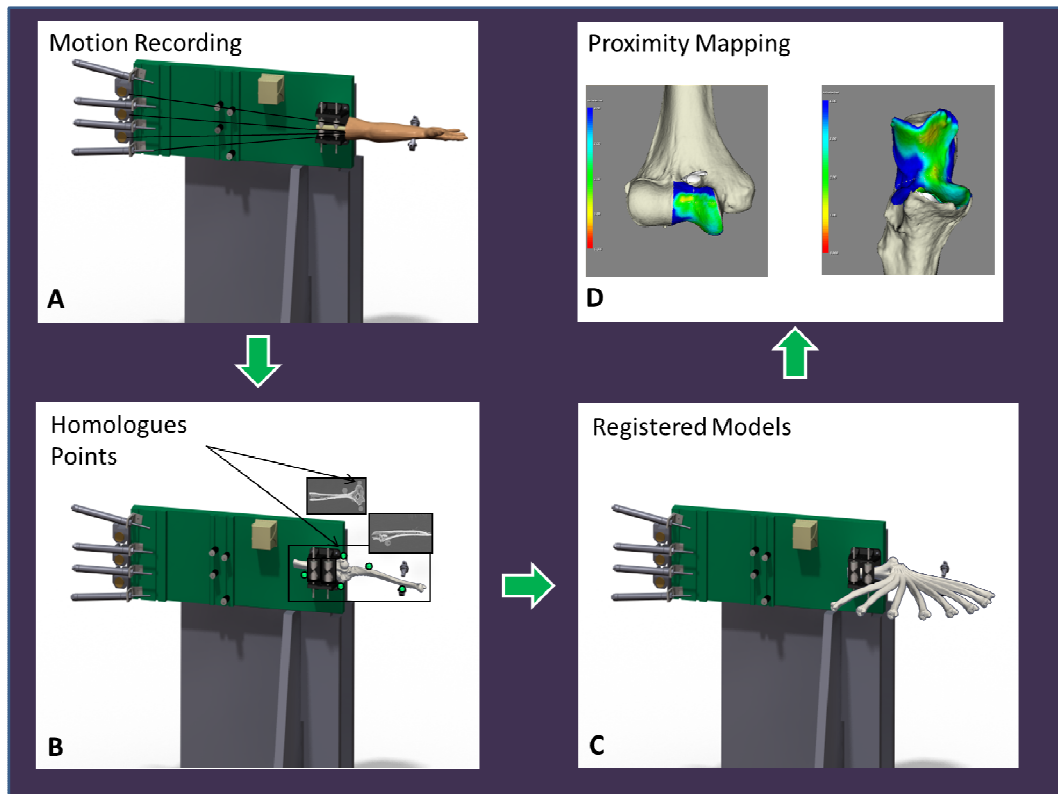
Figure 4.7: Registration Schematic and Implementation of Proximity Mapping
A) Simulated elbow flexion was achieved using cadaveric specimens and the upper extremity motion simulator (shown here in the valgus gravity dependent position).
B) Subsequent to testing, all soft tissues were removed and fiducial markers are secured for registration purposes. A second volumetric CT scan was acquired of the humerus and ulna and homologous points are used for registration.
C) The result of this registration was a visualization of the 3D rigid body motion of the ulna with respect to the humerus, throughout elbow flexion.
D) Subsequent to registration of the rigid bodies, the proximity mapping technique was applied to the registered models and the overall joint congruency can be identified for the humerus and ulna.

4.2.4.3   *Registration Error*

Fiducial registration error was obtained to measure the overall correspondence between these homologous rigid body landmarks. This error was determined by measuring the root mean squared distance between homologous fiducial makers after registration expressed in mm. Four fiducial markers were attached to each rigid body being registered and a fifth fiducial (target) was also secured to each bone on the articulation. When using paired-point registration, the number of corresponding points (the centre of each fiducial) should be maximized; however, this increase in accuracy of the registration rapidly decreases after 5 or 6 markers (Sadowsky *et al.*, 2002). For bone mounted marker systems, the traditional number of fiducials employed ranges from 3-5. This value typically corresponds to a fiducial localization error of less than 1mm (Sadowsky *et al.*, 2002; West *et al.*, 2001). In addition to determining FRE, Target registration error (TRE) was also examined.

4.2.4.4   *Proximity Mapping*

To measure the joint congruency, the inter-bone distance algorithm described and validated in Chapter 2 (Section 2.2.5) was used. The algorithm uses vertices of polygonal surfaces as points to measure relative distances between two surfaces defined by polygonal meshes. The overall proximity of the opposing bone surfaces can be visualized using a proximity map (inter-bone distance less than 4mm). Additionally, 'levels of proximity', as described in Chapter 2 (Section 2.2.5), corresponding levels of inter-bone distance values were employed to measure the surface area of the subchondral bone within high proximity (< 0.5mm), medium proximity (< 1.5mm), low proximity (<

2.5mm) and ultra-low proximity ($<$ 3.5mm). Figure 4.7D shows the final step in the overall technique with the implementation of the proximity mapping technique. The inter-bone distance algorithm can be used to investigate the joint congruency of the humeral or ulnar subchondral bone, and similarly for each of the four zones on the ulnar subchondral bone, during any frame of motion throughout elbow flexion.

4.3   Results

4.3.1   ELBOW SIMULATOR EXPERIMENTAL PROTOCOL

To illustrate the capabilities of this technique, simulated active elbow flexion was analyzed in a single specimen using the inter-bone distance algorithm to measure overall joint congruency throughout elbow flexion in the valgus gravity dependent position. This congruency was measured for each level of proximity across the entire humeral/ulnar bone surface and within each zone. The implementation of the proximity map and inter-bone distance algorithm into the registration algorithm is shown in Figure 4.8. The data presented is representative of the type of information regarding joint congruency that can be obtained using this described technique. Proximity maps for the humerus were also obtained, but are not shown here.
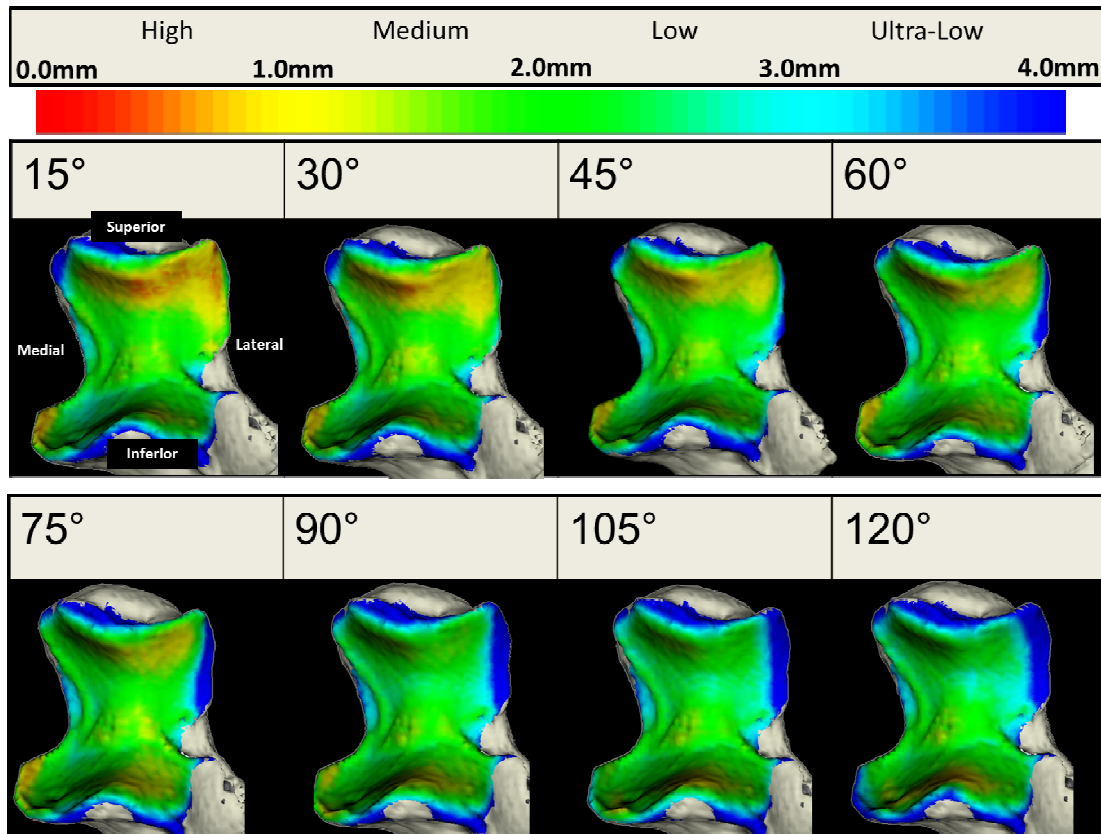
Figure 4.8: Proximity Maps for Ulna throughout Elbow Flexion
Anterior view of the ulna showing the regions of close proximity (less than 4mm). In general, it appeared that the total surface area of the close proximity region decreases with increasing flexion. More specifically, there was a decrease in the superior-lateral region of the ulna. Additionally, there was a large area of the superior region on the ulna that is in high proximity at early flexion as shown by the yellow-green contour. However, with increasing flexion, this area decreased and shifted to the inferior region of the ulna. These results are specific to this specimen.

Two repeated active motion recordings were used to assess the repeatability of the motion and the proximity mapping. A comparison of these trials at 15 ° for the ulna is shown in Figure 4.9. The measured contact area difference between the two scans was 0.09% for the humerus (proximity map not shown) and 0.05% difference for the ulna.
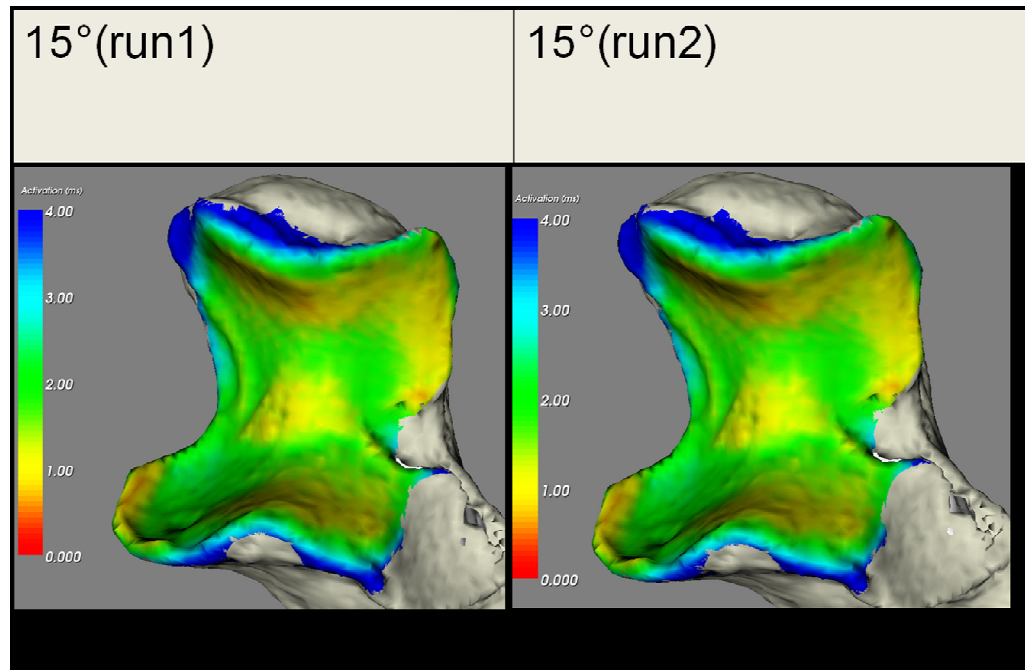
Figure 4.9: Proximity Maps showing Repeatability of Active Motion
Two subsequent active flexion motions were recorded and used with the registration and inter-bone distance algorithm to generate these two proximity maps. Using the anatomical coordinate system, it is possible to examine discrete angle of elbow flexion. The two motion runs qualitatively show excellent agreement.

In this single specimen, it appears that the total surface area of the close proximity region decreases with increasing flexion. Proximity levels for high, med, low and ultra-low proximity on the entire ulnar surface is shown in Figure 4.10. The area of the proximity region (<4mm) did not exceed 1000mm^2 throughout elbow flexion. The total surface area of the ulnar subchondral bone was 1511.1mm^2. Also, for this single specimen shown, there is an overall decrease in the size of the proximity region with increasing flexion, for each level of proximity. This is however, with the exception of the high proximity region which increases in late flexion, corresponding to the orange-yellow contour noted on the proximity map.
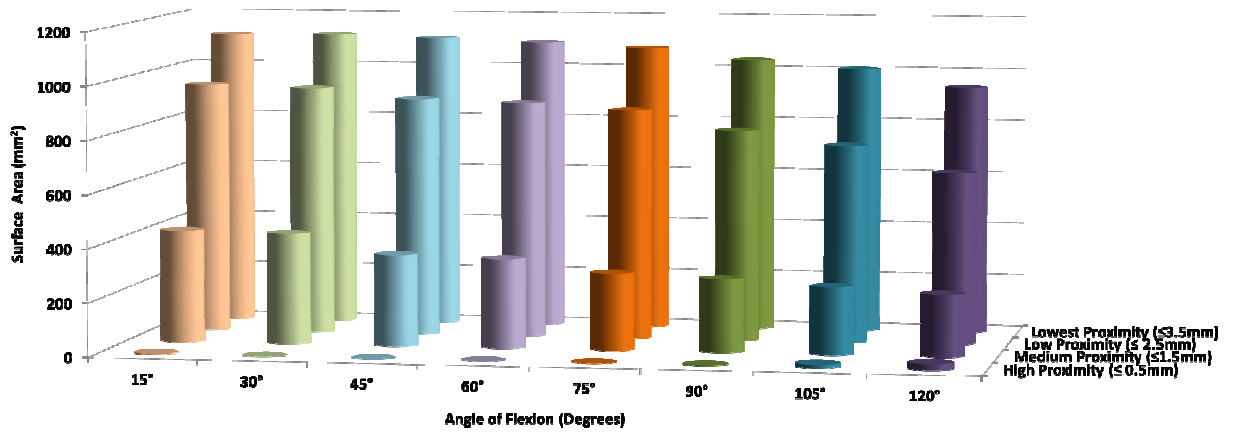
Figure 4.10: Surface Area throughout Elbow Flexion
Surface area values are shown for each level of proximity (high, med, low and ultra-low) (n=1). This graph also indicates that there was an overall decrease in the size of the proximity region with increasing flexion, for each level of proximity. This is with the exception of the high proximity region which increases in late flexion (corresponding to the orange-yellow contour noted on the proximity map)

Proximity levels were also examined for each of the four ulnar zones in this single specimen as shown in Figure 4.11. Medium level proximity (<1.5mm), which corresponds to the yellow-green contour interface, exhibited the most difference between zones.
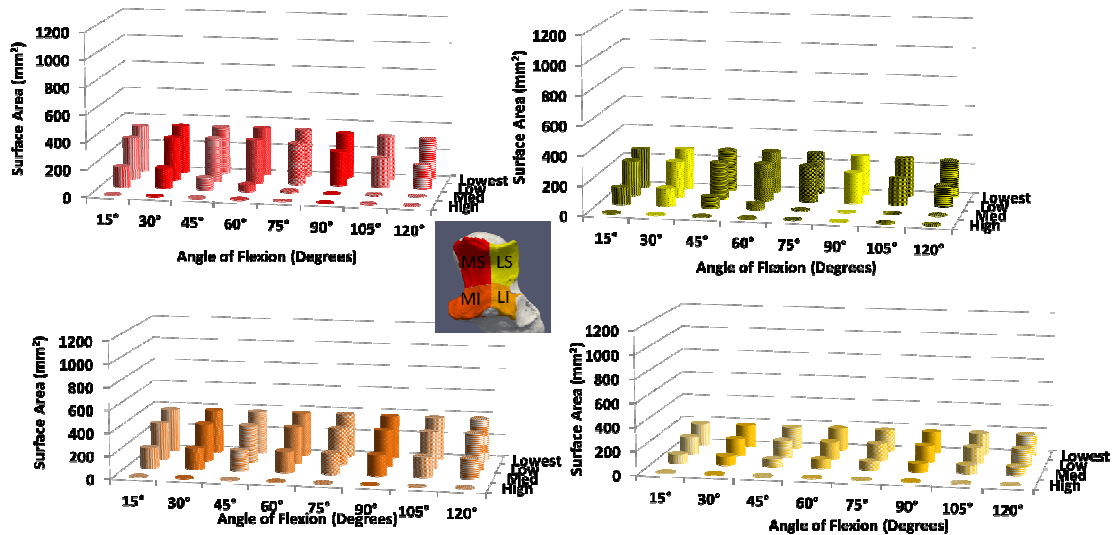
Figure 4.11: Zonal Surface Area throughout Elbow Flexion

Surface area values are shown for each zone and within each level of proximity throughout elbow flexion. (H: high, M:med, L: low and U:ultra-low) (n=1). For the superior regions (MS, LS) the area of the medium proximity region became zero at 75°. At the low level of proximity (<2.5mm), which corresponds to the green-blue contour interface, again, the superior regions showed a decrease in area with increasing flexion, while the inferior regions remained relatively constant. Finally, the ultra-low levels of proximity (<3.5mm), corresponding to the aqua-dark blue contour interface remained relatively constant during flexion in the inferior regions. The superior zones however showed a decrease in the surface area with increasing flexion.

4.3.1.1   *Target Registration Error*

The mean target registration error (TRE) was 0.24±0.1mm for the distal humerus and 0.88±0.3mm for the proximal ulna. The mean fiducial registration error (FRE) was 0.25±0.1mm for the humerus and 0.29±0.1mm for the ulna. Table 4.1 shows the individual target and fiducial registration error values for each specimen.

	FRE (mm)		TRE (mm)	
Specimen	**Humerus**	**Ulna**	**Humerus**	**Ulna**
1	0.17	0.30	0.32	1.21
2	0.23	0.28	0.19	0.65
3	0.23	0.17	0.14	0.61
4	0.36	0.41	0.32	1.07
Average	**0.25±0.1**	**0.29±0.1**	**0.24±0.1**	**0.88±0.3**

Table 4.1: Fiducial and Target Registration Error
Registration values for each specimen for the humerus and ulna respectively.

The centroid of each fiducial configuration was also measured and compared to the target fiducial located in the region of interest. Figure 4.12 shows the four fiducial configurations for each specimen on the humerus and ulna respectively. The geometric centroid was calculated and superimposed onto each reconstructed bone. The humerus and ulna bony models are transparent and shown from two positions to characterize the location of the centroid. This centroid location corresponds to the location across the registered rigid body where the accuracy is thought to be highest. In general the fiducial configuration centroid was located on the condyles of the humerus. Correspondence of this point with the region of interest would be ideal, but often difficult to achieve in a joint where the region of interest is at the end of a long bone. The mean distance between the centroid and target fiducial for the humerus was 53.25±5.24mm. In general the humeral fiducial configurations are consistent with each other. The centroid of the fiducial configuration on the ulna appeared just below the proximal radioulnar joint articulation on the ulna. The mean distance between the centroid and the target fiducial is 47.45±8.46mm.
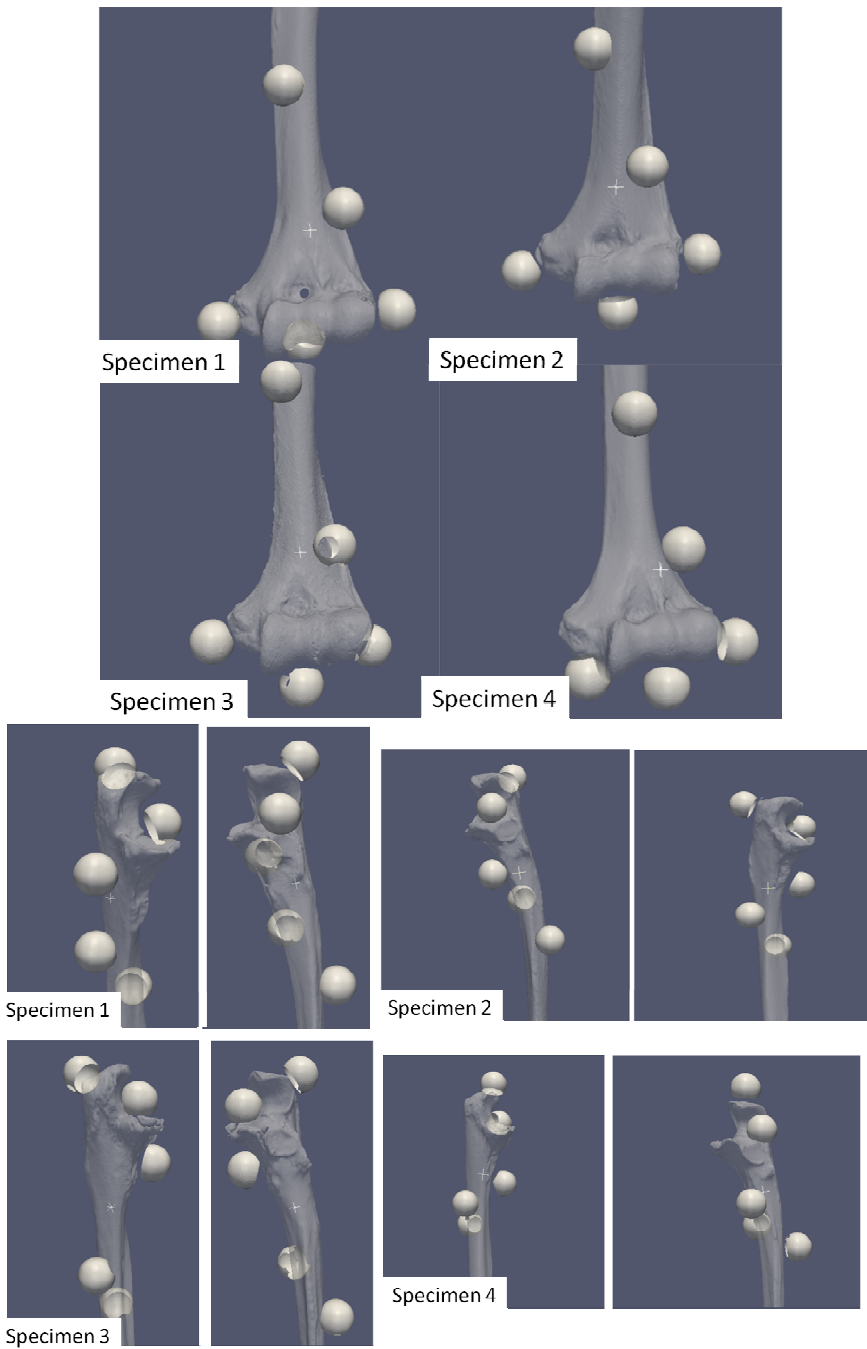
Figure 4.12: Fiducial Configuration and Geometric Centroids
The geometric centroid of each configuration is shown as an "+" for each specimen. Four fiducial markers were attached to both the humerus and ulna. Configurations are shown for all specimens.

4.3.2   REGISTRATION PHANTOM

Figure 4.13 shows the fiducial registration and target registration error at ten different threshold values. The threshold values are used for surface reconstructing the fiducial markers. In this experimental protocol, the configuration of the fiducial was consistent, and only the threshold values changed and a separate registration for each threshold value was completed. The mean FRE was 0.35±0.01mm and the mean TRE was 0.59±0.23mm. The overall coefficient of variation (CV) was 3.94% for all threshold values. For FRE, the CV was 2.33%. Both of these values indicate the variability of the measured TRE and FRE was very low.
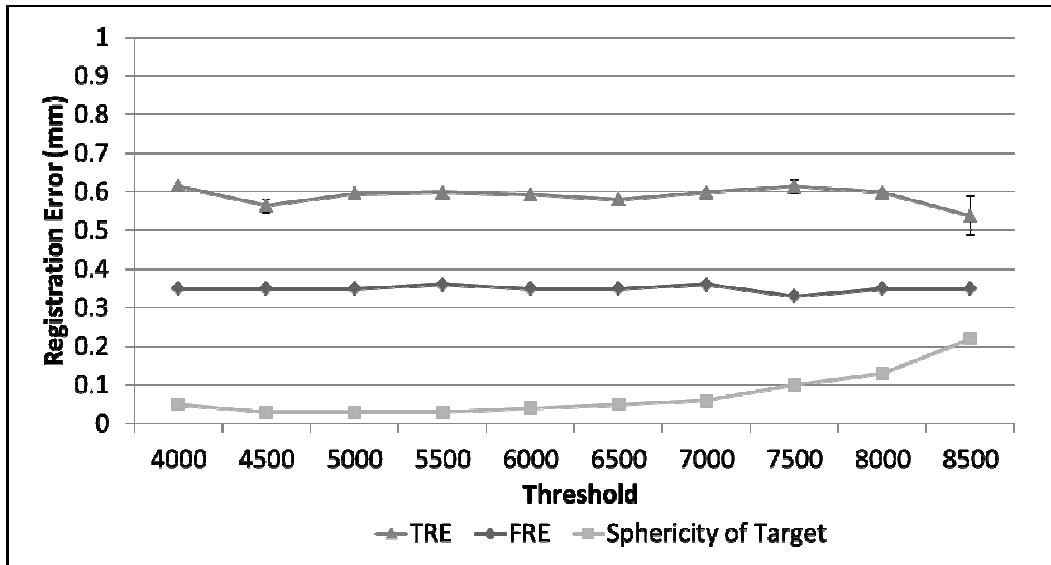
Figure 4.13: Effect of Threshold Selection on TRE, FRE and Sphericity
Target and fiducial registration error remain consistent regardless of threshold selection. However, this graph shows that the sphericity of the fiducial markers increases as the threshold increases.

Figure 4.14 shows concentric fiducial spheres created using a threshold value of 4000 and 8500. The sphericity of the target fiducial was also calculated for all threshold intensity values. It is important to note that the sphericity for a perfect sphere, using the algorithm employed, should be 0. With increasing threshold values, the surface of the fiducial becomes pitted and deformed which caused the sphericity value to increase.
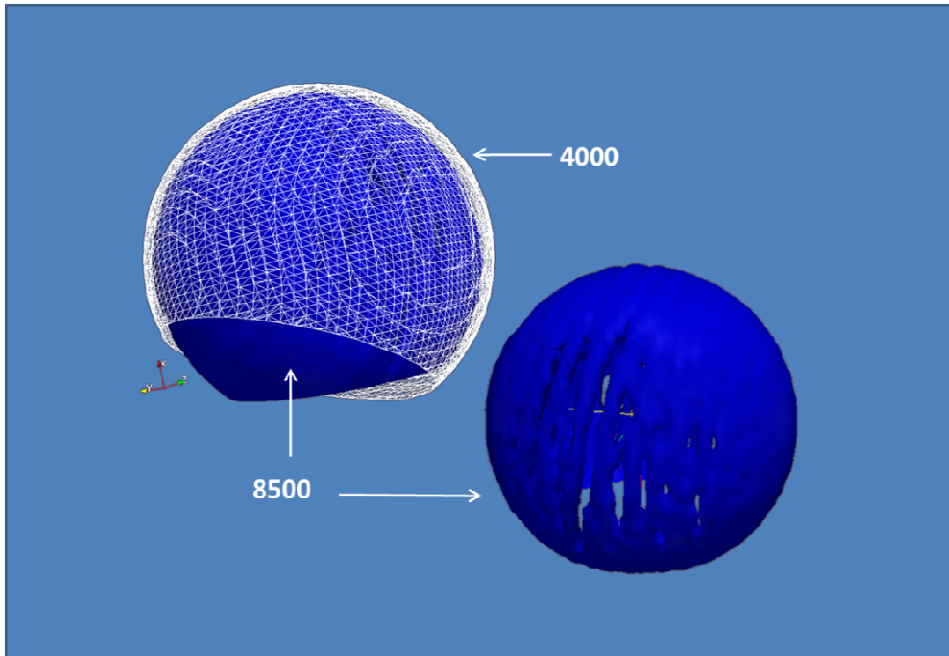
Figure 4.14: Reconstructed Fiducial markers
Reconstructed fiducial markers are shown using a threshold value of 4000 and 8500. Lower reconstruction threshold values reconstruct a fiducial with a larger diameter than lower threshold values as shown. Higher intensity values correspond to surfaces that are less dense.

Note: The actual dimension of the fiducial is 19mm in diameter.

The repeatability of localizing the fiducial markers was also examined. Figure 4.15 shows the fiducial and target registration error for the five separate registrations conducted using five independent sets of digitizations (threshold used was 4500). The mean FRE was 0.35±0.004mm and the mean TRE was 0.60±0.02mm. The overall coefficient of variation for FRE was 1.27% and 2.97% for TRE. The results of this phantom indicate that the localization of the fiducial markers and their use in the registration is very repeatable using the optical tracking system and tracked cupped-stylus.
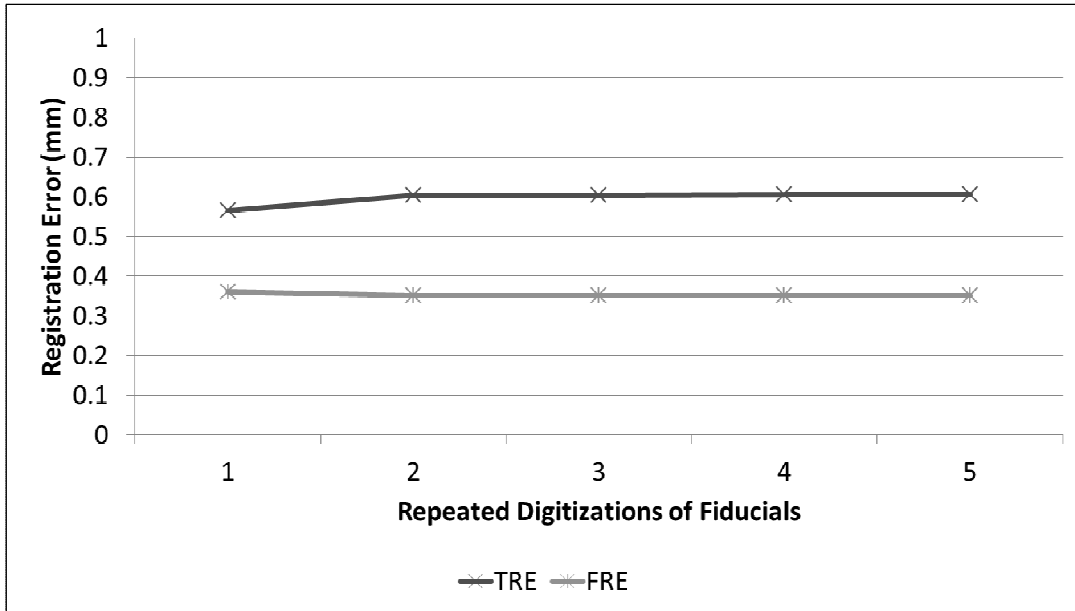
Figure 4.15: Repeatability of Localizing Fiducial Markers
Five separate registrations were conducted using repeated digitizations of the fiducial markers. The target and fiducial registration error are consistent for repeated digitizations as shown.

4.3.3   EXPERIMENTAL CAST VALIDATION

Figure 4.16 shows a comparison of the proximity map obtained using the technique described in this current study and the gold standard experimental cast. The vacant regions in the cast correspond to regions of joint contact. Comparing the proximity map with the casting technique, these two representations of the surface articular interactions are very similar. The total contact area of the cast was 362.10mm^2. The average joint space distance as measured for this specimen was 2.87mm. Figure 4.17 shows the cast contact area overlaid on the proximity map showing the surface area across the ulna that is within 2.87mm of proximity. Using this value as a threshold in the inter-bone distance algorithm, the resulting surface area was 429.06mm^2. This value is greater than the contact area as determined by the cast by 17.35%.
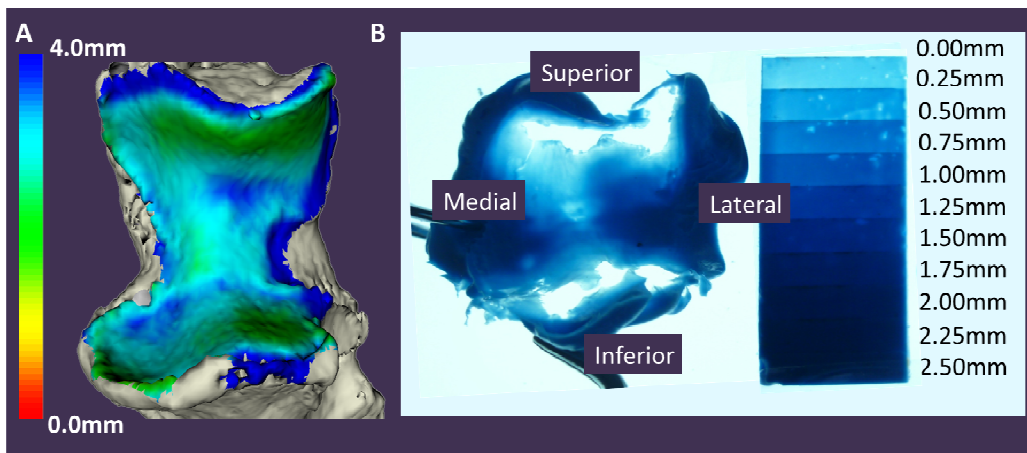
Figure 4.16: Proximity Mapping Validation using Experimental Casting
The proximity maps are shown and compared to the experimental cast. The overall qualitative similarity of the cast and proximity map was assessed and used to validate the implementation of the proximity mapping technique with the registration developed in this study to examine joint surface interactions.
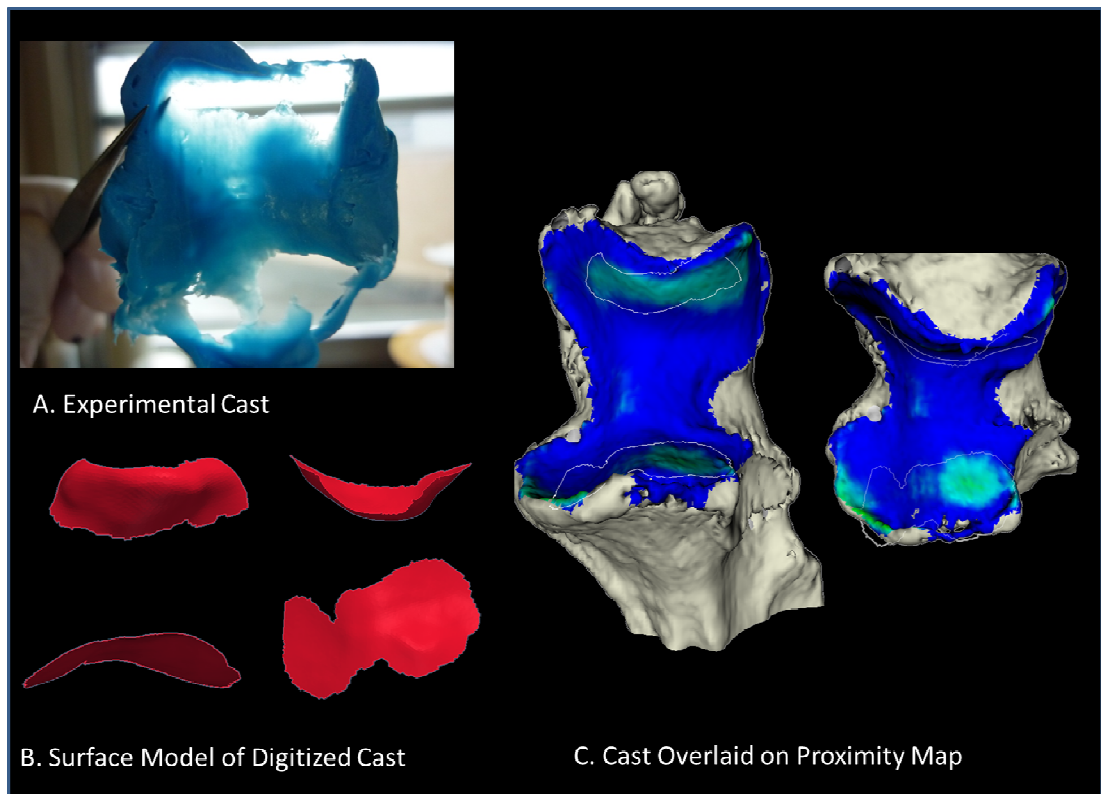
Figure 4.17: Comparison of Experimental Cast and Proximity Map
A) Experimental Cast
B) The vacant regions of the cast, corresponding to regions of joint contact were digitized using a tracked stylus. A surface model was created from this point cloud. An edge extraction filter was used to obtain the perimeter of this digitized surface. A superior view of the cast reconstruction is shown on the left and an inferior view is shown on the right. C) The digitized cast was overlaid onto a proximity map showing the surface area on the ulna. The threshold used to generate this map is 2.87mm as measured from the pre-operative CT. There was a 17.36% difference between the experimental cast digitization and the surface area obtained from the computational method.

4.4 Discussion

In vivo and *in vitro* studies have been conducted to elucidate the effect of joint alignment on resulting joint mechanics. *In vivo* studies, while are able to investigate *in vivo* joint mechanics in patients undergoing physiologic motion, they are either limited to a truncated range of motion (Anderst and Tashman, 2003; Boyer *et al.*, 2008; Li *et al.*, 2008), or involve patients undergoing repeated motion as is the case when using cine MRI (Sheehan *et al.*, 1998). Surface markers can be attached to patients undergoing motion in gait laboratories and when using various stereometric analysis systems (Bey *et al.*, 2006; Bey *et al.*, 2008b; Boyer *et al.*, 2008; Kedgley and Jenkyn, 2009). However, surface markers introduce skin artifacts and therefore limit the accuracy of such techniques. Recently, markerless radiostereometric analysis (RSA) techniques have been developed, but these techniques are also limited to a small field of view and therefore range of motion, and additionally yield data sets which are tedious and time consuming to analyze (Bey *et al.*, 2006; Bey *et al.*, 2008a; Bey *et al.*, 2008b). *In vitro* studies take place in a controlled environment and typically investigate joint mechanics using simplified non-physiologic loading protocols (Brechter and Powers, 2002; Eckstein *et al.*, 1995; Fischer *et al.*, 2001). In general, any static simplified motion does not inherently represent true physiologic motion because dynamic stabilizers and inertial effects are ignored. Therefore, new techniques must be developed to accurately examine joint surface interactions in joints undergoing large range of motions in continuous physiologic motion.

The registration technique developed in this study allowed the position and orientation of the two rigid bodies (reconstructed 3D bone models of the humerus and ulna obtained from CT) to be rendered according to the tracked continuous motion generated by a repeatable elbow motion simulator. Using this approach, any frame of tracked motion can be isolated, registered and rendered using the bony surfaces and landmark fiducials. Therefore, it is possible to investigate the effect of bony and soft tissue injuries on joint congruency and ultimately to evaluate the efficacy of various reconstructive procedures in restoring joint tracking to that of the intact, uninjured state. Visualization of mal-alignment caused by various injuries/traumatic events can predict the location across the articulating surface where excess cartilage wear might occur.

In this study, intact motion of a single cadaveric specimen undergoing simulated elbow flexion was examined to show the utility of this current technique. These results may not be representative of the typical ulnohumeral joint congruency patterns of a larger population.

In the registration phantom, the fiducial configuration was maintained while the threshold value was altered. The target registration error was not used in this experiment to comment on the accuracy of the overall registration. The experimental conditions as well as the fiducial configuration was very different from the experiment application of this registration in use with the simulator. The threshold selection used to reconstruct the fiducial markers appears to have a small effect on the overall fiducial or target registration values measured. This makes logical sense in that the intensity would only be created spheres around a concentric centre. Finally, the repeatability of the localization of the

fiducial markers in the laboratory setting in this experiment is very good which is not surprising given the accuracy of the optical tracking system and ease of use of the calibrated cupped-stylus.

The mean fiducial registration error was less than 0.30mm. Fiducial registration error is used to ensure that the experimental set up and data acquisition software and tracking are accurately collecting data. In this study, the location of the fiducials were accurately identified and corresponded to the CT fiducial markers. Additionally, the fiducials were properly segmented and sphere-fitted in the CT model and corresponded to the digitized fiducial markers in the laboratory. The overall target registration error for this study for the humerus and ulna was less than 1mm. Since the average joint space found in this elbow was approximately 2.87mm, we believe that a registration error of 1mm is acceptable when evaluating a registration algorithm.

The fiducial configuration of the humerus was in general very consistent between specimens and this was reflected in the standard deviation of the measured distance between the target fiducials and the geometric centroids. This was partially due to experimental factors. The optical position sensor for the humerus was located on the simulator. Therefore the positional relationship between the sensor and the rigid body cannot be changed. As a result, at the end of the experimental protocol, the fiducials had to be fixated to the humerus while remaining attached to the simulator such that only certain locations on the humerus could be accessed to attach a fiducial marker. Additionally, the humerus is a somewhat symmetrical bone lending well to medial and lateral landmarks to be used as reference points to attach the fiducial markers. Thus, the

overall fiducial configuration remained relatively consistent between specimens. The target registration error for specimens 2 and 3 was lower than that of specimens 1 and 4. This could be potentially because the centroid of the latter two specimens was somewhat lateral to the articulation and could partially explain the increase in the target registration error.

The fiducial configuration for the ulna was somewhat variable. A fiducial marker was always attached near the olecranon process. However the location of the other three fiducial markers varied. The target registration error of specimen 2 and 3 is lower than specimen 1 and 4. However, it appears as though the fiducial configurations in these latter specimens are somewhat co-linear. The configurations of specimens 2 and 3 have two fiducial markers in one plane and two fiducial markers in a roughly orthogonal plane. This could perhaps cause a decrease in the overall accuracy in the registration and should be avoided in future applications of the technique.

Considering the distance measured in this study between the centroid of the fiducial configuration and the target fiducial, in future applications of this registration, the fiducial configuration should be adjusted to minimize this distance.

The target registration error for the humerus was less than that of the ulna. During simulation, the ulna tracks around a stationary humerus. The tracking accuracy of the optical tracking system is anisotropic with the highest error found in the axis perpendicular to the camera (difference in tracking accuracy of 0.05mm between in-plane and out of plane directions). The ulna, as it tracks around the humerus, moves in the plane perpendicular to the camera as well as in-plane, and this might reduce the overall

registration accuracy of the ulna compared to the stationary humerus. This may explain why there is a discrepancy in the registration error found between the humerus and ulna. Additionally, during the post-hoc kinematic analysis used to generate the positional transformation matrices of the humerus and ulna, the relationship of the ulna is examined with respect to the humerus. Therefore any errors in the tracking of the two rigid bodies are compounded in this transformation reducing the registration accuracy of the ulna to be lower than the humerus.

Table 4.2 compares the registration accuracy values reported in previous studies (Fischer *et al.*, 2001; McDonald *et al.*, 2007; Sadowsky *et al.*, 2002; Sugano *et al.*, 2001) to the results of this current study. Sadowsky *et al.* used paired-point registration and obtained registration values less than 0.5mm (Sadowsky *et al.*, 2002). However, this study used a simplified phantom. This level of accuracy might be difficult to achieve in an experimental protocol examining bony surfaces with more complex geometries. In this current study, it was difficult to position the fiducials such that the centroid of the configuration corresponded to the articulation because the joint (area of interest) is located at the end of the long bones. Surface-based registration was employed in several of these studies, but with accuracy values lower than that of the current study. The use of surface-based registration is essential when using non-invasive approaches for registration, but has insufficient accuracy to examine joint articular tracking as reported in this *in vitro* study (Sadowsky *et al.*, 2002; Sugano *et al.*, 2001). In order to achieve the level of accuracy of the current study, a large region of the bony surface would be require for the registration making this surface-based technique also invasive.

Author	Type of Registration	Anatomy	TRE(mm)
Lalone et al.	*Paired-Point (external Landmarks)*	*Elbow*	*Humerus: 0.24± 0.09* *Ulna: 0.89± 0.30*
Sugano et al.	Surfaced Based	Hip	Pelvis: 1.2 Femur:1.4
McDonald et al.	Paired-Point(anatomical landmarks) Surfaced-based	Distal Humerus	1.9 ± 1.0 0.8± 0.3
Fischer et al.	Surface-based	Forearm	0.22
Sadowsky et al.	Paired-Point(fiducial landmarks)	Phantom	0.51 ±0.29 (10 fiducials) 0.55±0.22 (5 fiducials)

Table 4.2: Comparison of Registration Error
Accuracy values for previously developed registration techniques employing fiducial registration.

The implementation of the inter-bone distance algorithm was validated using the experimental casting approach at a single static angle of flexion. The overlaid regions of the cast on the proximity map show good correspondence. For this validation, the computational method overestimated the contact area by 17.35%. Digitizing the vacant regions of the cast is error prone because it is tedious and difficult to define the boundary of the contact region on the cast. There are regions on the cast that are not entirely vacant, but are 'thin' regions corresponding to regions that are in 'close' but not 'full' contact. Additionally, the vacant regions were digitized on the articular surface of the ulna; however, the proximity map is shown on the subchondral bone of the ulna model. Therefore, this could introduce a shift in the location of the contact as well as explain why in some regions it appears as though the cast outline is on the edge of the bone. Finally, a single value of 2.87mm was used as a threshold to joint space. However, regional variations in the thickness of the cartilage, especially near the transverse ridge cause the thickness of the overall joint space to change. Therefore, assuming a uniform joint space may introduce error into the calculated contact area.

The techniques employed in the current study are limited by the accuracy of the registration. Registration employing both point-based and surface-based registration can significantly increase the accuracy of the registration compared to using landmark based or surface based registrations in isolation (Maurer *et al.*, 1996). Therefore, future applications of this registration approach will include some surface digitizations to increase its accuracy. Additionally, refined approaches will be examined to attach the fiducial markers as the current technique is both time-consuming and tedious as it

requires complete disarticulation and dissection of the bones. For example, implanting metallic (tantalum/brass beads) (0.5-1.5mm in diameter) may reduce the overall time required to fixate the fiducial markers and ensure that the fiducials themselves will not be deflected during transportation between the laboratory and the CT suite. Currently, the registration and data analysis occur post-experimentation. Therefore, future directions using this technique will aim to improve this technique such that real time examination of the articular surface interactions can be achieved.

A novel approach for examining joint articular tracking has been developed and validated in this study. The accuracy of this registration was also assessed under experimental conditions similar to the actual *in vitro* experimental protocol. This technique is accurate and robust and can be applied to any joint undergoing tracked simulated motion *in vitro*. This technique can now be used to examine the effect of various injuries and resulting mal-alignment on the joint cartilage surface and therefore can be used to develop and evaluate new surgical techniques and rehabilitation (Chapter 5).

4.5   References

Anderst, W.J. and Tashman, S. (2003) A method to estimate *in vivo* dynamic articular surface interaction. *J Biomech.* 36[9], 1291-1299.

Besl PJ and McKay ND . (1992) A Method for Registration of 3-D Shapes. *IEEE Transactions on Pattern Analysis and Machine Intelligence* 14, 239-256.

Bey, M.J., Kline, S.K., Tashman, S., and Zauel, R. (2008a) Accuracy of biplane x-ray imaging combined with model-based tracking for measuring *in vivo* patellofemoral joint motion. *J.Orthop.Surg.Res.* 3, 38.

Bey, M.J., Kline, S.K., Zauel, R., Lock, T.R., and Kolowich, P.A. (2008b) Measuring dynamic *in vivo* glenohumeral joint kinematics: technique and preliminary results. *J Biomech.* 41[3], 711-714.

Bey, M.J., Zauel, R., Brock, S.K., and Tashman, S. (2006) Validation of a new model-based tracking technique for measuring three-dimensional, *in vivo* glenohumeral joint kinematics. *J.Biomech.Eng* 128[4], 604-609.

Boyer, P.J., Massimini, D.F., Gill, T.J., Papannagari, R., Stewart, S.L., Warner, J.P., and Li, G. (2008) *In vivo* articular cartilage contact at the glenohumeral joint: preliminary report. *J.Orthop.Sci.* 13[4], 359-365.

Brechter, J.H. and Powers, C.M. (2002) Patellofemoral joint stress during stair ascent and descent in persons with and without patellofemoral pain. *Gait.Posture.* 16[2], 115-123.

Eckstein, F., Lohe, F., Hillebrand, S., Bergmann, M., Schulte, E., Milz, S., and Putz, R. (1995) Morphomechanics of the humero-ulnar joint: I. Joint space width and contact areas as a function of load and flexion angle. *Anat.Rec.* 243[3], 318-326.

Felson, D.T., Lawrence, R.C., Dieppe, P.A., Hirsch, R., Helmick, C.G., Jordan, J.M., Kington, R.S., Lane, N.E., Nevitt, M.C., Zhang, Y., Sowers, M., McAlindon, T., Spector, T.D., Poole, A.R., Yanovski, S.Z., Ateshian, G., Sharma, L., Buckwalter, J.A., Brandt, K.D., and Fries, J.F. (2000) Osteoarthritis: new insights. Part 1: the disease and its risk factors. *Ann.Intern.Med.* 133[8], 635-646.

Ferreira, L.M., Johnson, J.A., and King, G.J. (2010) Development of an active elbow flexion simulator to evaluate joint kinematics with the humerus in the horizontal position. *J.Biomech.* 43[11], 2114-2119.

Fischer, K.J., Manson, T.T., Pfaeffle, H.J., Tomaino, M.M., and Woo, S.L. (2001) A method for measuring joint kinematics designed for accurate registration of kinematic data to models constructed from CT data. *J.Biomech.* 34[3], 377-383.

Fitzpatrick, J.M., West, J.B., and Maurer, C.R., Jr. (1998) Predicting error in rigid-body point-based registration. *IEEE Trans.Med.Imaging* 17[5], 694-702.

Hunter, D.J., Sharma, L., and Skaife, T. (2009) Alignment and osteoarthritis of the knee. *J.Bone Joint Surg.Am.* 91 Suppl 1, 85-89.

Hunter, D.J., Zhang, Y., Niu, J., Tu, X., Amin, S., Goggins, J., Lavalley, M., Guermazi, A., Gale, D., and Felson, D.T. (2005) Structural factors associated with malalignment in knee osteoarthritis: the Boston osteoarthritis knee study. *J.Rheumatol.* 32[11], 2192-2199.

Kedgley, A.E. and Jenkyn, T.R. (2009) RSA calibration accuracy of a fluoroscopy-based system using nonorthogonal images for measuring functional kinematics. *Med.Phys.* 36[7], 3176-3180.

Li, G., Wan, L., and Kozanek, M. (2008) Determination of real-time *in vivo* cartilage contact deformation in the ankle joint. *J Biomech.* 41[1], 128-136.

Maurer, C.R., Aboutanos, G.B., Dawant, B.M., Maciunas, R.J., and Fitzpatrick, J.M. (1996) Registration of 3-D images using weighted geometrical features. *IEEE Trans.Med.Imaging* 15[6], 836-849.

McDonald, C.P., Brownhill, J.R., King, G.J., Johnson, J.A., and Peters, T.M. (2007) A comparison of registration techniques for computer- and image-assisted elbow surgery. *Comput.Aided Surg.* 12[4], 208-214.

McKee, M.D., Bowden, S.H., King, G.J., Patterson, S.D., Jupiter, J.B., Bamberger, H.B., and Paksima, N. (1998) Management of recurrent, complex instability of the elbow with a hinged external fixator. *J.Bone Joint Surg.Br.* 80[6], 1031-1036.

Ring, D., Jupiter, J.B., and Zilberfarb, J. (2002) Posterior dislocation of the elbow with fractures of the radial head and coronoid. *J.Bone Joint Surg.Am.* 84-A[4], 547-551.

Sadowsky, O., Yaniv, Z., and Joskowicz, L. (2002) Comparative *in vitro* study of contact- and image-based rigid registration for computer-aided surgery. *Comput.Aided Surg.* 7[4], 223-236.

Schroeder W, Martin K, and Lorensen B . (1998) The Visualization Toolkit. Upper Saddle River, NJ, Prentice Hall.

Sheehan, F.T., Zajac, F.E., and Drace, J.E. (1998) Using cine phase contrast magnetic resonance imaging to non-invasively study *in vivo* knee dynamics. *J.Biomech.* 31[1], 21-26.

Sugano, N., Sasama, T., Sato, Y., Nakajima, Y., Nishii, T., Yonenobu, K., Tamura, S., and Ochi, T. (2001) Accuracy evaluation of surface-based registration methods in a computer navigation system for hip surgery performed through a posterolateral approach. *Comput.Aided Surg.* 6[4], 195-203.

Van de Velde, S.K., Bingham, J.T., Hosseini, A., Kozanek, M., DeFrate, L.E., Gill, T.J., and Li, G. (2009) Increased tibiofemoral cartilage contact deformation in patients with anterior cruciate ligament deficiency. *Arthritis Rheum.* 60[12], 3693-3702.

West, J.B., Fitzpatrick, J.M., Toms, S.A., Maurer, C.R., Jr., and Maciunas, R.J. (2001) Fiducial point placement and the accuracy of point-based, rigid body registration. *Neurosurgery* 48[4], 810-816.

Chapter 5 – Utility of an Image-Based Technique to Detect Changes in Joint Congruency Following Simulated Joint Injury and Repair: An *In vitro* Study of the Elbow

OVERVIEW

Chapter 4 described the implementation of the inter-bone distance algorithm (Chapter 2) to the registration technique developed in Chapter 3. The accuracy of this technique was assessed and validated. The objective of this chapter was to demonstrate the utility of the congruency mapping technique in an in vitro experimental setting, investigating a clinically relevant scenario. A model of collateral ligament injury and repair was employed in 5 cadaveric elbows using a previously developed elbow motion simulator. As well, the effect of muscle stabilizers on elbow joint stability was examined using both traditionally employed kinematic metric as well as the newly developed joint congruency technique.[4]

5.1 Introduction

Osteoarthritis commonly occurs as a result of a traumatic event to the articulation, however, as previously described in Chapter 4, the mechanism and sequence of this interaction is not well understood (Buckwalter and Lane, 1997; Felson *et al.*, 2000; Honkonen, 1995; Hunter *et al.*, 2005; Hunter *et al.*, 2009). Changes in the overall alignment of the joint or joint congruency are thought to be an important cause of long term cartilage injury (Beveridge *et al.*, 2011). Chapter 4 described a technique which can

---

[4]A version of this has been submitted for publication to Clinical Biomechanics. Lalone EA, Giles JW, Alolabi B, Peters TM, Johnson JA, King GJW. Utility of an image-based technique to detect changes in joint congruency following simulated joint injury and repair: an *in vitro* study of the elbow. Submitted to Journal of Biomechanics July 1, 2012.

be used to quantify joint congruency that combines a proximity mapping technique and a rigid registration technique to render 3D bone reconstructions undergoing simulated joint motion. Using the technique, overall joint congruency can be visualized and quantified for the whole articular surface and within sub-regions. Amongst the many applications of such a technique, would be the investigation of functional anatomy, providing assistance in intra-operative joint alignment and to investigate the etiology of various joint articular diseases following injury. The primary objective of this chapter was to employ this technique to investigate the effect of a common surgical repair on resulting joint congruency.

We chose an elbow ligament injury, repair and rehabilitation model to evaluate the utility of the joint congruency technique *in vitro*. Dislocations of the elbow are common, most frequently occurring as a result of a fall or more severe impact. Disruption of the anterior and posterior capsules as well as the medial and lateral collateral ligaments (MCL and LCL) has been documented following dislocation in a number of studies (Eygendaal *et al.*, 2000; Josefsson *et al.*, 1987; O'Driscoll *et al.*, 1992; Pollock *et al.*, 2009). In the majority of clinical situations, patients with elbow dislocations are treated non-operatively with a good short-term outcome following a closed reduction and early motion. While residual clinical instability is uncommon, the ligament healing is often incomplete resulting in slightly increased elbow laxity (Eygendaal *et al.*, 2000). Previous *in vitro* kinematic studies examining collateral ligament repair have reported restoration of elbow stability following surgical repair of the collateral ligaments. Despite these findings however, post-traumatic arthritis has been reported in up to 50% of patients

following dislocations at long-term follow-up (Eygendaal *et al.*, 2000; Josefsson *et al.*, 1984). The joint congruency mapping technique in this chapter was used to elucidate the relationship between ligament repair surgery and rehabilitation on subsequent joint alignment and overall congruency as it relates to the development of OA. The hypothesis was that while traditional techniques used to investigate elbow instability were able to detect gross changes in the motion pathways of the joint, they would not be sufficiently sensitive to detect more subtle changes within the joint, which may have long term implications with respect to the potential development of elbow arthritis.

The relationship between altered kinematics due to residual ligament insufficiency and joint congruency was examined in the elbow. Additionally, the effect of muscle stabilizers was examined in both active and passive elbow flexion using kinematics to detect changes in the motion pathways, and joint congruency.

5.2   Methods

5.2.1   SPECIMEN PREPARATION AND EXPERIMENTAL PROTOCOL

Five fresh-frozen upper extremities, sectioned mid-humerus were employed (76.6 ± 3.0yrs, Male, Left). A pre-testing x-ray computed tomography (CT) scan was acquired for each specimen and used to ensure each specimen had no existing joint pathologies (64-slice scanner, GE Discovery CT750 HD, Waukesha, WI). Approximately 1000 slices were acquired for each specimen with a 512x512 reconstruction matrix (292mAs, 120 kVp). The voxel dimensions were approximately 0.621x0.621x0.625mm.

Each specimen was thawed at room temperature for 20 hours. The specimen was clamped into the mount of a previously developed elbow motion simulator (Ferreira *et al.*, 2010). The tendons of the relevant muscles involved in pronated elbow flexion/extension were isolated and attached to servomotors/pneumatic actuators as described in Chapter 4 (Section 4.2.1). Ligament guides were secured to the medial and lateral epicondyles to guide the pronator teres/wrist flexors and the wrist extensors to achieve native muscle alignments on the medial and lateral sides respectively. Additionally, a ligament guide was positioned on the supracondylar ridge to guide the brachioradialis. Two (3D) optical position sensors were attached to the base of the simulator adjacent to the mounted humerus as well as directly onto the ulna near the distal end of the bone (dorsal side) using a bone-fixated mounting pedestal as described in Chapter 4 (Section 4.2.1).

The elbow motion simulator was positioned in the valgus gravity orientation, with the medial epicondyle of the elbow directed upward and the long axis of the humerus parallel to the ground. Ulnohumeral joint congruency was examined in this study. With the arm in this position, the radiohumeral joint acts as a bony stabilizer to resist valgus laxity, while the ulnohumeral joint tends tension the medial collateral ligament repair and gap open. As such, the valgus gravity dependent position is a provocative model to examine the effect of ligament deficiency on ulnohumeral joint stability. Additionally, previous studies have investigated the role of forearm rotation on elbow joint stability and determined that supination stabilizes the MCL deficient elbow (Armstrong *et al.*, 2000). As such, pronated elbow flexion was employed as the most provocative with the arm in

the valgus orientation to detect changes in joint biomechanics after simulated MCL injury and repair.

Active flexion was performed using previously developed muscle loading protocols which attempt to maintain constant velocity elbow flexion (Ferreira *et al.*, 2010). Due to technical difficulties in data collection during the first specimen, the active data was in total only available in four of the five tested specimens. Tone loading of 10N was applied to the wrist flexors and extensors to stabilize the wrist. Passive elbow flexion was achieved in all five specimens by the experimenter guiding the forearm throughout the arc of flexion, while maintaining the forearm in pronation. The elbow was first tested in the intact scenario during pronated, active and passive elbow flexion. As a model of residual mild elbow instability, the effect of collateral ligament injury and repair (MCL/LCL) was investigated. The anterior bundle of the MCL was released from its humeral origin, and the LCL was released from the lateral epicondyle and then repaired using a transosseous suture repair technique described previously (Fraser *et al.*, 2008; Pichora *et al.*, 2007). For the collateral ligament repairs, the elbow was positioned at 90° of elbow flexion in the valgus (MCL) and varus (LCL) gravity dependent position with the wrist in neutral rotation. The flexor-pronator mass was carefully sectioned from the MCL as was the extensor muscle mass from the LCL. Both ligaments were then released from their humeral origins. Two diverging transosseous tunnels were created using a 2mm drill bit on each epicondyle. On the medial side, the first tunnel was positioned on the anterior-inferior aspect of the epicondyle at the centre of the axis of motion of the elbow and exited the posterior aspect of the medial supracondylar ridge. The second

tunnel has the same starting point, but exited the anterior aspect of the supracondylar ridge. Similar tunnels were drilled from the lateral side, with a common origin located at the axis of motion of the elbow (capitellum). Sutures (#2 Hi-Fi ulta-high-molecular-weight polyethylene, ConMed, Linvatec, Largo, FL) were secured to each collateral ligament using a locking Krackow technique and the remaining ends were passed through the diverging bone tunnels, tied through a loop and then attached to a pneumatic actuator to provide accurate tensioning of the ligament. For this study, both the MCL and LCL were tensioned to 20N (with the arm in the dependent position and the elbow at 90° of flexion, neutral rotation) using the actuators and then attached to a clamp mounted to the base of the motion simulator. This magnitude of tension was selected based on the findings of previous studies (Fraser *et al.*, 2008; Pichora *et al.*, 2007). Active and passive elbow flexion with the arm in the valgus orientation and the forearm in pronation was then repeated with the ligaments repaired.

Subsequent to testing, each specimen was denuded. Anatomical landmarks were digitized to create clinically relevant coordinate systems using a calibrated tracked stylus on the humerus and ulna as previously described in Chapter 3 (Section 3.2.6). On the distal humerus, the capitellum surface was digitized (and sphere-fitted) and the trochlea groove was digitized (and circle-fit). A trace around the circumference of the distal shaft was also digitized and circle-fitted. On the ulna, the guiding ridge of the greater sigmoid notch was digitized (circle-fitted) as well as points on the medial side of the greater sigmoid notch and distal ulnar styloid. These points were used to create vectors including the flexion/extension axis defined by the centre of the capitellum and trochlea as well as

proximal and anterior vectors creating the 3D coordinate system. Additionally, four delrin spherical 19mm fiducial markers (two proximal (medial and lateral) and two distal (medial and lateral) were attached to the denuded humerus and ulna in previously described configurations and digitized using a calibrated-cupped stylus to record the position of each fiducial marker with respect to the bone optical sensor (humerus and ulna separately) (Section 4.2.1.4).

5.2.2   KINEMATIC DATA ANALYSIS

Motion of the ulna and stationary humerus was recorded using an optical tracking system throughout continuous elbow flexion (0-120°) (Optotrak Certus®, NDI, Waterloo, ON, Canada). To maintain the accuracy of the optical tracking, (in-plane of 0.1mm and perpendicular to the camera 0.15mm) a direct line of sight between the camera and the position sensors during all motion recordings was maintained and kept within 2.5m.

Valgus instability of a collateral ligament deficient elbow is maximal between 70-90° (Eygendaal *et al.*, 2000); therefore kinematic motion of the ulna with respect to the humerus was examined by selecting frames of motion at 30°, 60° and 90°. Valgus angulation, which describes the angulation between the long axis of the humerus and that of the ulna, was measured for each angle of flexion as a measure of valgus instability.

5.2.3   LANDMARK REGISTRATION PROTOCOL

A second CT scan (post-testing) of the denuded humerus and ulna, with the 19mm delrin spherical fiducial markers attached, was acquired using the same scanning protocol as the initial pre-testing CT. The subchondral surface and cortex of the humerus and ulna from both pre-testing and post-testing CT scans were reconstructed using the Marching

Cubes Algorithm within VTK (Visualization Toolkit, Kitware, Clifton Park, NY)(Schroeder W *et al.*, 1998). Two dimensional slices were overlaid with the reconstructed model to ensure that a proper threshold was selected. The protocol employed was described in Chapter 2. The subchondral surface of the ulna from the pre-testing CT was segmented into four zones; medial and lateral coronoid (MC, LC) and medial and lateral olecranon (MO, LO). Note that the zone names in the study were changed to be more consistent with clinical terminology as this was a clinical study. The reconstructed humerus and ulna from the pre-testing scan, the segmented subchondral region of the humerus and ulna, as well as the four zones of the ulna were registered to the post-testing CT using the Iterative Closest Point (ICP) surface-based registration algorithm with three coarse points chosen for initial course alignment (Besl PJ and McKay ND, 1992). Additionally, 3D models of each fiducial marker were reconstructed and sphere-fit.

Paired-Point registration was employed to render the 3D models into their respective position based on the tracked data. This registration protocol employing homologous fiducial markers has been described previously in Chapter 3 (Section 3.2.5). Using the relationship between the fiducial and the bone tracker, and the transformation matrices describing the position and orientation of each bone during elbow flexion, the position of each fiducial was determined with respect to the camera for each frame of motion. This paired-point registration described the relationship between the CT coordinate system (which the bone models are in) and the camera coordinate system. This was used to then render the bone models into the camera coordinate system for each

frame of motion. The accuracy of the registration technique was described in Chapter 4 (Section 4.3.1.1) by investigating target and fiducial registration error values (TRE: <0.88mm, FRE: <0.25mm).

5.2.4   DETERMINATION OF JOINT CONGRUENCY

To investigate the relative inter-bone distance and therefore overall joint congruency, the inter-bone distance algorithm described in Chapter 2 (Section 2.2.5) was employed. This algorithm uses points on the reconstructed subchondral surfaces to find the minimum distance between the two opposing surfaces. Proximity maps are used to visually examine the relative inter-bone distances using colour mapping. Inter-bone distances described the distance between the two opposing subchondral bone surfaces. This distance corresponds to the cartilage thickness on the humerus and ulna *as well* as any spacing between the articulating surfaces. The purpose of this inter-bone distance algorithm is to examine the overall distribution of the joint space. Therefore, in this study, a maximal inter-bone distance of 4mm was used to identify 'regions of close proximity' and is shown as a maximum value on the colour-map scale. This 4mm magnitude is not to reflect solely the cartilage thickness (which is not homogeneous across the humerus or the ulna), but rather serves as a limit in the inter-bone distances and as a scale in the proximity maps. The rationale behind this was described in Chapter 2. Once again, four 'levels of proximity' were also measured by finding the surface area on the subchondral bone that was less than 0.5mm, less than 1.5mm, less than 2.5mm and less than 3.5mm inter-bone distance. The surface area within each level of proximity was measured for the

humeral and ulnar subchondral surface as well as for each zone on the ulna at 30°, 60° and 90° degrees of flexion in the intact and ligament repaired scenario.

In three of the five specimens, the two registered bone surfaces became overlapped due to the accuracy of the registration technique. The amount of overlap on average did not exceed 0.5mm and was consistent. For specimen 1, the overlapping region, when present, was on the medial side of the olecranon near the olecranon process. For specimen 2 the overlapping region occurred right adjacent to the coronoid process on the medial side and on the lateral olecranon facet for specimen 4 (Appendix G). These regions occur where the two bones are closest and have the least inter-bone distance. Therefore, it is not surprising that these regions of overlap would appear at the two major prominences of the ulna. To account for these regions of overlap, at each point on the humerus or ulna, the dot product was calculated to measure the between the vector of minimum distance and the normal vector of each point. If the surfaces were opposing, the angle between these vectors would be less than 90°. However, if the surfaces were overlapping, the angle between these two vectors would be greater than 90° and as such, they would be assigned a negative value. A list of measured inter-bone distances from all the points on the humerus and ulna were obtained using this algorithm from which the surface areas within each 'level of proximity' were determined. On the proximity map, all values less than 0mm, corresponding to regions of overlap were assigned red. As these overlapping regions appear where the two surfaces are closest in proximity, these red regions appear concentric with the actual regions of close proximity (Figure 5.1).
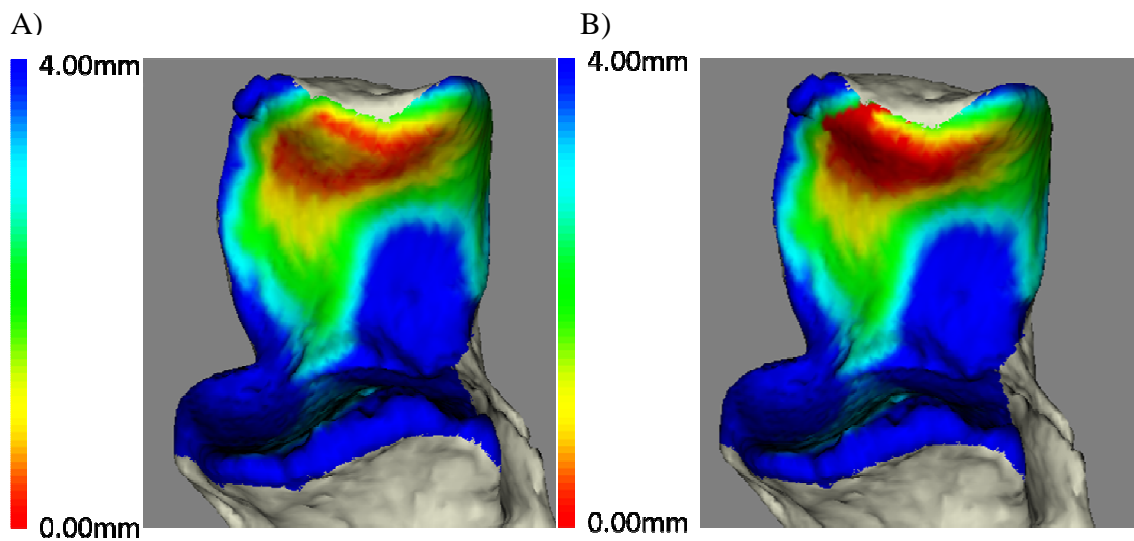
Figure 5.1: Overlap Regions
Negative values correspond to regions were the humerus and ulna overlapped. If these overlapped regions are not assigned negative values, they appear as positive values as shown in A. The proximity map indicates a 'ring' appearance with a central yellow region which is present due to overlap. The -1.00mm values and 1.00mm values both appear as yellow. Therefore, negative values were assigned to regions of bone overlap and the scale was then set to 0.00mm so that all overlapping regions appear as red.

5.2.5 STATISTICAL ANALYSIS

A repeated-measures analysis of variance test with a Bonferroni correction was used to detect statistical differences in the measured surface area for each level of proximity for the entire and zoned ulnar surface in the intact versus ligament repaired scenario. Additionally, this statistical test was used to evaluate differences between the medial and lateral zones in both ligament intact and repaired scenarios. The same statistical analysis was performed for the valgus angulation throughout elbow flexion in the intact and ligament repaired condition. To detect differences between active and passive trials, a repeated-measures analysis of variance test with a Bonferroni correction was used to compare active versus passive valgus angulation and joint proximity for the intact and repaired ligament scenario separately. Statistical significance was set at $p < 0.05$.

5.3 Results

5.3.1 ACTIVE/PASSIVE MOTION

Valgus angulation increased an average of $1.8\pm1.0°$ during passive compared to active elbow flexion for the intact ligament scenario (p=0.04) and increased $3.9\pm2.2°$ for the ligament repaired scenario (p=0.02) (Figure 5.2).
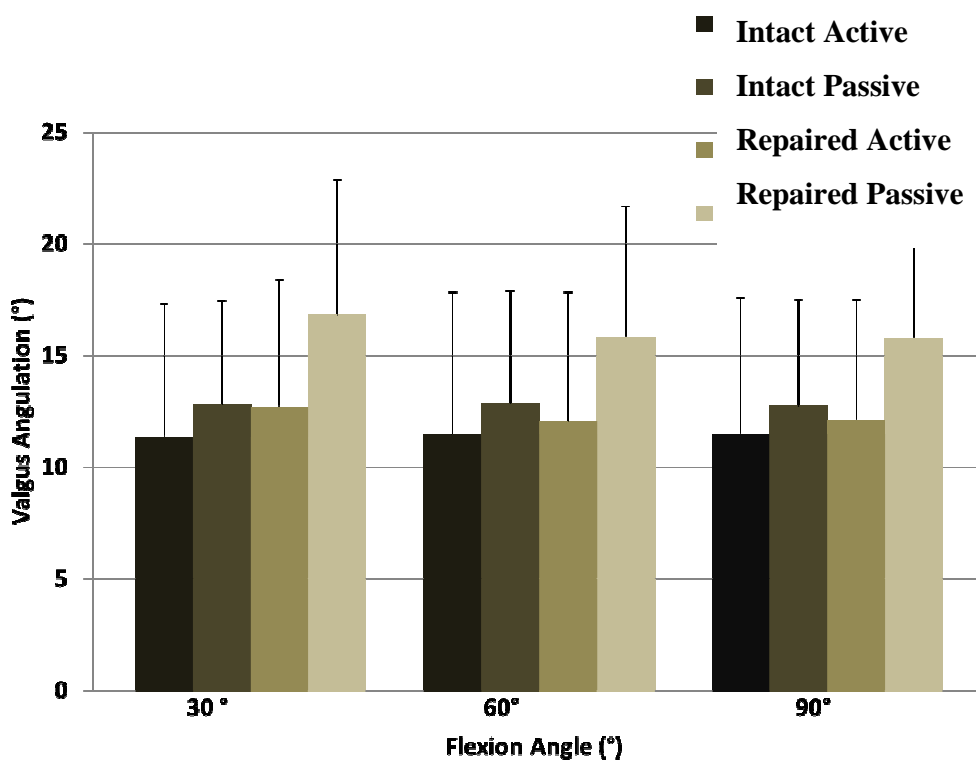
Figure 5.2: Valgus Angulation during Active and Passive Elbow Flexion
Valgus angulation is shown for the intact and ligament repaired scenarios. Valgus angulation increased an average of 1.8±1.0° during passive compared to active elbow flexion for the intact scenario (p=0.04) and increased 3.9±2.2° for the ligament repaired scenario (p=0.02) (n=4, mean+ 1SD).

Proximity maps for the intact elbow are shown for a representative specimen in active and passive elbow flexion at 30°, 60° and 90° of flexion in Figure 5.3. During passive elbow flexion, the joint is less reduced (larger inter-bone distances) as shown. Figure 5.4 shows the measured surface area having an inter-bone distance less than 3.5mm for active and passive elbow flexion in both intact and repaired ligament scenarios. The joint had a significantly larger surface area within close proximity on the subchondral bone during active versus passive flexion for the intact elbow at proximity less than 2.5mm (not shown) (p=0.02) and 3.5mm (p=0.004) (n=4). This means that in general, the joint is less reduced in passive than in active elbow flexion. Similarly, in the ligament repaired condition, significantly greater surface area was found for active versus passive flexion at proximity less than 2.5mm (not shown) (p=0.03) and 3.5mm of proximity (p=0.001). Overall joint congruency (<3.5mm) decreased 31.1±9.7% in passive elbow flexion for the intact elbow and 66.9±25.6% in passive flexion in the ligament repaired scenario relative to active motion. There was no effect of elbow flexion angle on valgus angulation or surface area when comparing active and passive elbow flexion (p>0.05).
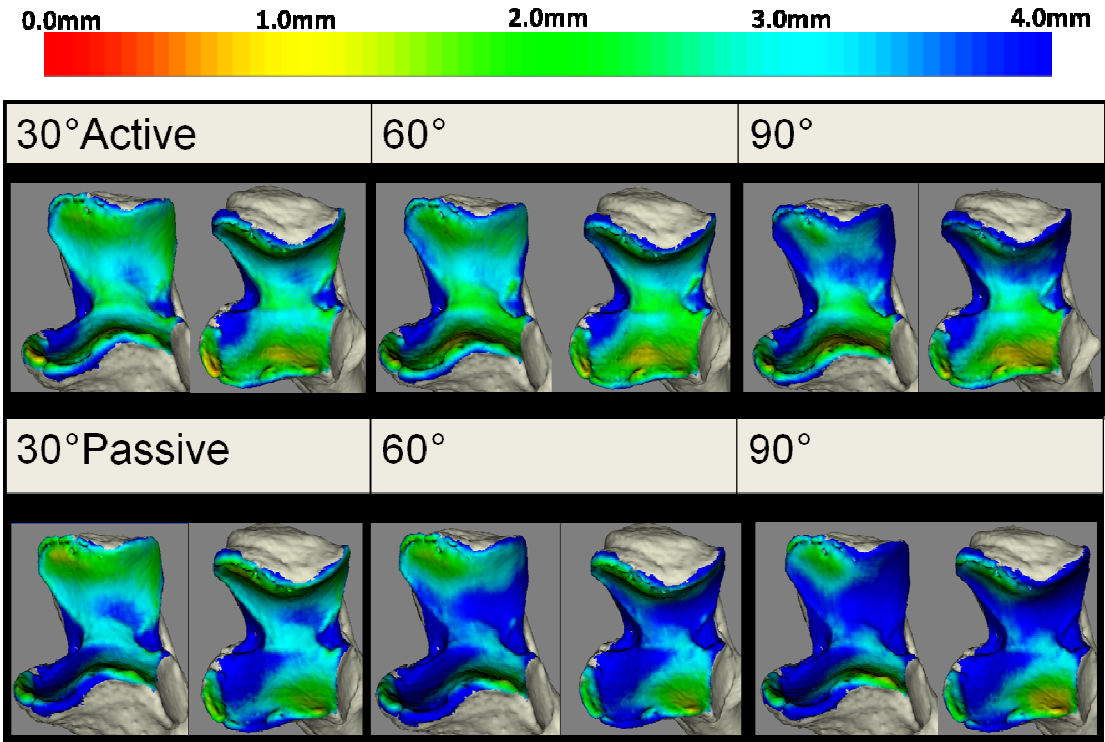
Figure 5.3: Ulnar Proximity Maps in the Intact Elbow during Active and Passive Flexion

Inter-bone distances are assigned a colour between red (0mm) and blue (4mm) to show overall joint inter-bone distances. Two views of the proximal ulna are shown to visualize the coronoid and olecranon regions.
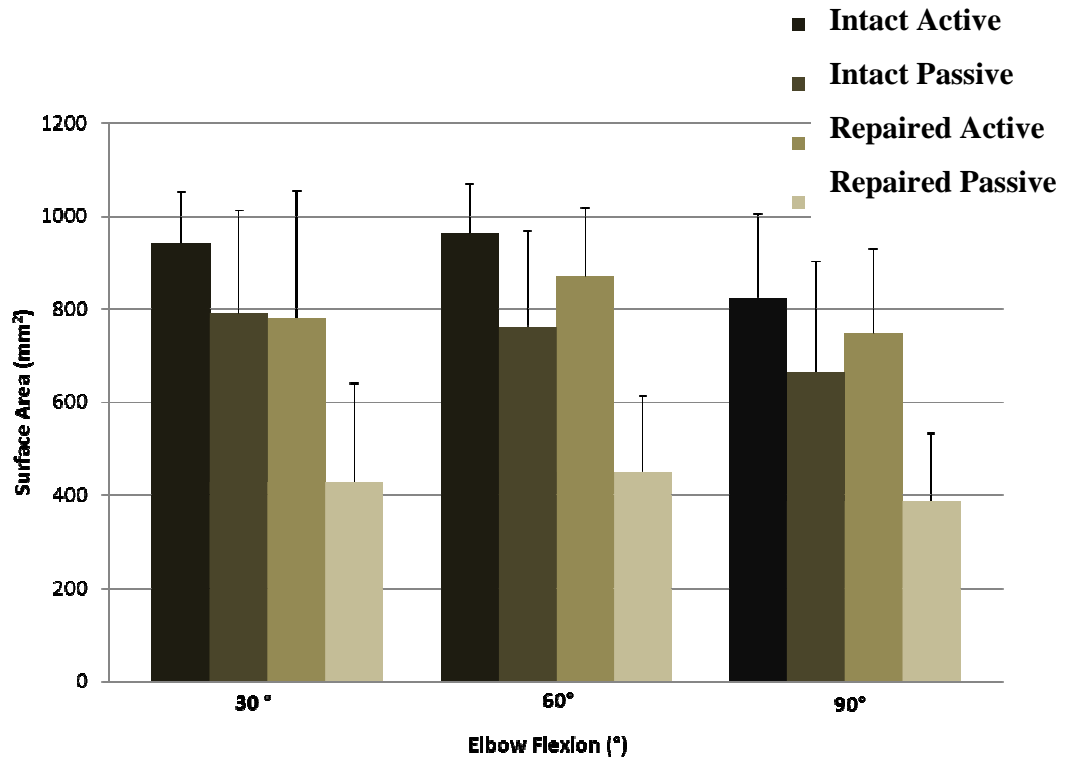
Figure 5.4: Surface Area during Active and Passive Elbow
Surface Area is shown for both the intact and ligament repaired scenarios (inter-bone distance <3.5mm) (n=4, mean +1SD). The joint had significantly larger surface area within close proximity on the subchondral bone during active versus passive flexion for the intact elbow (p=0.004) and ligament repaired scenario (p=0.001).

5.3.2   LIGAMENT STATE

Valgus angulation increased $1.2\pm1.0°$ after sectioning and repair of the collateral ligaments under active elbow flexion, however this was not statistically significant (p=0.09). Valgus angulation increased $3.3\pm2.2°$ after sectioning and repair of the collateral ligaments throughout passive elbow flexion (p=0.02). The difference in valgus angulation between intact and ligament repaired is shown in Figure 5.5 (active), and Figure 5.6 (passive) averaged for all specimens as well as for each specimen separately.
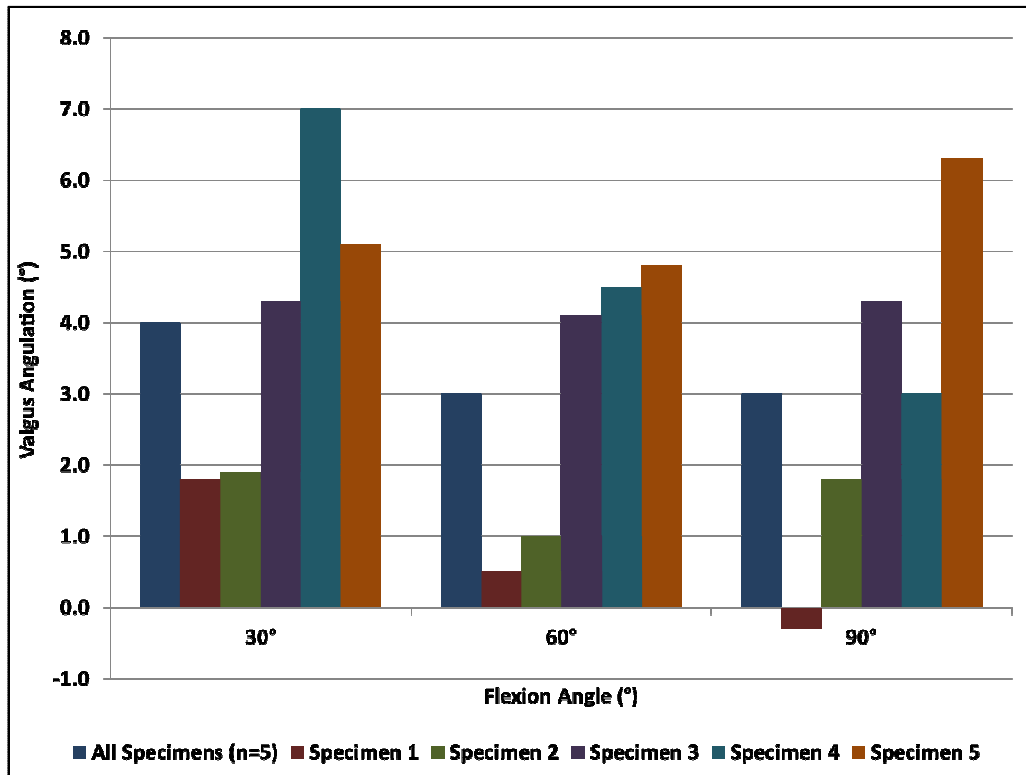
Figure 5.5: Difference in Valgus Angulation between Intact and Ligament Repaired
Values are shown for n=4 as well as for each specimen separately. Valgus angulation increases following ligament repair in all four specimens undergoing active elbow flexion (with the exception of 90°, Specimen 1).

Note: A positive value indicates an increase in valgus angulation subsequent to ligament repair.
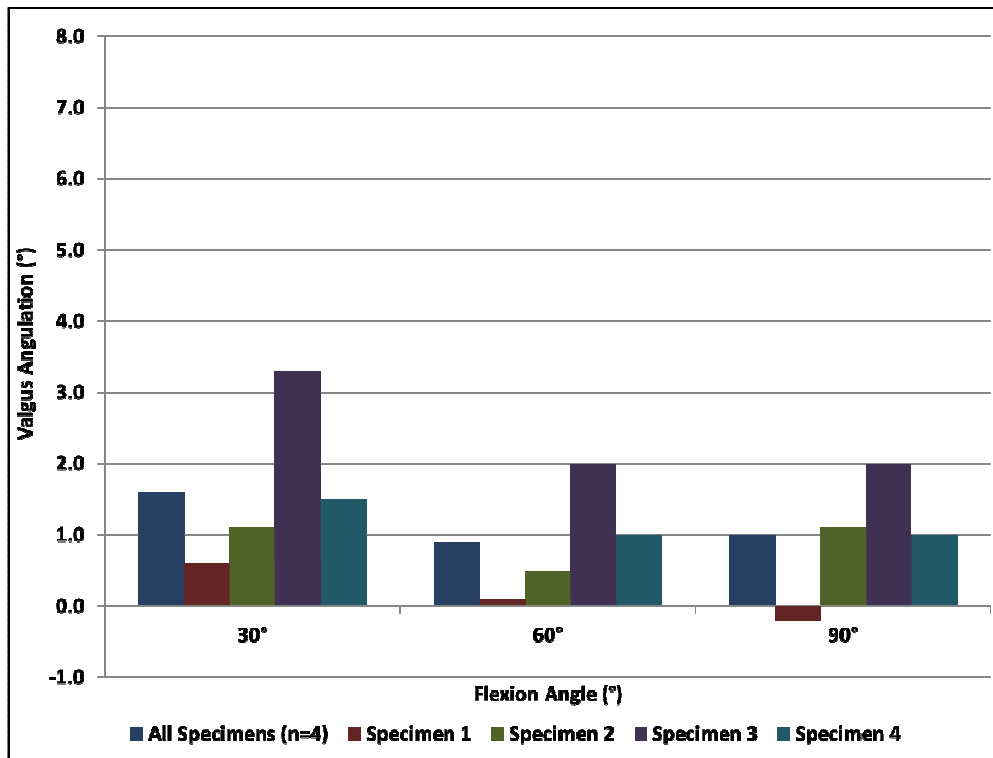
Figure 5.6: Difference in Valgus Angulation between Intact and Ligament Repaired
Valgus angulation increases following ligament repair in all five specimens (with the exception of 90°, Specimen 1) undergoing passive elbow flexion.

Note: A positive value indicates an increase in valgus angulation subsequent to ligament repair.

Small differences can be seen in the proximity maps shown in Figure 5.7 comparing the intact versus ligament repaired states during active motion. However, Figure 5.8 shows large differences in the shape and location of the regions of close proximity when comparing the two ligament states with the elbow undergoing passive elbow flexion. Overall joint congruency (<3.5mm) decreased 21.2±26.2% (p=0.14) in active elbow flexion and 57.9±39.9% (p=0.02) in passive flexion after ligament sectioning and repair.
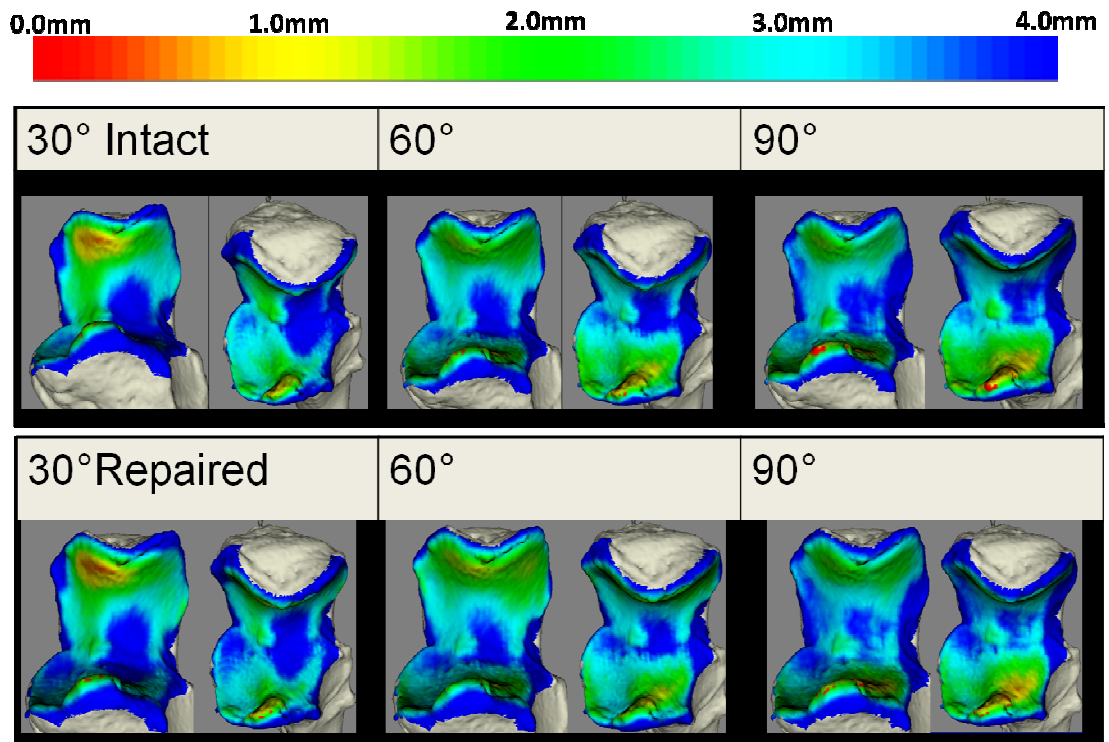
Figure 5.7: Proximity Maps with Intact and Repaired Ligaments during Active Flexion

Small differences exist between the intact and ligament repaired proximity maps when the elbow was undergoing simulated active elbow flexion.
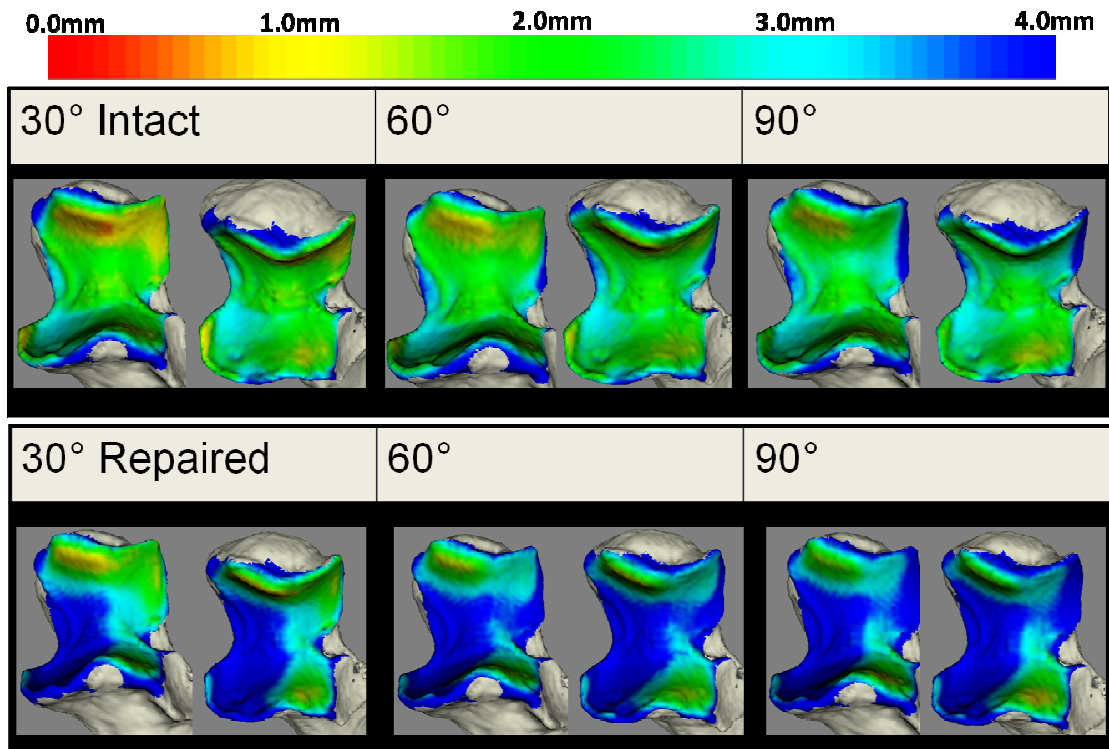
Figure 5.8: Proximity maps with Intact and Repaired Ligaments during Passive Flexion.
Large differences exist between the proximity maps of the elbow undergoing passive elbow flexion during the intact versus ligament repaired scenario.

In addition to ulnohumeral overall congruency, zonal joint congruency was examined to detect differences in the location of regions of close proximity before and after ligament repair. Only inter-bone distances less than 3.5mm, were examined for the zones. During active elbow flexion, the overall surface area on the proximal ulna was not statistically different between the intact and ligament repaired scenario as noted previously. However there were zonal differences as shown in Figure 5.9. The surface area within close proximity (<3.5mm) was higher on the medial side of the coronoid than the lateral region with both the ligaments intact (=0.02) and repaired (p=0.04). There were no differences in proximity between the medial and lateral zones of the olecranon (Intact: p=0.19, Repaired: p=0.13). The LC zone surface area increases throughout elbow flexion in both ligament scenarios while the LO zone decreases but no statistical effect of flexion was found. During passive elbow flexion with the ligaments intact, there was a significantly larger surface area on the medial side of the olecranon compared to the lateral side of the olecranon (p=0.006) (Figure 5.10). No significant differences were found between the medial and lateral side of the coronoid (p=0.24). However, after ligament sectioning and repair during passive motion there was a significant increase in surface area on the lateral coronoid region of the proximal ulna (p=0.04) and no medial and lateral differences on the olecranon region (p=0.2). Therefore, subsequent to ligament sectioning and repair the distribution of measured surface area shifted from the medial coronoid to the lateral coronoid and became balanced between the medial and lateral olecranon regions.
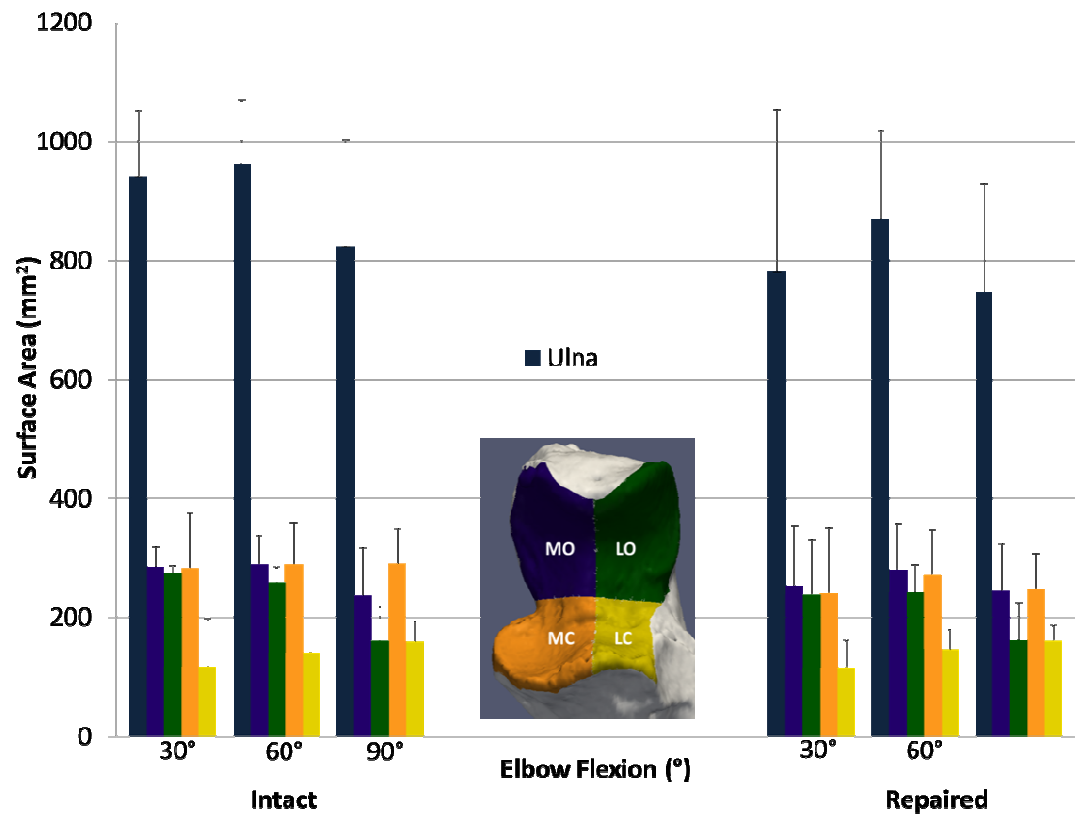
Figure 5.9: Surface Area values following Ligament Repair (Active Flexion)
Overall and zonal surface area are shown following ligament repair (inter-bone distance (<3.5mm) during active flexion (n=4, mean +1SD). The surface area within close proximity (<3.5mm) was higher on the medial side of the coronoid than the lateral region with both the ligaments intact (=0.02) and repaired (p=0.04). There were no differences in proximity between the medial and lateral zones of the olecranon (Intact: p=0.19, Repaired: p=0.13). The LC zone surface area increases throughout elbow flexion in both ligament scenarios while the LO zone decreases but no statistical effect of flexion was found.
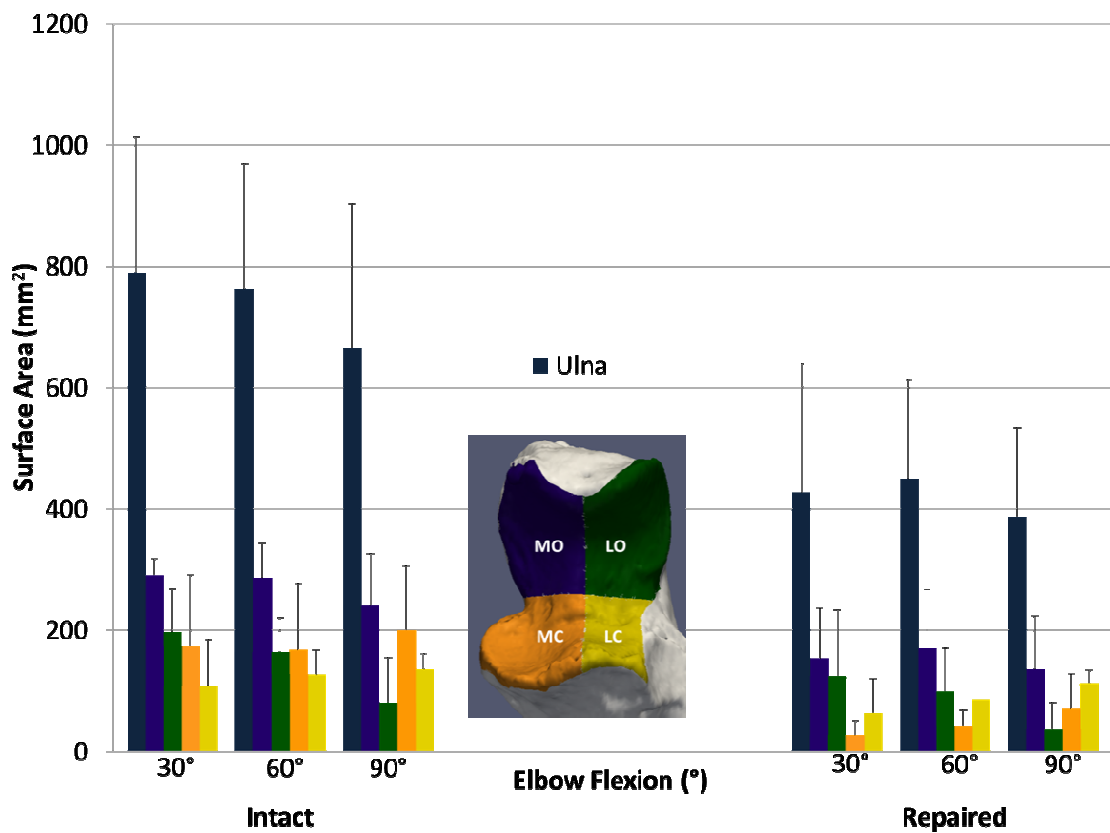
Figure 5.10: Surface Area values following Ligament Repair (Passive Flexion)
Overall and zonal surface area values following ligament repair (<3.5mm) during passive flexion (n=5, mean +1SD). During passive elbow flexion with the ligaments intact, there was a significantly larger surface area on the medial side of the olecranon compared to the lateral side of the olecranon (p=0.006)

To examine the differences in surface area values for the entire ulna and within each zone (inter-bone distance <3.5mm) percent differences were calculated for all specimens as well as individually. A graphical representation of these calculated percent differences is shown in Figure 5.11 for active and Figure 5.12 for passive elbow flexion. In general, the magnitude of decrease in joint congruency is larger during passive rather than active elbow flexion.

Surface areas (inter-bone distance < 3.5mm) were examined for each zone between the intact and ligament repaired scenario during active and passive flexion. There were no statistical differences between the intact and ligament repaired scenario for any zone when the elbow was undergoing active elbow flexion (MO: $p=0.497$, MC: $p=0.165$, LO: $p=0.165$, LC: $p=0.6780$). Statistical differences between intact and ligament repaired scenarios were found in the medial coronoid ($p=0.041$), medial olecranon ($p=0.018$) and lateral olecranon ($p=0.041$) zones when the elbow was undergoing passive elbow flexion (LC: $p=0.054$).

Figure 5.11: Differences between Intact and Ligament Repaired Joint Congruency (Active)

Difference between intact and ligament repaired joint congruency (inter-bone distance <3.5mm) during active elbow flexion.

Note: A negative number indicates that the surface area decreased from intact to ligament repair.
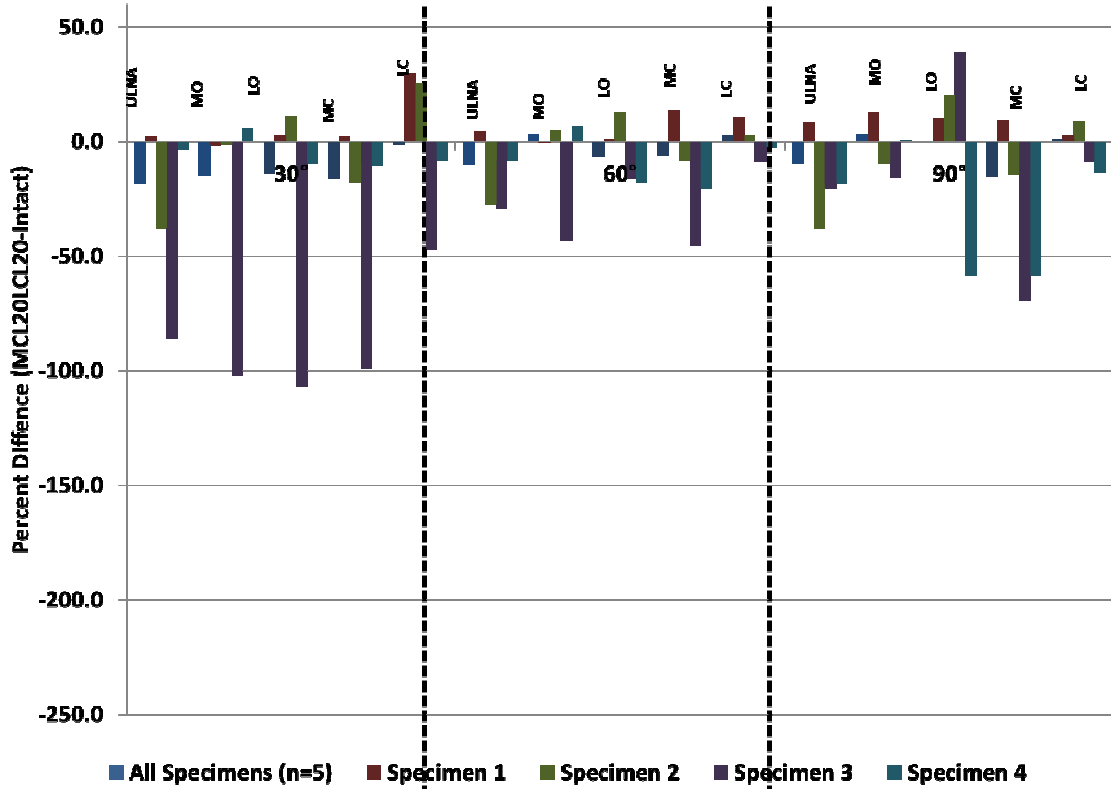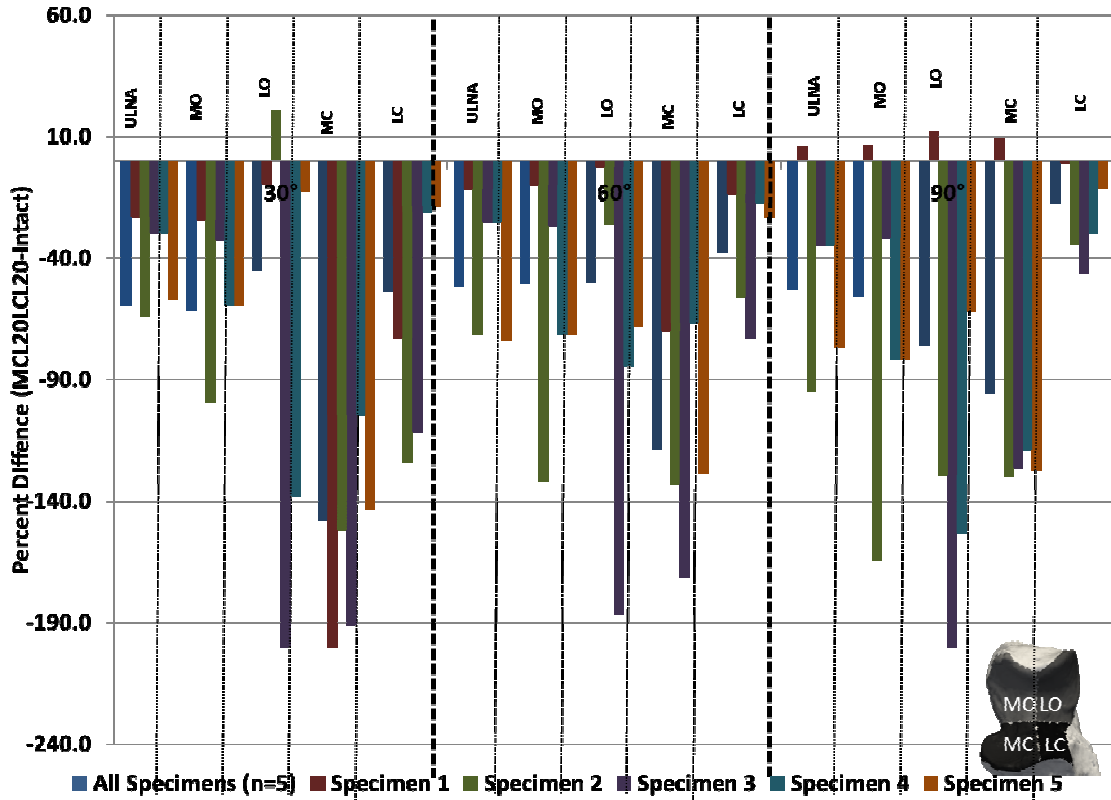
Figure 5.12: Differences between Intact and Ligament Repaired Joint Congruency (Passive Flexion)

Differences between intact and ligament repaired joint congruency (inter-bone distance <3.5mm) during passive elbow flexion

Note: A negative number indicates that the surface area decreased from intact to ligament repair.

5.4   Discussion

The objective of this study was to employ an image-based approach to investigate the relationship between subtle ligament instability and resulting ulnohumeral joint mechanics as well as the relationship between kinematics and measured joint congruency. Also, the effect of static and dynamic stabilizers was examined during passive and active elbow flexion to determine whether there was a relationship between measured joint laxity and resulting joint congruency. We hypothesized that proximity mapping would be more sensitive than traditional kinematic techniques to measure subtle alterations in joint mechanics. The technique employed in this study to quantify articular mechanics proved to be sensitive enough to detect large changes in joint congruency in spite of only small changes in kinematics following simulated ligament repair and the method of rehabilitation.

The literature indicates that while previous studies have investigated elbow joint contact area and mechanics (Black *et al.*, 1981; Eckstein *et al.*, 1993; Eckstein *et al.*, 1994; Eckstein *et al.*, 1995; Fujikawa *et al.*, 1983; Goodfellow and Bullough, 1967; Stormont *et al.*, 1985; Walker PS, 2008), these techniques were invasive, requiring direct exposure of the joint. Using the technique described in this current study, joint congruency can be quantified non-invasively and during continuous movements as this technique does not rely on direct access to the joint, and uses motion data collected during testing. A review of traditional ulnohumeral joint mechanics is found in Chapter 1 (Section 1.2.3). However, of specific interest in this study Goto *et al.* (2004), who also

used proximity maps to determine typical contact patterns at the ulnohumeral joint, found that on the humerus, the contact pattern on the trochlear surface was situated on the medial facet of the trochlea for any possible elbow position (Goto *et al.*, 2004). Similar results were found on the ulna. The same tendency was also noted by Stormont *et al.* (1985) and Goodfellow and Bullough (1967). By examining regional zones on the proximal ulna, we found that in the intact elbow, there is a tendency for the surface area within close contact to be concentrated on the medial side of the coronoid (lower half) region on the proximal ulna with the arm in the valgus orientation. This pattern however changed following ligament repair as the close contact region transferred to the lateral side of the coronoid zone during passive elbow flexion.

The optimal method of rehabilitation of the elbow has not been elucidated. Active motion, where the patient uses their muscles to initiate the joint motion may be preferred due to the tendency to dynamically stabilize the joint (Duck TR *et al.*, 2003; Dunning *et al.*, 2001a). The results of this current study indicate that with the arm in the valgus gravity dependent orientation, during active elbow flexion, there is no statistically significant difference in the kinematics before or after collateral ligament repair. Passive motion, where the elbow is moved with the patient's other arm or by therapist, is commonly employed in an effort to 'protect' the elbow. During passive motion in this current study, we found that with both collateral ligaments repaired there was a 3.3±2.2° increase in the valgus angulation. Clinically, this amount of increased instability may not be apparent to the patient, nor using routine clinical stability tests or imaging evaluations, but clearly alters joint congruency as demonstrated by the 57.9±39.9% decrease in surface

area following ligament repair. Previous studies have also reported an increase in valgus angulation following ligament repair in passive motion (Armstrong *et al.*, 2000; Dunning *et al.*, 2001b; Fraser *et al.*, 2008; Pichora *et al.*, 2007; Pollock *et al.*, 2009). This study confirms this finding and is able to relate this increase in angulation to reduced joint congruency indicating that the proximity mapping technique is sufficiently sensitive to detect changes in joint congruency with or without muscle activation. The results also agree with those reported by Ahmed *et al.* (1983) who investigated the effect of MCL insufficiency on posteromedial olecranon contact and found contact area significantly decreased with progressive MCL insufficiency (Ahmed *et al.*, 1983). Previous studies have shown that both overuse as well as underuse of the cartilage surfaces or any deviation from the native uninjured joint can cause deleterious effects to the underlying articular cartilage (Beveridge *et al.*, 2011). The change in the overall joint congruency (as a surrogate of joint contact) following ligament repair suggests that the normal contact mechanics have been altered. Therefore, it is not surprising that patients with compromised collateral ligaments may develop long-term post traumatic arthritis as a consequence of this abnormal articular biomechanics. It may also be suggested that valgus position and passive motion should be avoided during the rehabilitation of elbow dislocations, with or without ligament repairs; however the results of this current study were limited to a single provocative gravity dependent position.

Ligament tensioning has been examined extensively in the literature (Fraser *et al.*, 2008; Pichora *et al.*, 2007; Pollock *et al.*, 2009). Although examining ligament repair tension was not a specific goal of this study, the residual increase in valgus angulation

during passive flexion, following ligament repair, does require some explanation. Previous studies have indicated that in isolation, the LCL repair should be tensioned at 20N or less (Fraser *et al.*, 2008). Similarly, when repairing the MCL, previous studies have indicated that a wide range of MCL tension could be employed (up to 40N) (Pichora *et al.*, 2007).The residual increase in valgus angulation found in this current study indicates that the MCL is under-tensioned (at 20N) or the LCL is over-tensioned (20N) pulling the elbow into valgus. These effects are seen in the absence of the dynamic muscle stabilizers. King *et al.* investigated both under-tensioned and over-tensioned MCL repairs in a rabbit model and found that the tensioning in the ligament normalized over a period of 12 weeks (King *et al.*, 1995). It is not known whether or not this is the case in humans, but the results of our study indicate that even *small* changes in ligament function can markedly affect the overall amount and distribution of the regions of close proximity which may explain the degenerative changes that result following joint injuries.

Degenerative changes after ligament injuries are common. The results of this current study indicate that classic measurement techniques of joint kinematics *underestimate* the impact of ligament injury and repair on the articulation; current techniques may not be sufficient to detect the long-term effects of these injuries or their treatment. Future research efforts will be directed to modify the current protocols to allow this technique to be applied non-invasively in patients with disorders of the elbow and other articulations.

Previous chapters in this thesis were devoted to the design and assessment of a non-invasive image-based technique to examine ulnohumeral joint congruency

undergoing simulated, continuous elbow flexion. The accuracy of this technique and the utility of its use have been demonstrated. While the use of this technique in an *in vitro* environment will allow further insight into the cause of various clinical injuries and their effect of the resulting joint mechanics. However, we can also attempt to implement, as previously mentioned, these protocols into a clinical setting.

5.5 References

Ahmed, A.M., Burke, D.L., and Yu, A. (1983) *In vitro* measurement of static pressure distribution in synovial joints- -Part II: Retropatellar surface. *J Biomech.Eng* 105[3], 226-236.

Armstrong, A.D., Dunning, C.E., Faber, K.J., Duck, T.R., Johnson, J.A., and King, G.J. (2000) Rehabilitation of the medial collateral ligament-deficient elbow: an *in vitro* biomechanical study. *J.Hand Surg [Am.]* 25[6], 1051-1057.

Besl PJ and McKay ND . (1992) A Method for Registration of 3-D Shapes. *IEEE Transactions on Pattern Analysis and Machine Intelligance* 14, 239-256.

Beveridge, J.E., Shrive, N.G., and Frank, C.B. (2011) Meniscectomy causes significant *in vivo* kinematic changes and mechanically induced focal chondral lesions in a sheep model. *J.Orthop.Res.* 29[9], 1397-1405.

Black, J.D., Matejczyk, M.B., and Greenwald, A.S. (1981) Reversible cartilage staining technique for defining articular weight-bearing surfaces. *Clin.Orthop.Relat Res.* [159], 265-267.

Buckwalter, J.A. and Lane, N.E. (1997) Athletics and osteoarthritis. *Am.J.Sports Med.* 25[6], 873-881.

Duck, T.R., Dunning, C.E., King, G.J., and Johnson, J.A. (2003) Variability and repeatability of the flexion axis at the ulnohumeral joint. *J.Orthop.Res.* 21[3], 399-404.

Dunning, C.E., Duck, T.R., King, G.J., and Johnson, J.A. (2001a) Simulated active control produces repeatable motion pathways of the elbow in an *in vitro* testing system. *J.Biomech.* 34[8], 1039-1048.

Dunning, C.E., Zarzour, Z.D., Patterson, S.D., Johnson, J.A., and King, G.J. (2001b) Muscle forces and pronation stabilize the lateral ligament deficient elbow. *Clin.Orthop* [388], 118-124.

Eckstein, F., Lohe, F., Hillebrand, S., Bergmann, M., Schulte, E., Milz, S., and Putz, R. (1995) Morphomechanics of the humero-ulnar joint: I. Joint space width and contact areas as a function of load and flexion angle. *Anat.Rec.* 243[3], 318-326.

Eckstein, F., Lohe, F., Muller-Gerbl, M., Steinlechner, M., and Putz, R. (1994) Stress distribution in the trochlear notch. A model of bicentric load transmission through joints.

J.Bone Joint Surg Br. 76[4], 647-653.

Eckstein, F., Lohe, F., Schulte, E., Muller-Gerbl, M., Milz, S., and Putz, R. (1993) Physiological incongruity of the humero-ulnar joint: a functional principle of optimized stress distribution acting upon articulating surfaces? *Anat.Embryol.(Berl)* 188[5], 449-455.

Eygendaal, D., Verdegaal, S.H., Obermann, W.R., van Vugt, A.B., Poll, R.G., and Rozing, P.M. (2000) Posterolateral dislocation of the elbow joint. Relationship to medial instability. *J.Bone Joint Surg.Am.* 82[4], 555-560.

Felson, D.T., Lawrence, R.C., Dieppe, P.A., Hirsch, R., Helmick, C.G., Jordan, J.M., Kington, R.S., Lane, N.E., Nevitt, M.C., Zhang, Y., Sowers, M., McAlindon, T., Spector, T.D., Poole, A.R., Yanovski, S.Z., Ateshian, G., Sharma, L., Buckwalter, J.A., Brandt, K.D., and Fries, J.F. (2000) Osteoarthritis: new insights. Part 1: the disease and its risk factors. *Ann.Intern.Med.* 133[8], 635-646.

Ferreira, L.M., Johnson, J.A., and King, G.J. (2010) Development of an active elbow flexion simulator to evaluate joint kinematics with the humerus in the horizontal position. *J.Biomech.* 43[11], 2114-2119.

Fraser, G.S., Pichora, J.E., Ferreira, L.M., Brownhill, J.R., Johnson, J.A., and King, G.J. (2008) Lateral collateral ligament repair restores the initial varus stability of the elbow: an *in vitro* biomechanical study. *J.Orthop.Trauma* 22[9], 615-623.

Fujikawa, K., Seedhom, B.B., and Wright, V. (1983) Biomechanics of the patello-femoral joint. Part I: A study of the contact and the congruity of the patello-femoral compartment and movement of the patella. *Eng Med.* 12[1], 3-11.

Goodfellow, J.W. and Bullough, P.G. (1967) The pattern of aging of the articular cartilage of the elbow joint. *J Bone Joint Surg Am.* 49B, 175.

Goto, A., Moritomo, H., Murase, T., Oka, K., Sugamoto, K., Arimura, T., Nakajima, Y., Yamazaki, T., Sato, Y., Tamura, S., Yoshikawa, H., and Ochi, T. (2004) *In vivo* elbow biomechanical analysis during flexion: three-dimensional motion analysis using magnetic resonance imaging. *J Shoulder Elbow Surg.* 13[4], 441-447.

Honkonen, S.E. (1995) Degenerative arthritis after tibial plateau fractures. *J.Orthop.Trauma* 9[4], 273-277.

Hunter, D.J., Sharma, L., and Skaife, T. (2009) Alignment and osteoarthritis of the knee. *J.Bone Joint Surg.Am.* 91 Suppl 1, 85-89.

Hunter, D.J., Zhang, Y., Niu, J., Tu, X., Amin, S., Goggins, J., Lavalley, M., Guermazi, A., Gale, D., and Felson, D.T. (2005) Structural factors associated with malalignment in

knee osteoarthritis: the Boston osteoarthritis knee study. *J.Rheumatol.* 32[11], 2192-2199.

Josefsson, P.O., Gentz, C.F., Johnell, O., and Wendeberg, B. (1987) Surgical versus non-surgical treatment of ligamentous injuries following dislocation of the elbow joint. A prospective randomized study. *J.Bone Joint Surg.Am.* 69[4], 605-608.

Josefsson, P.O., Johnell, O., and Gentz, C.F. (1984) Long-term sequelae of simple dislocation of the elbow. *J.Bone Joint Surg.Am.* 66[6], 927-930.

King, G.J., Edwards, P., Brant, R.F., Shrive, N.G., and Frank, C.B. (1995) Intraoperative graft tensioning alters viscoelastic but not failure behaviours of rabbit medial collateral ligament autografts. *J.Orthop Res.* 13[6], 915-922.

O'Driscoll, S.W., Morrey, B.F., Korinek, S., and An, K.N. (1992) Elbow subluxation and dislocation. A spectrum of instability. *Clin.Orthop* [280], 186-197.

Pichora, J.E., Fraser, G.S., Ferreira, L.F., Brownhill, J.R., Johnson, J.A., and King, G.J. (2007) The effect of medial collateral ligament repair tension on elbow joint kinematics and stability. *J.Hand Surg.Am.* 32[8], 1210-1217.

Pollock, J.W., Pichora, J., Brownhill, J., Ferreira, L.M., McDonald, C.P., Johnson, J.A., and King, G.J. (2009) The influence of type II coronoid fractures, collateral ligament injuries, and surgical repair on the kinematics and stability of the elbow: an *in vitro* biomechanical study. *J.Shoulder.Elbow.Surg.* 18[3], 408-417.

Schroeder W, Martin K, and Lorensen B . (1998) The Visualization Toolkit. Upper Saddle River, NJ, Prentice Hall.

Stormont, T.J., An, K.N., Morrey, B.F., and Chao, E.Y. (1985) Elbow joint contact study: comparison of techniques. *J.Biomech.* 18[5], 329-336.

Walker PS (2008) *Human Joints and Their Artificial Replacements.*

Chapter 6 – The Effect of CT Dose on Glenohumeral Joint Congruency Measurements using 3D Reconstructed Patient-Specific Bone Models

OVERVIEW

Previous chapters in this thesis have focused on the development of an image-based technique to examine joint congruency at the elbow. These studies are all laboratory-based in vitro investigations. As well, all of the protocols described in this thesis rely on 3D bone reconstructions obtained using x-ray computed tomography. While the amount of radiation applied to the cadaveric models is not of major concern, moving these protocols into a clinical setting requires modifications to existing procedures to reduce the deleterious effects of this imaging modality. Hence, the objective of this study was to determine the optimal CT scanning techniques that would minimize radiation dose while accurately quantifying joint congruency. Glenohumeral joint congruency was chosen as this joint, and its proximity to highly radiosensitive organs, poses a significant challenge.[5]

6.1   Introduction

X-ray CT has become a valuable tool in orthopaedics both clinically as well as for biomechanical applications. Clinically, CT scans are routinely used to obtain diagnostic information. With the development of computer assisted orthopaedic procedures,

clinicians often employ CT images for use in pre-operative surgical planning (McDonald *et al.*, 2007; McDonald *et al.*, 2009), and to investigate joint alignment and deformity (Athwal *et al.*, 2003; Henckel *et al.*, 2006). CT is also a valuable tool for 3D joint modeling due to the high contrast images obtained between bone and soft tissue (Oka *et al.*, 2009). Specifically in this thesis, CT is required for all the techniques developed as they rely on 3D bone reconstructions obtained from CT volumetric image sets. One of the main factors affecting the accuracy of a 3D reconstruction is the quality of the image dataset used in the reconstruction (Zannoni *et al.*, 1998). While the number of biomechanical applications using CT for joint modeling has increased, little consideration has been given to the applied dose to the patients participating these studies (Van Sint *et al.*, 2006).

The shoulder provides a significant challenge both in its size and proximity to highly radiosensitive organs, as these procedures irritate the thyroid gland, lung and breast tissue, which are sensitive to the damaging effects of ionizing radiation (Biswas *et al.*, 2009). The glenohumeral articulation of the shoulder describes where the humeral head articulates with the glenoid, the articular surface of the scapula. The motion of this joint allows for shoulder flexion/extension, abducation/adduction and internal/external rotation of the humeral head with respect to the glenoid. Additionally, only ulnohumeral joint congruency has been examined in this thesis. Therefore, to demonstrate the utility of this joint congruency mapping technique to other joints, glenohumeral joint congruency is also examined.

The inter-bone distance algorithm described and validated in Chapter 2 assesses the relative congruency or relative joint space, of an articular joint for use in the study of joint mechanics. This algorithm, as previously mentioned, uses reconstructed bony models obtained from CT scans and has been used to investigate elbow joint mechanics *in vitro*. The clinical implications of using imaging to determine joint contact mechanics are significant, as they provide a powerful clinical tool to evaluate patients when performed *in vivo*. The clinical application of this work requires that ionizing radiation be minimized while still providing an accurate characterization of joint congruency.

The purpose of this study was to investigate the effect of radiographic CT scanning techniques on the accuracy of 3D surface models of the shoulder. Specifically, the objective of this chapter was to establish the minimum radiation dose required to create an accurate 3D reconstruction that could be used to quantify joint congruency.

6.2 Methods

6.2.1 SPECIMEN PREPARATION AND IMAGING

Five fresh-frozen male cadaveric shoulder specimens were employed in this study (75±8.9 yrs; 3L and 2R). Prior to testing, the specimens were thawed at room temperature for 20 hours. The joint capsule and all soft tissues remained intact.

Each specimen was placed on the CT gantry in the supine position with the shoulder adjacent to the chest (consistent with a clinical CT scan of a shoulder) (Bor *et al.*, 2004). To simulate the thorax that would be present in an intact *in vivo* shoulder scan, a 22 cm container filled with water was positioned adjacent to the shoulder specimen. The

width of the container was within the normal range (one standard deviation of the 50th percentile) of one-half of a male's shoulder breadth (Pheasant S and Halsgrave CM, 2006). Volumetric images were acquired using a helical 64-slice CT scanner (GE Discovery CT750 HD, Waukesha, WI). The specimen did not change position in the CT scanner between successive scans. Approximately 450 slices were acquired for each specimen with a field of view set at 20-22 x 20-22cm and a 512 x 512 reconstruction matrix.

Patient dose is highly dependent on the CT parameters used to acquire the volumetric image. The choice of radiographic techniques that most affects the effective dose are x-ray tube current (mA), tube peak voltage potential (kVp), and scan extent (cm length of the scanned volume) (Huda *et al.*, 2002). The patient dose is directly proportional to the selected mA and therefore was used in this study as a CT parameter that can be easily manipulated dose (Huda *et al.*, 2002). The relationship between patient dose and kVp is more complicated than mA as dose increases in a supra-linear manner with increasing kVp (Huda *et al.*, 2002). For helical scanners such as the CT scanner used in this current study, the pitch ratio (the increment of the length of table imaged per slice) directly affects the applied dose. As the pitch increases, the dose decreases as the same amount of radiation dose is applied to a larger area of the patient. Therefore in this study both mA (tube current) and pitch ratio were used to determine the minimum dose required to investigate joint congruency at the glenohumeral joint of the shoulder. Effective mAs, defined as (mA per rotation/pitch ratio) accounts for the tube current as

well as the spiral pitch factor and was also calculated. However, in this study a fixed mA value was used for the entire scan volume and no tube current modulation was used.

Four low-dose CT (protocols 1-4) and three normal-dose (protocols 5-7) scanning protocols were investigated in this study (Table 6.1: CT Scanning Protocols). Biswas *et al.* (2009) examined twenty CT scans of the shoulder and determined that the average x-ray tube current used was 365 ± 176 mA and 120 kVp. This referenced paper does not indicate what the average tube rotation time was for a typical shoulder examination. Therefore, to identify the protocol in this current study that represented the standard radiographic technique, protocol 6 was chosen as it used a tube current of 450mA which is within the range noted by Biswas *et al.* Radiographic tube voltage is typically kept constant at 120 kVp in most facilities in North America (Huda *et al.*, 2002). Therefore, protocol 6 represents the standard radiographic technique setting employed in a typical clinical CT shoulder examination (450mA (360mAs), 120 kVp, slice thickness 0.625mm, pitch ratio 0.969:1). The mean effective dose of a clinical shoulder examination is 2.06 ± 1.52mSv (Biswas *et al.*, 2009).

	CT Protocol	X-ray Tube Current (mA)	Revolution Time (mS)	mAs per Rotation	Pitch Ratio	Effective mAs (mAs per rotation/pitch ratio)	Voltage (kVp)	Slice Thickness (mm)
Low Dose	1	10	0.8	8	0.969:1	8.256	120	0.625
	2	15	0.8	12	0.969:1	12.384	120	0.625
	3	50	0.8	40	0.969:1	41.280	120	0.625
	4	150	0.8	120	0.969:1	123.839	120	0.625
Normal Dose	5	450	0.8	360	1.375:1	261.818	120	0.625
	6*	450	0.8	360	0.969:1	371.517	120	0.625
	7	450	0.8	360	0.531:1	677.966	120	0.625

Table 6.1: CT Scanning Protocols
Four low-dose protocols (1-4) and three normal-dose (5-7) scanning protocols were investigated.
*Indicates the standard clinical radiographic scanning protocol.

6.2.2   SEGMENTATION AND BONE MODELING

Successive DICOM files generated from each CT scan were converted to a MINC file (Montreal Neurological Institute and Hospital, 2010) using custom software as previously described in Chapter 2 (Section 2.2.3). MINC files were then used to create a 3D model by manually selecting a threshold value that separated soft tissue from bony tissue. Surface models were created using the Marching Cubes algorithm within VTK Version 4.2.1 (Visualization Toolkit, Kitware, Clifton Park, NY) (Schroeder W *et al.*, 1998). The subchondral bone region, representing the bone surface below the articular surface, of both the proximal humerus and glenoid (the articular surface of the scapula) was manually segmented from each 3D reconstruction and saved as a separate 3D model. The scanning protocol was blinded from the experimenter during this reconstruction process.

6.2.3   OUTCOME VARIABLES

Joint congruency was calculated using an inter-bone distance algorithm described in Chapter 2 (Section 2.2.5). The inter-bone distance algorithm measures the relative distance between the opposing subchondral bone surfaces. A colourmap was once again used to visualize these distances. Using the inter-bone distance algorithm, the surface area across the subchondral bone was measured for a given 'level' of proximity. A region in which inter-bone distances were less than 10mm was classified as a '(close) proximity region'. This value was chosen to reflect the geometry of the glenohumeral joint. Within this region, 'levels of proximity' were also employed measuring the surface area of the subchondral bone within high proximity (less than 1.25mm), medium proximity (less than

3.75mm), low proximity (less than 6.25mm) and distant proximity (less than 8.75mm). These values were chosen as they represent boundaries of colour regions. For example, less than 2.75mm is showing the boundary of the surface area on the glenoid or humerus where the colourmap transitions from 'yellow' to 'green'. The surface areas in this study are expressed as a percentage value of the total articular surface (subchondral bone) for the humerus or glenoid. A repeated-measures analysis of variance test with a Bonferroni correction was used to detect statistical differences in the measured surface area for each level of proximity (high, medium, low and distant proximity) for each CT scanning protocol. This statistical method was applied to the current varying protocols (#1, 2, 3, 4, and 6) and pitch varying protocols (#4, 5, and 6) separately. Statistical significance was set at $p < 0.05$.

6.2.4 DOSIMETRY

Two common quantities recommended by the Commission of the European Communities to express CT dose used in a clinical CT scanner are the weighted computed tomography dose index ($CTDI_w$) and the dose-length product (DLP) (Jessen *et al.*, 1999). $CTDI_w$, measured in mGy, takes into account modifications in tube current and voltage and allows direct comparison of one scanner to another as well as one scan technique to another (Wiest *et al.*, 2002). $CTDI_{vol}$ describes the average dose delivered to the scan volume for a specific examination and is equal to $CTDI_w$/pitch ratio. DLP is expressed in mGyxcm and can be obtained by taking the product of $CTDI_w$ and length of the scan (slice thickness x number of slices). In this study however, DLP values were not calculated, but rather obtained from the scanner display, specifically the dose report.

CTDI$_w$ and DLP are both examples of reference dosimetry values that are measured experimentally using imaging phantoms measured under constant conditions of exposure (Shrimpton PC and Wall BF, 2000). Shrimpton and Wall state that measurements of CTDI$_w$ and DLP can only be used to provide an average dose applied to the patient for a given anatomical region and patient size (Shrimpton PC and Wall BF, 2000). These values do not account for the radiosensitivity of the irradiated organs. These dosimetry values should not be interpreted as the applied dose received by any specific tissue or organ in the patient. Therefore in this study, effective doses were examined to incorporate the radiosensitivity of the relevant organs and tissues surrounding the shoulder and are expressed in milliSieverts (Huda *et al.*, 2002). The actual calculation of effective dose is quite complex, however broad estimates for effective dose may be derived from values of DLP using normalized coefficients (1996). Previous studies have determined these normalized coefficients for specific anatomical regions and these values were employed for the current investigation to obtain an averaged DLP normalized coefficient for a clinical shoulder examination (Hatziioannou *et al.*, 2003; Jessen *et al.*, 1999; Shrimpton PC and Wall BF, 2000).

6.3   Results

Proximity maps from the inter-bone distance algorithm, showing relative glenohumeral joint congruency as a function of tube current are shown in Figure 6.1. The images are of the joint in an 'opened' pose for visualization purposes. While the proximity maps are displayed for a single
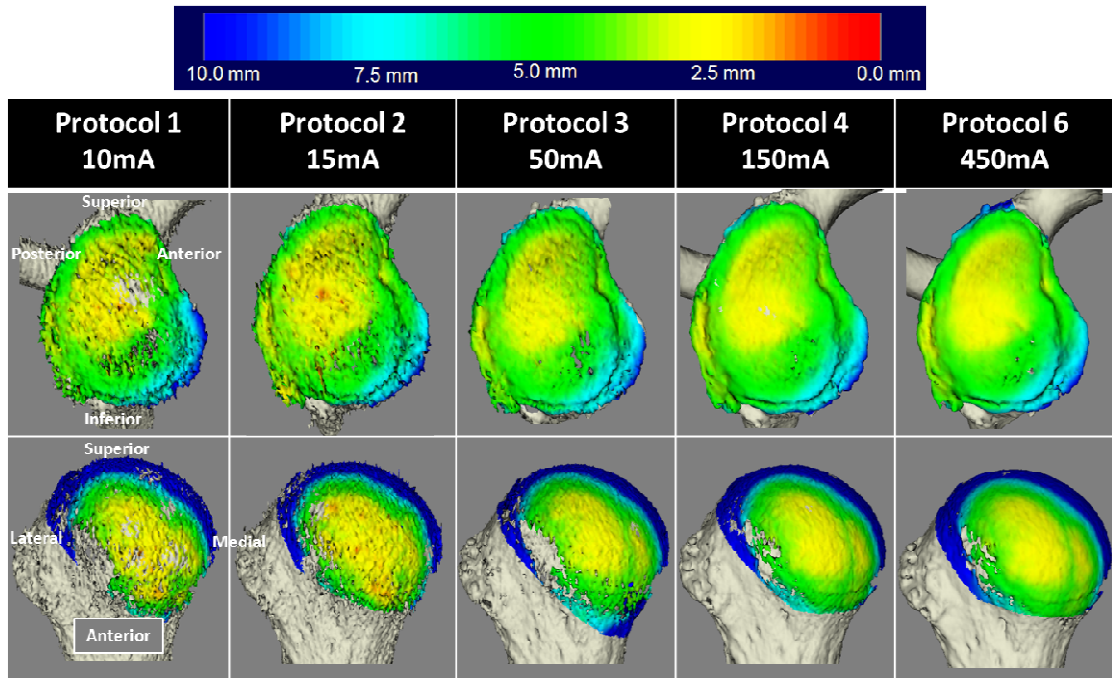
Figure 6.1: Proximity Maps of the Glenohumeral Joint for Protocols Examining mAs.

The proximity region (<10mm) is consistent between all scans from low (protocol 1) to standard dose scans (protocol 6). On the glenoid, the yellow region (approximately 2.5mm proximity) is located centrally and extends to the superior region of the articulation as a 'tear drop'. Additionally, on the posterior rim of the articulation, there is a yellow stripe slightly inferior to the central yellow region. On the humerus, the central yellow region is tilted laterally and is also consistently visualized between scans. The stripe on the humerus is on the medial side, but is only clearly seen in the higher mAs scans (50-450mA). With decreasing mA, the ability to resolve the stripe decreases until 10mA when there only appears to be a single yellow central region.

specimen, the results are representative of all specimens. The shape and location of the proximity region is consistent across all scans. Therefore the posterior region (not shown) is dark blue (>10mm). The surface models of both the glenoid and humerus that were reconstructed from the low mA scans appear rough and pitted. On both the glenoid and humerus, at the lower mA scans (protocol 1&2), there are reddish-orange 'dots' corresponding to a proximity less than 1mm. These regions correspond to regions of 'false proximity' as they do not appear on the high dose scans and are the result of increased noise in the low dose scans.

Proximity maps, showing relative glenohumeral joint congruency as a function of pitch ratio are shown in Figure 6.2. All of these scans were acquired at 360mAs and therefore generated smooth surface models. Qualitatively, there appears to be no difference in the proximity region between scans for the humerus or glenoid.
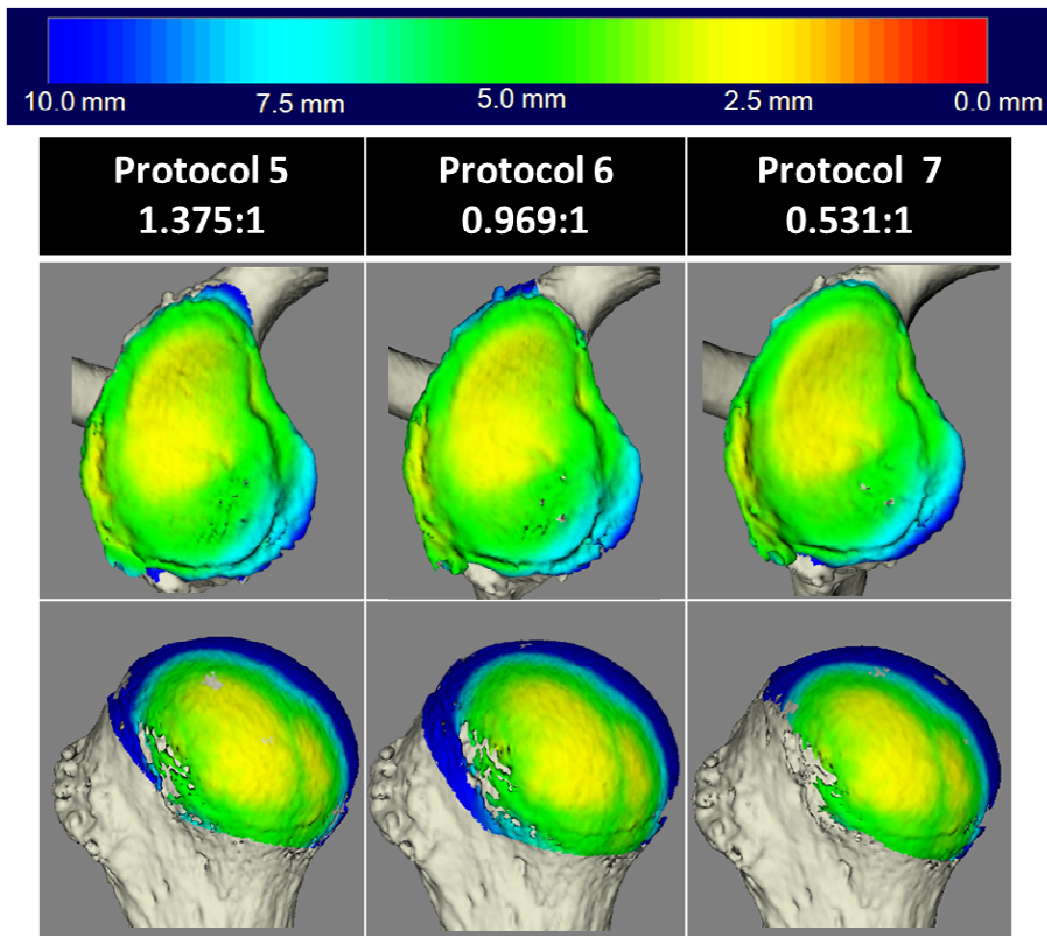
Figure 6.2: Proximity Maps of the Glenohumeral Joint for Protocols Examining Pitch Ratio.
The proximity region shown for varying pitch ratios is consistent across scanning protocols. The only visual difference between these proximity maps is small pits located on the medial/inferior region of the glenoid subchondral bone. As the pitch ratio decreases (dose increases) the size of these holes decreases.

Individual iso-contour maps for the glenoid are shown for each proximity level in Figure 6.3 (high proximity), Figure 6.4 (medium proximity), Figure 6.5 (low proximity) and Figure 6.6 (distant proximity). The outer edges of the glenoid articular surface area less defined for the low dose scan (protocol 1) compared to the high dose scan (protocol 7) for all levels of proximity. The low dose scan scenario shows only a small area of the subchondral bone in high proximity. However, on the high dose scan, there are no areas of the subchondral bone within high proximity. For the medium, low and distant proximity maps, the pattern of the proximity level is consistent between the high and low dose scans; however, there are large holes and pits in the low dose scans.
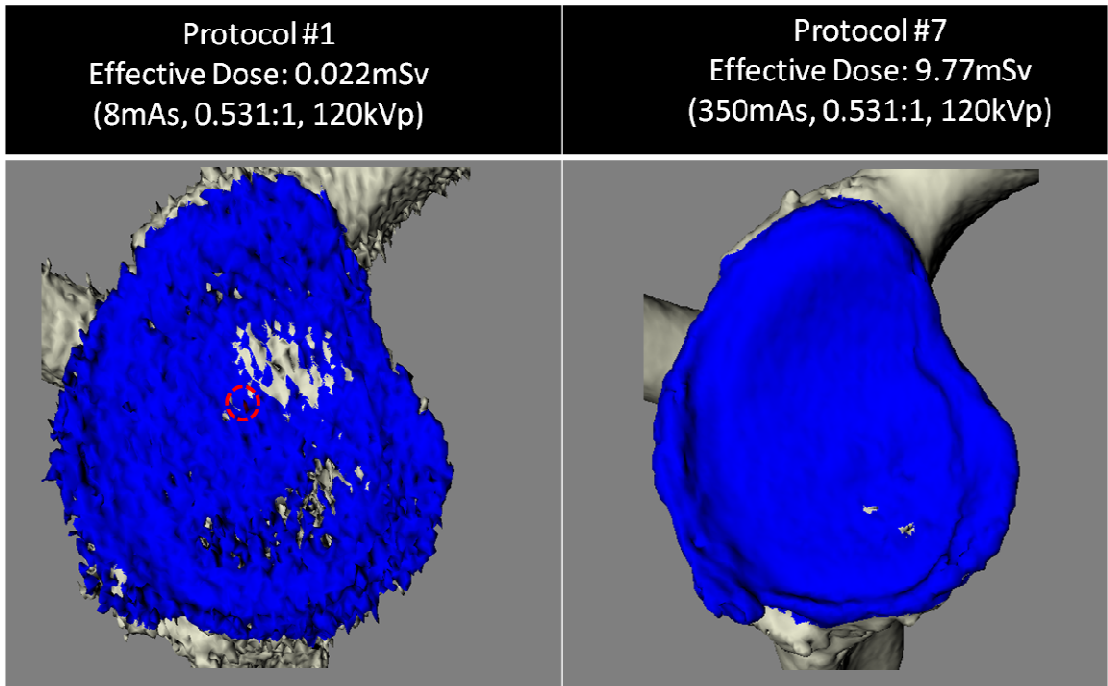
Figure 6.3: Iso-contour map of High Proximity (<1.25mm) (shown in red)
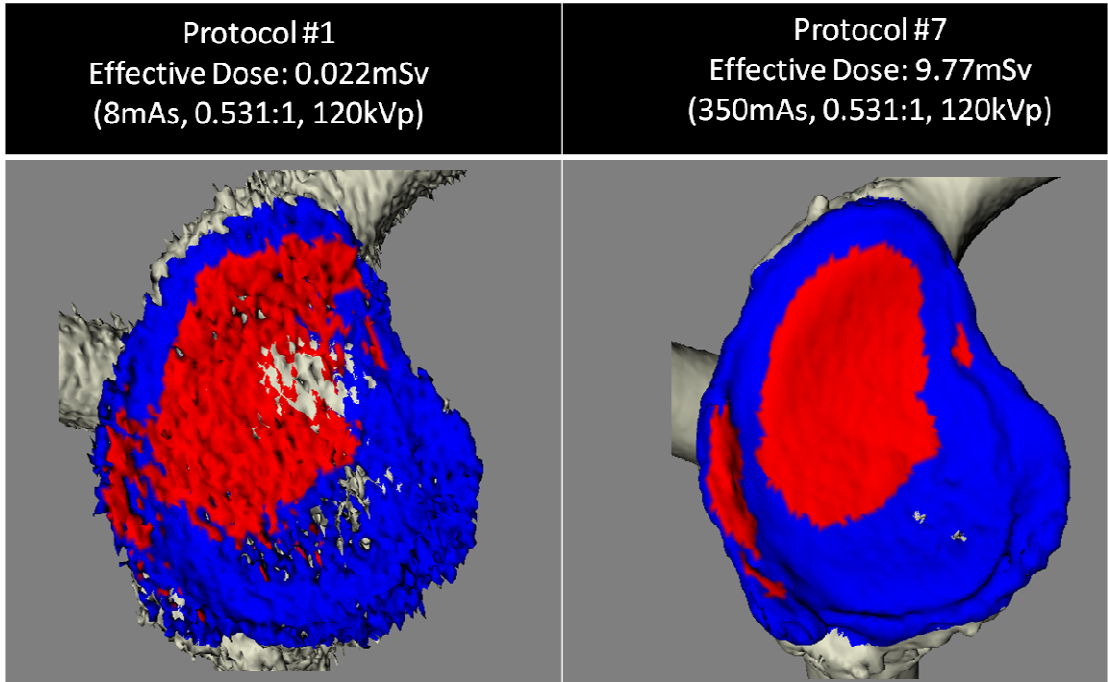
Figure 6.4: Iso-contour map of Medium Proximity (<3.75mm)
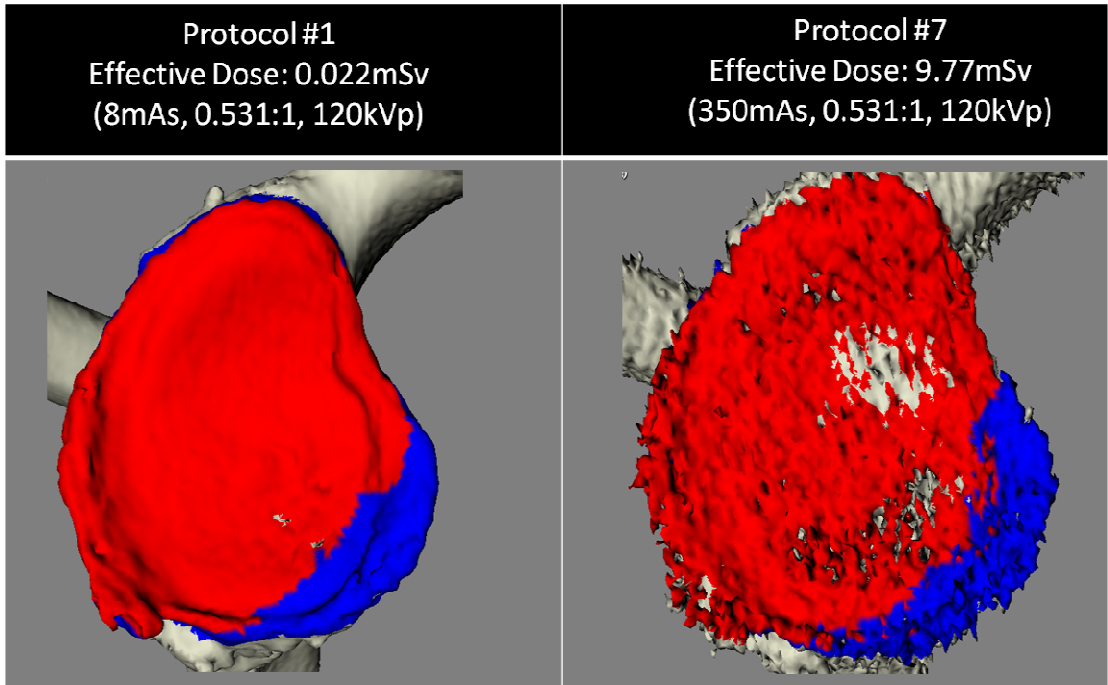
Figure 6.5: Iso-contour map of Low Proximity (<6.25mm)
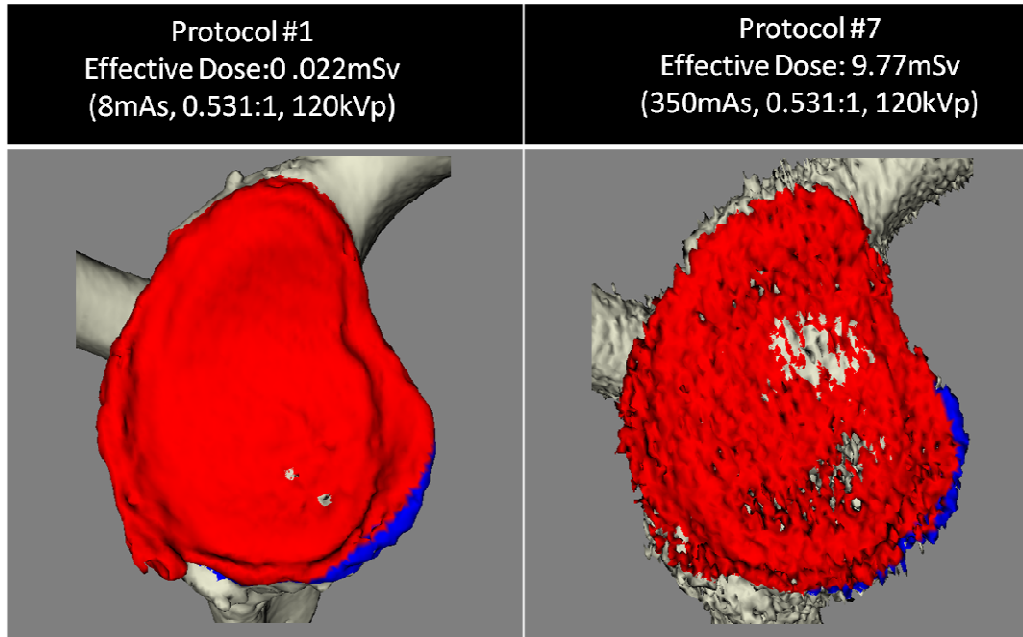
Figure 6.6: Iso-contour map of Low Proximity (<8.75mm)

Figure 6.7 shows the mean surface area on the glenoid for all five specimens that are in high, medium, low or distant proximity. These surface area values are expressed as a percentage of the total glenoid subchondral bone area as a function of mA. Similar results were also obtained for the humerus (not shown). There appears to be no visual trend in the surface area for any level of proximity as a function of mA.
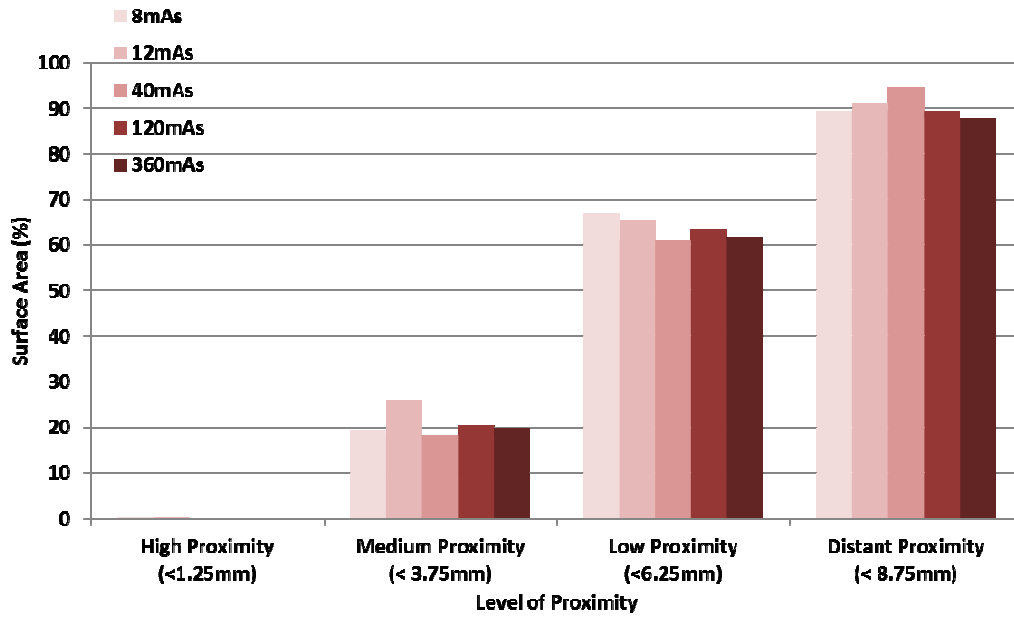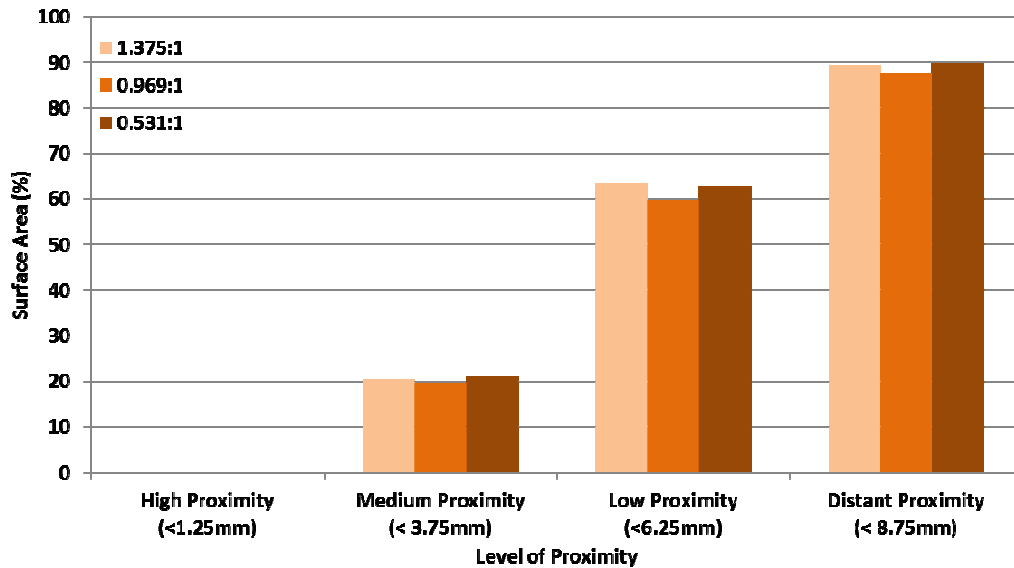
Figure 6.7: Effect of Total Current Flux on Glenoid Surface Area (%)
Mean surface area (%) + 1SD values for each level of proximity are shown between CT scanning protocols affecting mA (n=5). There appears to be no trend in the measured surface area for each level as a function of mA.

These results were consistent for all five specimens and statistical analysis confirms that for any proximity level, there was no significant difference in the surface area between scans ($0.059 \leq p \leq 0.226$).

Figure 6.8 shows the mean surface area as a function of changing pitch ratio. There was no significant difference in the surface area between the three pitch protocols ($0.338 \leq p \leq 0.768$).

The effective radiation doses calculated for the seven protocols are shown in Table 6.2. The normalized coefficient used to convert DLP values to effective dose was 0.0130 mSv-mGy-1cm-1 (Hatziioannou et al., 2003; Jessen et al., 1999; Shrimpton PC and Wall BF, 2000). The effective doses between specimens vary due to the differences in scan length.

Figure 6.8: Effect of Pitch Ratio on Glenoid Surface Area (%)

Mean surface area (%) + 1SD values for each level of proximity are shown between CT scanning protocols affecting the pitch ratio (n=5). There appears to be no trend in the measured surface area for each level as a function of pitch ratio.

CT Protocol: Effect of mAs	Effective Dose (mSv)					Mean Effective Dose (mSv)
	Specimen 1	Specimen 2	Specimen 3	Specimen 4	Specimen 5	
1	0.2	0.2	0.2	0.2	0.3	**0.2**
2	0.3	0.3	0.3	0.3	0.4	**0.3**
3	1.1	1.1	1.1	1.1	1.4	**1.2**
4	3.3	3.2	3.4	3.3	4.2	**3.5**
6*	9.8	9.5	10.2	10.0	12.7	**10.4**

CT Protocol: Effect of Pitch Ratio	Specimen 1	Specimen 2	Specimen 3	Specimen 4	Specimen 5	
5	7.2	7.0	7.5	7.4	9.3	**7.7**
6*	9.8	9.5	10.2	10.0	12.7	**10.4**
7	17.7	17.2	18.4	18.2	23.1	**18.9**

Table 6.2: Effective Dose

Effective doses were calculated using the normalized coefficient. The effective doses between specimens vary due to the differences in scan length (size of specimen) but are relatively constant for a particular scan between specimens.
*Indicates the standard clinical radiographic scanning protocol.

6.4 Discussion

The advances in the diagnostic utility and efficiency of CT have not surprisingly contributed to the drastic increase in the number of CT scans employed clinically. In Canada, CT scans grew by 8% from 2003/2004 to 2004/2005(Aldrich and Williams, 2005).It was estimated that approximately sixty-two million scans are obtained each year in the United States alone (Brenner and Hall, 2007). It is worth noting also that although CT examinations only represent 4% of all radiological examinations, their contribution to the total radiation dose to patients has been estimated to be approximately 35% (Buzug, 2008). In Canada, it is estimated that the attributable lifetime cancer risk from all diagnostic x-rays accounts for 784 cases of cancer per year based on data from 1991-1996, and therefore could even be higher today (Healthcare Human Factors Group Centre for Global eHealth Innovation University Health Network, 2006). With recent advances in CT technology such as multi-detector and helical scanning devices, the patient dose is not reduced and actually may increase (Buzug, 2008; Healthcare Human Factors Group Centre for Global eHealth Innovation University Health Network, 2006). These relatively high doses of radiation have raised concerns about the potential cancer-causing effects of using CT (Biswas *et al.*, 2009). Additionally, The Computer Tomography Radiation Safety Issues in Ontario Report notes that although extensive limits for radiation have been in place to protect people who work near radiation, there currently exists no specific level of radiation that is recommended for patients undergoing diagnostic x-ray procedure (Health Canada, 2002). Currently, technologists administer CT examinations using the

ALARA principle. This principle basically states that the minimum dose (As Low As Reasonably Achievable) should be used in the examination to provide images of diagnostic quality (Healthcare Human Factors Group Centre for Global eHealth Innovation University Health Network, 2006). This is however a very subjective criteria and efforts have been made to establish diagnostic reference levels (DRL), but these values have not been implemented (Healthcare Human Factors Group Centre for Global eHealth Innovation University Health Network, 2006).

Recent research efforts have been directed towards establishing standards for CT acquisition to reduce absorbed dose while maintaining high image quality (Oka *et al.*, 2009; Sugano *et al.*, 2001; Van Sint *et al.*, 2006). As such the objective of this study was to determine the minimum requirements for tube current and pitch ratio that can be used to accurately reconstruct bony models and examine joint congruency by taking measurements from these reconstructed models using a previously developed algorithm.

The results of this study indicate that there is no statistical difference in the measured surface area for any level of proximity for varying levels of mA and pitch ratio. Qualitatively the proximity region did not change with the scanning parameters investigated. However, the ability to resolve smaller regions of proximity decreases as the absorbed dose decreases. Additionally, regions of 'false proximity' appear in the 10 and 15mA reconstructed images. Therefore, we recommend using 50mA and 0.969:1 pitch ratio to reliably examine joint congruency, avoid false close proximity regions and resolve smaller regions of joint proximity. This will reduce the mean effective dose to 1.16mSv which is an 88.9% reduction compared to the effective dose of the typical

clinical shoulder examination. When considering pitch, the results of this study indicate that at 450mA, the effect of pitch on the measured joint congruency is negligible and therefore, it is recommended to use a pitch ratio of 1.375:1 which had an average effective dose of 7.65mSv. This will correspond to a 26.7% reduction in the effective dose at 450mA. This pitch ratio can also be used with 50mA as recommended by the results of this study, but has not been specifically examined here. Finally, these scanning parameters may be further modified to reduce radiation exposure by employing smoothing functions to the reconstructed models.

Oka *et al.* (2006) examined the effect of low-dose CT on the accuracy of 3D reconstructions of forearms. Distal forearm bone models were imaged using low and normal radiation dose CT parameters. The authors reported that an almost identical 3D reconstruction could be obtained using the low-dose protocol. Van Sint Jan *et al.*(2006) also examined low dose and standard dose CT parameters (scanning cadaveric lower extremities) and found that low dose scans were suitable for accurate 3D bone modeling and showed that overall x-ray radiation could be greatly decreased (up to 90%) without a loss of accuracy. The results of this current study are consistent with the findings of previous studies attempting to reduce radiation dose while preserving modeling accuracy.

Biswas *et al.* (2009) have indicated that the mean effective dose of a clinical CT shoulder examination is 2.06mSv ± 1.52mSv. This value corresponds to 68% of the total background dose due to natural radiation in one calendar year (3mSv)(Aldrich and Williams, 2005). Protocol six of this current study was considered the typical scanning protocol as it is consistent with the range normally used clinically. The effective dose for

a standard CT shoulder examination in our study was 10.44mSv. This value is higher than that estimated by Biswas and colleagues, who recorded their dose data from a single institution (Biswas *et al.*, 2009). Therefore the observed differences between the effective doses could be explained by differences in the mass of the shoulder specimen. The shoulders examined herein were resected at mid-humerus and separated from the trunk. Therefore, because this study only examined an isolated shoulder, the amount of absorbed radiation could be increased with adjacent structures, despite our attempts to account for this volume difference using the adjacent water block. As well, the normalized effective dose coefficients are reported for specific anatomical regions, and in this study three coefficients were averaged and used to estimate effective dose. However, these coefficients were intended for entire chest/trunk anatomical scans which we did not have access to. This could also explain the comparatively high values for effective dose estimated in our current study. However, the 88.9% decrease in radiation dose (as a result of the decreased mAs value suggested in this study) was a relative decrease from protocol 6 (10.44mSv) to protocol 3 (1.16mSv).

Image quality can be described by analyzing spatial resolution, contrast and noise. Various CT scanning techniques can be optimized to obtain images that are high in image quality. Biswas *et al.* (2009) explains that there has not been a single study that definitively establishes a direct relationship between the incidences of a malignant disease following any type of medical imaging. However, we know that X-ray CT is not a benign medical imaging technique, and as such, standards have been established to minimize the amount of radiation exposure necessary for clinical CT examinations. For example,

Henckel *et al.* (2006) noted that although there is no safe dose of radiation, CT technologists and imaging scientists should make all attempts to reduce the effective dose applied by manipulating and reducing dose parameters. However, reducing current, scan time, tube voltage, as well as increasing the pitch ratio all affects the quality of the image. Therefore, a different definition of image quality must be considered. Huda *et al.* (2002) refers to this as diagnostic image quality. Huda *et al.* noted that while lower dose CT scanning parameters produce a less aesthetically pleasing image, the important clinical issue is whether or not the imaging provides reliable diagnostic information. If it can, then any increase in the amount of radiation exposure applied requires significant justification. The results of this current study and previous studies examining the accuracy of low-dose CT scans demonstrate that it is possible to obtain accurate and suitable information from a low-dose CT scan while maintain accuracy and achieving diagnostic information that is consistent with high-dose CT scanning protocols (Oka *et al.*, 2009; Van Sint *et al.*, 2006). Additional research is necessary to further reduce the radiation exposure of various musculoskeletal CT examinations by investigating various smoothing algorithms, iterative reconstruction algorithms that incorporate noise models or alternatively examine the utility of alternative non-ionizing medical imaging modalities for model reconstructions. As well, future work in the examination of patient dose and diagnostic image quality of other radiosensitive musculoskeletal regions (the spine and pelvis) will also help to reduce the deleterious effects associated with x-ray computed tomography.

6.5 References

(1996) European Commission. European Guidelines on Quality Criteria for Computed Tomography.

Aldrich, J.E. and Williams, J. (2005) Change in patient doses from radiological examinations at the Vancouver General Hospital, 1991-2002. *Can.Assoc.Radiol.J.* 56[2], 94-99.

Athwal, G.S., Ellis, R.E., Small, C.F., and Pichora, D.R. (2003) Computer-assisted distal radius osteotomy. *J.Hand Surg.Am.* 28[6], 951-958.

Biswas, D., Bible, J.E., Bohan, M., Simpson, A.K., Whang, P.G., and Grauer, J.N. (2009) Radiation exposure from musculoskeletal computerized tomographic scans. *J.Bone Joint Surg.Am.* 91[8], 1882-1889.

Bor, D., Sancak, T., Olgar, T., Elcim, Y., Adanali, A., Sanlidilek, U., and Akyar, S. (2004) Comparison of effective doses obtained from dose-area product and air kerma measurements in interventional radiology. *Br.J.Radiol.* 77[916], 315-322.

Brenner, D.J. and Hall, E.J. (2007) Computed tomography--an increasing source of radiation exposure. *N.Engl.J.Med.* 357[22], 2277-2284.

Buzug, T. (2008) *Computed Tomography From Photon Statistics to Modern Cone-Beam CT*. Springer-Verlag.

Hatziioannou, K., Papanastassiou, E., Delichas, M., and Bousbouras, P. (2003) A contribution to the establishment of diagnostic reference levels in CT. *Br.J.Radiol.* 76[908], 541-545.

Health Canada . (2002) X-ray Equipment in Medical Diagnosis Part A: Recommended Safety Procedures
for Installation and Use. Safety Code 20A.

Healthcare Human Factors GroupCentre for Global eHealth InnovationUniversity Health Network . (2006) Computed Tomography Radiation Safety
Issues in Ontario.

Henckel, J., Richards, R., Lozhkin, K., Harris, S., Baena, F.M., Barrett, A.R., and Cobb, J.P. (2006) Very low-dose computed tomography for planning and outcome measurement in knee replacement. The imperial knee protocol. *J.Bone Joint Surg.Br.* 88[11], 1513-

1518.

Huda, W., Ravenel, J.G., and Scalzetti, E.M. (2002) How do radiographic techniques affect image quality and patient doses in CT? *Semin.Ultrasound CT MR* 23[5], 411-422.

Jessen, K.A., Shrimpton, P.C., Geleijns, J., Panzer, W., and Tosi, G. (1999) Dosimetry for optimisation of patient protection in computed tomography. *Appl.Radiat.Isot.* 50[1], 165-172.

McDonald, C.P., Brownhill, J.R., King, G.J., Johnson, J.A., and Peters, T.M. (2007) A comparison of registration techniques for computer- and image-assisted elbow surgery. *Comput.Aided Surg.* 12[4], 208-214.

McDonald, C.P., Peters, T.M., King, G.J., and Johnson, J.A. (2009) Computer assisted surgery of the distal humerus can employ contralateral images for pre-operative planning, registration, and surgical intervention. *J.Shoulder.Elbow.Surg.* 18[3], 469-477.

Montreal Neurological Institute and Hospital . (2010) MINC. *McConnell Brain Imaging Centre* .

Oka, K., Murase, T., Moritomo, H., Goto, A., Sugamoto, K., and Yoshikawa, H. (2009) Accuracy analysis of three-dimensional bone surface models of the forearm constructed from multidetector computed tomography data. *Int.J.Med.Robot.* 5[4], 452-457.

Pheasant S and Halsgrave CM (2006) *Bodyspace: Anthropometry, Ergonomics and the Design of Work*. Taylor and Francis Group.

Schroeder W, Martin K, and Lorensen B . (1998) The Visualization Toolkit. Upper Saddle River, NJ, Prentice Hall.

Shrimpton PC and Wall BF . (2000) Reference Doses for Paediatric Computed Tomography. *Radiation Protection Dosimetry* 90[1-2], 249-252.

Sugano, N., Sasama, T., Sato, Y., Nakajima, Y., Nishii, T., Yonenobu, K., Tamura, S., and Ochi, T. (2001) Accuracy evaluation of surface-based registration methods in a computer navigation system for hip surgery performed through a posterolateral approach. *Comput.Aided Surg.* 6[4], 195-203.

Van Sint, J.S., Sobzack, S., Dugailly, P.M., Feipel, V., Lefevre, P., Lufimpadio, J.L., Salvia, P., Viceconti, M., and Rooze, M. (2006) Low-dose computed tomography: a solution for *in vivo* medical imaging and accurate patient-specific 3D bone modeling? *Clin.Biomech.(Bristol., Avon.)* 21[9], 992-998.

Wiest, P.W., Locken, J.A., Heintz, P.H., and Mettler, F.A., Jr. (2002) CT scanning: a major source of radiation exposure. *Semin.Ultrasound CT MR* 23[5], 402-410.

Zannoni, C., Cappello, A., and Viceconti, M. (1998) Optimal CT scanning plan for long-bone 3-D reconstruction. *IEEE Trans.Med.Imaging* 17[4], 663-666.

Chapter 7- General Discussion and Conclusion

OVERVIEW

This chapter reviews the objectives and hypotheses outlined at the beginning of this thesis, summarizes the work that has been undertaken to address these hypothesis and objectives, discusses the strengths and limitations of this research, and outlines current and future research projects that emanate from this research.

7.1 Summary

Osteoarthritis (OA) affects 1 in 10 Canadians (Canadian Arthritis Society 2011). While a substantial proportion of OA is preventable, unfortunately the rates of arthritis following orthopaedic injury remain unacceptably high. Previous studies, as described in this thesis, have determined that there is a relationship between the development of OA and a traumatic event. However, both the cause and mechanism of OA development is not well understood. As stated in Chapter 1:Introduction, the current theory as to the mechanism of this disease is that OA develops as a result of joint mal-alignment, muscle weakness and altered joint congruency, within a context of susceptibility (Felson et al., 2000). Currently, there are no techniques that are able to examine the complex relationship between injury, loading and mal-alignment as contributors to the development and progression of OA in the upper extremity. The overall goal of this thesis therefore was to develop a non-invasive tool that could be used to elucidate the

relationship between joint injury and resulting alterations in joint congruency as these changes may relate to the development of OA.

The progression of this thesis follows the development of a tool that is able to examine joint congruency of the ulnohumeral joint of the elbow undergoing physiologic flexion. The first study (Chapter 2) examined the efficacy of employing medical imaging to measure joint mechanics. Previously in the laboratory, we examined joint contact area and joint contact pressure using an experimental casting and TekScan. The limitations of these techniques were that they required the joint to be statically loaded and they were invasive (joint capsule resected). While these techniques did prove to be useful, they were especially limited in their use when examining the ulnohumeral joint. As described in Chapter 1, the ulnohumeral joint has very complex osseous anatomy that makes these direct exposure techniques more difficult, typically requiring ligament sectioning and repair which increases the potential for errors. Therefore, the objective of the first study (Chapter 2) was to develop and employ a computational approach, using medical imaging, to examine the joint surface interactions. Chapter 2 describes the development of a proximity mapping technique that could be used to non-directly examine the interactions between the distal humerus and proximal ulna (Objective 1). In order to measure joint proximity, medical imaging was required to represent the bony surfaces accurately in three-dimensions. Therefore, the efficacy of employing x-ray CT imaging was examined in Chapter 2 (Objective 1). This technique was validated using the experimental casting technique. As this technique measures joint space (inter-bone distance), the use of the term "joint congruency" was developed to acknowledge that, in

the absence of cartilage data, this technique was an estimate of the joint surface interactions. The ability however, of this technique to accurately predict the regions across the ulna and humerus that were contacting (as determined by the cast) was encouraging. A single specimen was used to demonstrate the utility of this technique. The limitation of the inter-bone distance algorithm in isolation was that it was limited to statically loaded joints.

The objective of the next study was to develop a registration technique to render 3D models of joints that were undergoing simulated elbow flexion (Chapter 3, Objective 2). Previously in our laboratory, an elbow motion simulator was developed that could position the elbow in four gravity dependent positions. Active and passive elbow flexion and extension could be achieved using motors and actuators. This experimental simulator has been used extensively to investigate, in a repeated measures design, the effect of various orthopaedic injuries, surgical reconstructions and rehabilitation protocols on joint stability. Motion of the humerus/ulna/radius was tracked using a magnetic tracking system in this study. Therefore, the next step was to employ paired-point and a surface-based registration to relate the 3D reconstructions (obtained from CT) to the laboratory coordinate system. The effect of radial head arthroplasty was used as a clinical variable to examine the relationship between osseous position (rendered using the registration) and traditionally employed measures of joint stability (kinematic data). While this technique could examine gross bone alignment, within a bone¸ it was insufficient to examine joint congruency (Target Registration Error < 3mm).

The objective of the next study was to increase the accuracy of the registration technique developed in Chapter 3 and refine the experimental protocol (Chapter 4). The use of an optical tracking system increased the accuracy of this registration to <1.00mm. With this increased accuracy from refining the experimental protocol and employing the optical tracking system, the inter-bone distance algorithm was finally integrated with the registration technique to achieve the overall objective of this thesis which was to examine, non-destructively, congruency of joints undergoing simulated elbow flexion. In this study, we described in detail the methodology employed, assessed the accuracy of the registration and validated the ability of the overall technique to predict regions of joint contact as defined by the experimental cast.

Once the technique had been developed, and its accuracy assessed, it was applied to a clinical scenario. Using the techniques described in detail in Chapter 4, the effect of ligament stability on congruency at the ulnohumeral articulation was examined (Chapter 5, Objective 4). As well, the relationship between valgus angulation, a traditionally employed kinematic measurement of elbow stability, and measured joint congruency was examined. The results of this study concluded that the registration and inter-bone distance algorithm developed in this study was sensitive enough to detect subtle changes in joint stability, despite only very small changes in the measured valgus angulation. This study verified the suspicion that perhaps the reason that osteoarthritis develops, despite attempts to treat common orthopaedic injuries, is because there are alterations in joint surface interactions which lead to abnormal and excessive cartilage loading. Prior to this thesis,

there were no previously reported techniques that could assess joint congruency in a physiological scenario.

The objective of the final study was to extend the scope of this proximity mapping technique. The technique proved to be sufficiently accurate to examine orthopaedic injuries in our laboratory, but this was limited to cadaveric specimens undergoing simulated elbow flexion. When employing the inter-bone distance algorithm in isolation, the only invasive part of this protocol was the requirement to scan each patient using x-ray CT. Radiation has been of growing concern and was a limiting factor that would limit the application of this technique in a clinical environment. Chapter 6 examines the minimum dosage requirement to accurately obtain volumetric images of the shoulder joint so as to measure glenohumeral joint congruency (Chapter 6, Objective 5). The glenohumeral joint was chosen as it is close to the thyroid, which is particularly susceptible to harmful radiation. We also wanted to demonstrate the potential this technique has in quantifying joint congruency in other joints of the body. The results of this study indicated that the effective dose applied to the shoulder could be reduced by 88.9% compared to standard clinical CT imaging protocols while maintaining the accuracy of the joint congruency mapping technique.

7.2   Strengths and Limitations

It is recognized that these studies are not void of shortcomings. The major limitation of the joint congruency tool developed in this thesis is that, in the absence of cartilage, joint congruency is only an approximation to the actual joint contact area.

While every effort was made to validate and compare the joint congruency maps with actual measurements in joint contact, these measures provide only a surrogate. Cartilage was measured in Chapter 4 as well in Appendix B, to obtain an estimate of the average joint space. However, the location and thickness of cartilage in the ulnohumeral joint is not homogenous. The variable cartilage distribution in this joint is partly the reason that a proximity mapping technique was employed initially. While every attempt was made to avoid referring to the measured joint congruency as 'contact', this technique will always be an approximation of the actual joint contact in the absence of cartilage.

The use of x-ray CT is another limitation of this thesis. Clinically, CT is used to assess joint alignment and health. When developing this technique, CT was chosen given its frequent use in the clinic and its ability to provide high contrast images of bone. The ability of CT to provide soft-tissue contrast however is limited so it was used only to image the cortical and subchondral bone regions. The radiation exposure that CT requires is of major concern when implementing this technique in a clinical setting. While an attempt was made to reduce the radiation exposure required (Chapter 6), CT imaging is not benign and may limit the clinical application of this technique.

The use of cadaveric specimens, in an *in vitro* environment is another limitation of this thesis. While the elbow motion simulator has proven to be repeatable and representative of physiologic motion, it is still only an approximation of *in vivo* motion. The types of motions simulated in this thesis were limited to four gravity dependent positions undergoing constant velocity elbow flexion/extension. The specimens used in this thesis were elderly as expected for any cadaveric study and this was reflected in the

overall health of the tissues and bone structures. While CT images were examined by clinicians and determined to be free of radiographic arthritis prior to use, mild degenerative changes were often seen on the cartilage surfaces of these specimens.

Another limitation was the sample size was less than 6 specimens for Chapter 3 and Chapter 5. In these protocols 11 specimens were tested in Chapter 3 and 8 specimens were tested in Chapter 5. However, due to difficulties in the experimental protocol, specimens were excluded from these studies. This provides insight into the actual tedious nature of the experimental protocol employed. A protocol for a typical specimen would require four or more days to prepare, test and then perform the post-testing fiducial marker protocols. Several CT scans were required of each specimen which added to the tedious nature of the experimental protocol. Despite efforts to refine the registration protocol from Chapter 3 to Chapter 4, the use of fiducial markers was extremely time consuming. Although a power analysis was done to ensure that appropriate sample sizes were obtained to detect differences in measured joint congruency due to clinical variables, additional specimens would have increased the power of statistical analyses examining the effect of elbow flexion on joint congruency.

The length of the experimental protocol required may have also contributed to the overall registration error. While the average joint space of the ulnohumeral joint is < 3mm, the measured registration error in Chapter 4 was <1mm. Overlap was found in three of the five specimens in Chapter 5. Further refinement of this registration protocol will increase the accuracy of the registration and decrease joint surface overlap.

Despite these limitations, significant progress was made using the techniques developed in this thesis to examine joint surface interactions. Joint congruency could be analyzed post-hoc and did not require exposure to the joint surfaces during testing. This is important because it allows investigation of continuous elbow flexion and also preserves the native anatomy. In addition, although joint contact area was not measured directly, every attempt was made to validate the inter-bone distance algorithm to ensure that regions of proposed joint surface interaction did coincide with actual joint contact area.

The use of this technique to examine the effect of various clinical injuries on the resulting joint mechanics is novel. This technique is currently being used in the laboratory to examine the effect of humeral hemi-arthroplasty implants on resulting joint congruency. The effect of overstuffing and oversizing the humeral components is also being evaluated. This technique is also currently being used to investigate the effect of radial head arthroplasty on radiocapitellar joint congruency.

This is the first study that has incorporated kinematic data obtained from tracked motion with the 3D models obtained from CT. Using the techniques described in Chapter 3 and Chapter 4, 3D visualization of the osseous structures can be readily seen for any frame of elbow flexion. The registration technique developed in this thesis will continue to be used in other biomechanics studies employing the elbow motion simulator. Using this approach, small changes in the bony alignment can be readily visualized. These techniques can also be used in various computer-assisted techniques and when examining functional anatomy.

This is the first study in our laboratory to be able to, visualize and quantify joint congruency in 3D. Prior to this work, joint contact area was measured using experimental casting or dye-staining. With the techniques developed in this thesis, 3D images describing the joint surface interactions can be readily seen and compared across positions in elbow flexion as well as before and after a simulated clinical scenario. The inter-bone distance technique is also being used to measure cartilage thickness to create volumetric 'cartilage thickness maps'. As well the inter-bone distance algorithm is being used to compare similarities in geometries (implants versus native geometry), to measure registration and to validate the use of various 3D reconstruction algorithms. As well, the techniques developed in Chapter 4 to digitize the contact area casts and to reconstruct these digitizations into a 3D surface continue to be used in the laboratory.

Finally, the current registration protocol is for use in biomechanical *in vitro* studies. Typically, these biomechanical experiments investigating joint stability employ cadaveric specimens in an *in vitro* experimental protocol as previously noted. While there are limitations associated with their use, cadaveric specimens offer a significant advantage over *in vivo* patients in a clinical setting. *In vitro* studies allow surgical interventions and therapies to be carefully evaluated because of the controlled testing environment and repeatable simulated motion that can be achieved with advanced simulators. In this experimental approach, the intact, non-injured joint kinematics are first recorded. Ligamentous injuries or osseous fractures are then simulated and then are subsequently repaired or treated with surgical intervention. Various surgical techniques can be explored and the resulting kinematic motion can be recorded and compared with

the native, non-injured case. Because the motion pre and post surgical intervention is so repeatable, it is possible to examine only the effect of the surgical intervention on the joint kinematics and joint congruency in the absence of confounding variables seen in most *in vivo* studies. Therefore, this technique is very useful in the examination of various surgical techniques and rehabilitation procedures.

7.3 Current and Future Directions

There are two separate directions that the techniques developed in this thesis will take; *in vitro* experimental testing and *in vivo* patient analysis of joint congruency. The first is for use of these techniques in the experimental laboratory. As previously stated in Chapter 4, refinement in the fiducial protocol, perhaps by using tantalum beads, may increase the accuracy of the registration and reduce the experimental protocol. Increasing the accuracy of the registration will decrease the amount of overlap present after registration. As well, efforts will be made to automate the registration *and* data analysis as both of these were time consuming. Once these techniques are automated, 3D joint congruency can be examined in real time during testing and will provide feedback to the surgeon while undergoing surgery. By examining the joint congruency maps, surgeons can elect to use alternative reconstructive techniques to preserve the joint alignment and therefore the underlying cartilage.

Efforts should also be made to integrate the protocols developed in this thesis into a clinical environment in a knowledge translation research project. Chapter 6 attempts to reduce the potentially deleterious effects of radiation. However, further modifications to

the scanning parameters are required for other joints. As well, an assisted device may need to be created to statically hold the joint in a fixed position. Joint congruency is very sensitive to joint alignment. Therefore, to compare joint congruency in patients at two time points, or before and after a clinical intervention, the joint should be imaged in the same position and orientation for a direct comparison. This tool may also be used to investigate the effect of various non-surgical repair techniques (braces) on joint alignment and joint congruency.

Several studies are already undergoing in an effort to improve the techniques developed in this thesis. The first major study investigates the choice of x-ray CT as the medical imaging technique to acquire volumetric image sets. In a controlled and highly repeatable compression loading device, alternative imaging modalities are being compared. Specifically, MRI and microCT imaging devices are being used to obtain 3D datasets and used in conjunction with the inter-bone distance algorithm to determine which technique most accurately predicts joint contact area. As mentioned in Chapter 4, previous studies have suggested that bone-to-bone inter-bone distance techniques have a tendency to overestimate joint contact area. Therefore, these image data sets will be used to address this concern. MRI data will be employed to reconstruct bone reconstructions *and* cartilage reconstructions to measure joint congruency. Additionally, cartilage thickness studies are being conducted. The first experimental study examines cartilage thickness at the ulnohumeral joint using the MRI images. The second study uses isolated denuded bones with air contrast to measure cartilage thickness. These measurements are

being made in attempt to account for cartilage thickness in the current proximity mapping protocol to allow us to directly measure joint cartilage contact.

The second major study (Appendix H) involves assessing the accuracy of the 3D reconstructions employed in this thesis. The techniques developed herein rely on 3D reconstructions obtained using CT. However, the accuracy of this reconstruction has not been previously. Therefore in this second major study, the accuracy of the 3D reconstructions techniques employed in this thesis is being assessed by comparing the native bone geometry with the 3D reconstruction. Surface digitizations were recorded of cartilage-dissolved subchondral bone. The digitizations created a point cloud that was then used to reconstruct a 3D surface. This surface corresponds to the ground truth. The inter-bone distance algorithm is being employed in this study to compare the overall differences in geometry between the ground truth and the virtual reconstruction.

7.4 Significance

Despite attempts to restore function of the joint following injury or trauma, an unacceptable amount of patients develop arthritis. There is, as previously stated, a lack of understanding between the cause and subsequent progression of osteoarthritis. Joint mal-alignment has been previously shown to contribute to the progression of OA in the knee (Hunter *et al.*, 2009). This lack of understanding has prevented the development of novel therapies that can be used to prevent and stop the progression of this debilitating disease (Sharma *et al.*, 2001). Using the techniques described in this thesis, it is possible to examine the effect of various clinical injuries and subsequent repairs on joint alignment

and congruency using proximity mapping. Through this research, a better understanding of the relationship between joint load, injury and joint alignment can be obtained. In addition to the application of these novel approaches for use in our *in vitro* laboratory, the techniques developed in this thesis will also significantly contribute to the development of *in vivo* based measurements in patients. The techniques developed in this thesis have already been used by other researchers in our laboratory to elucidate the effect of joint arthroplasty on resulting joint mechanics as it relates to the development of osteoarthritis. These techniques can also be modified for use in all joints; there will likely be considerable interest in researchers studying both lower extremity and spine.

In conclusion, the knowledge gained in this thesis, and the techniques developed will contribute to improvements in our understanding of the causes and prevention of degenerative diseases of the joints in the upper extremity.

7.5   References

Felson, D.T., Lawrence, R.C., Dieppe, P.A., Hirsch, R., Helmick, C.G., Jordan, J.M., Kington, R.S., Lane, N.E., Nevitt, M.C., Zhang, Y., Sowers, M., McAlindon, T., Spector, T.D., Poole, A.R., Yanovski, S.Z., Ateshian, G., Sharma, L., Buckwalter, J.A., Brandt, K.D., and Fries, J.F. (2000) Osteoarthritis: new insights. Part 1: the disease and its risk factors. *Ann.Intern.Med.* 133[8], 635-646.

Hunter, D.J., Sharma, L., and Skaife, T. (2009) Alignment and osteoarthritis of the knee. *J.Bone Joint Surg.Am.* 91 Suppl 1, 85-89.

Sharma, L., Song, J., Felson, D.T., Cahue, S., Shamiyeh, E., and Dunlop, D.D. (2001) The role of knee alignment in disease progression and functional decline in knee osteoarthritis. *JAMA* 286[2], 188-195.

A.   Appendix A- Glossary

Anterior	Situated in or toward the front surface of the body
Arthritis	Acute or chronic inflammation of the joint often resulting in pain and structural changes to the joint
Arthroplasty	A surgical procedure to restructure the joint to restore it
Articular	Of or relating to a joint
Articular Cartilage	Cartilage that covers the articular surface of a synovial joint
Articulation	A place of anatomical union, usually movable between two or more bones
Biceps	Main extensor muscle of the elbow and supinates the forearm located on the front of the forearm
Brachialis	The largest of the muscles that act to flex the elbow
Brachioradialis	A flexor of the elbow located on the radial side of the forearm originating near the lateral epichondyl of the humerus and inserts into the base of the radial styloid
Cadaver	A dead body which may or may not be preserved, used for anatomical dissection
Cadaveric Study	A study employing the use of a dead body
Capitellum	Spherical shaped region on the lateral side of the distal humerus which articulates with the radial head forming the radiocapitaller joint. The motion of this joint in rotation.
Cartilage	In orthopaedics, cartilage is a collagen composite material covering the articular surfaces of a joint used to reduce friction between opposing bone surfaces.
Coronal Plane	Any vertical plane passing through the body dividing it into its frontal and backward regions extending from the nose the back of the head
Coronoid	An osseous process that appears on the inferior region of the proximal ulna. This process is the osseous structure that terminates elbow flexion as it gradually

	approaches the coronoid fossa on the humerus through the arc of motion
Cortical Bone	Compact bone that surrounds the outer surface of the bone found predominately in the bony shaft
Diarthrodial Joint	See Synovial Joint
Distal	Anatomically located far from a point of reference; opposite of proximal
Dorsal	Anatomically located on the back surface of the body
Epichondyl	A rounded projection of a bone providing a surface for the attachment of ligaments, tendons and muscles
Extension	The act of extending or straightening a limb
Flexion	The act of flexing or bending a limb
Fossa	A bony depression
Greater Sigmoid Notch	The articular surface of the proximal ulna which articulates with the trochlea of the distal humerus
Humerus	The long bone of the upper arm
Hyaline	A glossy or transparent surface
Inferior	Anatomically located below or under, closer to the bottom
Instability	A pathologic condition in which there is an inability to maintain the normal relationship of the distal humerus with the proximal surfaces of the radius and ulna
In vivo	Within a living body
In vitro	In an artificial environment, or using cadavers
Joint Capsule	A cartilaginous structure surrounding a joint containing the synovial fluid. Is also a joint stabilizer
Kinematic	The description, measurement, and recording of body motion without regard to the forces acting to produce the motion
Lateral	Anatomically pertaining to the outside of the midline of the body
Lesser Sigmoid Notch	A depression on the distal region of the proximal ulna that articulates with the radial head forming the proximal radio-ulnar joint
Ligament	A band of fibrous tissue connecting bones

	or cartilages
Medial	Anatomically pertaining to the inside of body, closer to the midline of the body
Muscle	An organ that contracts and produces movement of a person or animal
Olecranon	An osseous process located on the most proximal tip of the proximal ulna. This process serves as the structural limit to elbow extension as it approaches the olecranon fossa, of the humerus through the arc of motion
Orthopedics	The branch of medicine that deals with the preservation and restoration of the skeletal system
Osteoarthritis	Is a degenerative joint disease caused by the gradual loss of articular cartilage as a result of overuse mal-position of the bones within a joint
Posterior	Situated toward the back surface of the body
Process	A bony prominence or projection
Pronation	In the forearm, pronation is the rotation of the radius around a fixed ulna resulting in the palm down position
Proximal	Anatomically located close to a point of reference; opposite of distal
Radial Head	Located at the most proximal end of the radius, this disk shaped structure articulates with the capitellum on the lateral of the humerus and with the ulna at the lesser sigmoid notch of the ulna
Radiohumeral	Radiocapitellar joint describing where the radial head articulates with the capitellum to produce forearm rotation
Radioulnar	An articulation where the ulna and radius articulate. This occurs at the distal end of the forearm called the distal radioulnar joint (DRUJ) and at the proximal end of the forearm at the proximal radioulnar joint (PRUJ)
Radius	A long slightly curved bone what is on the lateral side of the forearm.
Subchondral	Bone in a joint situated beneath the

	cartilage
Superior	Situated higher above another
Suture	A stitch or a series of stitches
Synovial Joint	An articulation permitting motion, the union of bony elements surrounded by an articular capsule enclosing a cavity containing synovial fluid
Tendon	A cord of dense inelastic fibrous tissue serving to connect a muscle to bone
Triceps	The main extensor of the arm, located on the back of the forearm
Trochlea	The medial region of the distal humerus which articulates with the greater sigmoid notch of the proximal ulna. The motion of this joint is flexion and extension
Ulna	The medial long bone of the forearm
Ulnohumeral	The articulation described by the proximal ulna and the distal humeral components. The motion of this joint is flexion and extension. Also called the humeroulnar joint.
Valgus	Bent out, twisted, denoting a position of the anatomy away from the midline of the body
Varus	Bent in, denoting a position of the anatomy toward the midline of the body

B. Appendix B –Cartilage Thickness

B.1 Introduction

Synovial joints are remarkable bearings, capable of functioning *in vivo* under dynamic pressures of up to 1 MPa (Hodge *et al.*, 1986). Hyaline cartilage lines the surface of synovial joints and serves an important role in the lubrication of the joint (Modest *et al.*, 1989). It is avascular, aneural and possesses no intercellular connections. Composed primarily of water, this tissue is able to transfer enormous loads 3-5 times the body weight evenly to the subchondral bone below (Mow *et al.*, 1984; Mow *et al.*, 1993). Under physiologic loads, the cartilage is able to dissipate this load during motion and overall provide an almost frictionless gliding surface (Eckstein *et al.*, 2006a).

This was a parametric study investing the location and thickness of the cartilage on the surfaces of the distal humerus and proximal ulna. A review of the literature indicates that there is a wide distribution in the amount and location of cartilage found on the proximal ulna. Therefore, in order to investigate this inherent inhomogeneity in location of the cartilage in the ulnohumeral joint, the articulating surfaces were divided into zones. The articulating surfaces of the distal humerus and proximal ulna were manually sliced using a diamond saw and scanned using a computer scanner. The slices of the proximal ulna were then stained with Alcian Blue to improve the contrast between the cartilage and the subchondral bone.

B.2 Methods

A single fresh frozen specimen (90 years old, Male) showing minimal signs of cartilage degeneration was selected. All soft tissues were carefully dissected and removed. The humeral and ulnar shafts were cropped for potting purposes. The surfaces of the articulation were divided manually by drawing lines signifying cutting planes with a surgical marker. The humerus was divided into eight zones by creating three planes (Figure B.1). The first of these extended longitudinally through the trochlea grove dividing the medial and lateral facets of the trochlea. Secondly, a distal line was drawn sectioning the distal humerus coronally dividing the anterior and posterior sides of the trochlea.   Finally, a line was drawn transversely through the middle of the anterior surface dividing the trochlea in a superior and inferior region. The four posterior regions were combined to form the medial posterior region and the lateral posterior region. The articulating regions of the proximal ulna were divided into two zones (Figure B.2).   For the ulna, a transverse line was drawn segmenting the posterior and anterior regions of the ulna, namely the olecranon region and the coronoid region. The shaft of the ulna and humerus were then potted into small cardboard frames, using DenStone® (DenStone® Miles Inc. South Bend, IN, USA) as cement. This allowed the bones to be clamped into the guiding clamp of the diamond saw.   The potted bony surfaces were clamped into a diamond saw and oriented such that the articulating surface was perpendicular to the saw. They specimen was irrigated during sectioning and immediately placed in water. A rotary dial, located on the saw clamp was used to calibrate the slice thickness. Each rotation translated the saw 0.625mm. In order to prevent the slices from flaking off, a

ratio of two rotations per slice was used yielding a slice thickness of 1.252mm. The saw

started at the medial side of the humerus and ulna and traversed in 1.252mm increments

until it reached the lateral side. Each slice was stored separately.
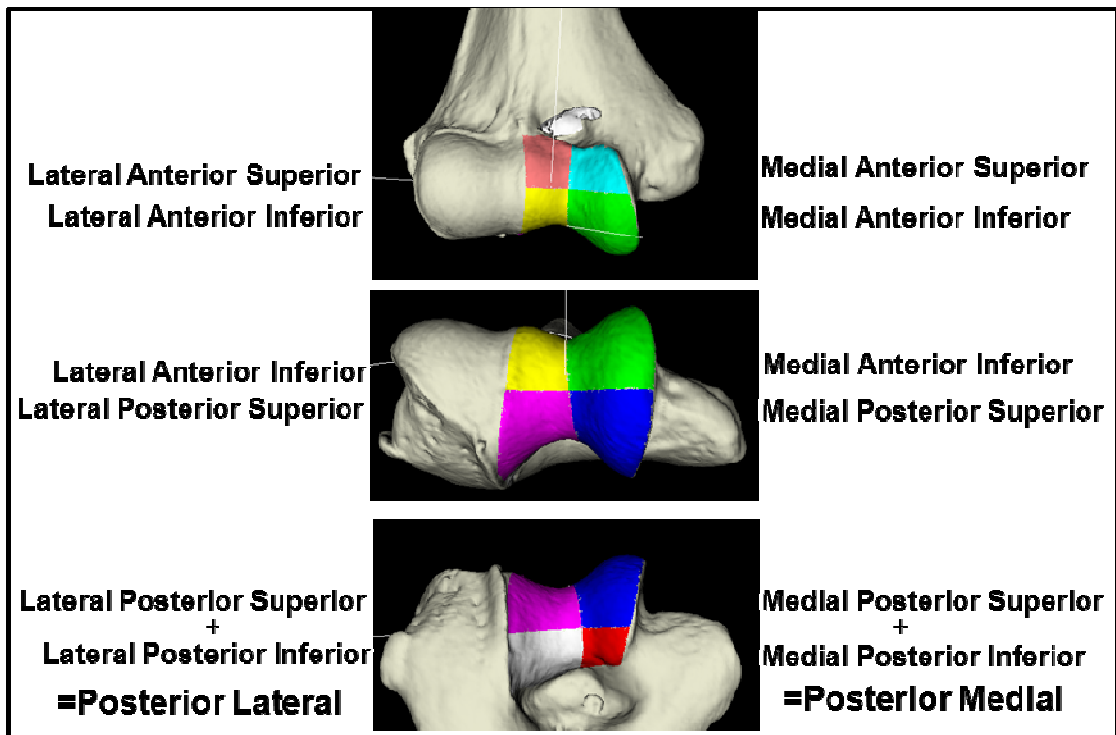
Figure B.1: Distal Humerus Zones
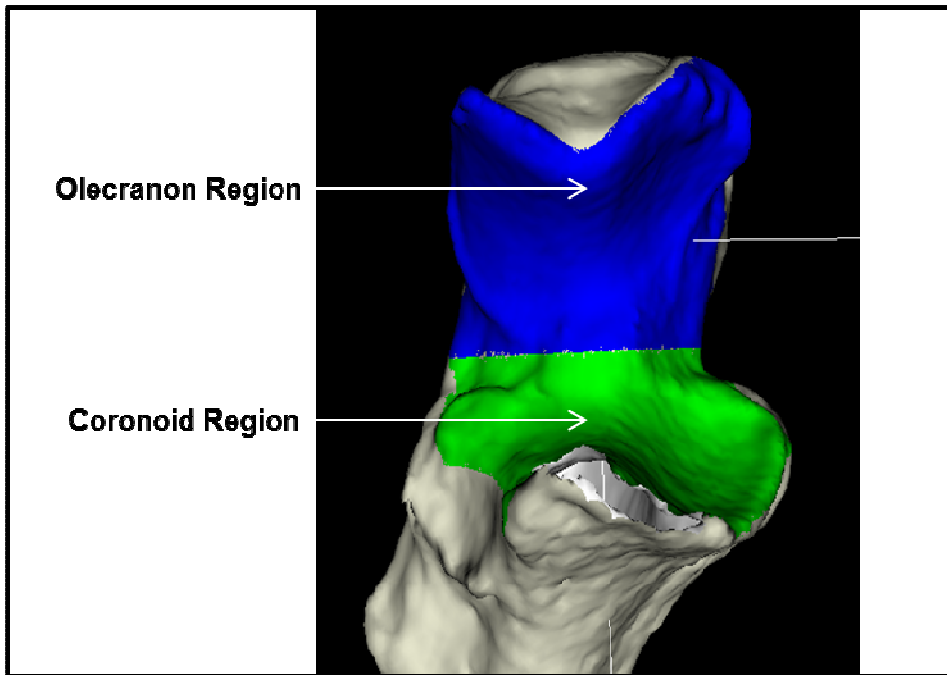
Figure B.2: Proximal Ulnar Regions

The ulnar slices of the coronoid and olecranon were stained to easily distinguish the cartilage from the subchondyl bone. The measurements made for the ulnar slices were taken from the start, end and middle of each section. The humerus on the other hand was separated into zones that were not anatomically bound and therefore required the marked zones regions to be present during slicing. Staining in this case would wash away the marker therefore the humeral slices were left unstained to delineate the zones using markers.
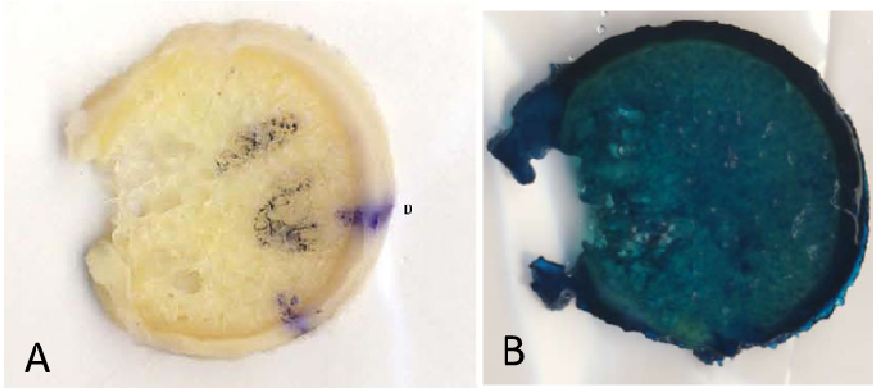
Figure B.3: Humeral Slice
A) Unstained
B) Stainted

Staining Protocol:

Alcian blue is often used to stain cartilage in embryonic specimen of frogs. The thickness of cartilage in these slices required an adapted protocol to account for this difference. Therefore, slices were stained for 5 nights and successive washes were often necessary to remove the blue stain from the subchondral bone. Alcian Blue is not water soluble; therefore the first part of this protocol involved dehydrating the slices with Ethanol. Subsequent to this, Alcian Blue was added to the vile and stored. In order to correctly identify the cartilage, slices were washed with varying solutions of potassium hydroxide and ethanol. The blue in the subchondral bone washed away with successive solutions until it appeared light in contrast to the still stained dark blue cartilage. Glycerol with a dilute solution of potassium hydroxide was used to preserve the stain in the cartilage. Slices were stored in primarily glycerol solutions until they were analyzed. The remaining of the protocol was as follows:

DEHYDRATE:

    a. Place slices into 10 mL of 95% EtOH for 5 min

    b. Empty container and place 10 mL of 95% EtOH for another 5 min (repeat 2 more times for a total dehydration time of 20 minutes)

STAIN:

    a. Place 10 mL of Alcian Blue Acetic Acid (for three nights)

WASH IN KOH:

    a. Make up a solution of 2% KOH

b. Rinse in 10 mL 95% EtOH for 15 minutes

c. Empty container and refill with 10mL of EtOH for 15 minutes (repeat this for 2 more times for a total time of 1 hour)

REHYDRATE:

a. Rinse with 7.5 mL EtOH and 2.5 mL 2% KOH (10 minutes)

b. Rinse with 5.0 mL EtOH and 5.0 mL 2% KOH (10 minutes)

c. Rinse with 2.5 mL EtOH and 7.5 mL 2% KOH (10 minutes)

d. Rinse with 10 mL 2% KOH (10 minutes)

e. Rinse with 10 mL 2% KOH (10 minutes)

f. Rinse with 10 mL 2% KOH (10 minutes)

WASH WITH GLYCEROL:

a. Wash with 2.0 mL glycerol and 8.0 mL 2% KOH (1 hour)

b. Wash with 4.0 mL glycerol and 6.0 mL 2% KOH (1 hour)

c. Wash with 6.0 mL glycerol and 4.0 mL 2% KOH (1 hour)

d. Wash with 8.0 mL glycerol and 2.0 mL 2% KOH (1 hour)

STORE:

e. Store in 8.0 mL glycerol and 2.0 mL 2% KOH

<u>Cartilage Measurement:</u>

Humerus:

Twenty-two slices of the trochlea were obtained and scanned. The digital image of the slice was analyzed in ImageJ. A pixel-to-mm conversion was obtained using a scanned ruler where 15.7 pixels were equal to 1mm. The conversion was obtained by taking 5 readings of (1mm, 2x1cm, 2cm, and one 5mm) on the ruler. On the humerus, measurements were obtained at the anterior line and then 2mm around the circumference of the slice in either direction. Subsequent to this, cartilage was measured at the distal line and every 2mm away from this line. The humeral slices (22 slices) were not stained in order to preserve the marker lines delineating each zone. Therefore measurements for the humerus were taken from unstained slices.

Ulna:

Prior to measuring the cartilage thickness, all 24 slices of the proximal ulna were stained. Cartilage thickness values were obtained for the posterior and anterior surface of the ulna. Slices started at the olecranon and coronoid process respectively and ended at the transverse, medial section of the ulna where the cartilage gradually tapered to a value of zero right at the centre. Subsequent to staining, images were brought into ImageJ and measurements of cartilage, at approximately every 2mm were obtained around the circumference of the slice.

B.3   Results
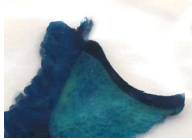
Olecranon 2	Olecranon 3	Olecranon 4	Olecranon 5	Olecranon 6
Olecranon 7	Olecranon 8	Olecranon 9	Olecranon 10	Olecranon 11
Olecranon 12				
Coronoid 1	Coronoid 2	Coronoid 3	Coronoid 4	Coronoid 5
Coronoid 6	Coronoid 7	Coronoid 8	Coronoid 9	Coronoid 10
Coronoid 11	Coronoid 12			

Figure B.4: Stained Ulna Slices
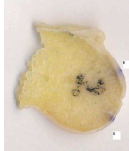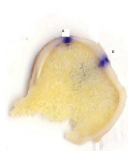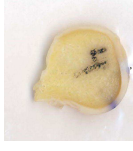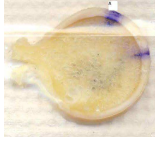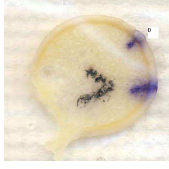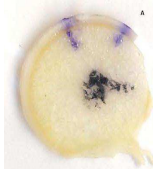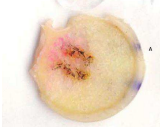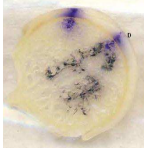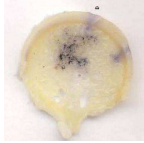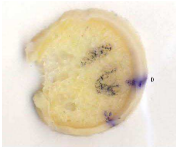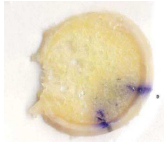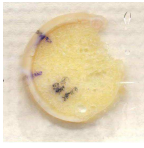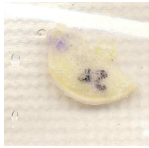
Humerus 1	Humerus 2	Humerus 3	Humerus 4	Humerus 5
Humerus 6	Humerus 7	Humerus 8	Humerus 9	Humerus 10
Humerus 11	Humerus 12	Humerus 13	Humerus 14	Humerus 15
Humerus 16	Humerus 18	Humerus 19	Humerus 20	Humerus 21
Humerus 22				

Figure B.5: Humeral Slices
NOTE: slices might not be in order from medial to lateral side
NOTE: also note that slice 17 ripped and was therefore discarded

Ulna	Mean (mm)	Max (mm)	Min (mm)	SD(mm)
Whole Ulna	**1.3**	2.07	0.35	0.38
Coronoid (n=54)	1.56	2.00	1.13	0.21
Olecranon (n=89)	1.15	2.07	0.35	0.37
Humerus				
Whole Humerus	**1.44**	2.84	0.51	0.38
MAS (n=38)	1.38	2.52	0.84	0.38
LAS (n=44)	1.58	2.84	0.68	0.53
MAI (n=28)	1.64	2.68	0.9	0.41
LAI (n=38)	1.48	2.4	0.51	0.4
PM (n=59)	1.44	2.02	0.81	0.28
PL (n=100)	1.33	1.97	0.68	0.3

Table B.1: Cartilage Thickness Measurements

n= the number of measurements taken

C.   Appendix C –Scale Considerations

C.1   Introduction

The objective of this appendix was to decide on the maximum scale value that will be used in this thesis. From Appendix A, the mean ulnar cartilage thickness was found to be 1.30mm and the mean humeral cartilage thickness was 1.44mm. Therefore, the mean combined cartilage thickness (adding these two values) was equal to 2.74mm. The surface area of entire humeral articulation (specifically this specimen) was 2533.39mm^2 which is roughly 1.5 times as large as the surface area of the ulnar articulation found to be 1636.55mm^2. The objective of this appendix was to, with the understanding of the typical cartilage thickness values found for the ulnohumeral joint, determine the scale that would be used for the proximity maps.

C.2   Methods

Proximity maps were created using 11 different maximum scale values. These images correspond to data collected in Chapter 2 in the unloaded scenario at full extension. The two views are of the anterior ulna and of the posterior humerus. For the posterior humerus, the two surfaces are contacting on the posterior side of the humerus as the olecranon process contacts the olecranon fossa.

C.3   Results

Figure C.1 shows the proximity map of the proximal ulna and distal humerus (posterior view as the elbow is in full extension) for each maximum scale value. In all of the images, it is apparent where the two surfaces are closest in their proximity. On the ulna, the region of closest proximity extends transversely across the superior/posterior region of the greater sigmoid notch and then extends distally along the medial side This pattern is shown in every maximum-scale scenario, however the size of this pattern and the color of this pattern change as the maximum value of the scale changes. However, when the maximum value is set to 20mm, this pattern is lost due to the fact that the entire scale and range of values is not used and is only located at the red end of the colour bar. This does not provide enough dynamic range to see the proximity pattern.

Max Value (mm)	Scale	Ulna (Medial: Right Side, Lateral: Left Side)	Max Value (mm)	Scale	Ulna (Medial: Right Side, Lateral: Left Side)	Max Value (mm)	Scale	Ulna (Medial: Right Side, Lateral: Left Side)
1			2			3		
4			5			6		
7			8			9		

Figure C.1: Proximity Maps created using different scales.
The values correspond to maximum values used on the scale. A final value of 0-4mm was chosen as this scale provided sufficient dynamic range of intensities shown and also was appropriate given the cartilage thickness values found in Appendix B.

D.   Appendix D–Distal View of Ulna 3D Model –Additional Specimen Specific Data

D.1   Results

Chapter 3 contains the distal view of the ulna near the wrist for a single specimen. This appendix contains this data for the remaining specimens in this study. Valgus angulation is also shown for the intact, radial head resected and radial head replaced scenario. All data shown is during active elbow flexion in the valgus gravity dependent position.
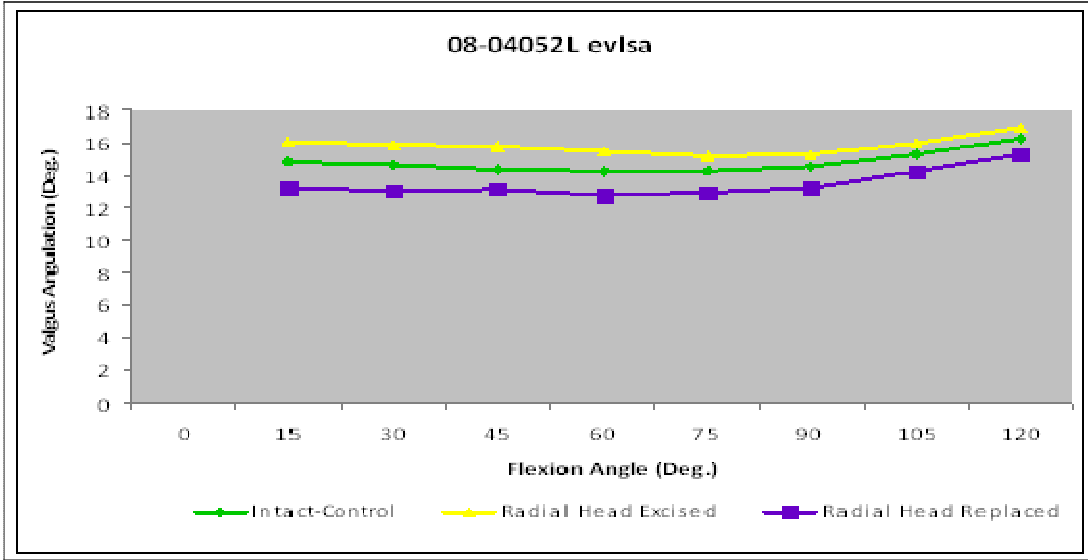
Figure D.1: Valgus Angulation_08-4052L
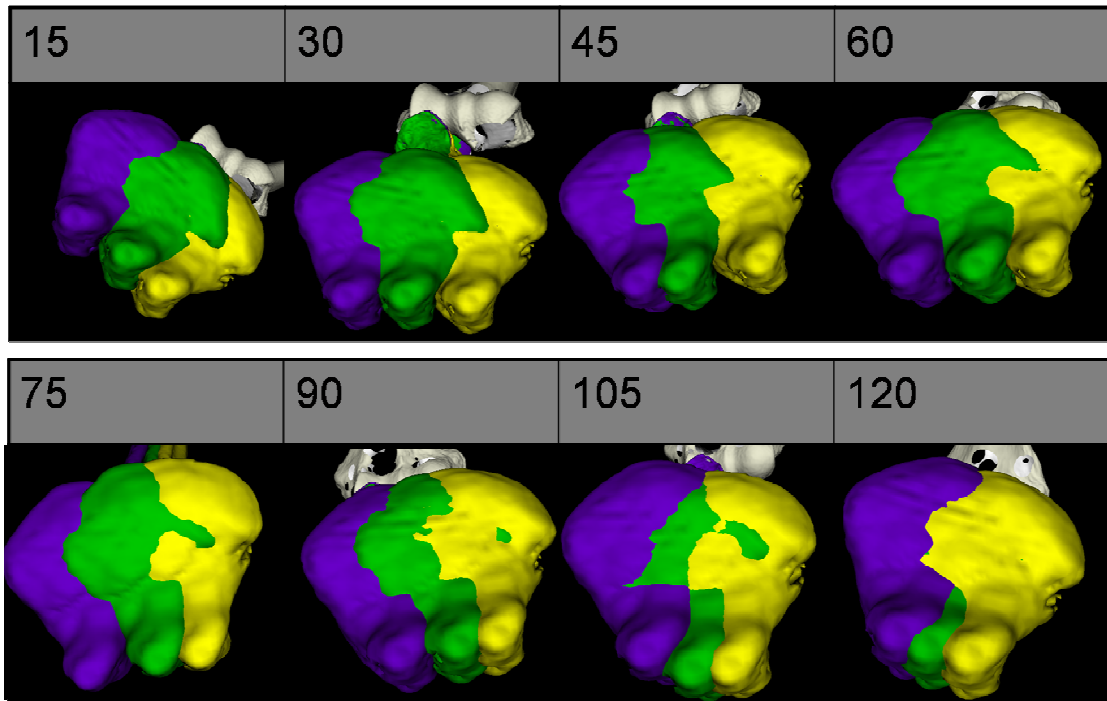
Figure D.2: Distal Ulna_08-04052L

Notes:

- Valgus angulation is a more provocative gravity dependent position for the radial head deficient elbow. The VA between intact, resected and replaced remains

relatively constant throughout flexion. However, the differences between all three decrease slightly with increase flexion. This is consistent graphically and visually.
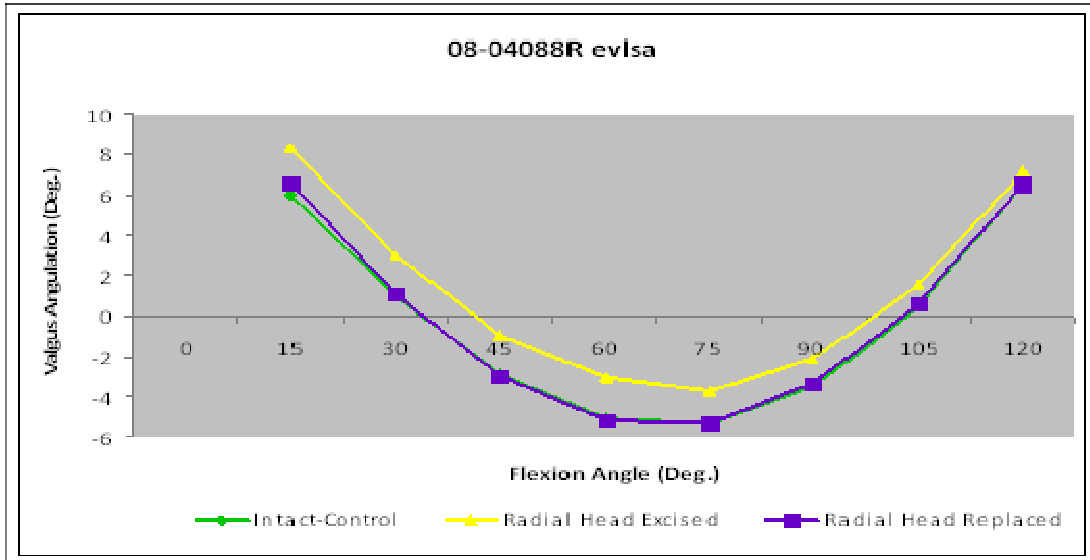
Figure D.3: Valgus Angulation _08-04088R
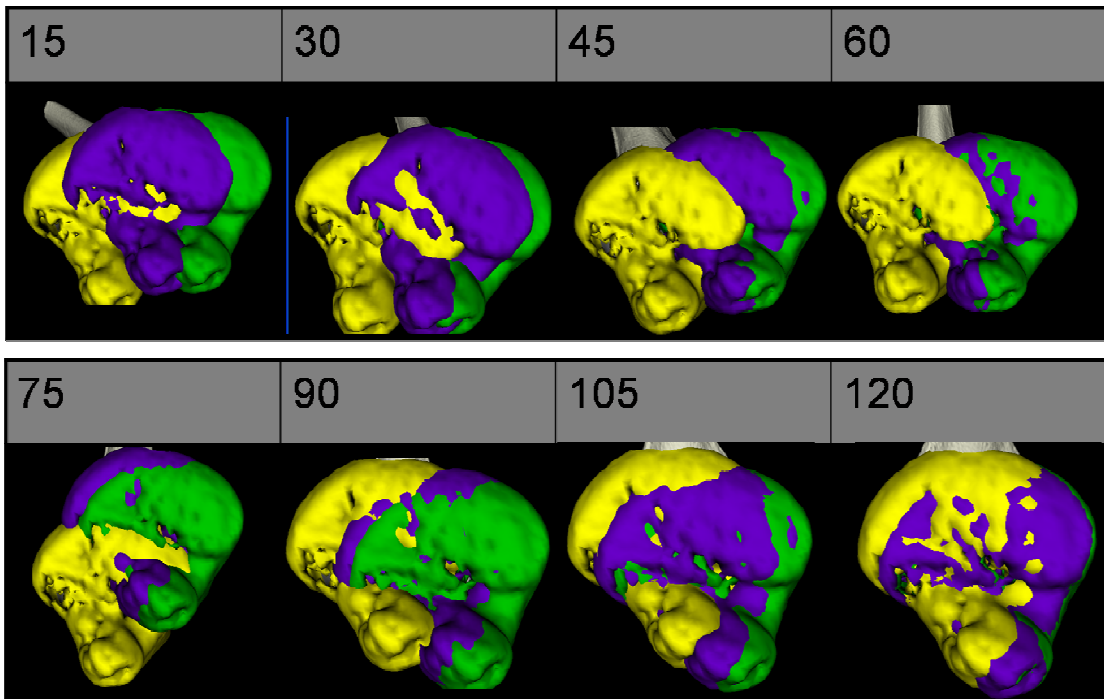
Figure D.4: Distal Ulna_08-04088R
Notes:
- In the valgus gravity loaded position, the elbow no longer appears to be overstuffed (graph + visual show this).
- The largest difference in VA between intact/replaced is at 15 degrees which agrees graphically and visually

- The increase in VA for resection does decrease with increasing flexion
- At 75 degrees, it appears that the resected ulna moves dorsally which could also be examined graphically
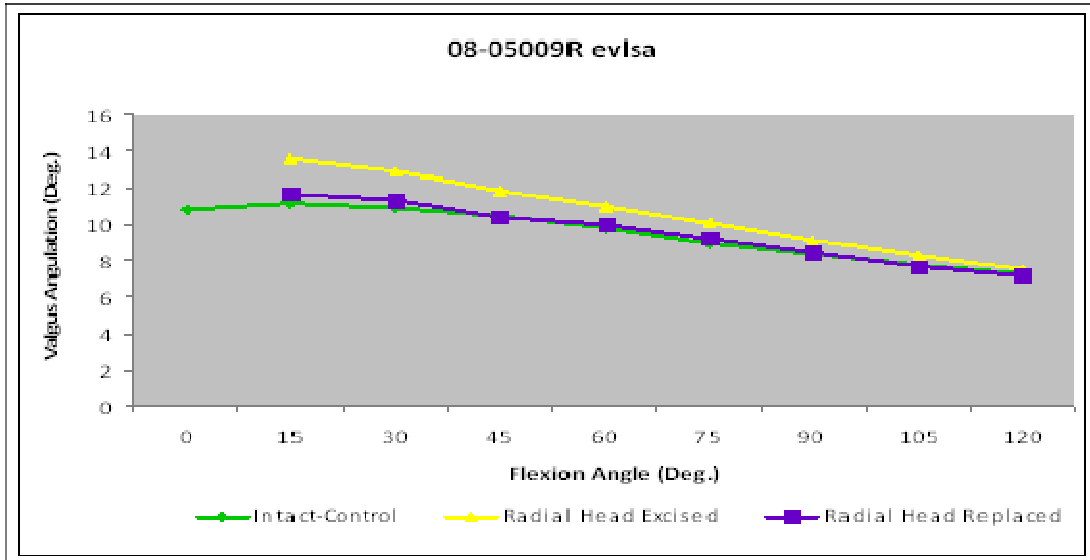
Figure D.5: Valgus Angulation_08-05009R
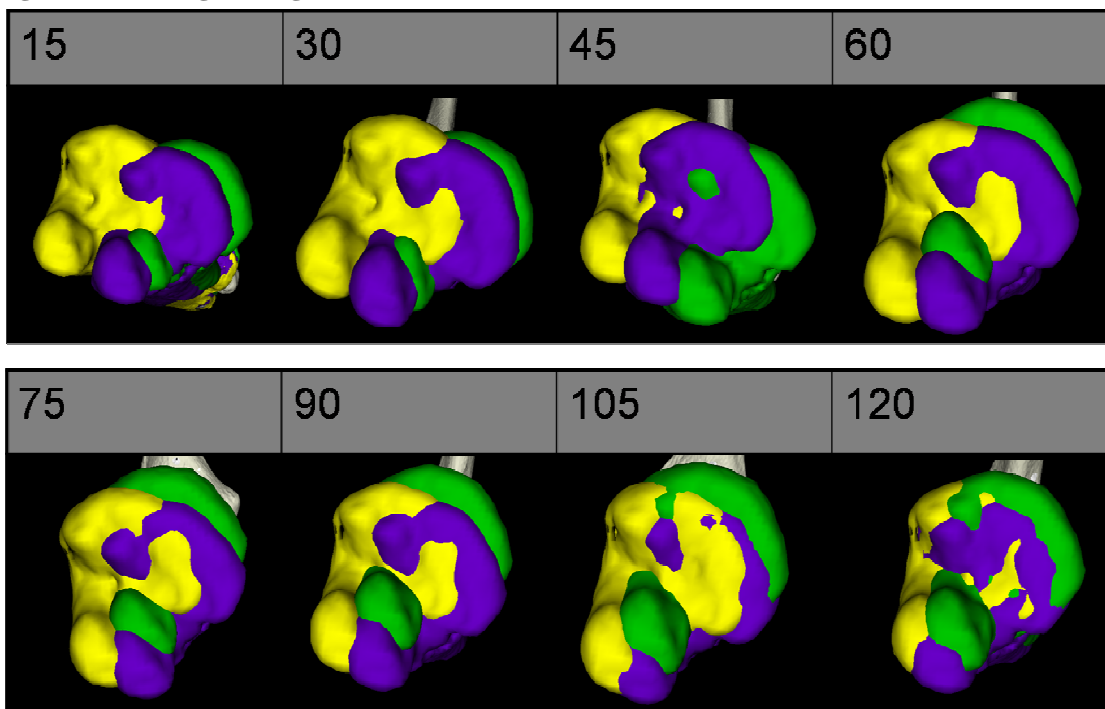
Figure D.6: Distal Ulna_08-05009R
Notes:
- However in the valgus position, overstuffing is not seen
- The replaced and intact VA remains very similar (but differ the most at 15º, 30º and 45º which is consistent visually). However, the dorsal/volar angulation appears different in all angles of flexion
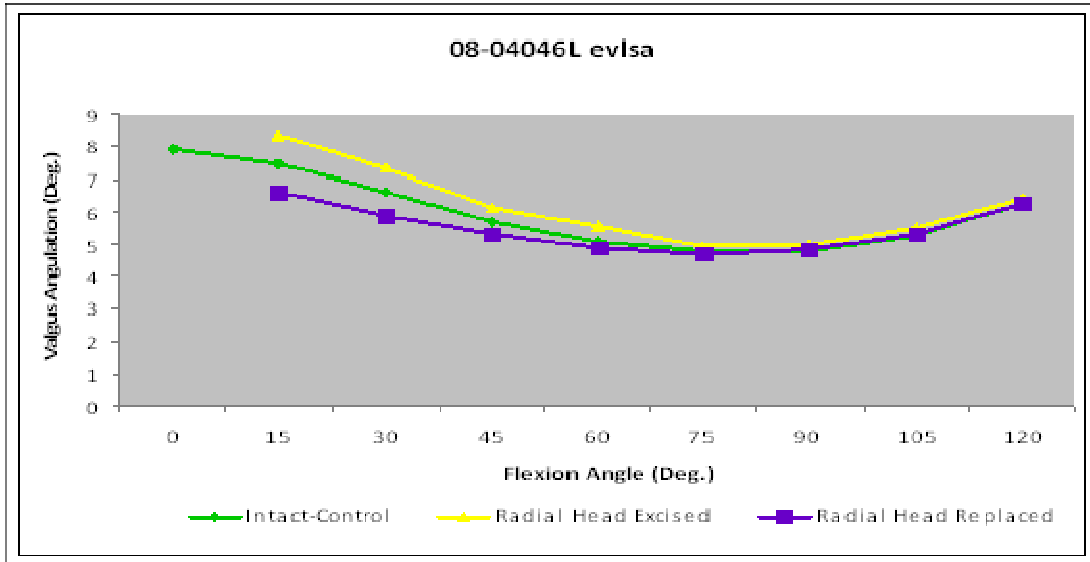
Figure D.7: Valgus Angulation _08-04046L
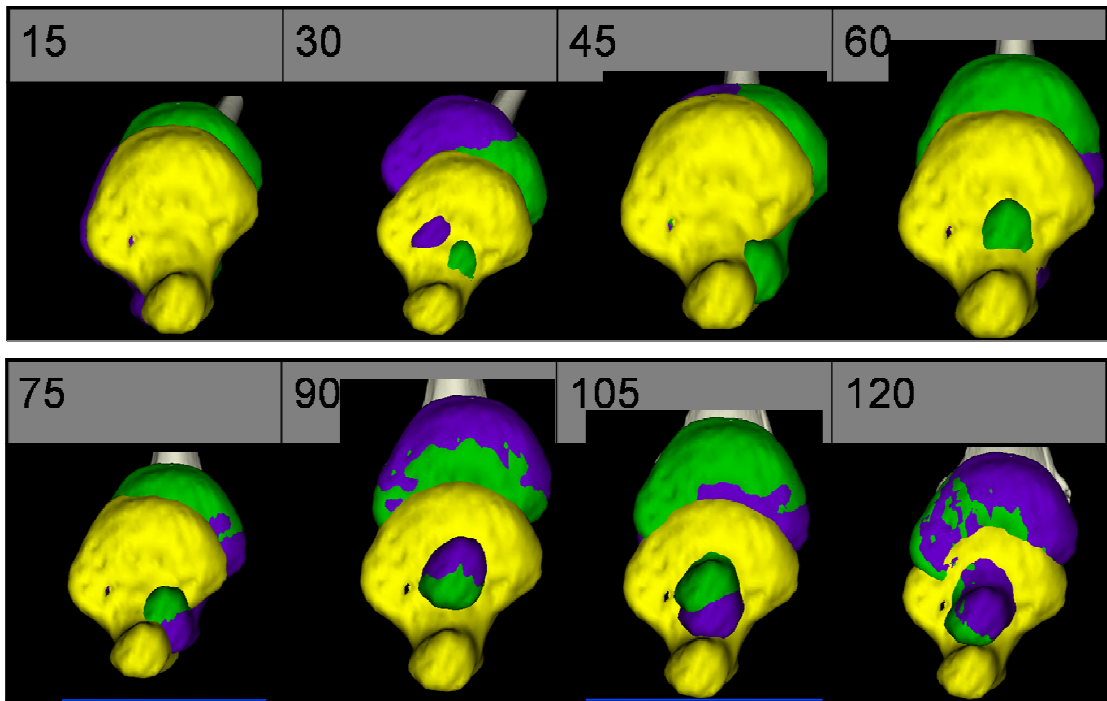
Figure D.8:Distal Ulna _08-04046L
Notes:

- Now in this valgus gravity dependent position, the same ulnar lengthening is shown, but to a lesser extent.

E. Appendix E–Additional Subject Specific Proximity Maps during Intact and Ligament Repaired Sceneries

E.1 Results

This appendix contains this data for the remaining specimens from Chapter 5. Proximity maps are shown for the intact and ligament repaired scenarios during active and passive elbow flexion (valgus gravity dependent).

Active:
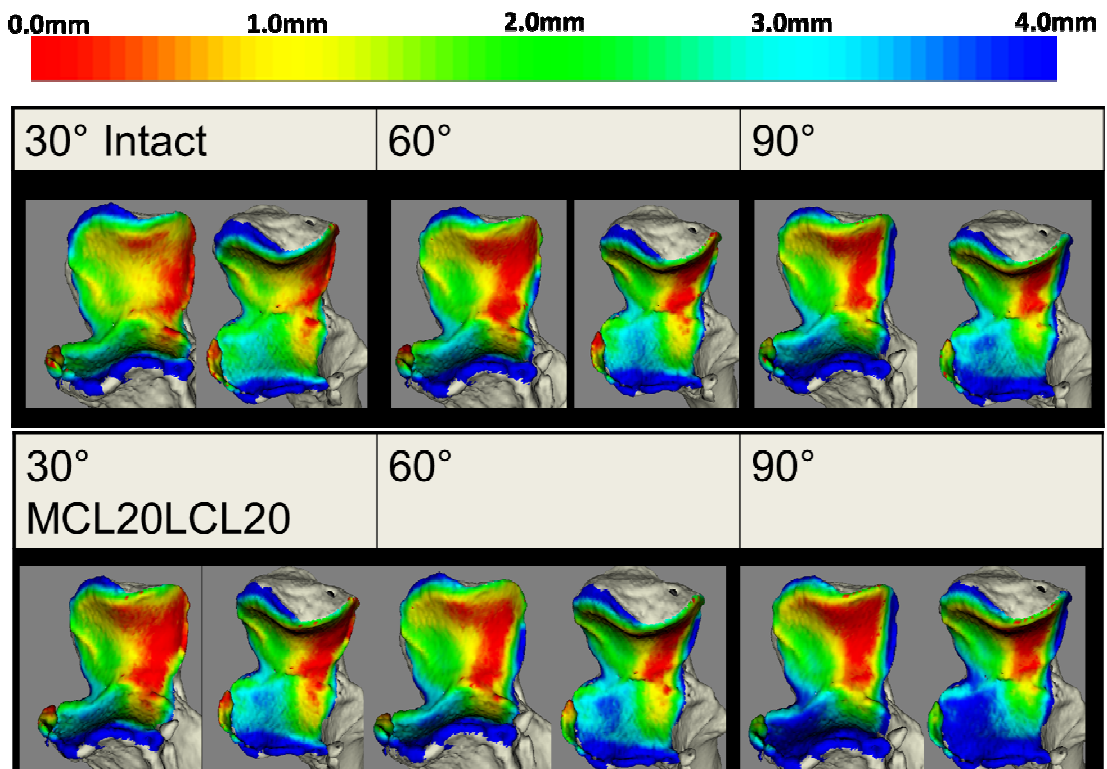
Figure E.1: Proximity Maps_1459L
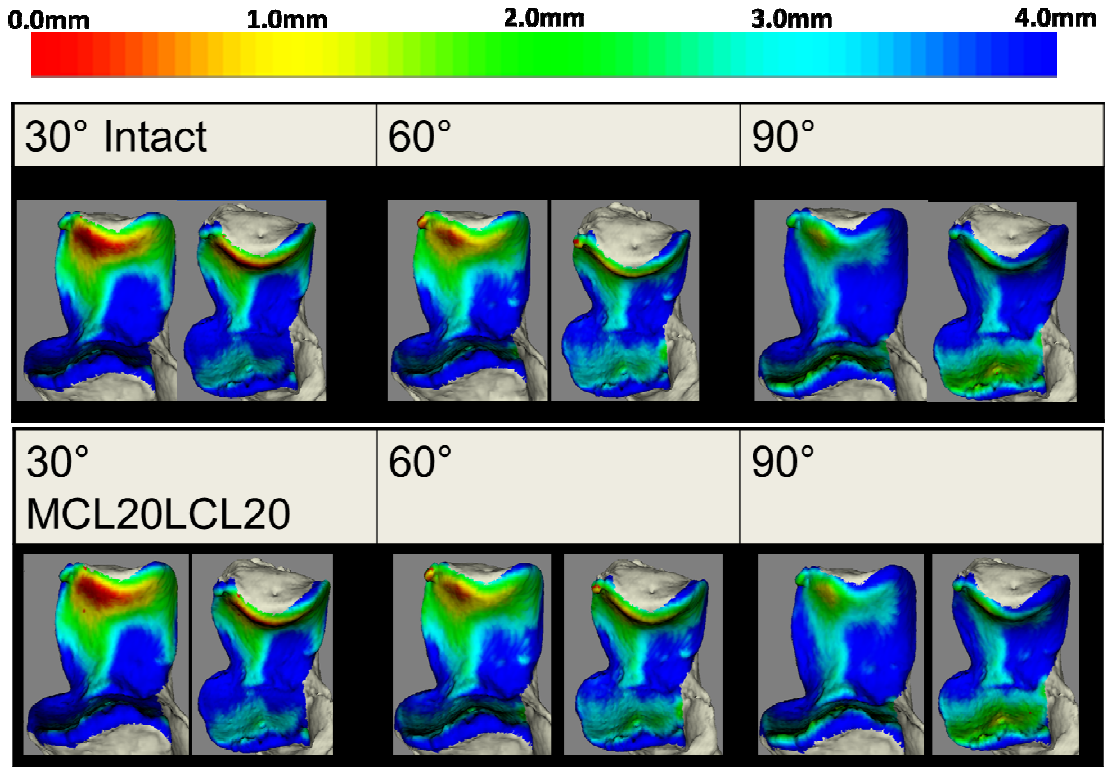
Figure E.2: Proximity Maps_09-12055L
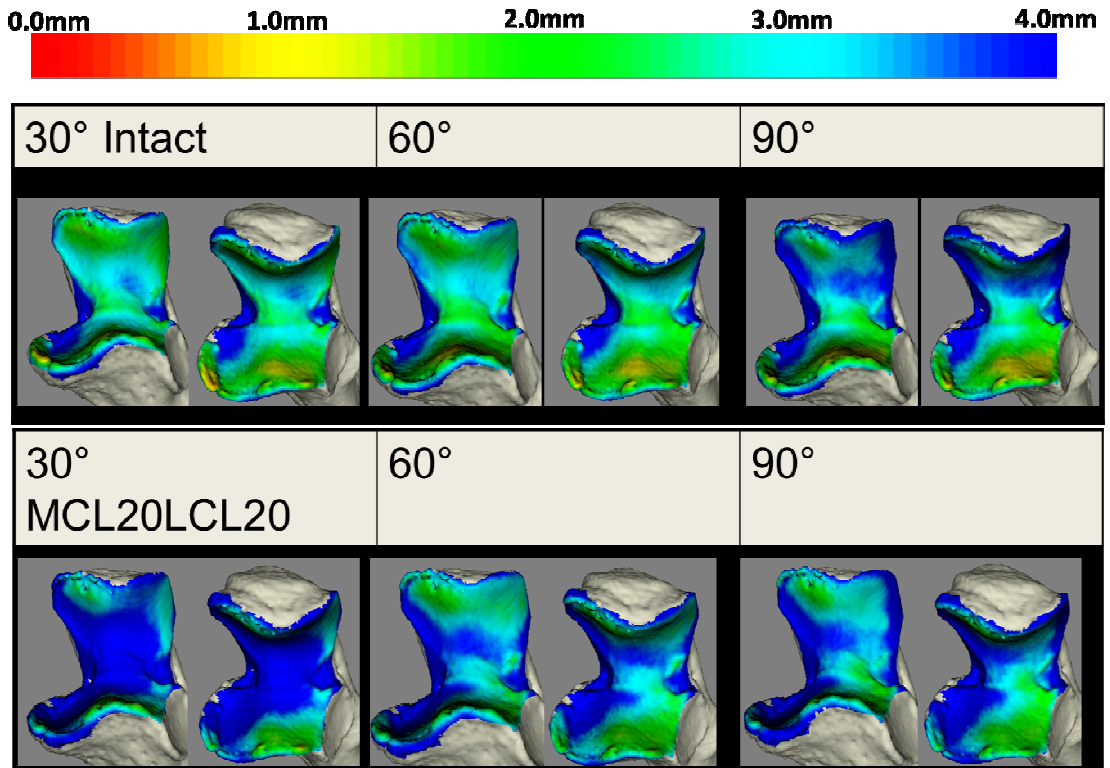
Figure E.3: Proximity Maps_10-01021L
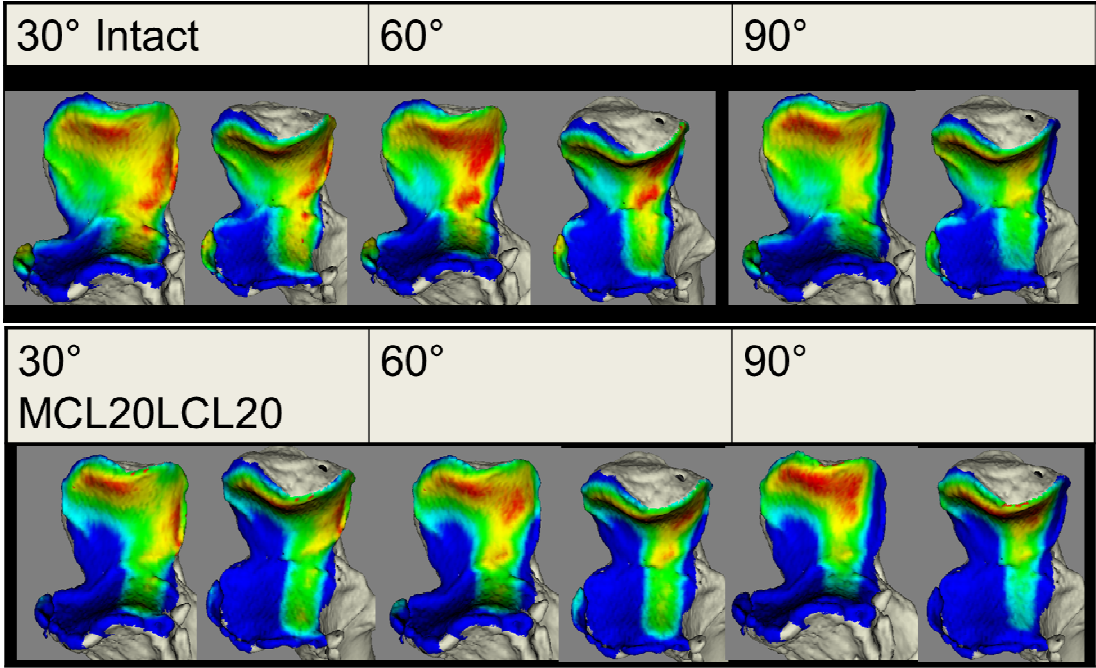
Figure E.4: Passive Flexion Proximity Maps_1459L
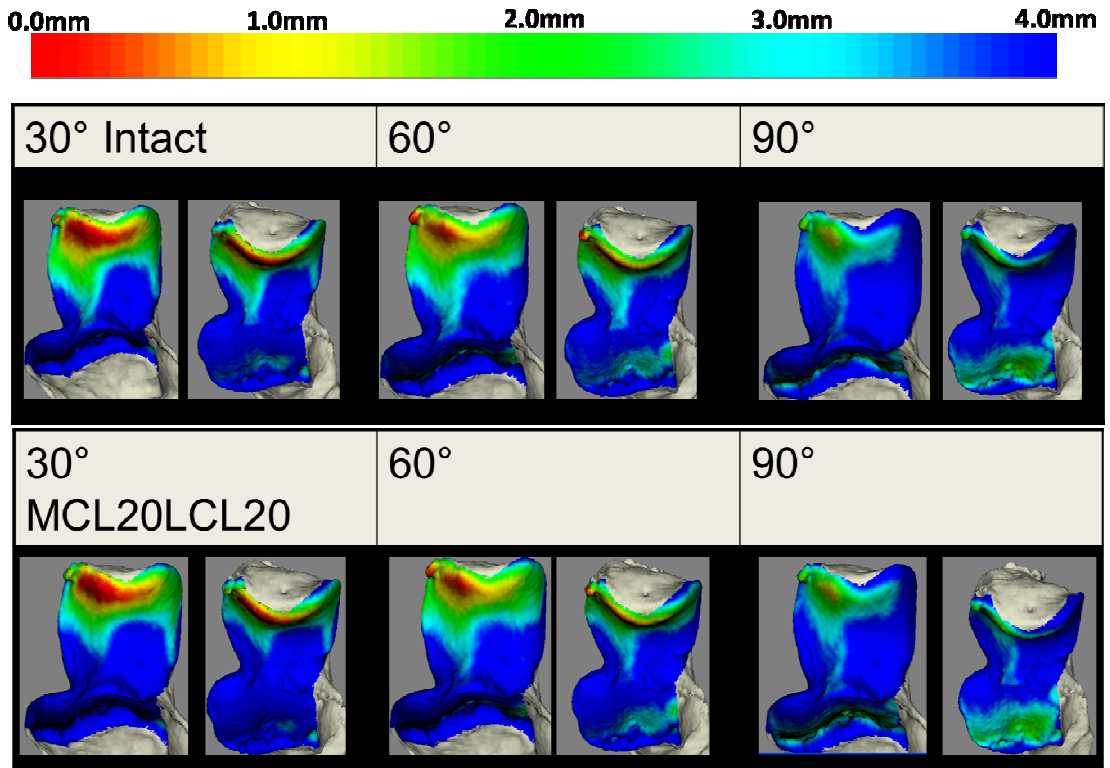
Figure E.5: Passive Flexion Proximity Maps _09-12055L
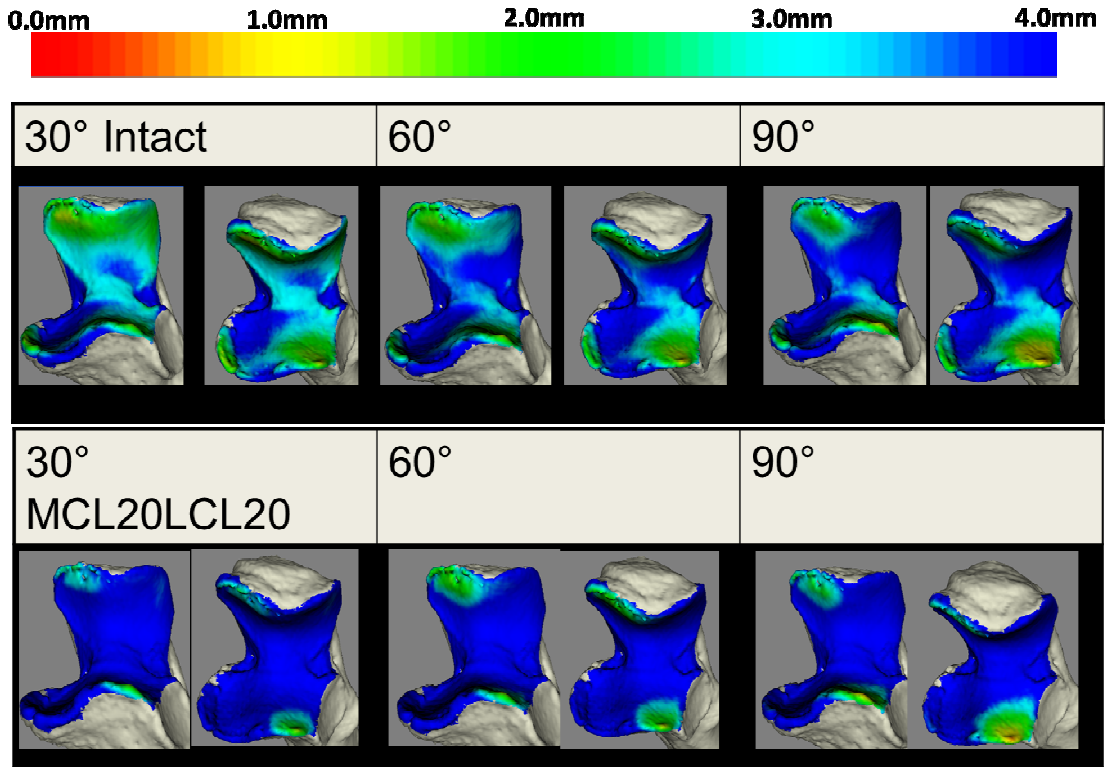
Figure E.6: Passive Flexion Proximity Maps _10-01021L
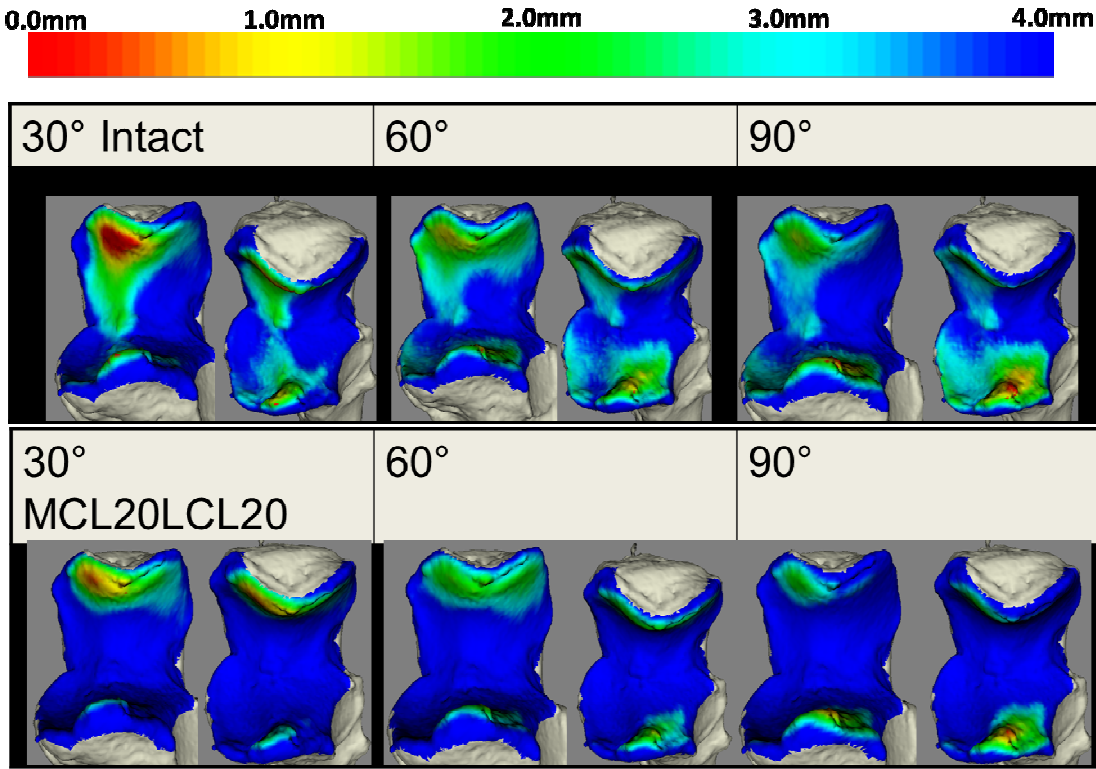
Figure E.7: Passive Flexion Proximity Maps_09-12057L

F.   Appendix F–Investigating the Effect of Ligament State during Passive Elbow Flexion

F.1   Methods

In Chapter 5, the intact and ligament repaired scenario is presented. In addition to these states, the effect of successive medial ligament repair was also examined. In this study, passive elbow flexion in the valgus gravity dependent position was tested. Four ligament 'states' were considered: MCL20LCL20 (both ligaments repaired), MCL20LCL0 (only the MCL repaired), MCL0LCL20 (only the lateral ligament repaired), and MCL0LCL0 (neither ligaments were repaired).

F.2   Results
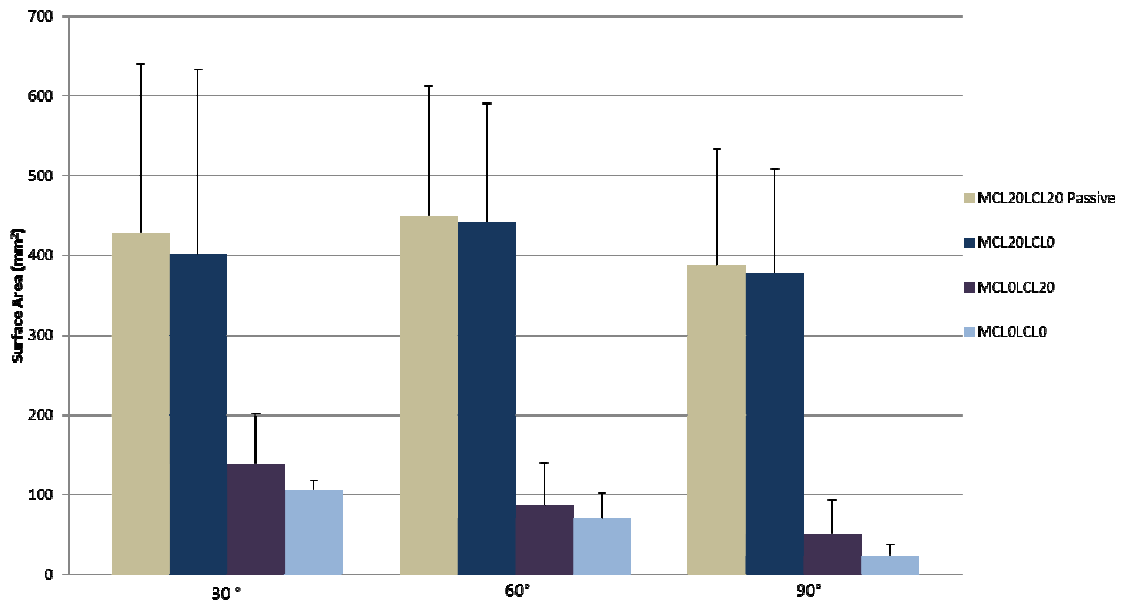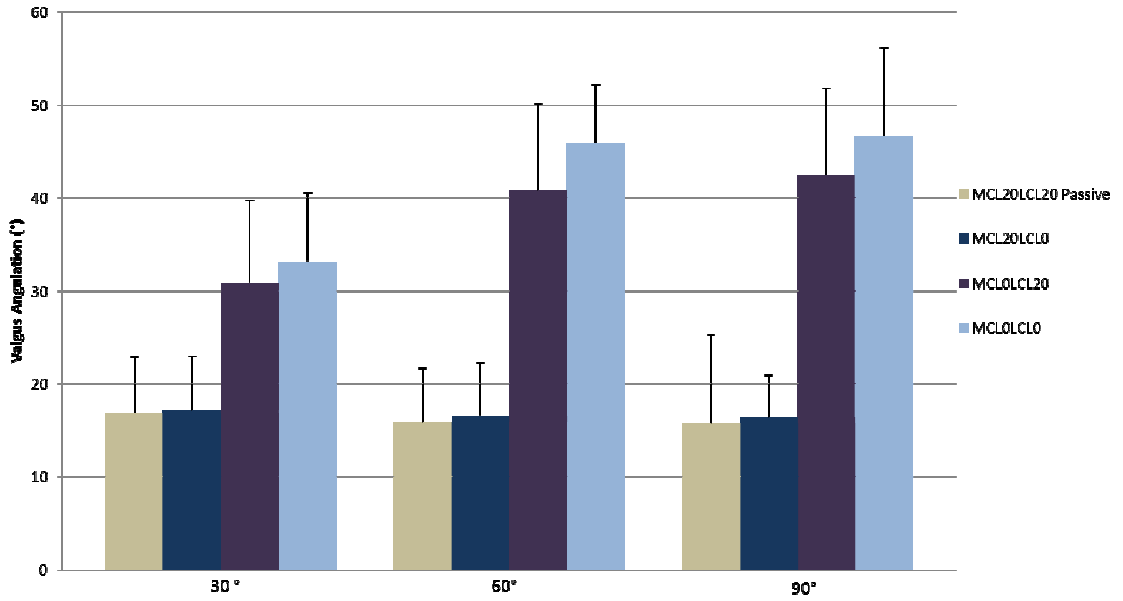

Figure F.1: Surface Area (< 3.5mm) of Proximal Ulna
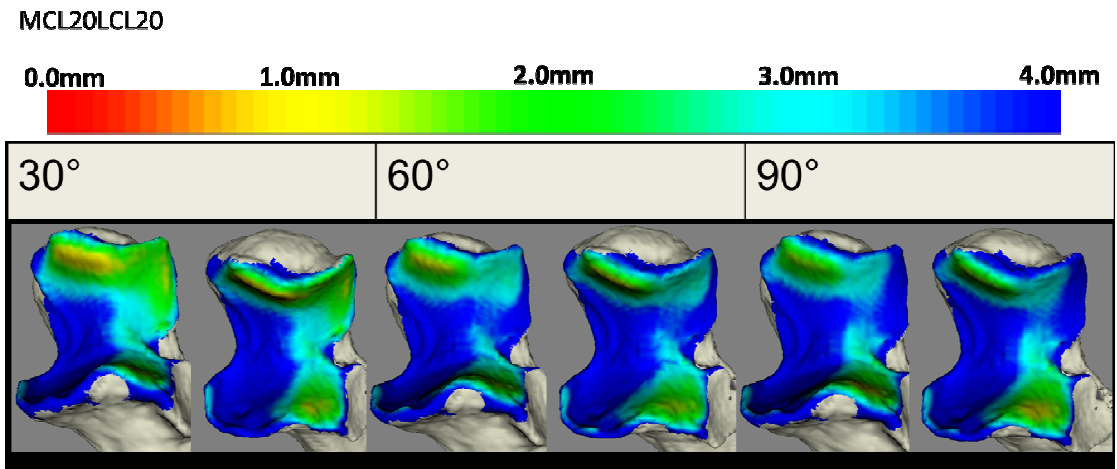
Figure F.2: Valgus Angulation

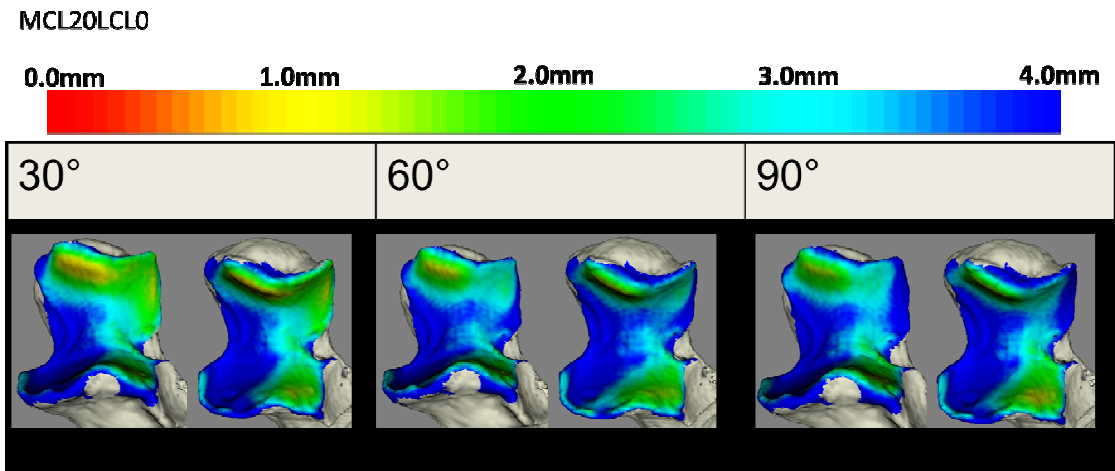**Figure F.3: Proximity Maps of Proximal Ulna (MCL20LCL20)**

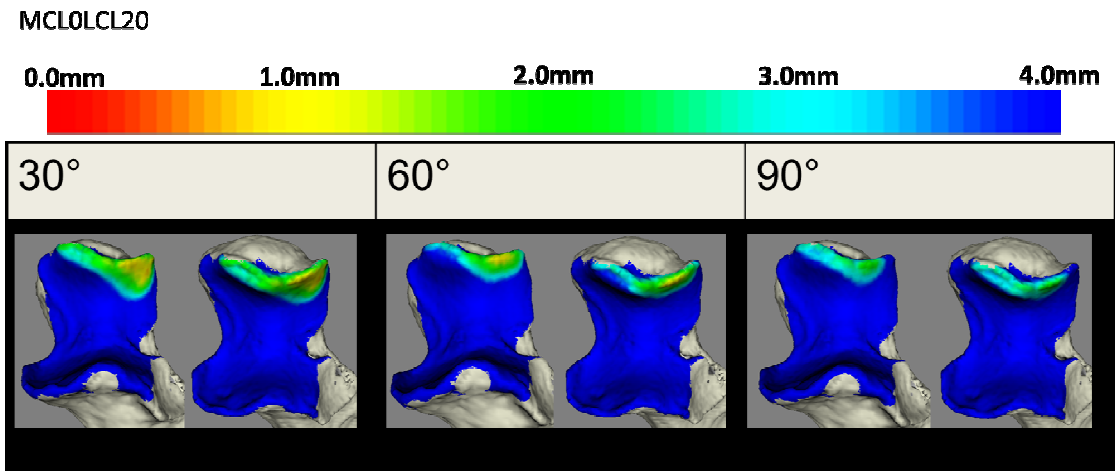**Figure F.4: Proximity Maps of Proximal Ulna (MCL20LCL0)**

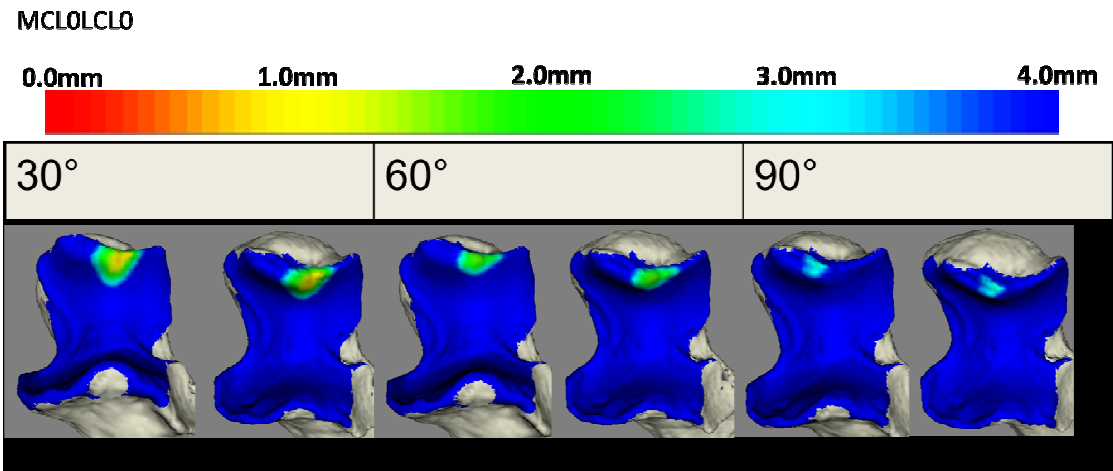**Figure F.5: Proximity Maps of Proximal Ulna (MCL0LCL20)**

Figure F.6: Proximity Maps of Proximal Ulna (MCL0LCL0)
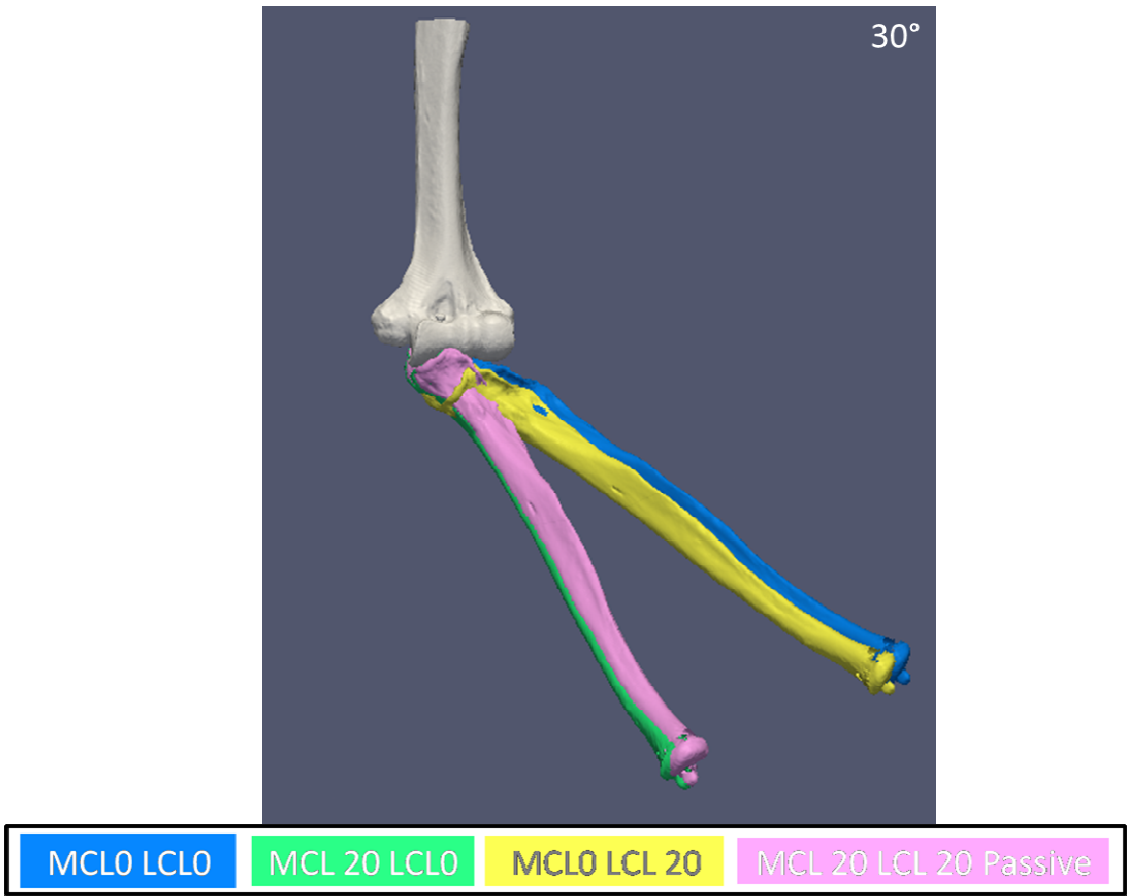
Figure F.7: Anterior View of Ulnohumeral Joint at 30° of Elbow Flexion

Figure F.8: Anterior View of Ulnohumeral Joint at 60° of Elbow Flexion
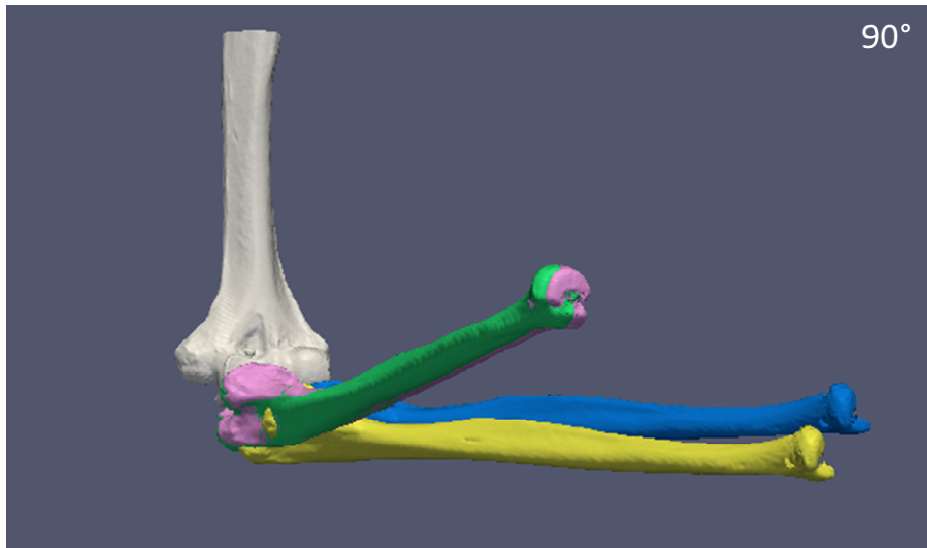
Figure F.9: Anterior View of Ulnohumeral Joint at 90° of Elbow Flexion

G.   Appendix G–Subject Specific Overlap Data

G.1 Methods

In Chapter 5, overlap between the proximal ulna and distal humerus was found in 3 of the 5 specimens. The location of overlap for each specimen is shown below.

G.2 Results
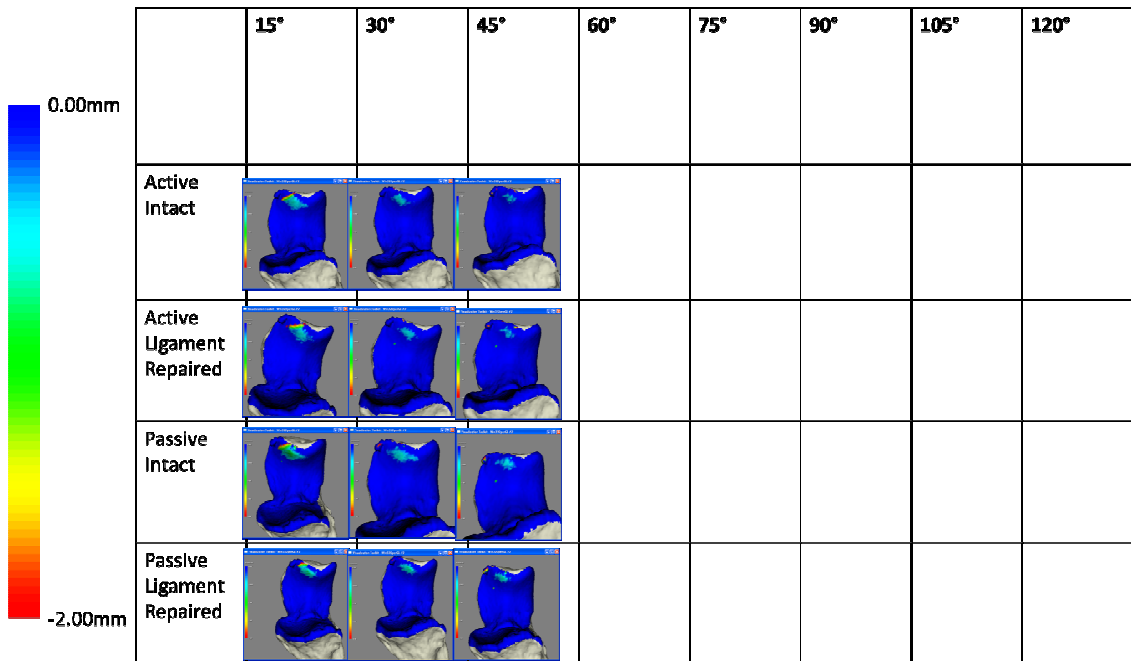
Figure G.1: Overlap_09-12055L_Intact_Ligament Repaired

	15°	30°	45°	60°	75°	90°	120°
MCL20LCL0							
MCL0LCL20							
MCL0LCL0							

0.00mm

-2.00mm
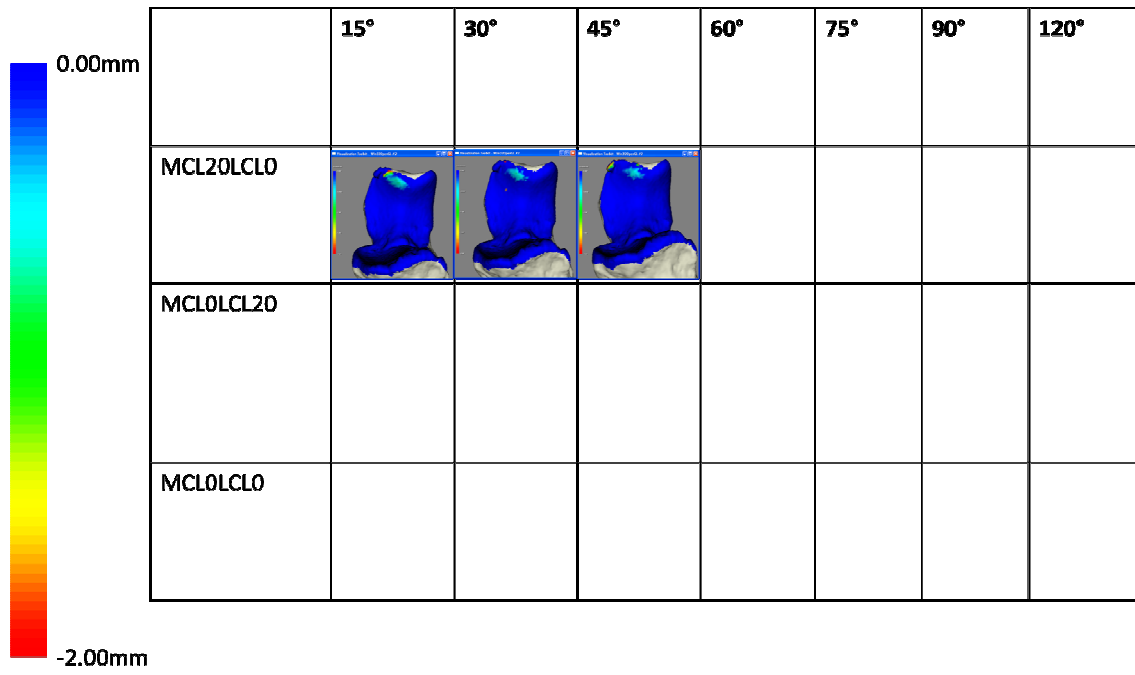
Figure G.2: Overlap_09-12055L_Passive Ligament Data
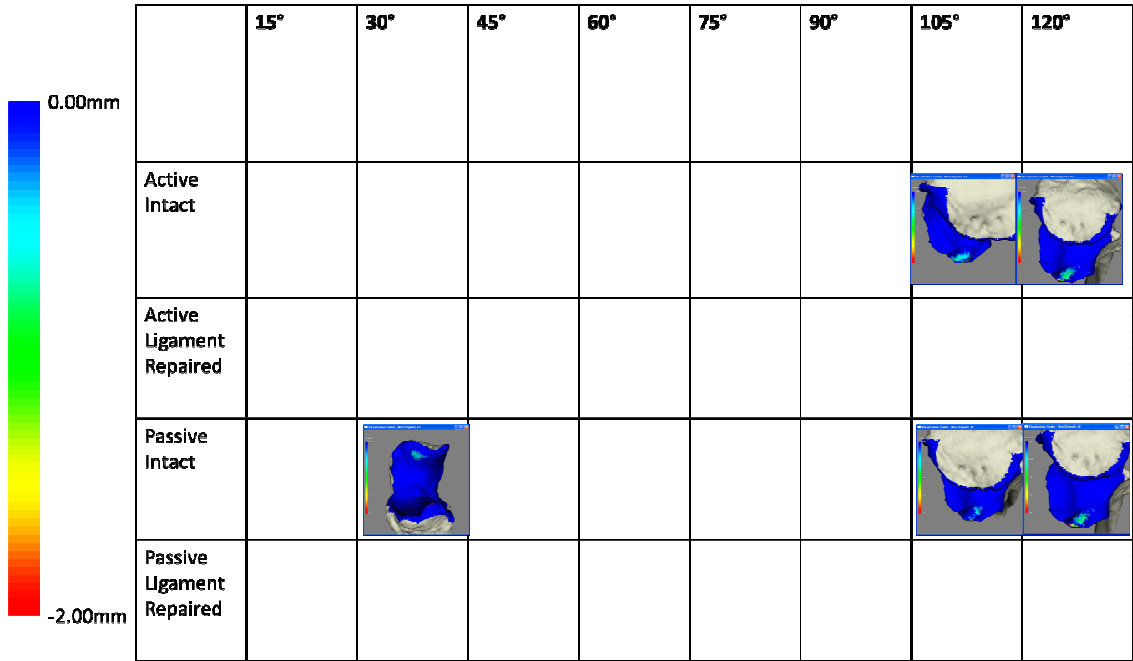
Figure G.3: Overlap_09-12057L_Intact_Ligament Repaired
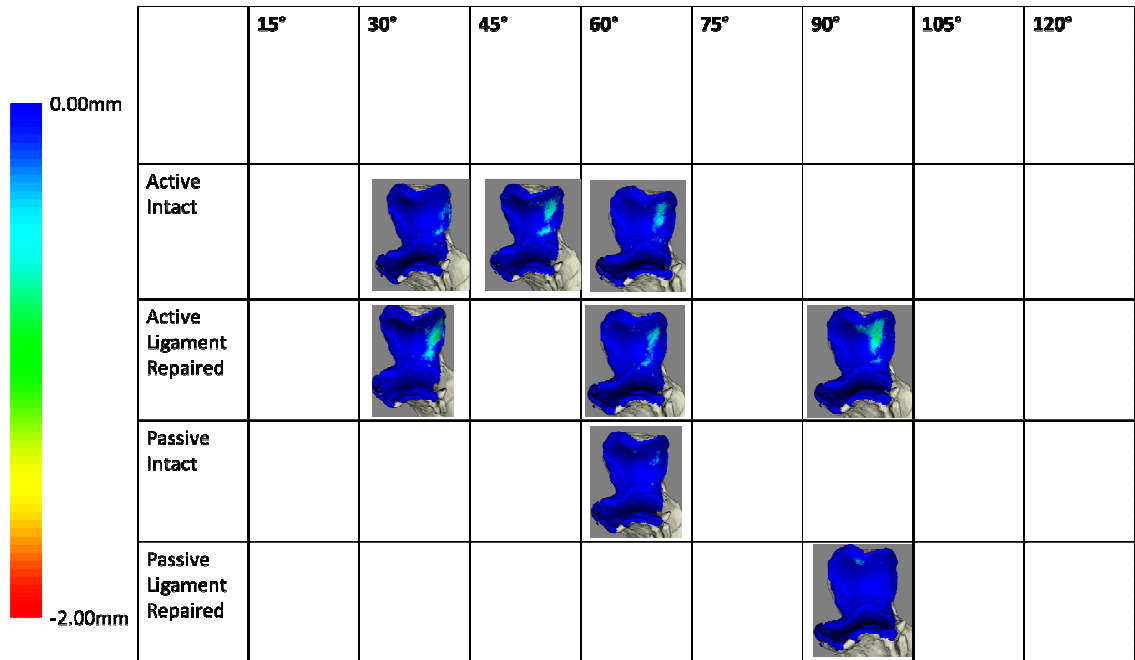
Figure G.4: Overlap_1459L_Intact_Ligament Repaired

307
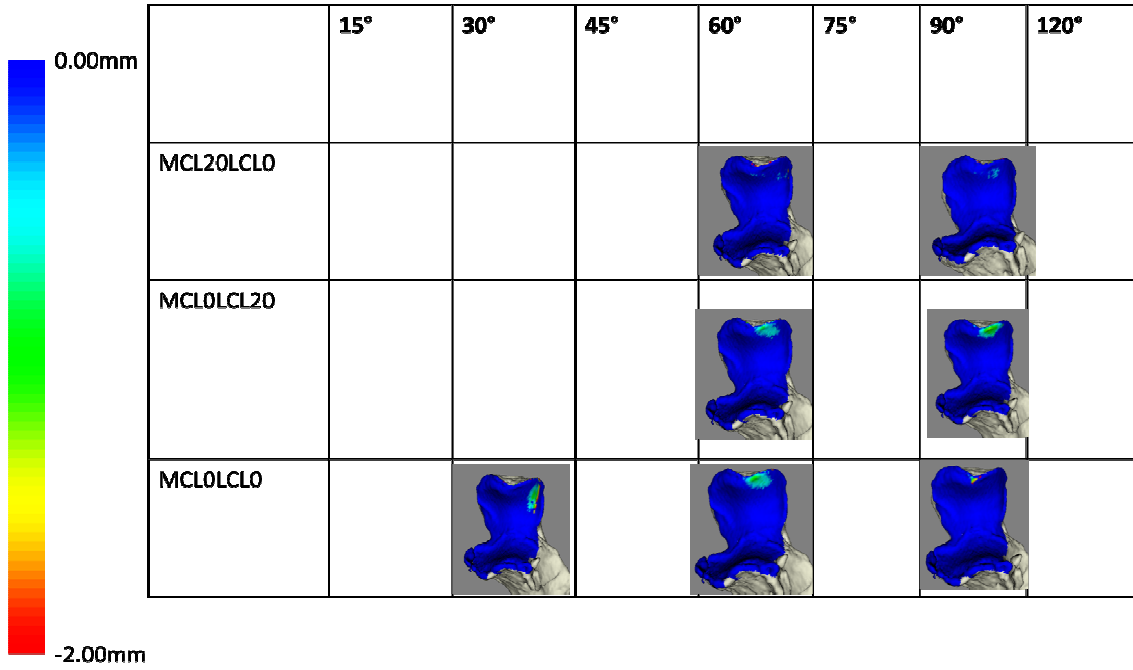
Figure G.5: Overlap_1459L_Passive Ligament Data

H. APPENDIX H–Subject Specific Proximity Maps comparing the Effect of mA and Pitch Ratio

H.1 Methods

In Chapter 6, results were shown for a single specimen. This appendix contains the data for the remaining specimens.

H.2 Results
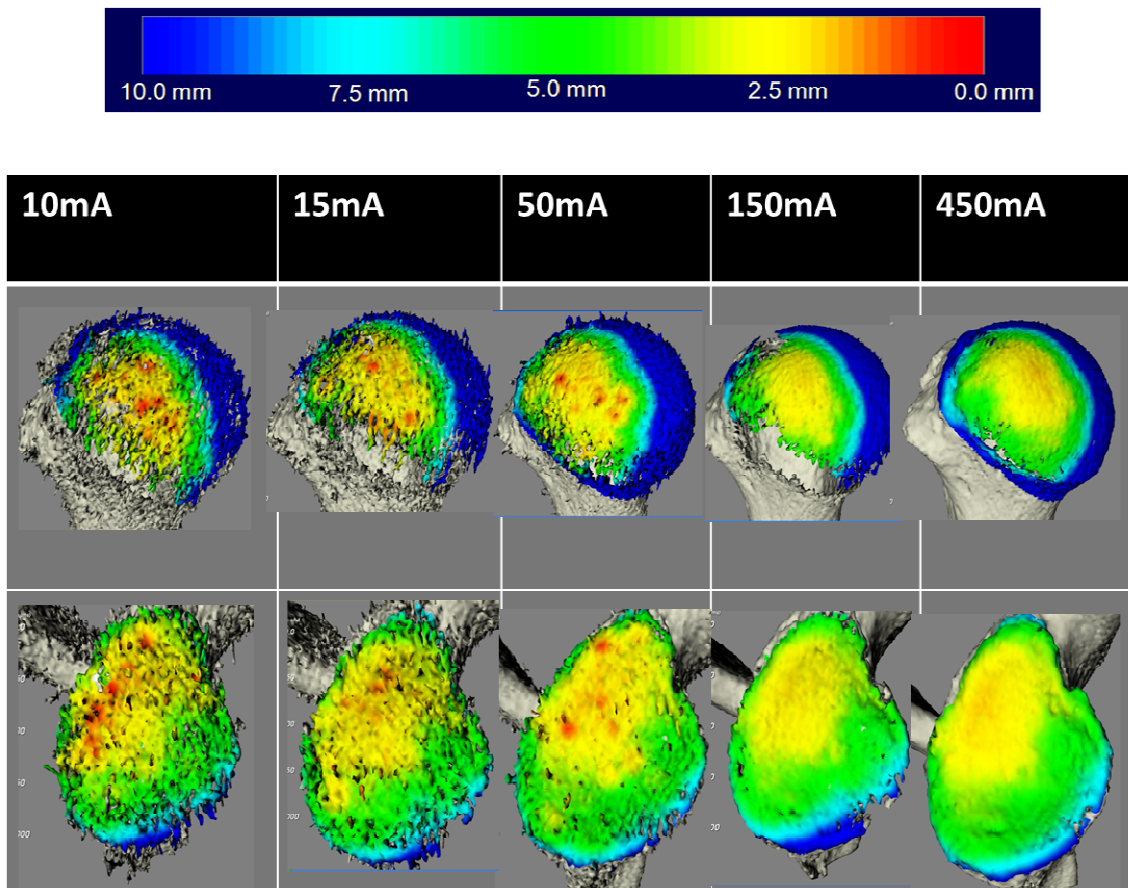
Figure H.1:08-02006R Effect of mA
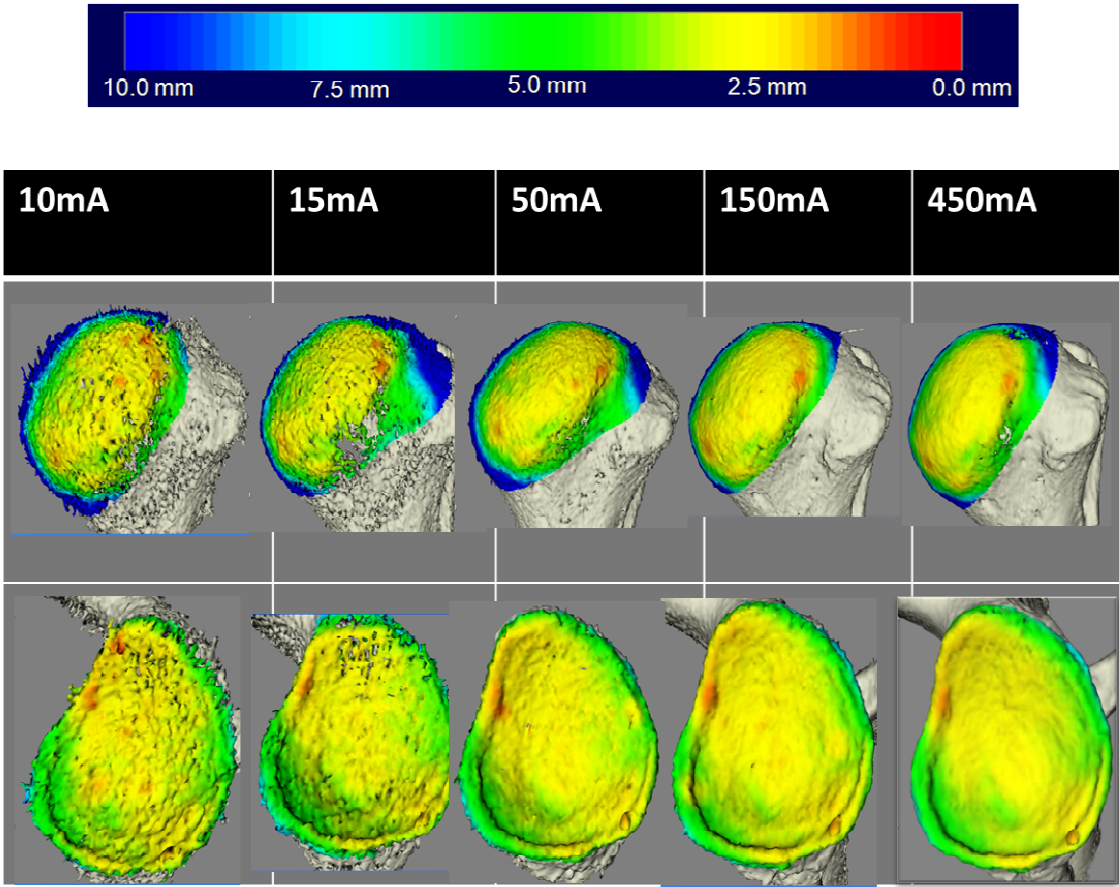
Figure H.2: 08-02024L Effect of mA
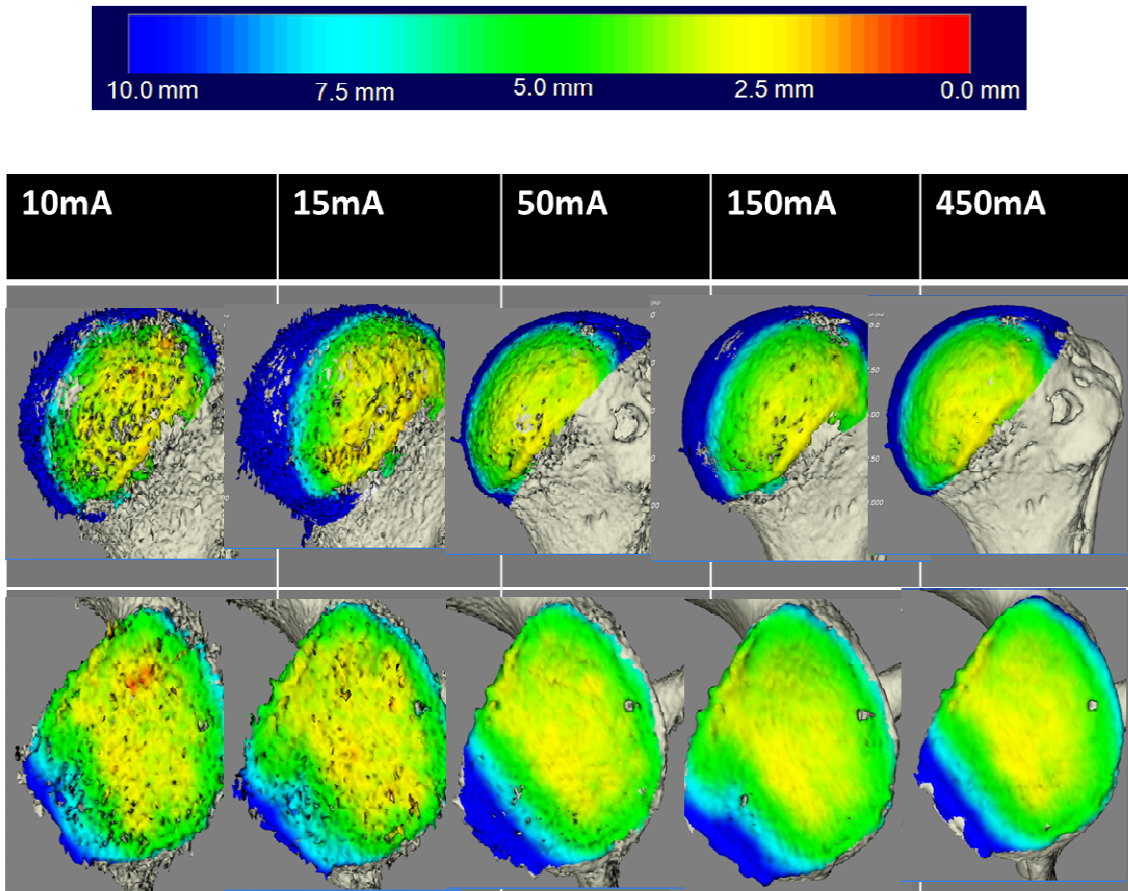
Figure H.3: 08-02070L Effect of mA
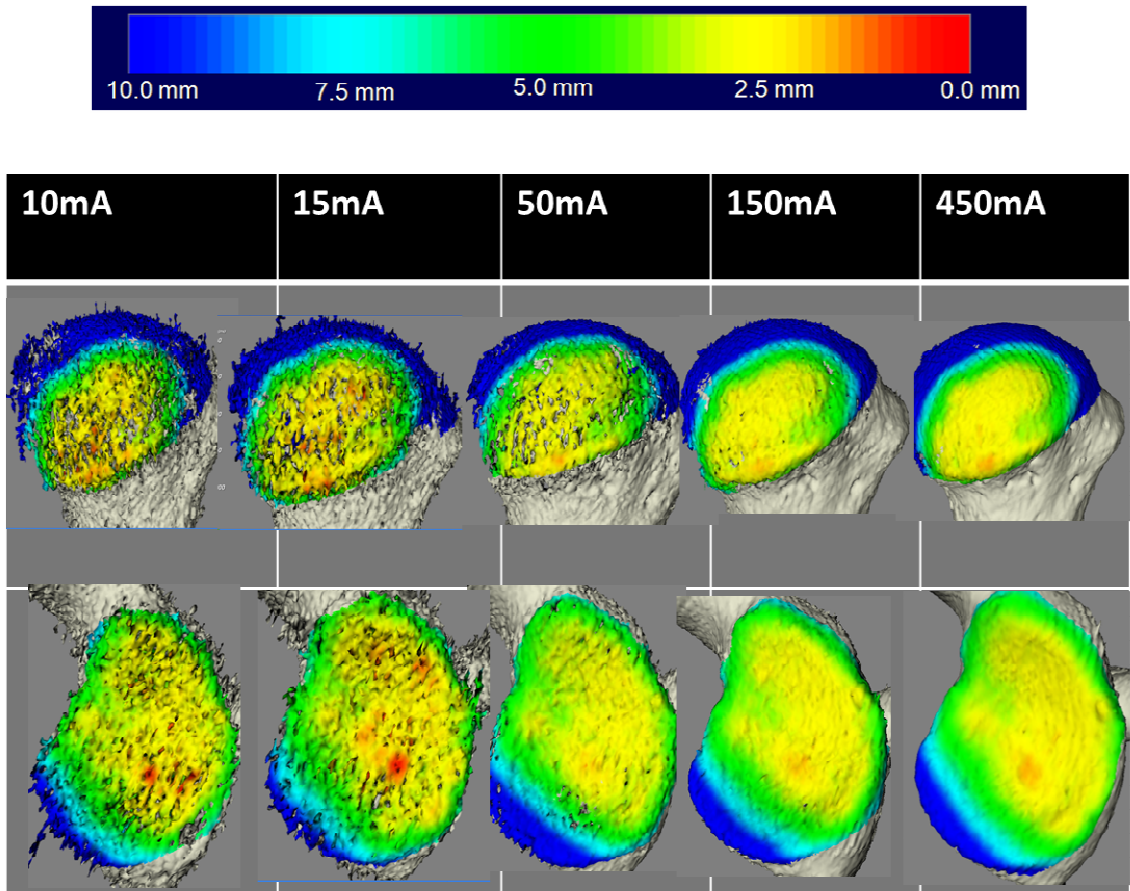
Figure H.4: 09-05056L Effect of mA
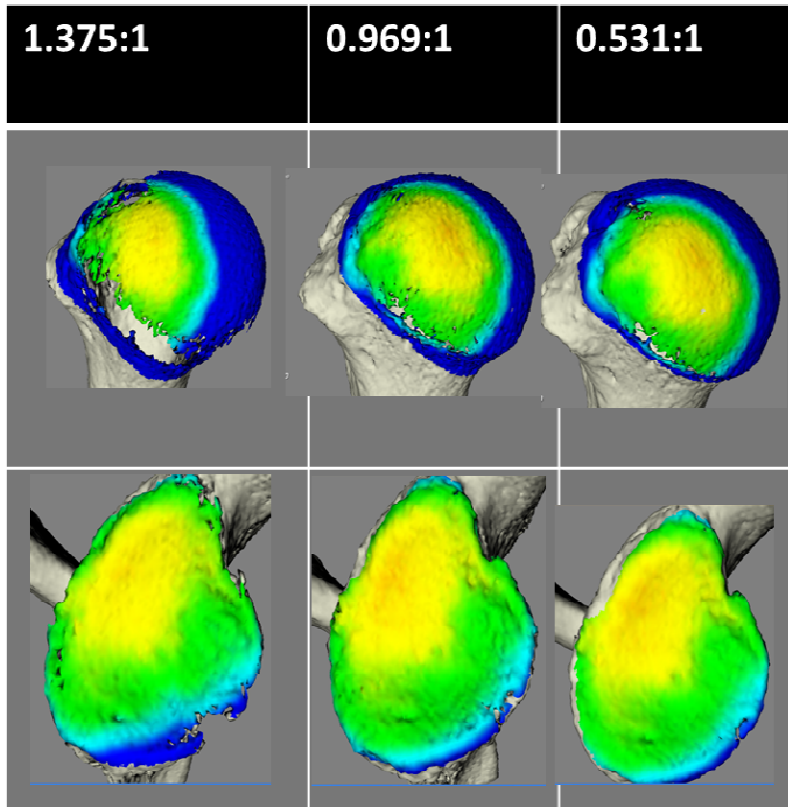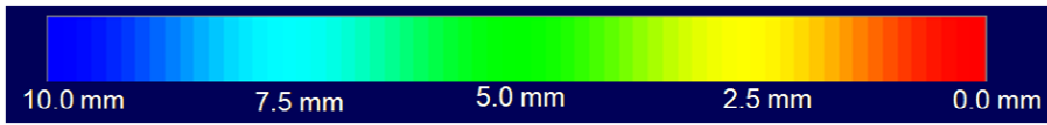
Figure H.5: 08-2006R Effect of Pitch
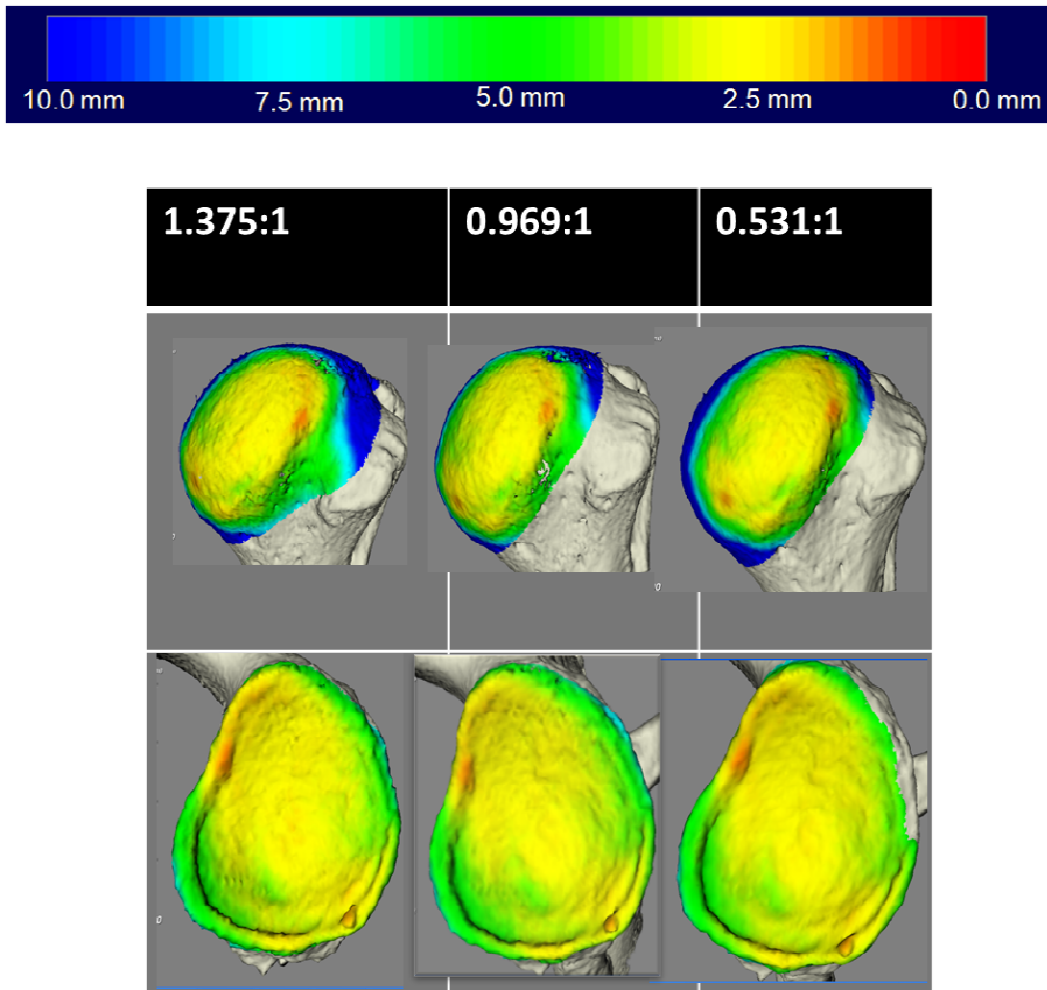
Figure H.6: 08-02024L Effect of Pitch
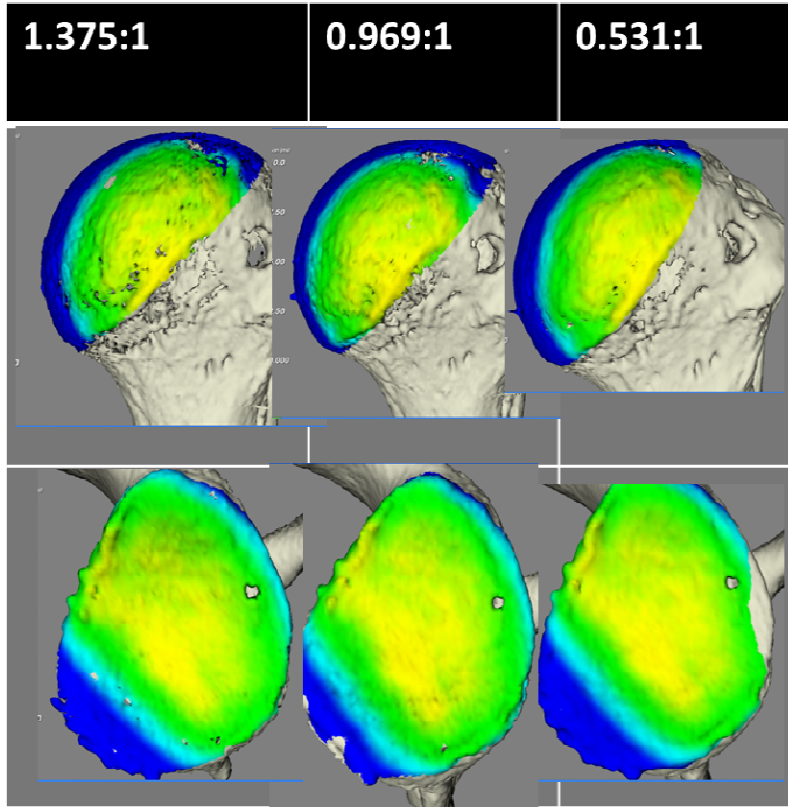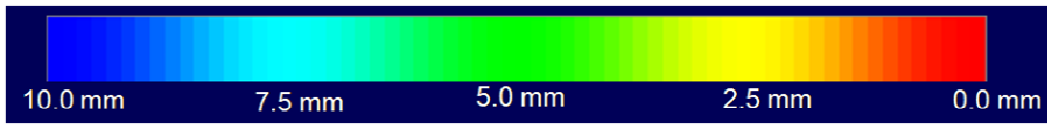
Figure H.7: 08-02070L Effect of Pitch
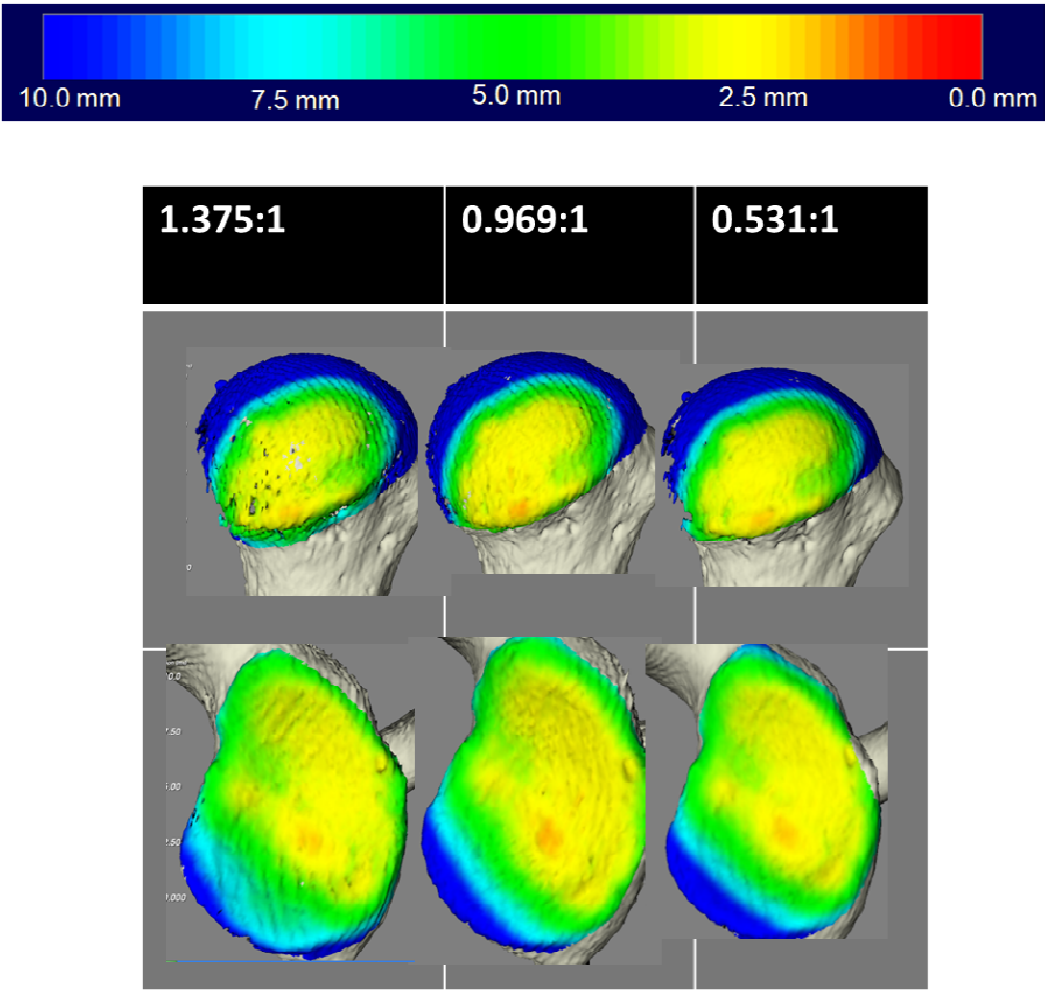
Figure H.8: 09-05056R Effect of Pitch

I. Appendix I –Accuracy of ICP /Accuracy of Bone Reconstructions

I.1 Introduction

The objective of this study was to assess the accuracy of the ICP algorithm employed throughout this thesis as well as the accuracy of the 3D bone reconstructions created. This appendix used the inter-bone distance developed in Chapter 2 (Section 2.2.5) to assess the overall similarity in geometry. To assess the accuracy of the ICP algorithm, a comparison of the registered geometries was performed. To assess the accuracy of the 3D bone reconstruction (Marching Cubes, VTK), a comparison of the reconstructed model and the actual bone surface were compared.

I.2 Methods

Accuracy of ICP

Two 3D bone reconstructions were created (pre-testing and post-testing) of the distal humerus and proximal ulna. When the 3D models are created, the inner surfaces (corresponding to the trabeculae) need to be segmented from the 3D model. This is to reduce the computational time for the inter-bone distance algorithm. Therefore, the final 3D models appear as a shell of a bone. This process is described in detail in Chapter 2 (Section 2.2.3). To reduce the processing time, the post-testing CT is coarsely segmented. The pre-testing 3D models are then registered to the post-testing position and orientation using the surface-based ICP registration. During the ICP registration, there is a target and a source model. The registration calculates a transformation matrix that can be used to

map the pre-testing 3D model (target) to the location of the post-testing 3D model (source). To assess the accuracy of this registration a comparison of two registered models was performed. The similarity of the two registered bodies was then compared using the inter-bone distance algorithm developed in Chapter 2. This algorithm was used not to measure joint congruency, but to measure the relative distance between points on the two surfaces. The post-testing CT was larger than the pre-testing reconstruction 96.1% (humerus) 96.5% (ulna) of the time, but not by more than 1mm.

Accuracy of 3D Reconstruction

A single fresh frozen specimen (Male, 64 years) was denuded and disarticulated. Prior to testing, a CT scan of the intact specimen was acquired (120kVp, 292mA/rotation). Using the reconstructive techniques described in Chapter 2 (Section 2.2.3), a 3D reconstruction of the distal humerus and proximal ulna were created. The specimen, once disarticulated, was then soaked for 22 hours in 5.25% Sodium Hypoclorite to dissolve the cartilage. Optical position sensors were then secured to the distal humeral and proximal ulna. The surface of the subchondral bone and cortical bone were digitized using a tracked stylus as described in Chapter 4. Point cloud surfaces were then reconstructed as described in Chapter 4 and used to create a 3D surface of the digitized points. This surface represented the ground truth. Using the ICP algorithm, the position of the 3D reconstruction was registered to the position of the digitized reconstructed point cloud. The digitization from the cortical bone and subchondral bone was used in the ICP to register the two surfaces. Once overlaid, the overall similarity of

their geometry was assessed using the inter-bone distance algorithm. Only the subchondral bone surfaces were assessed.

I.3   Results

Accuracy of ICP

Figure A.1 shows the reconstructed surfaces of the pre-testing CT (highly segmented) and the post-testing CT (coarsely segmented). Figure A.2 shows the overlaid surfaces registered using the ICP algorithm. The overall mean distance between the two registered surfaces was 0.38±0.12mm (max: 1.06mm, min: 0.02mm, 43377 points) for the humerus and 0.31±0.13mm (max: 1.60mm, min: 0.01mm, 41898 points) for the ulna. Figure A.3 shows the distance map between the two registered surfaces for the humerus and ulna. Figure A.4 and Figure A.5 show the distances measured (error) using the inter-bone distance algorithm between the two registered bone models for each point on the humerus and ulna respectively.
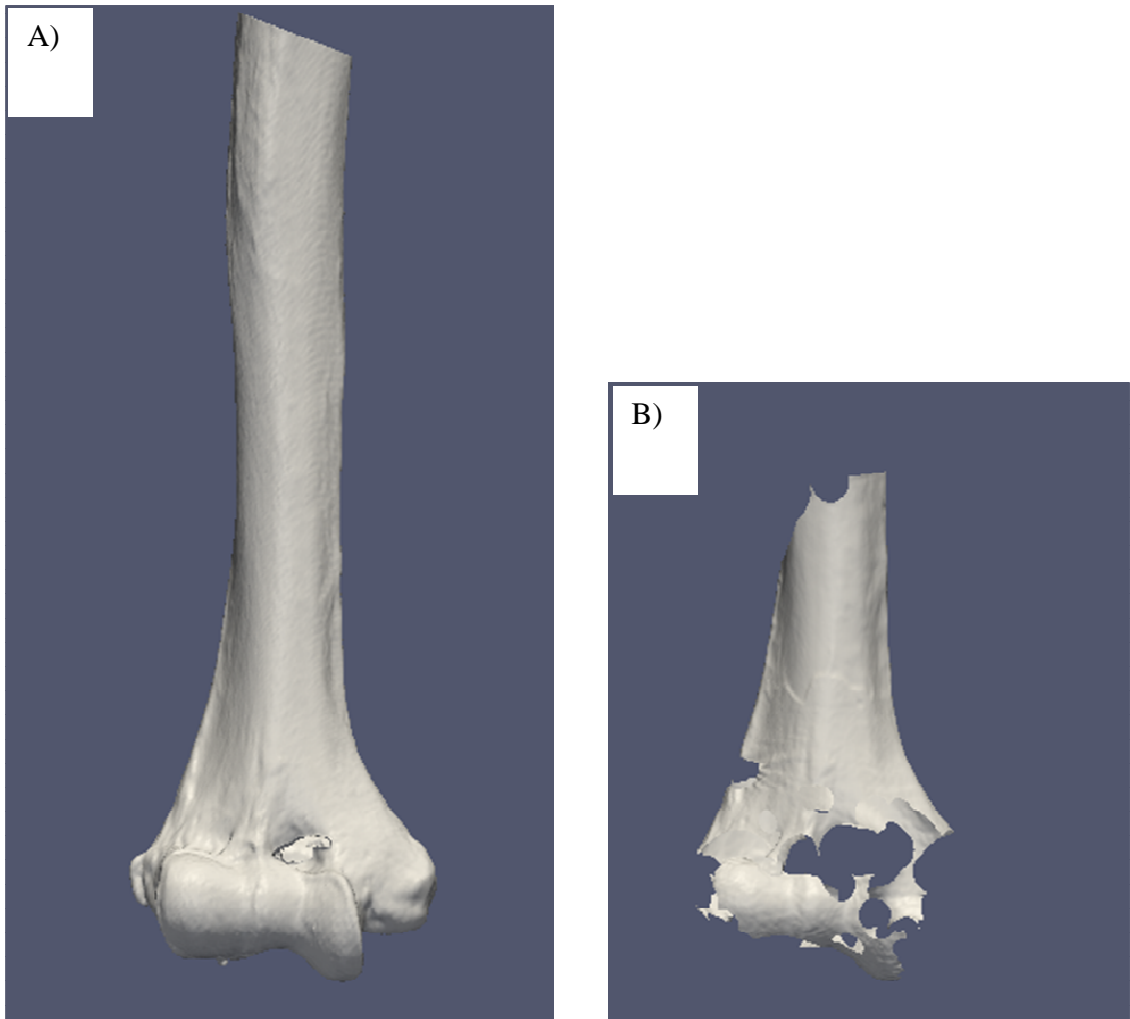
Figure I.1: 3D Bone reconstruction
A) Pre-testing CT 3D bone reconstruction
B) Post-testing CT 3D bone reconstruction

Figure I.2: Registered Surfaces
Target and source registered humeri are shown overlaid to compare relative position.
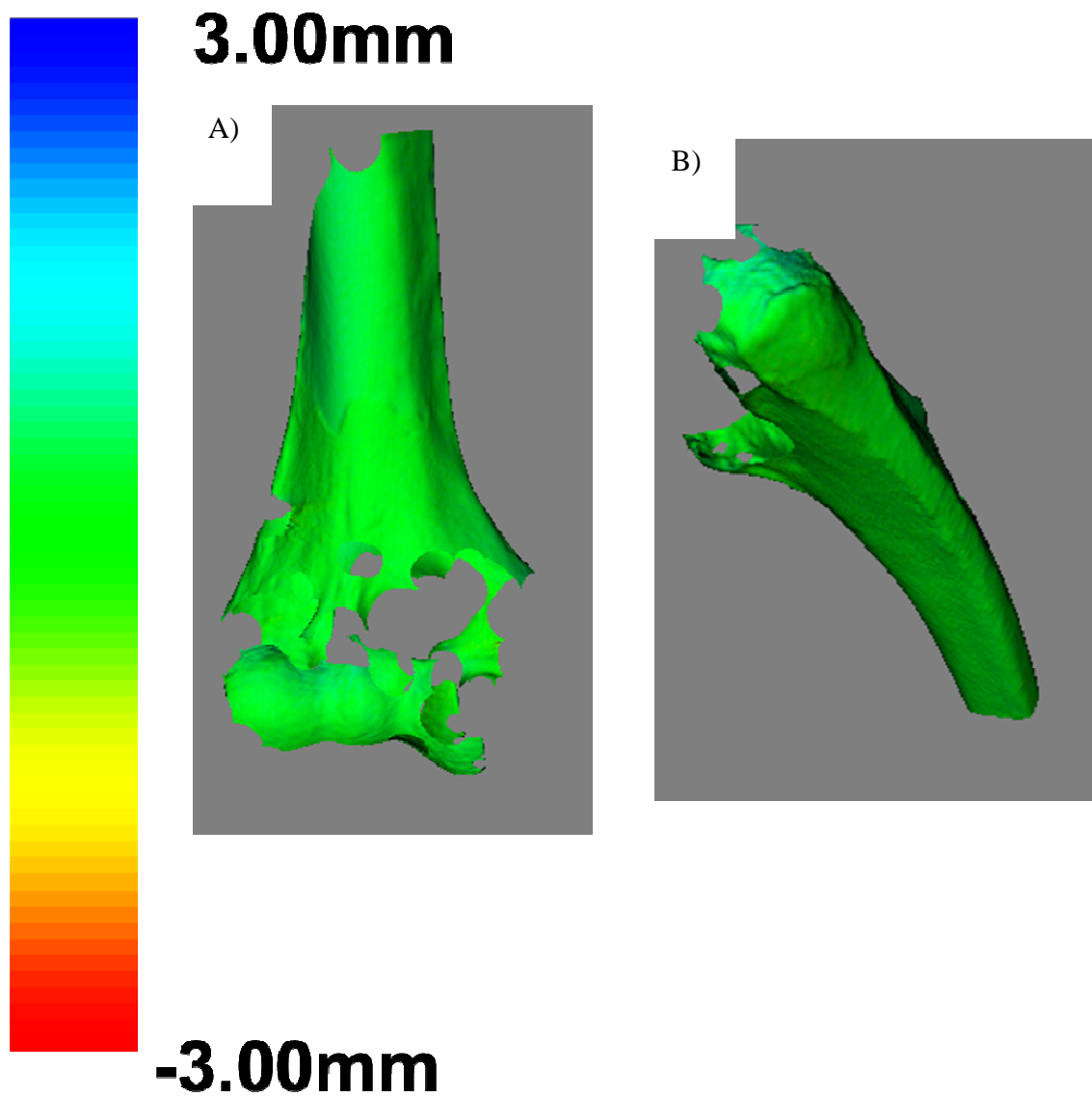
Figure I.3: Distance Maps measuring the distance between two registered surfaces
Colourmaps are shown for the registered post-testing humerus (A) and ulna (B).
Note: only the post-testing reconstruction is shown. Corresponding pre-testing 3D
reconstruction colourmaps were also generated but not shown.
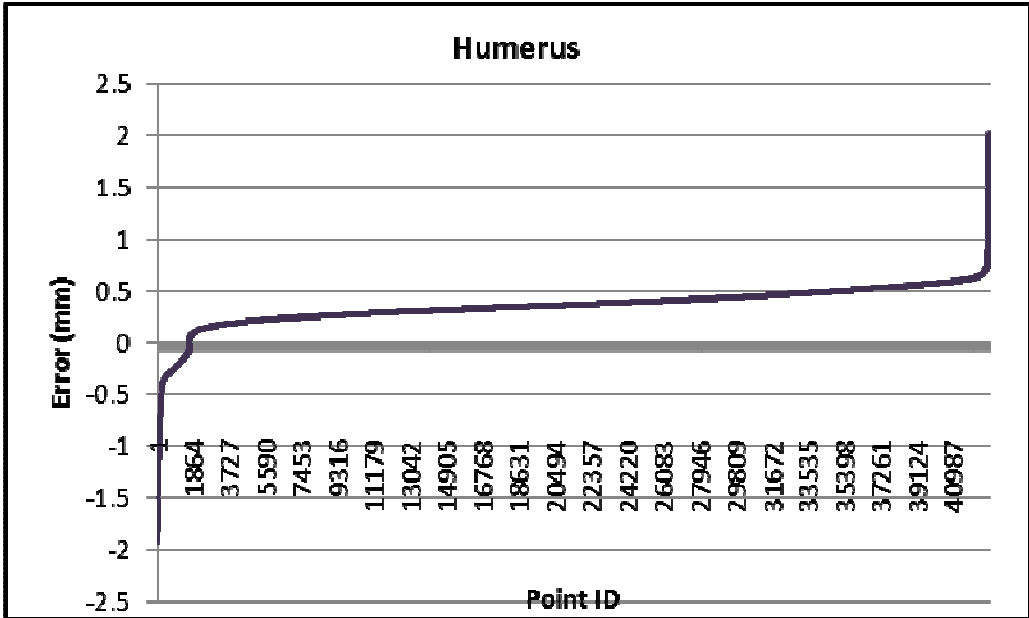
Figure I.4: Distance (error) between two registered humeri
Inter-surface distances were measured between two registered models to determine the accuracy of the surface based registration.
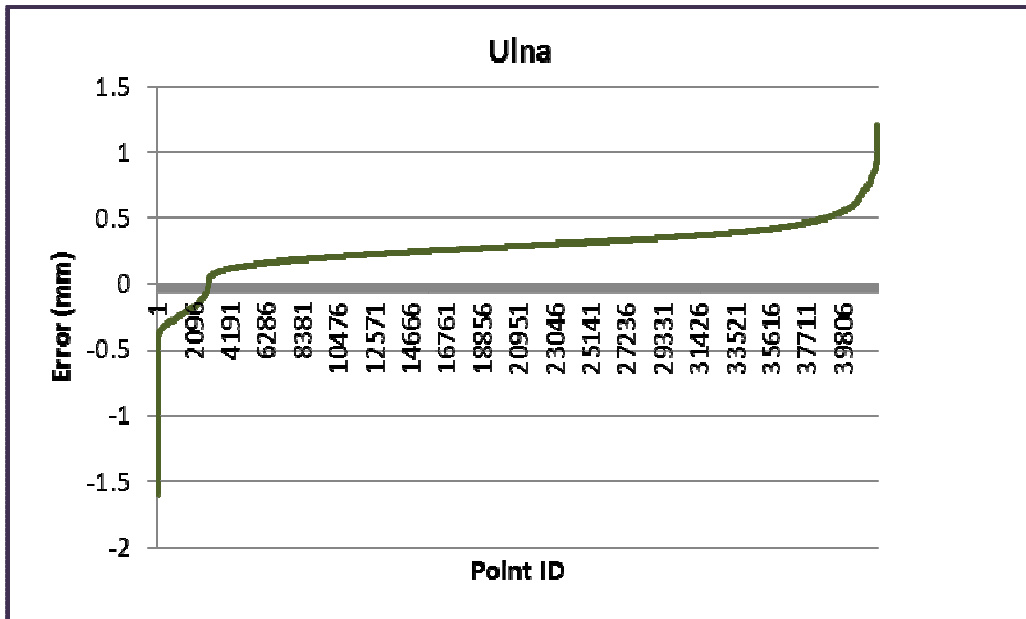
Figure I.5: Distance (error) between two registered ulna
Inter-surface distances were measured between two registered models to determine the accuracy of the surface based registration.

Accuracy of 3D Reconstruction

Figure A.6 shows the cartilage before and after it has been dissolved. Figure A.7 shows the reconstructed surface created from the point cloud digitization. Distance maps were created using the inter-bone distance algorithm comparing the geometry of the registered 3D reconstruction and the reconstructed digitized subchondral bone surface. The error between the two surfaces is shown Figure A.8 (humerus) Figure A.10(ulna).The number of points at each distance (error) interval between the registered 3D reconstruction of the humerus and ulna and the reconstructed digitization is shown Figure A.9(humerus) Figure A.11(ulna). Distances were measured from vertices on corresponding surfaces. In total, 17 322 points on the humerus and 11627 points on the ulna were used to measure inter-surface distances. The mean error for the humerus was 0.30±0.16mm and 0.28±0.15mm of the ulna. Overall, 87.5% of the points on the humerus and 92.5% of points on the ulna were within 0.50mm indicating that the overall geometries of the two surfaces were similar. The 3D bone reconstruction over-estimated the geometry by 63.1% for the humerus and 38.0% for the ulna.

In summary, the accuracy of the surface-based ICP registration employed in this thesis (using two 3D models generated from CT) as well as verified the accuracy of the 3D reconstruction itself. Both techniques proved to be accurate given the scanning parameters, reconstruction algorithms used.
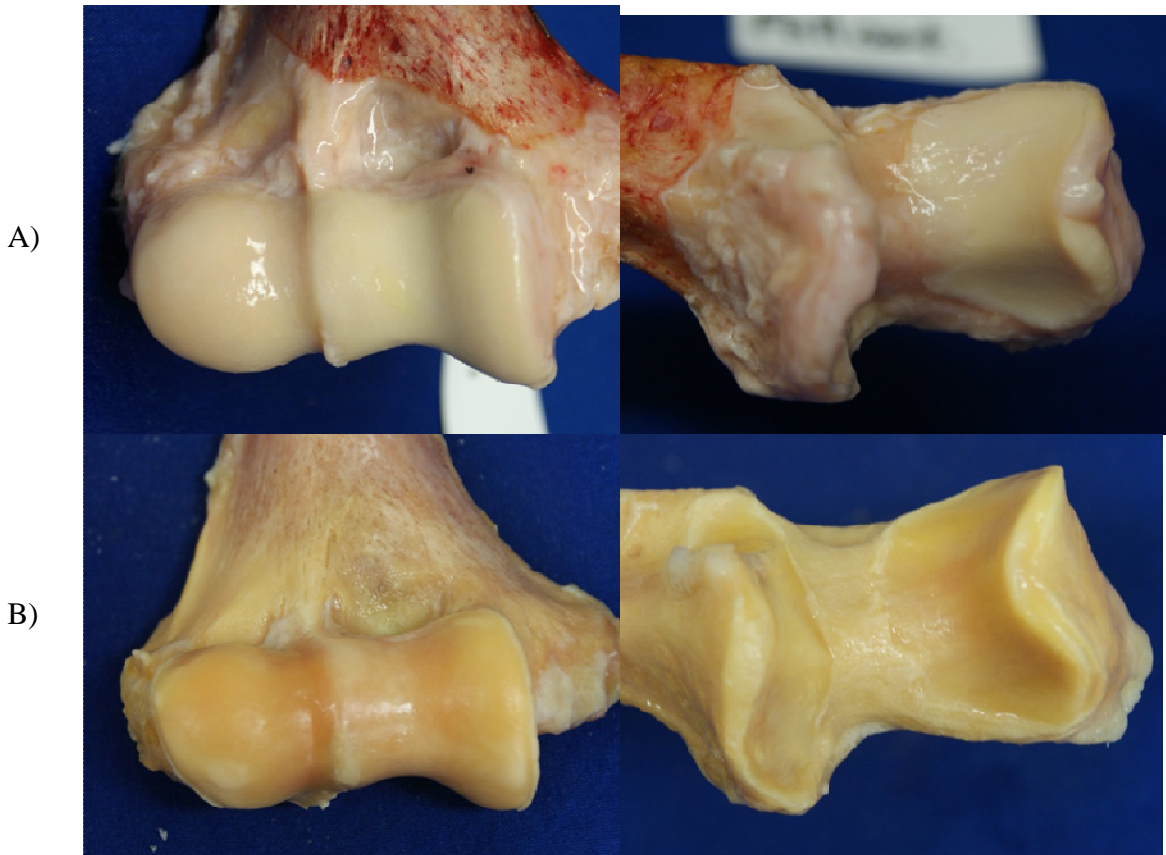
Figure I.6: Cartilage Surface
A) Intact Cartilage
B) Dissolved Cartilage Subchondral bone
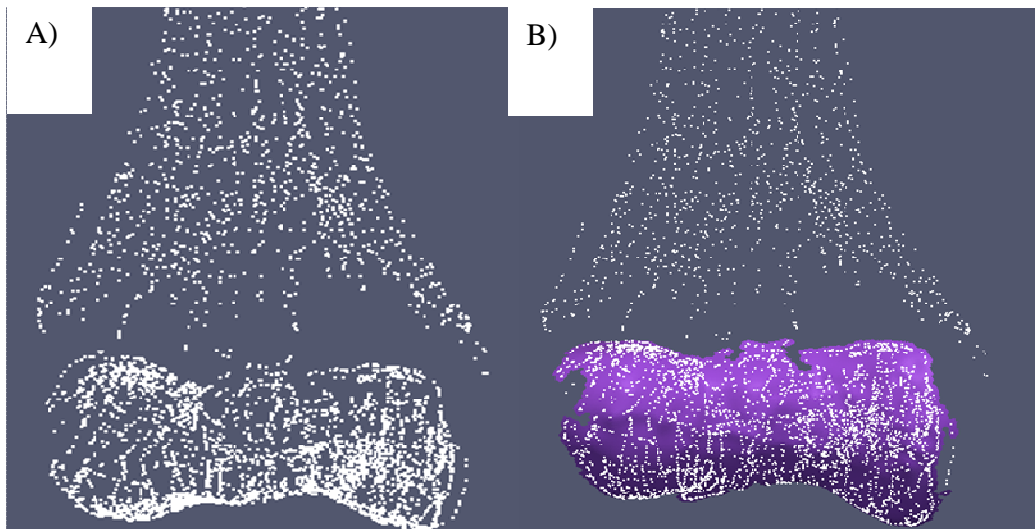
Figure I.7: Reconstructed Point Cloud
A) Digitized points were recorded using the tracked stylus
B) Points were used to reconstruct a 3D surface

2.00mm

-2.00mm
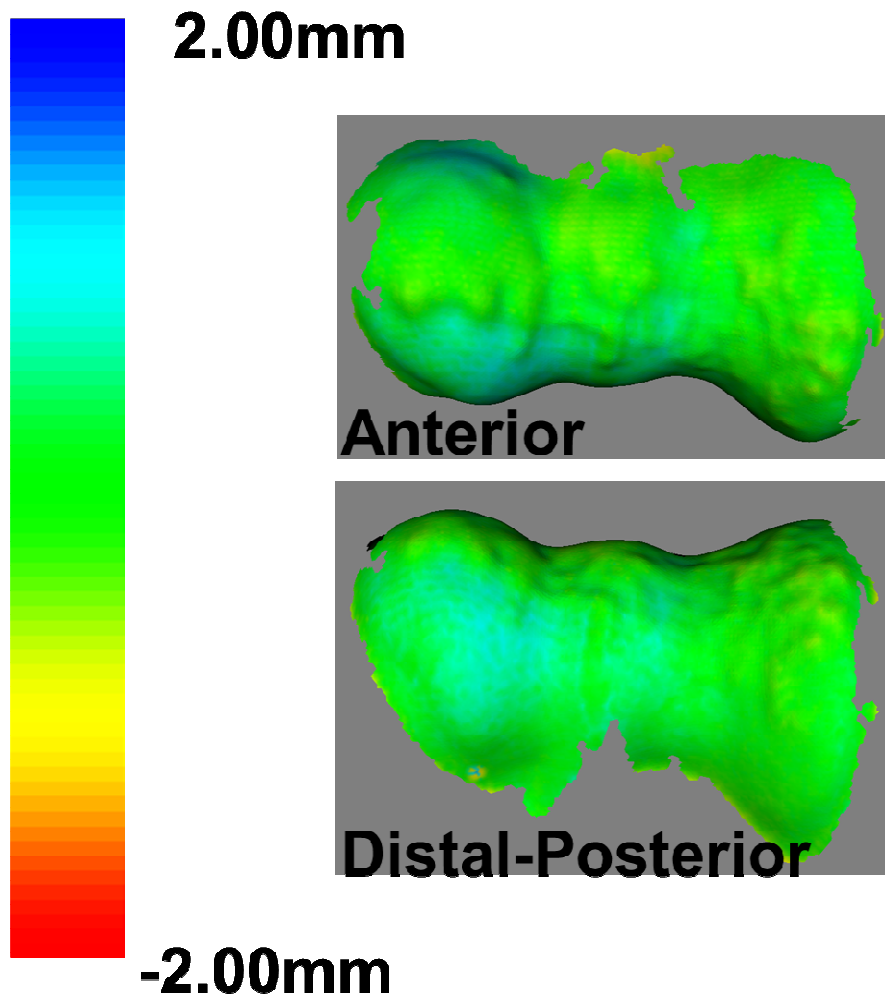
Figure I.8: Distance maps of the distal humerus
Colourmaps were created using the inter-bone distance algorithm to compare the geometry of the registered 3D reconstruction and the reconstructed digitized subchondral bone surfaces. An anterior and distatl-posterior view of the distal humeral subchondral bone surface is shown.

Note: Corresponding colourmaps were also created for the reconstructed digitized bone surface but are not shown.
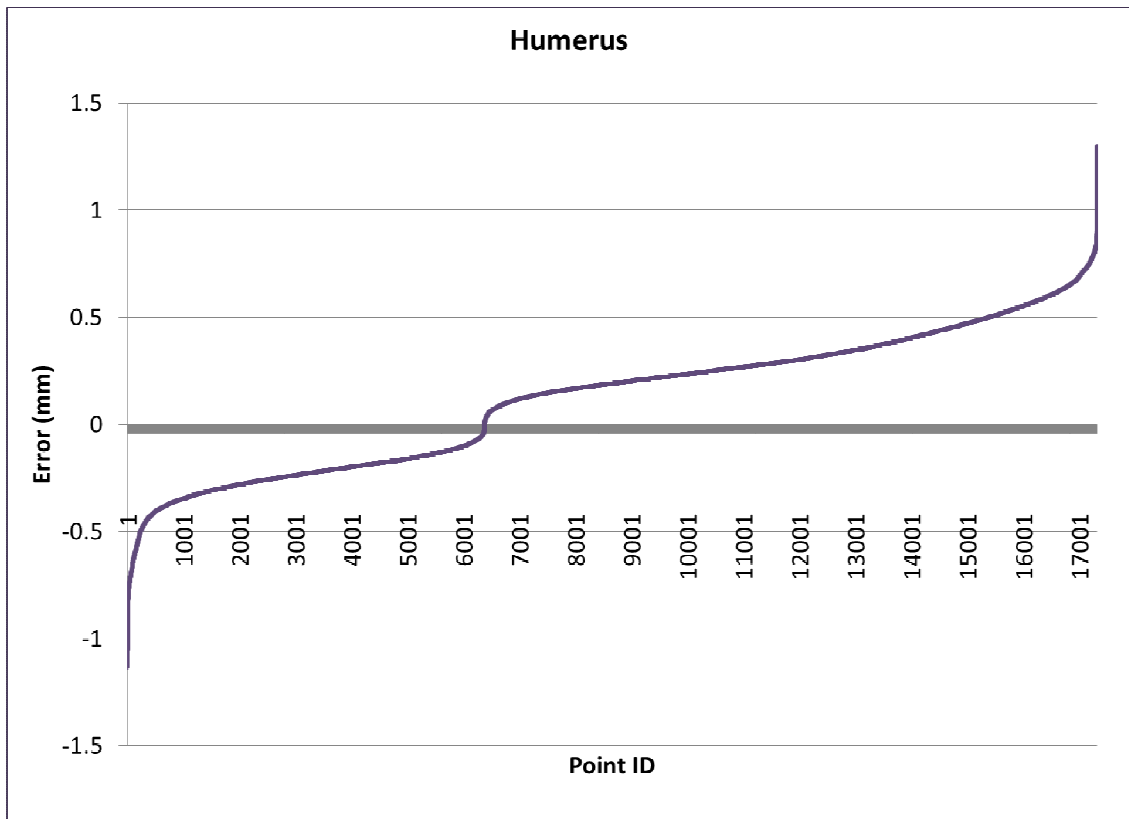
Figure I.9: Distance (error) for the humeral surface
Distances were measured between the registered 3D reconstruction and the reconstructed digitized subchondral bone surface (ground truth). The points, which were given a specific ID, used to measure the inter-surface distances were the vertices of the triangles on the 3D model.
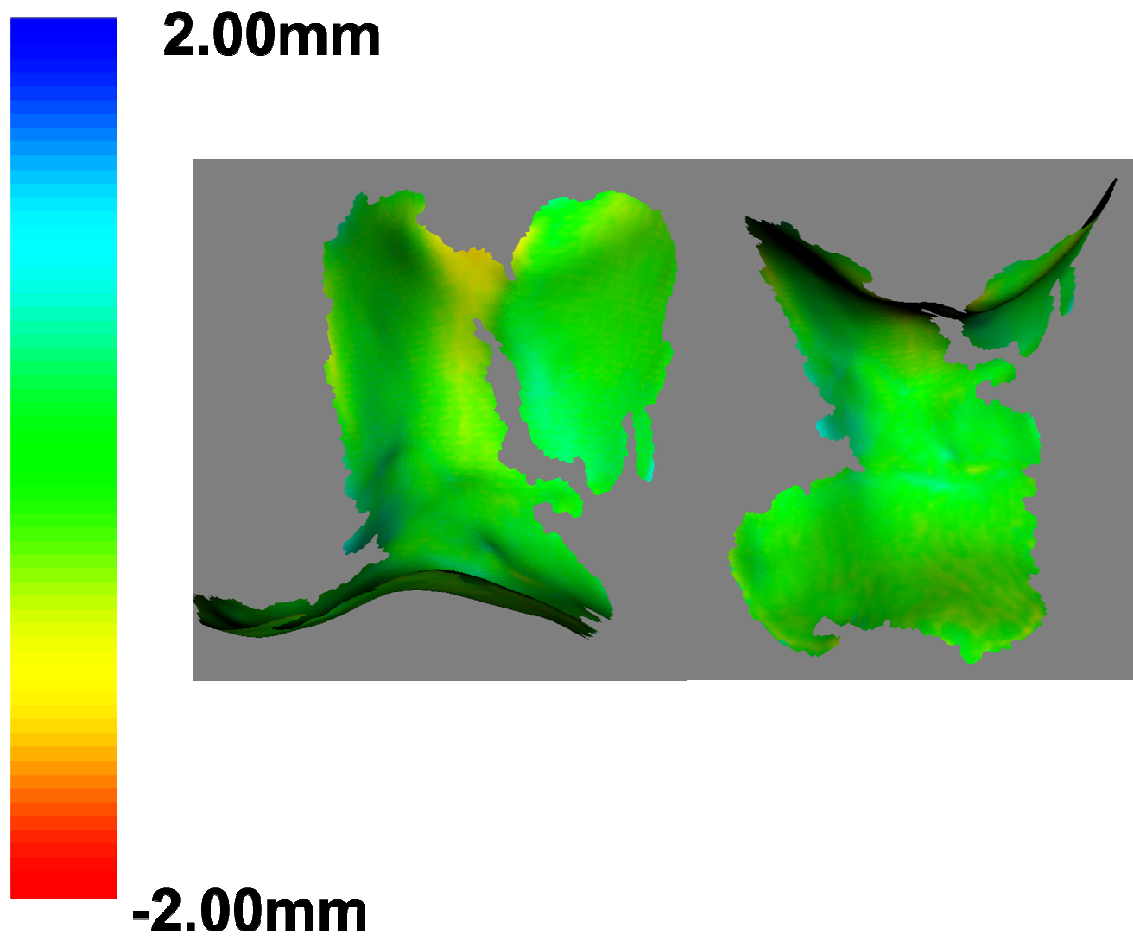
Figure I.10: Distance maps of proximal ulna
Colourmaps were also created for the proximal ulna. A superior and inferior view is shown.
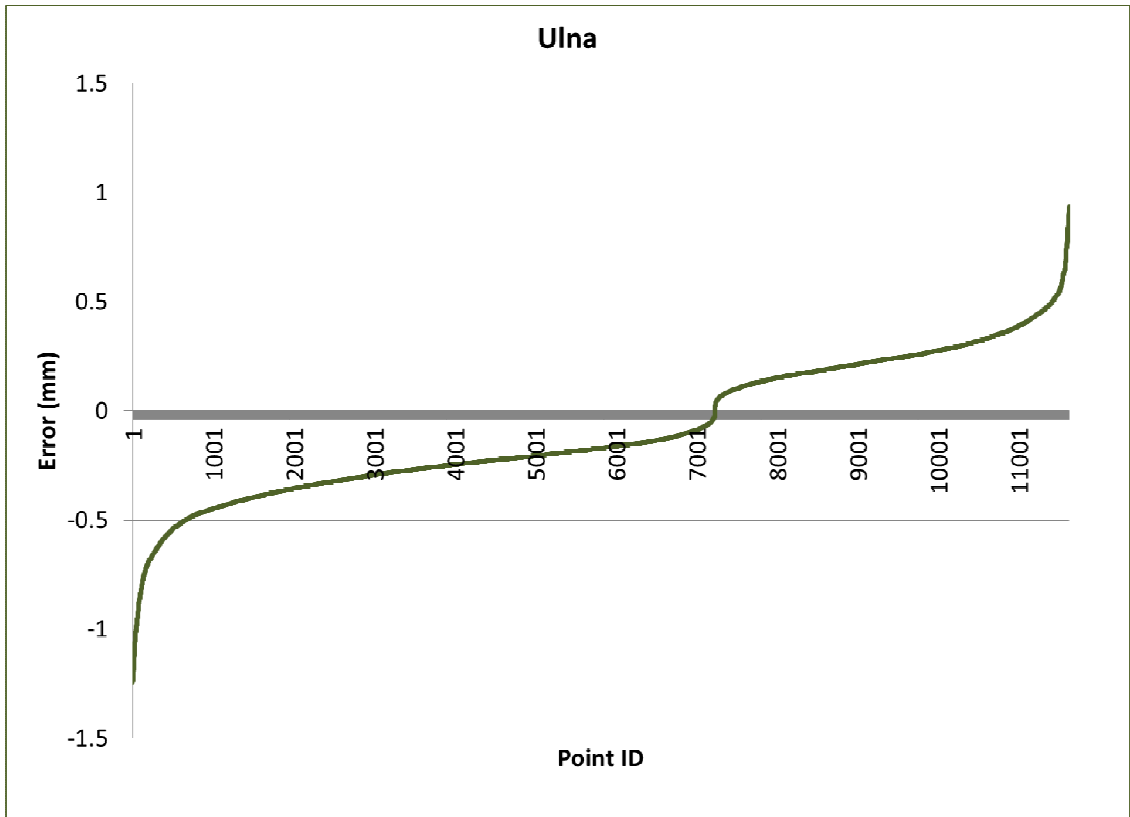
Figure I.11: Distance (error) for the ulna surface
Distances were measured between the registered 3D reconstruction and the reconstructed digitized subchondral bone surface (ground truth).

J. Appendix J –Copyright Releases

J.1 Chapter 2 Copyright Releases

Special Rightsholder Terms & Conditions

The following terms & conditions apply to the specific publication under which they are listed

Computer methods in biomechanics and biomedical engineering

Permission type: Republish or display content

Type of use: reuse in a thesis/dissertation

Taylor and Francis: Terms and Conditions for Book, Periodical and Brochure reuse

Permission is granted for a fee for non exclusive world rights for one edition only. Use beyond this edition requires obtaining another license. This license is granted strictly according to the details of use you specified during the order process and are found in the order details above.

Entire article electronic reuse is excluded with the exception of eBooks.

This license does not cover usage in a Custom Publishing Programme and or database.

This license does not cover cases in which Taylor and Francis material consists of more than 20% of your new work.

This permission does not cover any third party copyrighted work which may appear in the material requested.

Full acknowledgement must be included showing article title, author, full Journal title, date of publication and publisher, reprinted by permission of the publisher (Taylor & Francis Ltd, http://www.tandf.co.uk/journals).

All reasonable efforts must be made to contact the author(s) to notify them of your intentions and confirm they are happy with the permission being granted.

No alterations may be made to our work without written consent.

Permission is valid only when payment has been received.

Permission is granted by Copyright Clearance Center Inc (CCC) on Taylor and Francis's behalf and by agreeing to the terms and conditions listed above you also agree to (CCC's) additional terms and conditions as the administrators of this licensing service, these terms and conditions are agreed to as a condition of establishing an account and

may be seen at any time at http://myaccount.copyright.com.

Special Conditions

The following terms only apply to signatories of the International Association of Scientific, Technical and Medical (STM) Publishers guidelines. http://www.stm-assoc.org/about-stm. Taylor and Francis adheres to STM guidelines, providing some reuse licenses for free as specified in the guidelines. We are pleased to grant you non exclusive world rights in English and in all languages, in print and electronic editions of this Work in its first and future editions and revisions, on the following conditions:

The original source of publication and Taylor & Francis Ltd., are acknowledged in the caption, including a reference to the Journal's web site: http://www.informaworld.com

You do not license to any third party permission to reproduce this copyrighted material, in any form, and at any time.

This permission does not cover any third party copyrighted work which may appear in the material requested.

Other Terms and Conditions: None

v1.6

Permission type selected:

Republish or display content

Type of use selected:

reuse in a thesis/dissertation

Select different permission

Article title:Development of an image-based technique to examine joint congruency at the elbow

Date:Jan 13, 2012

J.2 Chapter 4 Copyright Releases

INFORMA   HEALTHCARE

ORDER DETAILS

Jun 18, 2012

This is an Agreement between ("You") and Informa Healthcare ("Informa Healthcare"). It consists of your order details, and the payment terms and conditions.

Order Number

500679578

Order date

Jun 12, 2012

Licensed content publisher

Informa Healthcare

Licensed content publication

Computer Aided Surgery

Licensed content title

Accuracy assessment of an imaging technique to examine ulnohumeral joint congruency during elbow flexion

Licensed content author

Emily A. Lalone, Terry M. Peters, Graham W. King et al.

Licensed content date

May 1, 2012

Volume number

17

Issue number

3

Start Page

142

End Page

152

Type of Use

Dissertation/Thesis

Requestor type

Author of this article

Format

print and electronic

Portion

Full article

Will you be translating?

no

Number of copies

50

Order reference number

Title of your thesis / dissertation

Examining Joint Congruency at the Elbow

Expected completion date

Aug 2012

Estimated Size (pages)

350

Billing Type

Invoice

Billing address

Informa Healthcare: Terms and Conditions for reuse of Figures, Tables, Questionnaires, Images, Excerpts, Full Article/Chapter in a Thesis/Dissertation

Informa Healthcare (or a company within the group of which Informa Healthcare forms a part) is the publisher of the Journal/Book. The material you have licensed (hereafter "Material") was published in the Journal/Book and Informa Healthcare has the right, title and authority to grant licenses for the use of the Material.

Informa Healthcare grants You license to use the Material on the terms set out in this license (hereafter "License"). Informa Healthcare reserve all rights not expressly granted in this License.

This License is non-exclusive, revocable, worldwide and personal to You.

This permission authorization is valid for a period of 12 months commencing from the date as specified in the order details and is granted strictly according to the details of use specified in the order details.

This License is granted for the lifetime of one edition of the Thesis/Dissertation up to the production run figure as specified in the order details, as applicable, only. You agree further editions require a further license.

The Material is licensed to You in hard copy, reprinted, format only for academic study, research and evaluation purposes only. Your educational institution is permitted to deposit one electronic version in a their Institutional Repository. You shall ensure that use in that Institutional Repository is password protected.

You are permitted to distribute the quantity ordered to third parties for use under the terms of this License but otherwise no rights are granted to any third party and You will not assign, transfer, sub-license or otherwise deal with Your rights and obligations under this License.

All rights in the Material (including, without limitation, copyright and all other intellectual property rights), remain the sole and exclusive property of Informa Healthcare.

This permission does not cover any third party copyrighted work which may appear in the material requested or articles where Informa Healthcare does not control the copyright.

Full citation shall be given by you in the reference list or bibliography of the Thesis/Dissertation and an acknowledgment in the following format shall follow each table or figure legend where reproduced separately from the full article: [Author], [Book title], [Edition], copyright © [Year of publication], Informa Healthcare. Reproduced with permission of Informa Healthcare Or [Author], [Journal title], [Year; Volume (Issue): page range], copyright © [Year of publication], Informa Healthcare. Reproduced with permission of Informa Healthcare

No alterations may be made to our work without written consent. Where alterations are made the citation shall read as follows: [Author], [Book title], [Edition], copyright © [Year of publication], Informa Healthcare. Adapted with permission of Informa Healthcare Or [Author], [Journal title], [Year; Volume (Issue): page range],

copyright © [Year of publication], Informa Healthcare. Adapted with permission of Informa Healthcare.

You will pay any cost detailed above (hereafter " License Fee") in accordance with the Terms and Conditions of CCC. The grant of this License is conditional upon full payment by You of the License Fee. Whilst you may exercise the rights licensed immediately upon the grant of this License, this License will be automatically revoked if you do not pay the License Fee as required.

In the event that You breach any of the terms of this License and fail to remedy such breach (if the same is capable of remedy) within 14 days of receiving written notice of the breach, Informa Healthcare will be entitled to terminate this License with immediate effect. You shall cease all use of the Material if this License is revoked or terminated. Any continued use of the Material after revocation or termination will be a breach of the rights (including, without limitation, intellectual property rights) of Informa Healthcare.

You shall indemnify Informa and keep it fully indemnified against any claims, losses, damages, costs, expenses (including reasonable legal expenses) or other liability incurred by it in respect of any infringement of its rights (including intellectual property rights) arising from Your use of the Material in breach of this license.

You have requested a license to use the Material. You are deemed to have full knowledge of the Material and Informa Healthcare will not be liable for:

any loss of revenue, profit, data, information: or

for Your use or inability to use the Material; or

for any indirect, special or consequential damages arising in connection with the License or the Material, even if Informa Healthcare has been advised of the possibility of such damages.

Informa Healthcare's liability to You in contract, tort (including negligence) or otherwise in relation to this License is limited to the License Fee. However, Informa Healthcare does not exclude or limit liability for fraud or for death or personal injury resulting from its negligence.

The publication contains information from reputable sources and although reasonable efforts have been made to publish accurate information, Informa Healthcare makes no warranties (either express or implied) as to the accuracy or fitness for a particular purpose of the information or advice contained herein. Informa Healthcare wishes to make it clear that any views or opinions expressed in the publication by individual authors or contributors are their personal views and opinions and do not necessarily reflect the views/opinions of Informa Healthcare.

To the extent that any information or guidance contained in this publication is intended for use by medical professionals, it shall serve strictly as a supplement to the medical professional's own judgement, knowledge of the patient's medical history, relevant manufacturer's instructions and the appropriate best practice guidelines. Because of the rapid advances in medical science, any information or advice on dosages, procedures, or diagnoses should be independently verified. The publication does not indicate whether a particular treatment is appropriate or suitable for a particular

individual. Ultimately it is the sole responsibility of the medical professional to make his or her own professional judgements, so as appropriately to advise and treat patients. Save for death or personal injury caused by the Informa Healthcare's negligence and to the fullest extent otherwise permitted by law, neither Informa Healthcare nor any person engaged or employed by Informa Healthcare shall be responsible or liable for any loss, injury or damage caused to any person or property arising in any way from the use granted herein.

Permission is granted by Copyright Clearance Center Inc (CCC) on Informa Healthcare's behalf and by agreeing to the terms and conditions listed above you also agree to CCC's additional terms and conditions as the administrators of this licensing service, these terms and conditions are agreed to as a condition of establishing an account and may be seen at any time at http://myaccount.copyright.com. Should any inconsistency exist between Informa Healthcare Terms and Conditions and CCC's additional terms and conditions, this License shall prevail, but only to the extent of the inconsistency.

This Agreement is the whole agreement between You and Informa Healthcare and supersedes any previous agreement relating to the Material. You acknowledge and agree that in entering into this Agreement You shall not rely on, and shall have no remedy in respect of, any statement, representation, warranty or understanding (whether negligently or innocently made) other than as expressly set out in this Agreement as a warranty.

This License is governed by English law and You and Informa Healthcare submit to the exclusive jurisdiction of the Courts of England and Wales.

On termination of this Agreement, the following clauses shall remain in force: 1, 8, 14-18, 20-22.

Other Terms and Conditions:

v1.0

J.3 Chapter 6 Copyright Releases

To: permissions@iop.org,
Cc:
Bcc:
Subject: Phys. Med. Biol. 56 (2011) 6615-6624- Permission to publish in dissertation
From: Emily Lalone · - Wednesday 13/06/2012 16:30
Sent by:

To whom it may concern,

I am writing to you to seek permission to reprint published in Physics in Medicine and Biology into my dissertation. The title of the work is, "The effect of CT dose on glenohumeral joint congruency measurements using 3D reconstructed patient-specific bone models". I am an author on this paper as well as the following:

Anne-Marie Fox
Angela Kedgley
Thomas Jenkyn
Graham King
George Athwal
James Johnson
Terry Peters.

The reference for this is, "Phys. Med. Biol. 56 (2011) 6615-6624".

The expected date of publication of my thesis is August 2012.

Please let me know if you need further information to seek this permission and what the associated costs are.

Thank you

--

Emily Lalone, B.MSc.
Ph.D. Candidate, University of Western Ontario
Bioengineering Research Laboratory
Hand and Upper Limb Centre, St. Joseph's Health Centre

PERMISSION TO REPRODUCE AS REQUESTED IS GIVEN PROVIDED THAT:

(a) the consent of the author(s) is obtained
(b) the source of the material including author, title of article, title of journal, volume number, issue number (if relevant), page range (or first page if this is the only information available), date and publisher is acknowledged.
(c) for material being published electronically, a link back to the original article should be provided (via DOI).

IOP Publishing Ltd
Temple Circus
Temple Way
BRISTOL   14/06/2012
BS1 6BE   Date   Rights & Permissions

K.   Appendix K –Curriculum Vitae

Emily Allen Lalone, Ph.D. Candidate

Biomedical Engineering Graduate Program, Faculty of Graduate Studies
Hand and Upper Limb Centre St. Joseph's Hospital
Lawson Health Research Institute
The University of Western Ontario

EDUCATION

September 2007-current	**Ph.D. Candidate in Biomedical Engineering** at The University of Western Ontario, London, ON **Thesis Title:** Development of an Image-based Technique to Quantify Articular Contact in the Ulnohumeral Joint of the Elbow **Supervisors:** Dr. James Johnson, Dr. Graham King, Dr. Terry Peters **Expected Graduation Date:** August 2012
June 2007	**Bachelor of Medical Sciences,** Honours Specialization in Medical Biophysics (Medical Sciences Concentration) at The University of Western Ontario, London, ON

ACADEMIC SCHOLARSHIPS

Sept. 2012-Aug. 2014	Lawson Internal Research Fund: Funding for Pilot Project to work as a Postdoctoral Fellow $7500/year
Sept. 2012-Aug. 2013	Joint Motion Program: CIHR Training Program in Musculoskeletal Health Research and Leadership Postdoctoral Fellow $40 000/year
May 2012	Western Graduate Research Scholarship (WGRS) for outstanding academic achievement, $2835
September 2011	Western Graduate Research Scholarship (WGRS) for outstanding academic achievement, $2835
May 2011	WGRS for outstanding academic achievement, $2349

January 2011	WGRS for outstanding academic achievement, $3269
Sept. 2010-Aug. 2012	Joint Motion Program: CIHR Training Program in Musculoskeletal Health Research and Leadership Graduate Student Trainee $25 000/year
Sept. 2010-May 2011	Ontario Graduate Scholarship, $15000
September 2010	WGRS for outstanding academic achievement, $2756
May 2010	WGRS for outstanding academic achievement, $2185
January 2010	WGRS for outstanding academic achievement, $2235
September 2009	WGRS for outstanding academic achievement, $2235
May 2009	WGRS for outstanding academic achievement, $2235
January 2009	WGRS for outstanding academic achievement, $2235
September 2008	WGRS for outstanding academic achievement, $2235
May 2008	WGRS for outstanding academic achievement, $2224
January 2008	WGRS for outstanding academic achievement, $2150
September 2007- 2009	Canadian Arthritis Network Graduate Training Scholarship, $18 000
September 2007	Western Graduate Research Scholarship for outstanding academic achievement, $2150
September 2003-2007	UWO Faculty Dependent's Tuition Scholarship, $9600
September 2003	The University of Western Ontario Entrance Scholarship $2000

HONOURS

March 2009	Awarded 2nd place for podium presentations at Lawson Research Day

June 2007	Graduated from the Medical Biophysics program with Honours, overall average >80%, The University of Western Ontario
September 2003-2007	Dean's Honours List 4 consecutive years

RESEARCH EXPERIENCE

Sept. 2007-current	**Graduate Research Assistant** The Hand and Upper Limb Centre, St. Joseph's Hospital, Department of Biomedical Engineering, **Supervisors:** Dr. James Johnson, Dr. Graham King

- Conduct biomechanical research related to congruency of the distal Radioulnar and Ulnohumeral joints
- Assist with drafting grant proposals
- Co-supervise undergraduate students enrolled in the Undergraduate Medical Biophysics Program
- Mentor master's and junior doctoral students and orthopaedic residents in projects relating to medical imaging, registration, segmentation, computer modelling and programming

Sept. 2006-Dec. 2007	**Research Assistant,** Department of Communication Science and Disorders, Faculty of Health Sciences, The University of Western Ontario **Supervisor**: Dr. Ruth Martin **Title:** Effects of Oropharyngeal Stimulation on Swallowing Recovery and Cortical Plasticity in Hemispheric Stroke: A Randomized Controlled Trial with Functional Magnetic Resonance Imaging (fMRI)

- Project leader for the healthy control portion of this project
- Responsible for all subject recruitment and screening, assisting in fMRI subject preparation and data acquisition during swallowing therapy
- Managed two students who assisted in providing swallowing therapy
- Fabricated custom designed dental splints used to provide the therapy

September- April 2007	**Honours Thesis**, Department of Medical Biophysics, The University of Western Ontario **Supervisors**: Dr. James Johnson and Dr. Graham King **Co-investigators:** Dr. Colin McDonald and Gillian Fraser, PhD Candidate **Title:** Estimating Joint Contact Area in the Distal Radioulnar Joint · Developed a technique using various imaging modalities to non-invasively estimate joint contact area in the distal radioulnar joint

January-April 2006	**Introductory to Medical Biophysics Six Week Project**
	Supervisor: Dr. James Johnson Dr. Graham King
	Co-Supervisor: Gillian Fraser, PhD
	    · Mentored with Gillian while she conducted research investigating The Effect of Colles Distal Radial Fracture: An In-vitro Cadaveric Study
	    · Presented preliminary results to faculty and students in the Medical Biophysics Department

May-August 2006	**Research Assistant,** Department of Communication Science and Disorders, Faculty of Health Sciences
	Supervisor: Dr. Ruth Martin
	Title: Oropharyngeal Swallowing Therapy: A Novel Approach to Swallowing Rehabilitation in Head and Neck Cancer Patients
	    · Provided swallowing therapy for Head and Neck cancer patients during a clinical trial conducted at Victoria Hospital, London, ON
	    · Responsible for fabricating custom designed dental splints

PUBLICATIONS

1. **Lalone E.A.,** Fox A.M., Kedgley A.E., Jenkyn T.R., King G.J.W., Athwal G.S., Johnson J.A., Peters T.M. **(2011)**, "The Effect of CT Dose on Glenohumeral Joint Congruency Measurements using 3D Reconstructed Patient-Specific Bone Models", *Physics in Medicine and Biology,* Oct 21; 56(20), p 6615-24.

2. Fox A.M., Kedgley A.E., **Lalone E.A.,** Johnson J.A., Athwal G.S., Jenkyn T.R. **(2011)**, "The Effect of Decreasing Computed Tomography Dosage on

Radiostereometric Analysis (RSA) Accuracy at the Glenohumeral Joint", *Journal of Biomechanics,* Sept 29 (Epub ahead of print).

3. **Lalone E.A.,** McDonald, C.P., Ferreira L.M., Peters T.M., King G.J.W., Johnson J.A. (**2011**), "Development of an Image-Based Technique to Examine Joint Congruency at the Elbow", *Computer Methods in Biomechanics and Biomedical Engineering.* Article in Press

4. Rafehi S., **Lalone E.A.,** Johnson M., King G.J., Athwal G.S. (**2011**), "An Anatomic Study of Coronoid Cartilage Thickness with Special Reference to Fractures", *Journal of Shoulder and Elbow Surgery,* Aug 30 (Epub ahead of print).

5. Sabo M.T., Shannon H.L., Deluce S., **Lalone E.A.,** Ferreira L.M., Johnson J.A., King G.J. (**2011**), "Capitellar Excision and Hemiarthroplasty Affects Elbow Kinematics and Stability", *Journal of Shoulder and Elbow Surgery,* Aug 3 (Epub ahead of print).

6. **Lalone E.A.,** McDonald, C.P., Ferreira L.M., Peters T.M., King G.J.W., Johnson J.A., (**2010**) "Visualization of 3D Elbow Kinematics using Reconstructed Bony Surfaces", *Medical Imaging 2010*: Visualization, Image-Guided Procedures, and Modeling, Proceedings of SPIE Vol. 7625 (SPIE 7625).

7. Tutunea-Fatan O.R., Bernick J.H., **Lalone E.A.,** Johnson J.A., (**2011**) "Application of Collision Detection to Assess Implant Insertion in Elbow Replacement Surgery", *Medical Imaging 2010*: Visualization, Image-Guided Procedures, and Modeling, Proceedings of SPIE Vol. 7625 (SPIE 7625).

8. Soros P., **Lalone E.**, Smith R., Stevens T., Theurer J., Menon R.S., Martin R.E. (**2008**), "Functional MRI of Oropharyngeal Air-Pulse Stimulation"; *Neuroscience,* 153, 1300-1308.

9. Sabo M.T., Shannon H.L., Deluce S., **Lalone E.A.,** Ferreira L.M., Johnson J.A., King G.J., (**2012**) "Elbow Kinematics After Radiocapitellar Arthroplasty". *Journal of Hand Surgery.* Feb 15 (Epub ahead of print)

10. **Lalone E.A.,** Peters T.M., King G.J.W., Johnson J.A. (**2012**), "Accuracy Assessment of an Imaging Technique to Examine Ulnohumeral Joint Congruency During Elbow Flexion", *Computer Aided Surgery.* Mar 25 (Epub ahead of print)

11. Mostafavi K., Tutunea-Fata R., **Lalone E.A.,** King G., Johnson J. "Determination of Elbow Flexion-Extension Axis Based on Planar and Closed B-Splines-."*Computer-Aided Design and Applications.* Mar 11 (Epub ahead of print)

MANUSCRIPTS IN SUBMISSION

1. **Lalone E.A.,** Giles J., Alolabi B., Peters T.M., Johnson J.A., King G.J. "Application of an Image-Based Technique to Detect changes in Ulnohumeral Joint Congruency Following Collateral Ligament Repair." Submitted to Journal of Biomechanics.

2. Haverstock J.P., Katchky R.N., **Lalone E.A.,** King G.J., Athwal G.S., "Regional Variations in Radial Head Bone Density- Implications for Fracture Patterns and Fixation". JSES

MANUSCRIPTS IN PREPARATION

1. Willing R.T., **Lalone E.A.,** Shannon H.L., King G.J., Johnson J.A. "Validation of a Finite Element Model of the Human Elbow for Determining Cartilage Contact Mechanics".

ABSTRACTS/PRESENTATIONS AT SCIENTIFIC MEETINGS

1. Mostafavi K., Tutunea-Fata R., **Lalone E.A.,** King G., Johnson J. "Determination of Elbow Flexion-Extension Axis Based on Planar and Closed B-Splines-."CAD12 Conference,Niagara Falls, Canada June 11-14, 2012.

2. Desai S.J., Athwal G.S., Ferreira L.M., Johnson J.A., Welsh M.,**Lalone E.A.**, King G.J.W. **(June 2012)**, "Distal Humerus Hemiarthroplasty: The Effect of Implant Sizing on Elbow Joint Kinematics". Canadian Orthropaedic Association, Ottawa, ON; <u>Podium</u>

3. Nishiwaki M., Greeley G., **Lalone E.A.,** Ferreira L.M., Johnson J.A., King G.J.W. **(June 2012)**, "Load Transfer at the Distal Ulna Following Simulated Colles' Malalignment". Canadian Orthropaedic Association, Ottawa, ON; <u>Podium</u>

4. **Lalone E.A.,** Willing R.T., Peters T.M., King G.J.W., Johnson J.A. **(June 2012)**, "Accuracy Assessment of 3D Bone Model Reconstructions". Canadian Orthropaedic Association, Ottawa, ON; <u>Poster</u>

5. Ferreira L.M., Fay K.E., **Lalone E.A.**, Johnson J.A., King G.J.W. **(June 2012)**, "The Effect of Radial Head Excision and Arthroplasty on Medial Collateral Ligament Tension". Canadian Orthropaedic Association, Ottawa, ON; <u>Podium</u>

6. Willing R.T., **Lalone E.A.,** King G.J.W., Johnson J.A. **(June 2012)**, "Comparing Two Constitutive Material Models of Cartilage for Hemiarthroplasty Articular

Contact Mechanics using Computational Analyses". Canadian Orthropaedic Association, Ottawa, ON; <u>Poster</u>

7. Sabo M.T., Shannon H., **Lalone E.A.,** Deluce S., Ferreiar L.M., Johnson J.A., King G.J.W. **(June 2012)**, "Capitellar Hemiarthroplasty Can Restore Normal Elbow Kinematics Compared with Capitellar Excision". Canadian Orthropaedic Association, Ottawa, ON; <u>Poster</u>

8. Sabo M.T., Shannon H., **Lalone E.A.,** Deluce S., Ferreiar L.M., Johnson J.A., King G.J.W. **(June 2012)**, "Radiocapitellar Arthroplasty and Elbow Kinematics". Canadian Orthropaedic Association, Ottawa, ON; <u>Poster</u>

9. Willing R.S., **Lalone E.A.,** King G.J., Johnson, J.A. **(Feb 2012)**, "Comparing Two Constitutive Material Models of Cartilage for Hemiarthroplasty Articular Contact Mechanics using Computational Analyses ", Orthopaedic Research Society, San Francisco, CA; <u>Poster</u>

10. Rafehi S., **Lalone E. A.,** Johnson M., King, G.J.W., Athwal G.S. **(June 2011)**, "An Anatomic Study of Coronoid Cartilage Thickness with Special Reference to Fractures", Canadian Orthopedic Association, St. Johns, NF; <u>Podium</u>

11. Haverstock, J.P., Katchky R. **Lalone E.A.,** King, G.J.W., Athwal G.S.**(June 2011)**, "Regional Variations in Radial Head Bone Density – Implications for Fracture Pattern and Fixation", Canadian Orthopedic Association, St. Johns, NF; <u>Poster</u>

12. **Lalone E.A.,** Giles, J., Deluce, S.R, Peters T.M., King G.J.W., Johnson, J.A., **(June 2011), "**The Effect of Collateral Ligament Repair on Ulnohumeral Joint Congruency" Canadian Orthopedic Association, St. Johns, NF; <u>Poster</u>

13. **Lalone E.A.,** McDonald C.P., Ferreira L.M., King G.J.W., Johnson J.A**. (June 2010)**, "Visualization of 3D Elbow Kinematics Using Reconstructed Surfaces", Canadian Orthopedic Association, Edmonton, AB ; <u>Podium</u>

14. **Lalone E.A.,** McDonald C.P., Ferreira L.M., King G.J.W., Johnson J.A**. (June 2010)**, "An Image-Based Method to Track Articular Motion at the Elbow", Canadian Orthopedic Association, Edmonton, AB; <u>Poster</u>

15. Fay K.E., Ferreira L.M., **Lalone E.A**., King G.J.W., Johnson J.A. **(June 2010)**, **"**The Measurement of Tension in the MCL of the Elbow", Canadian Orthopedic Association, Edmonton, AB ; <u>Podium</u>

16. Ng.J., **Lalone E.A.**, Ferreira L.M., King G.J.W., Johnson J.A. **(June 2010)**, "Determination of the Centre of the Capitellum for Elbow Reconstructive Procedures: The Effect of Digitization Protocols", Canadian Orthopedic Association, Edmonton, AB ; Podium

17. **Lalone E. A.**, McDonald C.P., Ferreira L.M., King G.J.W., Johnson J.A.**(May. 2010),** "Visualization of 3D Elbow Kinematics Using Reconstructed Bony Surfaces", 4th International Workshop on Imaging Based Measures of Osteoarthritis., Vancouver, BC; Poster

18. **Lalone E. A.**, McDonald C.P., Ferreira L.M., King G.J.W., Johnson J.A.**(Mar. 2010),** "Visualization of 3D Elbow Kinematics Using Reconstructed Bony Surfaces", Orthopedic Research Society, New Orleans, LA, USA; Poster

19. Fay K.E., Ferreira L.M., **Lalone E.A**., King G.J.W., Johnson J.A.**(Mar. 2010), "**The Measurement of Tension in the MCL of the Elbow", Orthopedic Research Society, New Orleans, LA, USA; Poster

20. **Lalone E. A.**, McDonald C.P., Ferreira L.M., King G.J.W., Johnson J.A. **(Feb. 2010)** "Visualization of 3D Elbow Kinematics Using Reconstructed Bony Surfaces", SPIE Medical Imaging; Poster

21. Tutunea-Fatan O.R., Bernick J.H., **Lalone E.A.,** King G.J.W., Johnson J.A.**(Feb 2010)** "Application of Collision Detection to Assess Implant Insertion in Elbow Replacement Surgery", SPIE Medical Imaging; Podium

22. **Lalone E.A.,** McDonald C.P., Ferreira L.M., King G.J.W., Johnson J.A**. (2009)**, "An Image-Based Method to Track Articular Motion at the Elbow", Lawson Research Day-London; Podium

23. **Lalone E.A.,** McDonald C.P., Ferreira L.M., Fraser G.S., King G.J.W., Johnson J.A**. (2008)**, "Development of an Image –Based Method of Quantifying Articular Contact in the Ulnohumeral Joint", Canadian Arthritis Network Annual Scientific Conference-Toronto, ON; Poster

24. **Lalone E.A.,** McDonald C.P., Ferreira L.M., Fraser G.S., King G.J.W., Johnson J.A**.; (2008)**, "Development of an Image –Based Method of Quantifying Articular Contact in the Ulnohumeral Joint"; 2nd Annual Workshop on Imaging Based Measures of Osteoarthritis "Why Aren't We There Yet?" Boston, MA, USA; Poster

25. McDonald C.P., Fraser G.S., **Lalone E.A.,** King G.J.W., Johnson J.A.; **(2008)**, "Development of X RAY Computed Tomography Based method of Quantifying

Articular Contact for the Distal Radioulnar Joint"; Canadian Orthopaedic Research Society 2008- Quebec City, QC; <u>Poster</u>

OTHER PRESENTATIONS

1. **Lalone E.A.,** McDonald C.P., King G.J.W., Johnson J.A.; **(2009)** "An Image-Based Method to Track Articular Motion at the Elbow"; Talks of Fridays (TOFS) Lawson Health Research Institute, The University of Western Ontario, London, ON; Oral Presentation

2. **Lalone E.A.,** McDonald C.P., Fraser G.S., King G.J.W., Johnson J.A**.; (2008)**, "An Image –Based Method of Quantifying Articular Tracking at the Elbow"; Biomedical Engineering Seminar Series, Faculty of Graduate Studies, The University of Western Ontario, London, ON; Presentation

3. **Lalone E.A.,** McDonald C.P., Fraser G.S., King G.J.W., Johnson J.A**.; (2008)**, "Development of an Image –Based Method of Quantifying Articular Contact in the Ulnohumeral Joint"; Communications Course, Faculty of Graduate Studies, The University of Western Ontario, London, ON; Poster

4. **Lalone E.A.,** McDonald C.P., Fraser G.S., King G.J.W., Johnson J.A**.; (2008)**, "Development of an Image –Based Method of Quantifying Articular Contact in the Ulnohumeral Joint"; Communications Course, Faculty of Graduate Studies, The University of Western Ontario, London, ON; Presentation

5. **Lalone E.A.,** McDonald C.P., Fraser G.S., King G.J.W., Johnson J.A**.; (2008)**, "Development of an Image –Based Method of Quantifying Articular Contact in the Ulnohumeral Joint"; Biomedical Engineering Seminar Series, Faculty of Graduate Studies, The University of Western Ontario, London, ON; Presentation

6. **Lalone E.A.,** McDonald C.P., Fraser G.S., King G.J.W., Johnson J.A**.; (2007)**, "Estimating Joint Contact in the Distal Radioulnar Joint"; Undergraduate Year Thesis Presentation, Department of Medical Biophysics, London, ON

TEACHING EXPERIENCE

Supervisory Experience:

July 2011	**Western Engineering Summer Academy, Biomechanics:** Course instructor on Joint Mechanics and Medical Imaging used in Biomechanical Research.
March 2011	**PGSY-4 Orthopaedic Resident Project:** **Resident: Sagar Desai**

Co-investigated a project where Sagar developed hemi-arthoplasty elbow replacements and examined joint kinematics and stability. Additionally, we examined the effect of implant size on stability and congruency at the ulnohumeral joint.

July 2010	**Dean-Western Engineering Summer Academy, Biomechanics:** Coordinator of the summer engineering academy biomechanics course. I designed five individual biomechanics topics, organized six instructors and coordinated a two-one week long summer academy workshops.
May 2011	**Co-investigator of Biomedical Engineering Master's Research Project** **Student: Hannah Shannon** Mentored and co-investigated a study examining the effect of radial head implant design on result joint contact mechanics.
March 2010	**PGSY-4 Orthopaedic Resident Project:** **Resident: Bashar Alolabi** Co-investigated a project investigating a novel coronoid implant and investigated the effectiveness of this implant at restoring joint kinematics and mechanics.
January 2010-May 2010	**Co-supervision of 3rd year Medical Biophysics Student** **Student:** Jessica Kishimoto is investigating the effect of CT dose and bone reconstruction quality of a cadaveric glenohumeral joint.
May 2009-August 2010	**Co-supervision of Anatomy & Cell Biology Graduate S student** **Student:** Samah Rafehi is investigating cartilage thickness at the coronoid process using computed tomography scans and reconstructed surfaces
May-August 2009	**Co-supevision of summer NSERC Student** **Student:** Jennifer Ng analyzed 25 reconstructed distal humeral and ulnar surfaces to examine the effect of region location and size of digitization used on calculated geometric centres of anatomical landmarks

May-August 2009	Collaboration with undergraduate summer student Student: Josh Bernick worked on a study developing a program to detect collision of implant stems with bony canals.
January – April 2009	**Co-supervision of 3rd year Medical Biophysics Student** **Student:** Hannah Shannon analyzed kinematic motion data statistical significance to investigate the effect of Radial Head Arthroplasty on elbow kinematics
January –April 2008	**Co-supervision of 3rd year Medical Biophysics Student** **Student:** Truc Tran assisted with data collection in the investigation of the effect of radial head excision and replacement on Ulnohumeral joint congruency
January –April 2008	**Co-supervision of 3rd year Medical Biophysics Student** **Student:** Rachel Brown designed a project to measure cartilage deformation at the Ulnohumeral joint under axially loaded conditions

Teaching Assistant:

Sept 2011-Dec 2011	Biomedical Engineering Seminar Series Organizer Organize seminar schedule, take attendance and collect evaluations of weekly seminar series
Sept 2010-April 2011	Biomedical Engineering Seminar Series Organizer
Sept 2009-April 2010	Biomedical Engineering Seminar Series Organizer
Sept-Dec 2008	Introductory to Engineering Design and Innovation Studio **Professor:** Dr. James Johnson • Attended weekly studio design sessions, organized presentations and graded first year engineering assignments
Sept-Dec 2007	Medical Biophysics: Introductory to Transport Systems **Professor:** Dr. Ian MacDonald • Responsibilities included tutoring students with course content during weekly lab sessions and grading all assignments
January –April 2008	Medical Biophysics: Introductory to Medical Imaging

Professor: Dr. Ian MacDonald
- Graded assignments and assisted students with course material on an individual basis and during office/lab hours

INSTRUMENTATION EXPERIENCE

Laboratory:
- Computer Programming in Python
- Use the Visualization Toolkit as well as (ITK, ITK Snap, Paraview)
- Assist surgeons with preparation of cadaveric specimens for lab protocols
- Efficient with staining technique using Alcian Blue for determining cartilage thickness
- Competent with Reprosil dental casting for joint cavity contact measurements
- LabVIEW and Flock of Birds electromagnetic tracking device
- Fabricated custom oral splints made from dental impressions and vacuum formed resin
- Familiar with imaging modalities such as XRAY computed tomography, Micro XRAY Computed tomography, functional magnetic resonance imaging(fMRI) and FastSCAN laser scanner

Computer:
- Attended Brain Voyager Workshop at The University of Western Ontario (June 2007)
- Familiar with Matlab languages, Office XP Professional, Reference Manager, Mimics Software, LabVIEW, Visualization Toolkit and Powerlab

ACADEMIC EXTRACIRRUCILAR ACTIVITIES

March 2010	Lawson Research Day Poster Judge, London, ON
December 2009	Advisory Committee for the selection of Associate Dean, Graduate & Postdoctoral Studies
October 2008	Canadian Arthritis Network Annual Scientific Conference, Toronto, ON
March, 2008	Canadian Arthritis Network Trainee Workshop, Toronto, ON
May 2007, 2008	Computer Assisted Orthopaedic Surgery, Discovery Day Presenter, University of Western Ontario, and London, ON
February 2007	Orthopaedic Research Society 53rd Annual Meeting, San Diego, CA

March 2007	Sister Mary Doyle Research Day, London, ON
June 2007	Canadian Orthopaedic Research Society, Halifax, NS
February 2008	Attended Orthopaedic Research Society 54th Annual Meeting, San Francisco, CA